Introduction to the Nuclear and Particle Physics Lab Course

Joachim Wolf (Editor)

(based on the script by F. K. Schmidt)

Institute of Experimental Particle Physics

Karlsruhe Institute of Technology (KIT)

Edition: November 17, 2023

This book is based on the so-called "Blue Book" of F.K. Schmidt, who wrote this introduction in the course of his decades of work as head of the nuclear physics students lab. After the text went through different Microsoft Word versions, the Blue Book has been converted into LaTeX in 2015. Hundreds of formulas have been transcribed by Steffen Albert in LaTeX. At this point I would also like to thank the many assistants who revised and updated the individual experimental descriptions time and again. Special thanks is due to Mrs. Knoch who keeps this script up to date. In particlular, I want to thank Roxanne Turcotte-Tardif, who translated the original German version into English.

During past semesters the data acquisition of several experiments was upgraded. In previous versions, most of the measured spectra were accumulated by so-called multichannel-analyzers, usually as plug-in boards in PCs (some experiments still use this hardware). The modernized hardware consists mostly of data acquisition systems with fast ADCs, which digitize the pulse shapes of the signals from the detectors. The data are transfered to a computer, where they are analyzed with Python-based code. The code usually runs in a Jupyter notebook, a specialized software environment for Python. Several templates are available, which provide examples for the analysis and error calculation. A new chapter on error calculation has been added by Günter Quast in 2021.

Since the upgrade of the experiments is still ongoing, it is recommended to check for a new version of the "Blue Book" before starting to prepare for the experiment. It is also possible that the description of the experiment has not been updated to the latest hardware changes. In this case, the tutors will advise you on the updated analysis methods. This mostly concerns the selection of events and the filling of histograms.

Karlsruhe, 01.09.2021, Joachim Wolf

Contents

Chapter 1

Introduction

The present introduction to the nuclear and particle physics part of the Advanced Physics Lab Course at the Karlsruhe Institute for Technology will assist you in the preparation, execution, and analysis of the experiments. On one hand, this should help you to negotiate your way in a new or at least less familiar field of physics, saving you a considerable amount of time, by covering in a handy way the most important concepts and methods, which would otherwise be only accessible by researching from multiple sources.

On the other hand, this work aims to present the measurement methods and problems, which at first sight can appear confusingly diverse, to classify measurement problems with regard to similarities, and to present them in a clear manner. **Of course, it is not intended to replace a lecture on nuclear and particle physics nor the study of literature.**

The introduction is divided into three parts. In the first part, (Chap.2-4), the basics are explained; the types and most important properties of radiation regarding this lab course, the matter-radiation interactions, and the radiation detectors. This part contains the most important concepts of nuclear physics, as far as used here, and the basics for nuclear physics measurements. This provides the foundation required for understanding and carrying out each experiment in this course. Note that this only applies to a limited extend to the detectors section, where a more extensive description is given on the properties and modes of operation than required.

In the second part (Chap.5-6), the electronics and the structure of the experiments are explained by block diagrams. These chapters also include data acquisiton methods, analysis, and fitting procedures. Some experiments use plug-in technology, in which the operation of the electronics are implemented in separate units, combined in a single crate with a common power supply. It is possible to set up all experiments by combining a few plug-in modules. The block diagrams, which describe the functioning of the electronics, are therefore principally a schematic representation of the actual structure. To obtain and process the data generated in the experiments, only a few standard set-ups are required, which will be explain here. Recent updates of the data acquisition systems include fast digitization of the measured signal pulses. The physical hardware is more and more replaced by software analysis of the digitized pulse shape. Still, the process of selecting a valid signal (event) includes methods that emulate the functions of the hardware moduls.

The third part, the experimental part, contains the tasks, the description of the experimental setup, the execution steps, the evaluation of the individual experiments, and, if necessary, an introduction to the underlying physics principles. All quantities and useful formulas are given here, but it will be nevertheless often beneficial to consult the literature given for each experiment for a deeper understanding.

In addition to tables for β spectroscopy, the appendix includes the term diagrams of all radioactive sources used in the lab course, the bibliography, and an index to facilitate the use of this book.

Chapter 2

Type and properties of radiation

In the lab course, we will work with the radiation from radioactive decays, with muons from cosmic rays and with data from the CMS particle detector (LHC, CERN). In most experiments, artificially produced isotopes are used, which can undergo α (helium nuclei), β^- (electrons), β^+ (positron), γ (photons) or neutrons decays. The energy of these quanta lies in the order of several keV to a few MeV. The experiments are limited to the study of the properties of these particles and through them it is also possible to access the properties of the nuclei, as well as their electromagnetic interaction with matter. Not represented here is the large area of nuclear reactions, i.e. the strong interaction and the related issues of interaction and core models.

In the following section, the radioactive decay and the most important properties of the emitted particles in this process are discussed. This is followed by a sub-chapter on neutron sources and an introduction to the most important elements of the standard model of particle physics.

2.1 The α decay

In an α decay, a parent nucleus with an atomic number Z and a mass number A emits a ^{4}He nucleus, i.e. an α particle ($Z = 2$, $A = 4$), then the nucleus decays into a nucleus with an atomic number $Z - 2$ and a mass number $A - 4$ (Fig. 2.1). The decay can be written symbolically by

$$ {}^{A}_{Z}X \rightarrow {}^{A-4}_{Z-2}Y + {}^{4}_{2}He \tag{2.1} $$

On both sides of the decay equation, the number of protons (Z) and the number of nucleons (A) stay the same. This is a property of all radioactive decays; the baryon number and the charge obey conservation laws.

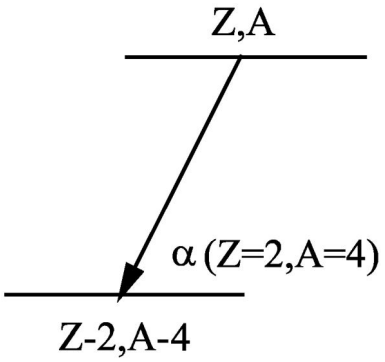

Figure 2.1: α-decay.

The decay in Fig. 2.1 is energetically possible only if the nuclear mass on the left side is greater than the sum of the nuclear masses on the right. If one adds on both sides Z times the electron masses, then the nuclear masses can be expressed by the atomic masses M and the condition for the decay is that the decay energy Q is positive. So

$$Q = \left[M(Z,A) - M(Z-2,A-4) - M(^4_2He)\right] \cdot \mathrm{c}^2 \tag{2.2}$$

According to the law of conservation of energy

$$Q = E_{\mathrm{kin}}(\alpha) + E_{\mathrm{kin}}(Y) \tag{2.3}$$

The law of conservation of momentum demands (non-relativistic)

$$m_\alpha \cdot E_{\mathrm{kin}}(\alpha) = m_Y \cdot E_{\mathrm{kin}}(Y) \tag{2.4}$$

It follows from this

$$E_{\mathrm{kin}}(\alpha) = Q \cdot \frac{m_Y}{m_Y + m_\alpha} \tag{2.5}$$

Thus, the α particle receives a discrete energy during decay, which is determined by the Q-value and the mass of the parent nucleus. The radioactive α radiation is therefore monochromatic.

Using the semi-empirical mass formula of Weizsäcker [1], which gives the dependence of the nuclear masses on the atomic number and mass number, it is possible to estimate for which nuclei the decay condition is fulfilled. According to this, all nuclei with $A > 150$ should be unstable with respect to the α decay. It is indeed observed that all the α-instable nuclei have in fact a mass numbers greater than 150. There are, however, nuclei in this range that are stable. The explanation for this is that in many cases, the available decay energies are very small, so that, as will be discussed further below, the probability of decay is extremely low and the decays can no longer be detected.

The experimentally determined lifetimes lie in the wide range of 10^{-6} s to 10^{17} s. But even the shortest lifetimes are still very large compared to the lifetime of 10^{-21} s characteristic for strong interaction, which is equivalent to the time need for a fast particle to go through a nucleus. This means that the α-radioactive nuclei are relatively stable.

The mean lifetime τ or the probability of decay λ depend on the kinetic energy E_{kin} of the α particles. First, an empirical relation (Geiger-Nuttal) of the form

$$\begin{aligned} \log_{10}(\lambda) &= a - b \cdot Z \cdot (E_\alpha)^{-1/2} \\ a, b &= \text{const.} \end{aligned} \tag{2.6}$$

was found, which expresses that as α energy increases, the probability of decay increases very rapidly.

An explanation of the α decay, like any radioactive decay in general, is not possible in classical physics. As in classical physics, a particle with a determined kinetic energy cannot overcome a potential barrier higher than its energy. Thus, once surrounded by that potential well, the particle would remained trap in it forever.

In quantum mechanics, however, the so-called tunnel effect exists. According to this, there exists a finite probably for a particle when colliding with a potential well to penetrate it. This is not to be understood in such a way that when experimentally trying to detect the particle, a fraction of it would be inside the well and the rest outside. In order to verify the quantum probability statement, *many* particles have to be detected. We can then experimentally observe that from all the particles, a *determined number* of particles is beyond the well. This correspond

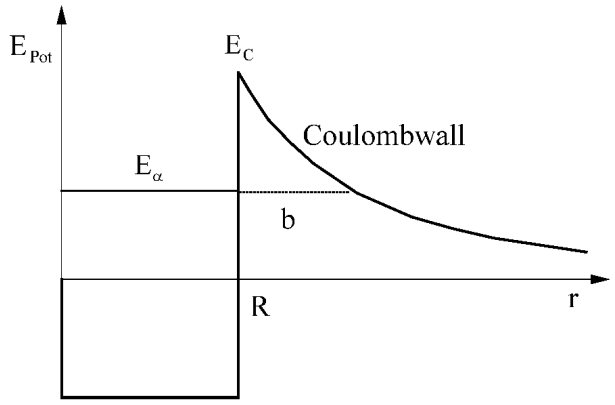

Figure 2.2: tunnel effect on the α decay.

exactly to the probability density of an individual particle traversing the barrier. These particles behave as if they tunneled through the barrier, hence the naming of tunnel effect.

It was Gamov, who, based on the tunnel effect, developed a theory of theα-decay. This is based on the following ideas. The nucleus is composed of a finite collection of protons and neutrons, in which an α particle with a determined kinetic energy is formed. The nucleons and the α particles are subjected to the strong interaction which ensures the (relative) stability of the nucleus and which can be describe as a potential well because of its finite range effect on the α particle. This well has a finite deepness, it is cylindrically symmetric, with its radius equal to the nucleus radis R. Outside the nucleus, the α particle subject only to the electromagnetic Coulomb interaction. The Coulomb energy increases with the approach to the nucleus, reaches its maximum value at the nucleus edge and disappears at infinite distance.

$$E_{\mathrm{c}} = \frac{1}{4\,\pi\,\epsilon_0} \cdot \frac{z \cdot Z \cdot \mathrm{e}^2}{R} \tag{2.7}$$

where Z is the charge of the nucleus and z the charge of the α particle.

The potential of the α particle as a function of its distance r from the center of the nucleus has therefore the specified values shown in Fig. 2.2. Within the nucleus ($r < R$), the nuclear forces act with short range that are represented by the potential well. Outside ($r > R$) the long-range Coulomb force is dominant. In classical physics, there is no possibility for a particle with an energy smaller than the Coulomb energy E_{c} located within the nucleus to escape it. With quantum mechanics, it is only the case for particles with a negative energy for whom the potential barrier is infinitely wide. For particles with positive energies, e.g. E_α in fig. 2.2, there is a certain probability of going through the finitely wide potential barrier. If this happens, then it behaves as if it has tunneled through the barrier along the dashed line.

The probability of going through the barrier can be calculated and is approximately

$$T = \exp - \left(\frac{1}{4\,\pi\,\epsilon_0} \cdot \frac{8 \cdot z \cdot Z \cdot \mathrm{e}^2 \cdot m \cdot b}{\hbar^2} \right)^{1/2} \tag{2.8}$$

where

$$b = \frac{1}{4\,\pi\,\epsilon_0} \cdot \frac{z \cdot Z \cdot \mathrm{e}^2}{E_\alpha} \tag{2.9}$$

E_α is the kinetic energy of the α particle at a great distance from the nucleus and m its mass. T is the transmission coefficient and is defined as the ratio of the flux passing through the potential barrier to the incident flux.

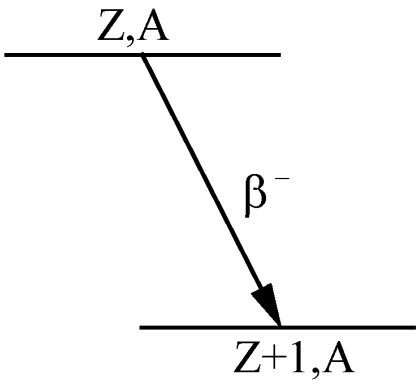

Figure 2.3: β^- decay.

The equation 2.8 contains the most important properties of the tunnel effect. The transmission decreases very strongly with increasing energy of the height of the barrier, which in the case is given by the charge $Z{\cdot}e$ of the nucleus and $z{\cdot}e$ of the particle. It also decreases sharply with increasing width b, which is equivalent to decreasing energy of the particle because of equation 2.9. The dependence on m states that light particles tunnel faster than heavy ones. At the transition to classical mechanics ($h = 0$) the transmission disappears, the penetration of a potential barrier is then no longer possible.

With Eqn. 2.8 the decay constant λ can be written

$$\lambda = \frac{v}{2\,R} \cdot T \tag{2.10}$$

This formula is based on a very simple idea. It is assumed that the α particle inside the nucleus moves freely at the velocity of v. Each time it reaches an edge, there is a probability T to leave the nucleus. The probability of an α decay per unit time is then given by the product of T and the number of appearances at the edge of the nucleus per time unit. The latter is the reciprocal time required for the particle to traverse the nucleus, and that is $2R/v$.

The Eqn. 2.10, which is only a rough approximation, since for example the dependence of T on the nuclear radius is not taken into account, explains the experimentally found fact that λ can change in a very wide range when E_α changes only slightly.

2.2 The β decays

The β decay is understood as all the decay possibilities of a nucleus in which the number of nucleons, i.e. the mass number A, remains constant, and the atomic number Z changes by one unit. There are three types of these: β^- decay, β^+ decay, and electron capture.

2.2.1 The β^- decay

In the β^- decay the nucleus emits an electron and increases its atomic number from Z to $Z+1$ (Fig. 2.3). Energetically, this process is allowed when the mass of the parent nucleus is greater than that of the daughter nucleus and an electron mass m_0. The transition energy E^{β^-} is the difference between these masses. This can be expressed either with the nuclear masses m or with the atomic masses M. It is

$$\begin{aligned} E^{\beta^-} &= [m(Z,A) - m(Z+1,A) - m_0] \cdot \mathrm{c}^2 \\ &= [M(Z,A) - M(Z+1,A)] \cdot \mathrm{c}^2 \end{aligned} \tag{2.11}$$

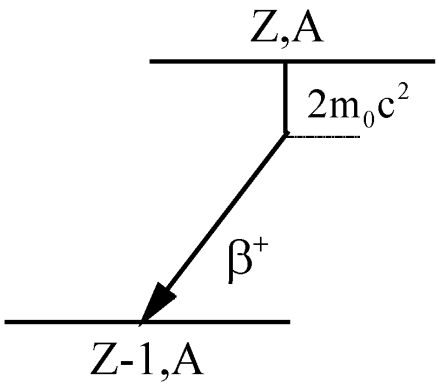

Figure 2.4: β^+ decay.

Of course, the two representations are equivalent, thus

$$M(Z,A) = m(Z,A) + Z \cdot m_0$$

and the difference of the binding energies of the shell electrons of two atoms which differ by one atomic number can be neglected.

2.2.2 The β^+ decay

In the β^+ decay the nucleus emits a positron and decrease its atomic number from Z to $Z-1$. The transition energy E^{β^+} must be positive.

$$\begin{aligned} E^{\beta^+} &= [m(Z,A) - m(Z-1,A) - m_0] \cdot \mathrm{c}^2 \\ &= [M(Z,A) - M(Z-1,A) - 2 \cdot m_0] \cdot \mathrm{c}^2 \end{aligned} \tag{2.12}$$

The term diagram of the decay is shown in Fig. 2.4. In it, the ground states of the nuclei are given in *atomic* masses and not in *nucleus* masses. This way of representation has historical and practical reasons. Masses were and are still measured with mass spectrometers, and they measure *atomic* masses. As one can see, not the entire energy difference is available for the decay, but only the energy difference reduced by the rest energy of the two electrons. If one would have used the *nuclear* masses as energy scale instead, the ground state would have been lower by exactly that amount and the picture would be analogous to that of the β^- decay.

2.2.3 The electron capture

In electron capture (EC), the nucleus captures an electron from the shell, thereby decreasing its atomic number by one. The transition energy is determined by the mass excess of the parent nucleus plus an electron mass over the mass of the daughter nucleus.

$$\begin{aligned} E^{\mathrm{EC}} &= [m(Z,A) - m(Z-1,A) + m_0] \cdot \mathrm{c}^2 \\ &= [M(Z,A) - M(Z-1,A)] \cdot \mathrm{c}^2 \end{aligned} \tag{2.13}$$

The comparison of Eqn. 2.12 and Eqn. 2.13 shows that electron capture and β^+ decay simultaneously occur when the parent atom is heavier by more than two electron masses than the daughter atom. Pure electron capture exists only for smaller mass differences.

The capture of electrons from the inner shells is preferred. The reason for this is that these (especially in the K-shell) have a greater probability of being at the location of the nucleus than the outer ones.

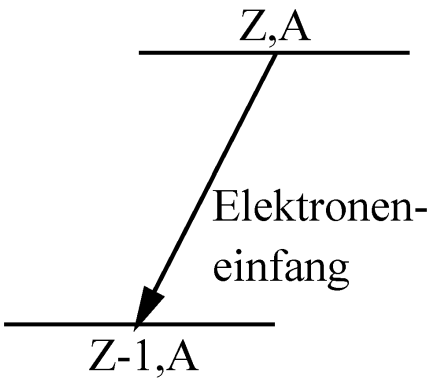

Figure 2.5: Electron capture.

2.2.4 The β decay as a three particles problem

The β^+ or β^- decays can be detected directly by measuring the energy spectra of the emitted particles. Unlike the α decay, their spectrum is continuous. If the decays do not go to the ground state but to an excited state, then electrons with discrete energies can also appear. They arise by internal conversion of the excitation energy. More details are given in the chapter on the γ decay (2.3).

It's different with electron capture. Since no charged particles are produced here, the decay can only be detected indirectly via the radiation emitted by the daughter nucleus. This radiation comes as follows: after the electron capture of the parent nucleus, the daughter atom is in a highly excited state because of its inner shell electron missing. The electron hole is then filled by the transfer of an electron from a higher shell or from the continuum (e.g. metal). In this process, the excitation energy (equal to the binding energy of the electron that has disappeared into the nucleus) is released. Then, there are two possibilities, either a photon is emitted, the so-called characteristic X-ray(characteristic stands for the atomic number of the atom), or the excitation energy is transferred to an electron in a higher shell. This is called the Auger effect . Thus, the electron will be emitted with a discrete energy, namely the difference between the excitation energy of the hole and the binding energy of the Auger electron.

The continuous shape of the energy spectra (Fig. 2.6) of the emitted electrons and positrons in the β decays could not be explained immediately after discovery. From the decay diagrams Eqn. 2.3 and Eqn. 2.4, one would expect that the leptons, just like the α particles in the α decay, would have a discrete energy that is equal to the available transition energy. However, experimentally it was found that only a few particles have the transition energy E_0, and that this is equal to the *maximum* energy of the spectrum. It was hypothesized that the β particles are emitted with the transition energy, but as the move away, they more or less loose energy. This view was disproved by calorimetric measurements, where it was shown that the average kinetic energy of the β particles is smaller than the transition energy. Thus, the law of energy conservation seemed to be violated.

The way out of this tricky situation was shown by Pauli. He postulated that in the β decay, aside from the charged particles, another uncharged particle is emitted. This particle was called neutrino because it was expected to behave neutrally, although it could not be detected with any apparatus of that time. In the meantime, this has been achieved and it is known today that the neutrino is uncharged and very light and that is only subject to the weak interactions, which is why it is so difficult to detect.

Now we know that in the β decay, there are three particles in the final state. The conservation of energy and momentum allows that the transition energy can be distributed arbitrarily amongst them. The recoil energy of the daughter nucleus can be neglected because it's much heavier than

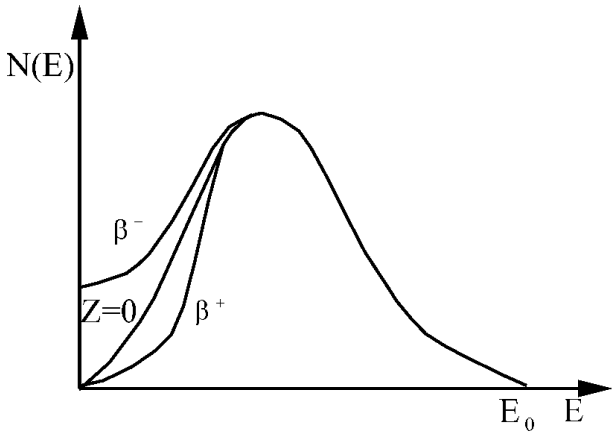

Figure 2.6: Shape of the β spectrum.

a lepton. So the β particle can appear with all energies from zero up to the transition energy. The neutrino gains the missing energy. It has zero kinetic energy when the β particle has the maximum energy and vice versa. The shape of the β spectrum is thus understood. Taking into account the neutrino, the β^- decay can be written as follows

$$\mathrm{n} \rightarrow \mathrm{p} + \mathrm{e}^- + \bar{\nu}_\mathrm{e} \tag{2.14}$$

A neutron transform into a proton, thereby producing an electron and an anti-neutrino. This decay actually occurs because a neutron is heavier than a proton and an electron together. The free neutron is unstable, its half-life is about 10 min. The need to introduce here the neutrino's anti-particle does not follow from the previous energetic consideration. Rather, it has emerged only in the course of the development of the theory of β decay that the leptons, to which the neutrinos belong, are always created as a lepton-antilepton pair. Therefore, when the neutron decays, the particle electron and the antiparticle anti-neutrino are produced together.

With the β^+ decay

$$\mathrm{p} \rightarrow \mathrm{n} + \mathrm{e}^+ + \nu_\mathrm{e} \tag{2.15}$$

the emitted antiparticle positron is accompanied by the particle neutrino. The β decay of a free proton is energetically not possible, it is stable. Only when bound in a nucleus, can the binding energy provide the necessary energy for the decay.

The lepton number, a quantum number, is assigned to the leptons in such a way that a lepton has the lepton number +1 and an anti-lepton receives the lepton number -1, then the occurrence of an anti-neutrino in Eqn. 2.14 and a neutrinos in Eqn. 2.15 can be understood as a conservation law of lepton numbers. One can see that on both sides of these relations are the lepton numbers equal to zero. For the β decay, therefore, the conservation laws of the electrical charge, baryon number and lepton number are valid.

It becomes clear that with electron capture

$$\mathrm{e}^- + \mathrm{p} \rightarrow \mathrm{n} + \nu_\mathrm{e} \tag{2.16}$$

a neutrino and not an anti-neutrino are emitted and that, in this case, the lepton number on both sides is +1.

The three decay equations for the β decay can be combined into a single, symmetric one. It does not contain any more antiparticles and reads as follow

$$\mathrm{n} + \nu_\mathrm{e} \leftrightarrow \mathrm{p} + \mathrm{e}^- \tag{2.17}$$

It says that the conversion of the leptons happens simultaneously with the conversion of the nucleons. When the Eqn. 2.17 is read from right to left, it expresses the electron capture. The β^- decay results from adding one anti-neutrino on both side. The left side then contains a neutrino – anti-neutrino pair that annihilates and is no longer carried in the equation. In the same way, adding a positron gives the β^+ decay

2.2.5 The shape of the β spectrum

The shape of the β spectrum is essentially determined by the phase space available to the particles in the final state. It can be derived by a simple observation. According to Fermi's *Golden Rule*, the transition probability per time unit in an energy interval $\mathrm{d}E_0$ of the final state is given by

$$\omega_{fi} = \frac{2\,\pi}{h} \cdot \frac{\mathrm{d}n}{\mathrm{d}E_0} \cdot |H_{fi}|^2 \tag{2.18}$$

where H_{fi} is the transition matrix element and $\mathrm{d}n/\mathrm{d}E_0$ is the density of final states in the interval $\mathrm{dE_0}$. The quantity ω_{fi} is observable by the number of β particles emitted per time unit. If the energy interval $\mathrm{d}E_0$ corresponds to the momentum range of the electron between p and $p + \mathrm{d}p$, then

$$N(p) \cdot \mathrm{d}p = \omega_{fi} \tag{2.19}$$

The density of states $\mathrm{d}n/\mathrm{d}E_0$ can be calculated as follows. The phase space of a particle cannot be smaller than h^3 according to the uncertainty principle :

$$\Delta x \cdot \Delta y \cdot \Delta z \cdot \Delta p_x \cdot \Delta p_y \cdot \Delta p_z \geq h^3 \tag{2.20}$$

Thus, if an electron possesses an momentum between p and $p + \mathrm{d}p$ and is located in the volume V, its phase space is

$$V \cdot 4\,\pi \cdot p^2 \cdot \mathrm{d}p \tag{2.21}$$

The number of electrons possible in this phase space is

$$\mathrm{d}n_{\mathrm{e}} = \frac{1}{h^3} \cdot V \cdot 4\,\pi \cdot p^2 \cdot \mathrm{d}p \tag{2.22}$$

The same is true for neutrinos with a momentum between p_ν and $p_\nu + \mathrm{d}p_\nu$

$$\mathrm{d}n_\nu = \frac{1}{h^3} \cdot V \cdot 4\,\pi \cdot p_\nu^2 \cdot \mathrm{d}p_\nu \tag{2.23}$$

Thus, the total number of states in $\mathrm{d}E_0$ is

$$\frac{\mathrm{d}n}{\mathrm{d}E_0} = \frac{\mathrm{d}n_{\mathrm{e}} \cdot \mathrm{d}n_\nu}{\mathrm{d}E_0} = \left(\frac{4\,\pi}{h^3}\right)^2 \cdot V^2 \cdot p^2 \cdot \mathrm{d}p \cdot p_\nu^2 \cdot \mathrm{d}p_\nu \cdot \frac{1}{\mathrm{d}E_0} \tag{2.24}$$

Two approximations are made for the further calculation. First, the recoil energy of the daughter nucleus is neglected. Then

$$E_0 = E + E_\nu \tag{2.25}$$

where E and E_ν are the kinetic energies of the electron and the neutrino, respectively. Second, it is assumed that the neutrino has a negligible rest mass. Then the following holds for the momentum of the neutrino.

$$p_\nu = \frac{E_\nu}{\mathrm{c}} = \frac{1}{\mathrm{c}} \cdot (E_0 - E) \tag{2.26}$$

Now the neutrino momentum can be removed, because

$$p_\nu^2 \cdot \frac{\mathrm{d}p_\nu}{\mathrm{d}E_\nu} = \frac{1}{\mathrm{c}^3} \cdot (E_0 - E)^2 \tag{2.27}$$

Finally, the result is

$$N(p) \cdot \mathrm{d}p = K \cdot p^2 \cdot (E_0 - E)^2 \cdot |H_{fi}|^2 \cdot F(Z, E) \cdot \mathrm{d}p \tag{2.28}$$

where K is an energy independent constant. The factor $F(Z, E)$, which depends on the atomic number of the daughter nucleus, is added. It is called the Fermi function and takes into account the Coulomb interaction of the emitted lepton with the daughter nucleus. It is different for electrons and positrons and is tabulated in the appendix A.2 for different nuclei.

In Fig. 2.6, according to Eqn. 2.28, the number of electrons is plotted versus the kinetic energy, *at which they are detected*. The spectrum extends continuously from zero to the maximum energy E_0. Not drawn to scale is the different behavior of electrons and positrons due to the Coulomb interaction. The central curve applies to an uncharged daughter nucleus where the electrostatic forces are turned off and the Fermi function is constant and equal to one. It therefore gives the "pure" spectrum of a three-body decay. It can be seen that the number of electrons become smaller and smaller as the kinetic energy approaches zero. The Coulomb energy changes the shape of the spectrum at low energies. The *electrons* are *decelerated* after emission. So if they are detected with a certain energy, they must have had initially a higher one. However, at higher energy, according to the "pure" spectrum, more electrons appear. Therefore, the electron spectrum starts with a finite value at zero (detection) energy and is overall higher at low energies than without attraction. Contrarily, *positrons are accelerated*, resulting in a thinning of the spectrum at low energies.

With the equation 2.28, the transition matrix element H_{if} and the transition energy E_0 can be determined. For this purpose, it is written in a linearized form with respect to the energy E, which is called Curie plot after its inventor.

$$\sqrt{\frac{N(p)}{p^2 \cdot F(E, Z)}} = C \cdot (E_0 - E) \cdot |H_{fi}| \tag{2.29}$$

The count rate $N(p)$ is measured as a function of the electron momentum p. On the left side, next to the measurable quantities $N(p)$ and p, is the calculable Fermi function. On the right, the constant C is known and the energy E can be calculated from the momentum. If the left hand side is plotted over the kinetic energy of the lepton, then, provided that the matrix element is independent of the energy, a straight line results (Fig. 2.7). The variable E_0 can be obtained by the intersection with the E axis and H_{fi} by the slope.

The condition for the linearity of the Curie plot is the energy independence of the matrix elements. It is true for allowed β transitions. For forbidden transitions, the dependence on energy is considered by the so-called Shape-Factor.

The curie plot has the advantage over the Eqn. 2.28 that E_0 can be obtained just by extrapolating a straight line. This is more accurate than determining the curve by measuring the count rates, which, after all, go towards zero just at the end of the spectrum. Moreover, it makes possible a simple estimation of the rest mass of the neutrinos. In the derivation, it was assumed to be zero. If, on the other hand, it is assumed to be finite, then the spectrum changes in the upper part. It deviates from the straight line to intersect perpendicularly to the E-axis. The difference ΔE of the intersection to E_0 is the rest energy of the neutrino. Therefore, by measuring the high-energy end of the spectrum, extremely accurately, an upper limit for the value of the neutrino mass can be derived. If the neutrino mass is not too small, its value can be derived from such a measurement, for instance with the KATRIN experiment at KIT [3]. It

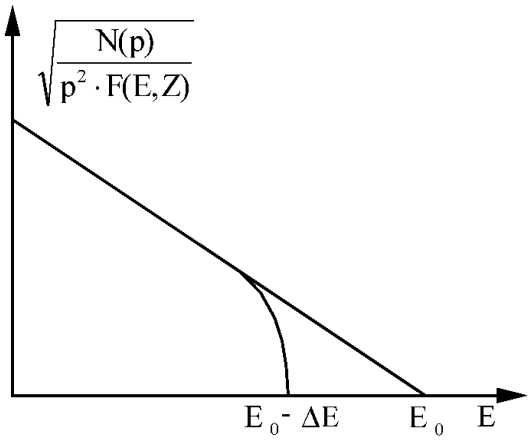

Figure 2.7: Curie plot.

is advantageous to measure nuclides with a small transition energy, such as tritium, because the effect of a finite mass is then greater.

There are three types of neutrino. The three flavor eigenstates of the leptons (electron, muon, tau) are conserved in the weak interaction. If neutrinos have mass, it may be that the three mass eigenstates are not equal to the three flavor eigenstates. If a neutrino is produced with a unique flavor state (e.g. electron neutrino in the β decay), it consists of a mixture of the three mass eigenfunctions. Since these mass eigenfunctions propagates at different speeds, depending on the mass eigenvalue, a phase shift can occur at some distance from the neutrino source. Thus, the neutrino wave function is not a unique flavor eigenfunction anymore. A neutrino detector can then, with a known probability, detect a neutrino with a different flavor than that of the original neutrino. Since the probability for this effect varies periodically with distance, it is called neutrino oscillation. In recent years, neutrino oscillation experiments have detected flavor oscillations in neutrinos from the sun, the atmosphere, from accelerators, and from nuclear reactors. Since this effect only occurs when neutrinos have a rest mass, albeit a small one, it is now assumed that neutrinos do have a mass.

The current upper limit for the mass of the electron anti-neutrino is 0.8 eV (90% C.L.). This value was measured with the β spectrum of tritium in the KATRIN experiment [4, 5] located at KIT. It is expected to improve its sensitivity over time to about 0.2 eV/c^2.

2.3 The gamma γ decay

The γ decay occurs in conjunction with the α- and β-decay when the transitions do not lead to the ground state but to an excited state of the daughter nucleus. These excited states then decay to the ground state under emission of γ-radiation.

The γ radiation is electromagnetic. As is usual in electrodynamics, the radiation field can be developed using multipoles. Electric (EL) and magnetic (ML) multipole radiation occurs, whose order is given by the angular momentum L of the radiation field. The multipole order is 2^L. The magnetic multipole radiation differs from the electric one by the parity. The parity of the electric is $(-1)^L$, that of the magnetic $(-1)^{L+1}$. Electric multipole radiation of an even L therefore has even parity. Due to the conservation of angular momentum, the number of multipole orders occuring at the transition between two nuclear states is limited. There is a vectorial relation between the angular momenta of the initial state J_i, the final state J_f, and the multipole field L.

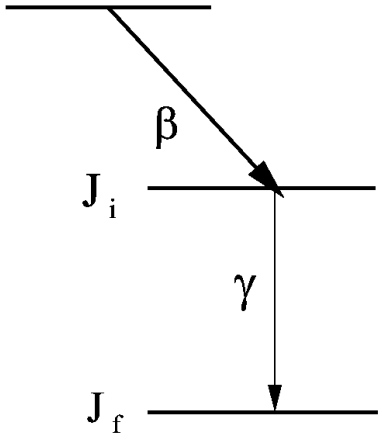

Figure 2.8: γ-decay.

$$\vec{J_i} + \vec{L} = \vec{J_f} \tag{2.30}$$

from which it follows

$$\Delta J = |J_f - J_i| \leq L \leq |J_i + J_f| \tag{2.31}$$

The probability for the emission or absorption of dipole radiation is essentially given by

$$W \approx \left(\frac{R}{\lambda}\right)^{2L} \tag{2.32}$$

where R is the radius of the nucleus and λ is the wavelength of the radiation. The probability for the magnetic radiation is one order of magnitude smaller than that of the electric radiation of equal multipolarity. Therefore, it can be observed in emission only if the electric one is forbidden by selection rules (parity).

For γ-radiation, $R/\lambda \approx 1/100$. Therefore, the radiation with the lowest order predominates. However, higher orders can still be detected in contrast to optical transition where R/λ is smaller by another order of magnitude.

Typical average lifetimes of excited nuclear states with respect to E1-radiation are $10^{-12}\,s$. However, if the spins of the initial and final states are very different and, moreover, the states are closely neighbouring (high multipolarity and large λ), then average lifetimes up to 0.1 s are possible. One speaks then of isomeric transitions.

2.4 The internal conversion

In connection with the γ decay occurs the internal conversion. Here, the excitation energy of the nucleus is not released by emission of a γ-quantum but is directly transferred to an electron in the atomic shell in a 1st order process. It is most likely to happen for the K-electrons because of their bigger probability of being in the vicinity of the nucleus. This must not be understood as a photoelectric effect, in which a γ quantum is first emitted from the nucleus, which in a further step releases an electron. This would be a 2nd order process, which is much less probable than it is observed experimentally.

The electron leaves the shell with a discrete energy equal to the excitation energy minus the binding energy of the electron, e.g. for a K-electron

$$E_e = E_\gamma - E_K \tag{2.33}$$

The strength of the internal conversion is expressed by the total conversion coefficient α. It is defined as the ratio of the probability λ_e that a conversion occurs and the probability λ_γ of a γ transition.

$$\alpha = \frac{\lambda_e}{\lambda_\gamma} = \frac{N_e}{N_\gamma} \tag{2.34}$$

These probabilities are proportional to the total rate of conversion electrons N_e created and the rate of the γ quanta N_γ. According to Eqn. 2.33, the energy of the conversion electrons depends on the shell in which the conversion occurs. Therefore, when measuring with high energy resolution, it is possible to distinguish between the conversion electrons of the different shells. One introduces partial conversion coefficients α_K, α_L, α_M, etc., which are related to the individual shells.

$$\begin{aligned} \alpha_K &= \frac{\lambda_{eK}}{\lambda_\gamma} = \frac{N_{eK}}{N_\gamma} \\ \alpha_L &= \frac{\lambda_{eL}}{\lambda_\gamma} = \frac{N_{eL}}{N_\gamma} \end{aligned} \tag{2.35}$$

and accordingly for the higher shells. The following then applies

$$\alpha = \alpha_K + \alpha_L + \alpha_M + \cdots \tag{2.36}$$

Sometimes it is advantageous to work with the conversion *ratios*. It is the ratio of the conversion coefficients of two shells and independent of the probability of the γ decay (or the rate of the γ quanta).

The values of the conversion coefficients become considerably large for γ-transitions of high multipolarity, which are strongly suppressed. Their measurement is an essential part of nuclear spectroscopy. They depend on spin and parity of the nuclear states, and can therefore be used to determine these quantities. The practical approach is to compare the measured values with the theoretical values tabulated for each quantum number. Since the microscopic structure of the nucleus is also included in the calculation, one also obtains a statement about the different nuclear models.

2.5 Neutron sources

Neutrons are emitted during nuclear transformations, which can be divided into three groups:

Nuclear fission: Heavy nuclei split spontaneously or induced by nuclear reactions into (usually two) fragments. In the process, some of the excess neutrons evaporate. Each fission produces a few fast neutron, e.g. with ^{235}U on average 2,7.

Nuclear fusion: The fusion of e.g. a deuteron with a tritium nucleus produces a neutron in addition to the α particle.

Nuclear reactions, of which the two first groups are special cases. Reactions with a high effective cross section are selected for neutron production. The most common are the (γ,n)- and (α,n)-reactions, in which a γ quantum or an α particle is captured by a nucleus and a neutron is emitted.

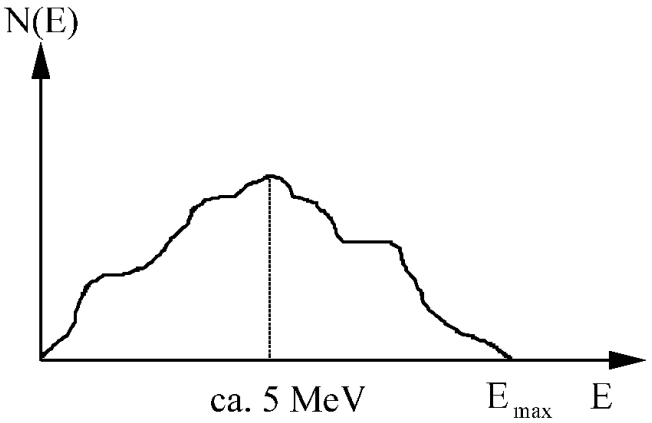

Figure 2.9: Energy spectrum of a neutron source.

An example of a (γ-n) reaction is the photo fission of the Deuteron

$$\mathrm{d} + \gamma = \mathrm{n} + \mathrm{p} + Q \tag{2.37}$$

with which one can determine the binding energy of the deuteron. Q is called the Q-value of the reaction and is an indicator for the heat released. It is defined as either the difference of the kinetic energies of the reactants after and before the reaction or equivalently as the difference of the particle masses before and after the reaction. In the present case, the Q-value is -2.2 MeV. It's negative, which means that energy must be applied to split the deuteron. This is precisely the binding energy. The deuteron is lighter by exactly this amount than the neutron and proton combined.

In the lab course, an Am-Be source is used as neutron source, in which the neutrons are produced by a (α,n)-reaction with ^{9}Be

$$^{9}\mathrm{Be} + \alpha \rightarrow \mathrm{n} + ^{12}\mathrm{C} + Q \tag{2.38}$$

It has a positive Q-value of 5.7 MeV. Thus, a considerable amount of energy is released, which is essentially taken by the neutron, since the recoil energy of the ^{12}C is small. The α source is ^{241}Am, which emits several groups of α particles, of which the most energetic ones have an energy of 5.49 MeV and 5.44 MeV. The isotopes ^{241}Am and ^{9}Be are thoroughly mixed in the source so that the α particles meet a Be-nucleus within their range.

The neutrons produced in this way have a continuous energy spectrum, which is qualitatively shown in Fig. 2.9. It is continuous because the neutrons in Eqn. 2.38 are emitted at arbitrary angles with respect to the incident α particles and thus receive different energies, and because the α particles loose already part of their kinetic energy in the source by deceleration before the reaction occurs. The most likely neutron energy is about 5 MeV. The spectrum cuts off at the maximum energy E_{max}.

$$E_{\mathrm{max}} = Q + E_{\alpha} - E_{\mathrm{R}} \tag{2.39}$$

It occurs when the neutrons are emitted forward, i.e. in the direction of the incoming α particles. E_{α} is the highest α energy with 5.49 MeV and E_{R} is the small, negligible recoil energy of the ^{12}C nucleus. E_{max} is then 11,19 MeV.

A neutron source always emits γ quanta, which originate from α transitions to excited states. ^{241}Am has the advantage compared to other α emitters, such as Ra and Po isotopes, that the γ radiation has lower energies and is therefore easier to shield.

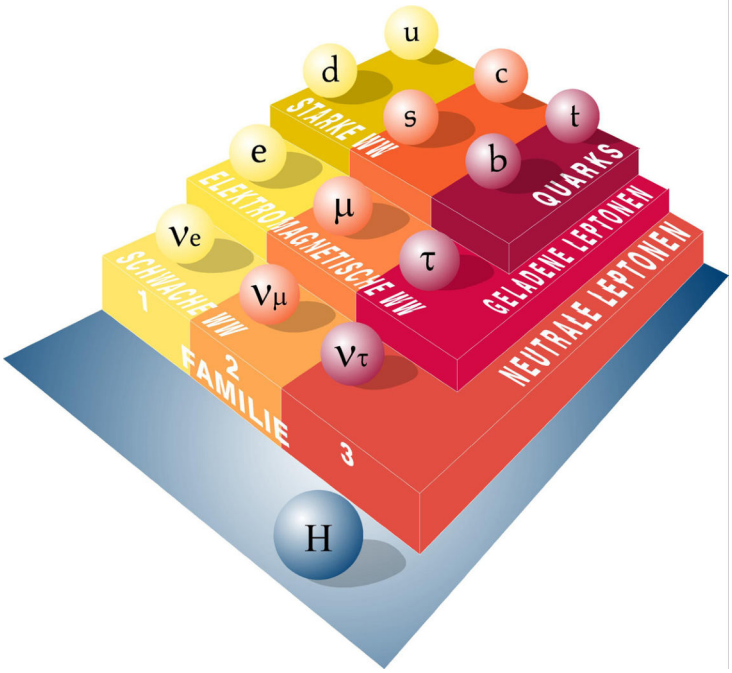

Figure 2.10: Schematic representation of the 3 particle generations and the interaction. Neutrinos only interact weakly (weak), while charged leptons interact weakly and electromagnetically. Quarks also take part in the strong interaction.

2.6 Standard model of particle physics

The Standard Model (SM) is the current model, in which the elementary particles and their interactions are described. It is based on a gauge theory in which the re-normalizable parameters can be compared with experimentally measurable quantities of the particles.

A distinction is made between two large groups of elementary particles. On the one hand, there are the fermions (spin 1/2 - particles) and on the other hand, the bosons (spin 1 - particles).

The fermions represent the elementary building blocks of matter and can be divided into leptons and quarks. They are sorted into three generations, each generation comprises 2 leptons and 2 quarks. The first-generation contains as leptons the electron (e^-) and the corresponding electron neutrino (v_e) and as quarks the *up* (u) and *down* quarks (d). These four particles are the basis of all ordinary matter.

In addition, there is an associated antiparticle for every particle. While leptons, such as the electron, are freely observable, quarks only exist in bound states. These bound quark states are called hadrons, those with 3 quarks (qqq) are called baryons and those with 2 quarks ($q\bar{q}$) are called mesons. The nucleons are thus baryons. For example, the proton consists of two u-quarks (electrical charge $2 \times +2/3\,|e|$) and one d-quark (electrical charge $1 \times -1/3\,|e|$), leading to the well-known total electric charge of $+1e$. The neutron has the composition udd, which results in an total electrical charge of 0. The second and third generation have a similar structure (see Fig. 2.10 and table 2.1), however the particles in these generations are heavier. These particles can decay into the particles of the first family and therefore do not appear as stable particles in nature. Nevertheless, they can be generated in cosmic-rays or in accelerators.

The bosons (gauge bosons) are the exchange particles for the interactions. The massless gauge boson for electromagnetic interactions is the photon (γ), which couples to all electrically charged particles. The massive bosons of the weak interactions are the Z^0 (91.2 GeV) and the $W^{\pm}$ (80.4 GeV), which couple to all fermions. Those of the strong interactions are called

Table 2.1: Properties of fermions.

leptons			Quarks			
Particle	**Mass (GeV/c^2)**	**Electr. Charge**	**Particle**	**Mass (GeV / c^2)**	**Electr. Charge**	**Color**
ν_e (electron-neutrino)	$< 1 \times 10^{-9}$	0	u (up)	0.004	2/3	r, g, b
e^- (electron)	0.000511	-1	d (down)	0.0075	-1/3	r, g, b
ν_μ (muon neutrino)	$< 1 \times 10^{-9}$	0	c (charm)	1.23	2/3	r, g, b
μ^- (muon)	0.106	-1	s (strange)	0.15	- 1/3	r, g, b
ν_τ (tau neutrino)	$< 1 \times 10^{-9}$	0	t (top)	175	2/3	r, g, b
τ^- (Tau)	2	-1	b (bottom)	4,2	- 1/3	r, g, b

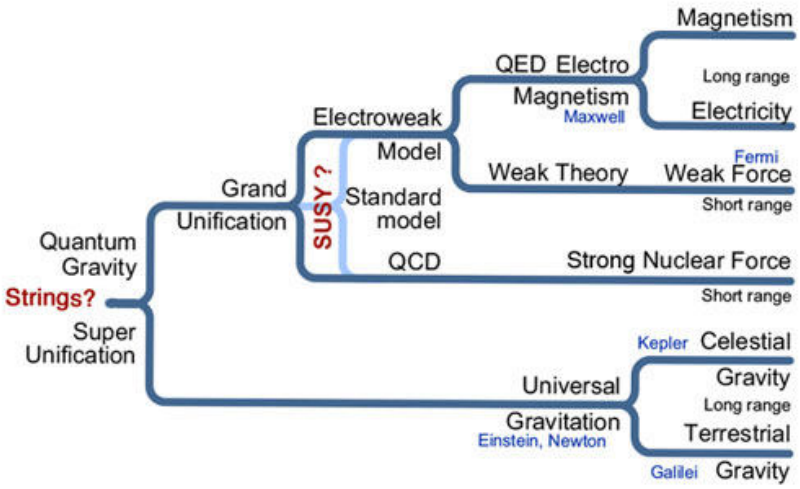

Figure 2.11: The unification of interactions.

gluons (g), which only couple to carriers of color charge, the quarks. Gravity is currently not described by the standard model. Every interaction is characterized by a coupling constant that determines the strength of the interaction. The electromagnetic coupling constant is the well-known fine structure constant (α) in atomic physics. For instance, it determines the coupling between photons and electrons. For the weak interaction, there is the weak coupling constant (α_w), which describes couplings with W and Z bosons. Similarly, the coupling constant of the strong interaction (α_s) determines the coupling between quarks and gluons.

The standard model is a quantum field theory based on the gauge symmetry $SU(3)_C \times SU(2)_L \times U(1)_Y$. This gauge group contains the symmetry group of the strong interactions, $SU(3)_C$, and that of the electroweak interactions, $SU(2)_L \times U(1)_Y$. The symmetry group for the electromagnetic interaction, $U(1)_{em}$, occurs in the SM as a subgroup of $SU(2)_L \times U(1)_Y$ and is to be understood in the framework of the unification of the weak and electromagnetic interactions. This formalism was mathematically developed by S. Glashow, A. Salam and S. Weinberg, for which they received the Nobel Prize in 1979.

However, the SM also poses a number of problems. Some of them are :

Table 2.2: Properties of the interactions and their bosons.

interaction	**Boson**	**mass** ($\mathbf{GeV/c^2}$)	**range (m)**	**charge**	**electr. charge**	**spin parity**	**coupling constant**	**dimensionless coupling constant**
electro-magnetic	γ (Gamma)	0	∞	electrical	0	1^-	–	$\alpha = e^2/4\pi\,\hbar c = 1/137$
weak	Z^0	91,173	10^{-18}	weak	0	1^+	G_F (Fermi)	$(Mc/\hbar)^2\,G_F/\hbar c = 1.02\times10^{-5}$
	$W^{\pm}$	80.22	10^{-18}	weak	± 1	1^-	G_F (Fermi)	$(Mc/\hbar)^2\,G_F/\hbar c = 1.02\ \times10^{-5}$
strong	8 g (Gluons)	0	$\leq 10^{-15}$	color	0	1^-	-	$\alpha_s \approx 1$, r large $\alpha_s < 1$, r small
Gravitation	G (Graviton)	0	∞	mass	0	2^+	K (Newton)	$KM^2/\hbar c = 0.53\times10^{-38}$

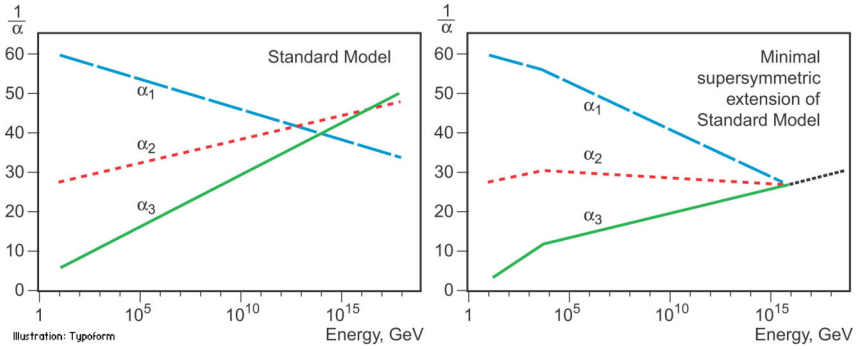

Figure 2.12: Variable coupling constants.

- Where does the "strange" number of matter and exchange particles come from? Are there possibly super symmetric partners for every existing particle?
- How can one explain the missing mass in the rotation of galaxies? Are there still missing particles here which almost only interact gravitationally (dark matter)?
- Why does one need to introduce around 20 free parameters? Are there any other unifications or extensions?
- How do you describe high energies with the SM? Do all the forces known up to now unite into one?

The process in which the particles gain their mass was explained with the discovery of the Higgs boson in 2012. This is contained in an extension of the SM by the so-called Higgs mechanism (named after Peter Higgs). Another field is postulated therein, a field that is almost indistinguishable from the vacuum, the Higgs field. The idea is that the particles get their mass by interacting with this Higgs field. Particles that interact strongly with the Higgs field are heavy, whereas those that only interact weakly are light. At least one other new particle is associated with the Higgs field, which is the Higgs boson with a mass of 125 GeV. However, depending on further expansions of the SM, there may be other Higgs bosons that are yet to be discovered. In order to get a "visual" impression of the Higgs mechanism, one can visit the website of the Particle Data Group (`http://pdg.lbl.gov` or `http://www.particleadventure.org`).

The figures 2.11 and 2.12 are shown for possible further expansions of the SM. These extensions then lead to the *Minimal Supersymmetic Standard Model* (MSSM) or the *Great Unified Theory* (GUT).

Chapter 3

The interaction of radiation with matter

3.1 Charged particles

There are four types of interaction in physics. They are usually classified according to the size of the dimensionless coupling constants, which are a measure of the strength of the interaction between the representing fields. The numerical values are slightly model-dependent, but here we only look at the order of magnitude.

The strong interaction acts between mesons and nucleons and is responsible for the cohesion of the nuclei. Its essential characteristic is the short range of approximately 10^{-13} cm. The coupling constant is in the order of 1.

The electromagnetic interaction works between charged particles and is mediated by photons. Between two charged particles it takes the form of the Coulomb interaction, where the force F between the particles with the charges e_1 and e_2 as function of their distance r is

$$F = \frac{1}{4\,\pi\,\epsilon_0} \cdot \frac{e_1 \cdot e_2}{r^2} \tag{3.1}$$

and the potential U of a point charge e is

$$U = \frac{1}{4\,\pi\,\epsilon_0} \cdot \frac{e}{r} \tag{3.2}$$

It is two orders of magnitude weaker than the strong interaction. The coupling constant is the Sommerfeld fine structure constant (equal to 1/137). The range is infinite.

The weak interaction describes the transformation of hadrons and in particular the β-decays. It determines the scattering and reactions of Leptones, independend of their electric charge. It can be used, for example, to detect neutrinos. Its relative strength is about 10^{-14}.

Gravity , of all the interactions, it is the longest known. It was discovered by Newton, who formulated the law of gravitation. The force between two masses m_1 and m_2 as a function of their spacing r is

$$F = \gamma \cdot \frac{m_1\,m_2}{r^2} \tag{3.3}$$

with the gravitational constant γ. Like the Coulomb force, the gravitational force has an infinite range, but it is 37 orders of magnitude weaker. The coupling constant is $2 \cdot 10^{-39}$.

The different strengths of the interactions can be illustrated by comparing the corresponding forces or cross sections. The Coulomb force between two electrons or two protons at a distance of 10^{-8} cm (atomic distance) is $1.44 \cdot 10^{-8}$ N. On the other hand, the gravitational force is $1.11 \cdot 10^{-44}$ N for two protons and $3.3 \cdot 10^{-51}$ N for electrons. The total effective cross section for the electromagnetic process of Compton scattering of a γ-quantum of 1 MeV on an electron is $2 \cdot 10^{-25}\,\mathrm{cm}^2$. Of the same order of magnitude is the total cross section for the scattering of two electrons. In comparison, the scattering of a Neutrinos on an electron is much less likely. The cross section is $10^{-43}\,\mathrm{cm}^2$. An example for the strong interaction is the neutron–proton scattering with the total cross section of $2 \cdot 10^{-23}\,\mathrm{cm}^2$ for neutrons with the energy of 100 eV.

In collisions of charged particles with matter, the electromagnetic interaction dominates. Four types of processes can be distinguished. According to the probability of their occurrence, these are:

1. **Inelastic scattering on electrons:** The charged particle is decelerated and loses its kinetic energy to the atoms, molecules or crystals that are excited or ionized. The impact parameters for this process are in the order of the atomic diameter (10^{-10} m). The energy loss is determined by the Bethe-Bloch formula, which will be discussed below.

2. **Elastic scattering on nuclei:** The particles are scattered when approaching the positively charged, stationary nucleus, losing recoil energy to the nucleus. The larger the mass difference of the colliding bodies, the smaller the energy loss. The frequency of these events is considerably lower than the inelastic scattering in the electron shell, because they are only possible for smaller impact parameters, due to the shielding of the nuclear charge by the electrons.

3. **Inelastic scattering on nuclei:** The frequency is comparable with the elastic scattering, in processes in which a charged particle is subjected not only to the recoil energy caused by kinematics, but also to an additional energy loss. This includes Bremsstrahlung. This is electromagnetic radiation, which is produced when light particles, especially electrons, are decelerated in the coulomb field of the nucleus. In this process, the nucleus is not exited. It is described in more detail below. Another possibility is the Coulomb excitation of nuclei. It is particularly likely in the case of heavy nuclei, where the forces are large at close range.

4. **Elastic scattering on electrons:** This is only important for very light particles, thus only for electron-electron collisions, and only at energies below 100 eV.

3.1.1 The Bethe-Bloch formula

As already mentioned, the inelastic scattering at electrons is the most frequent interaction of charged particles in matter. The resulting energy loss can already be calculated with the means of classical physics by summing up the momentum transfer at the individual collisions. The result, first found by Bethe and Bloch [1], changed only marginally when applying quantum mechanics.

The incident particle is characterized (Fig. 3.1) by the number z of its elementary charges and by its velocity v, the matter by the electron density $N \cdot Z$ and the mean ionization potential I. An approximate value for I is $I = 13.5 \cdot Z\,\mathrm{eV}$, with Z, the nuclear charge number. The stopping power of matter, which is the energy loss $\mathrm{d}E$ of the particle on a sufficiently small path $\mathrm{d}x$ (the energy loss $\mathrm{d}E$ should be small compared to the remaining energy E at the location x) is

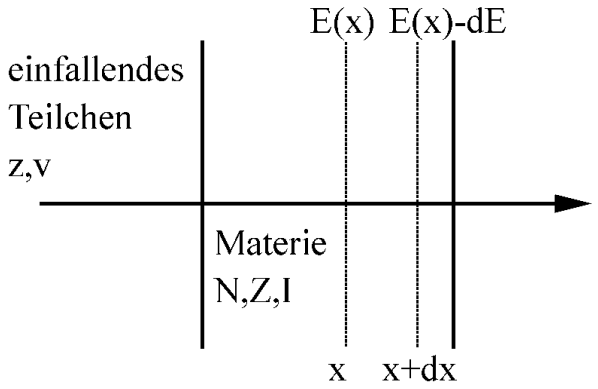

Figure 3.1: Calculating the energy loss of a charged particle.

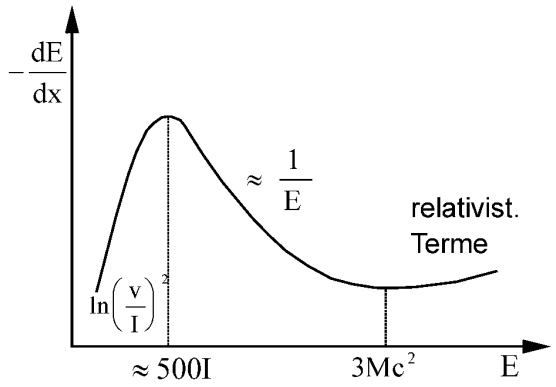

Figure 3.2: Stopping power as a function of energy.

$$\frac{\mathrm{d}E}{\mathrm{d}x} = -\frac{e^2}{m_0 \cdot \epsilon_0} \cdot N \cdot Z \cdot \frac{z^2}{v^2} \cdot \left[\ln\left(\frac{2 \cdot m_0 \cdot v^2}{I}\right) - \ln\left(1-\beta^2\right) - \beta^2 - \frac{A}{Z} \right] \tag{3.4}$$

with $\beta = v/\mathrm{c}$. A is a constant which determines the binding of electrons in the different states, m_0 is the rest mass of the electron, and ε_0 is the dielectric constant. The stopping power is proportional to the electron density in the bulk, i.e. the number of collisions the particle makes on its way. The charge of the particle enters quadratically. This means that highly charged particles, e.g. nuclear debris from uranium fission, are very strongly slowed down in matter and therefore travel only short distances. The stopping power depends on the square of the velocity of the particle, but it is independent of its mass and therefore the same for all particles with the same amount of mass and the same speed. Qualitatively, the curve is drawn as a function of the energy in Fig. 3.2. For very small energies in the order of the ionization energy I, the curve is not defined. Here, the particles frequently change their charge during the impact, due to electron loss or electron capture, so that they have no fixed charge and can even neutralize themselves. In the subsequent range, up to an energy of about $500 \cdot I$ the strong rise of the first logarithmic term in parentheses outweighs the decline by the square of the speed v in the denominator. At higher energies for $I \ll E \ll M\,c^2$ (M is the rest mass of the particle), the logarithmic term changes only slowly, while the other terms in the parentheses are still small. The stopping power in this area has approximately the same shape as a hyperbola.

$$-\frac{\mathrm{d}E}{\mathrm{d}x} \approx \frac{1}{E} \tag{3.5}$$

At even higher energies the increasing relativistic terms become noticeable. First, at approximately three times the rest energy of the particle the curve goes through a minimum of ionization, followed by a continuous rise afterwards.

For very fast particles, the stopping power and thus the number of ion pairs generated per distance (specific ionization), is low at first. For air under normal conditions it is in the minimum approx. 2 keV/cm. During the further deceleration, it increases and reaches a maximum value, for air about 1 MeV/cm. The specific ionization is greatest shortly before the particle comes to rest.

The Eqn. 3.4 describes the behavior of heavy and highly charged particles, for instance fission fragments, not particularly well at high energies. Due to the large charge and the corresponding Coulomb forces, they can easily accumulate electrons. However, it can still be used in these cases, if an experimentally determined medium charge is introduced.

Also, for the calculation of the stopping power of electrons a modification is necessary, because we are dealing with the scattering of identical particles. However, the form of the expression remains essentially the same.

There is one important point to keep in mind: charged particles can lose their entire energy in sufficiently extended matter. They have a finite range given by

$$R = \int_{E_0}^{0} \frac{\mathrm{d}E}{\mathrm{d}E/\mathrm{d}x} \tag{3.6}$$

It depends on the initial energy E_0, but can only be calculated approximately, because the stopping power at the end of their track is not known. The range is therefore determined empirically. For this, a medium range is introduced that takes into account the statistical nature of the deceleration, which leads to a spread of the measured values, even for particles with exactly the same initial energy. An empirical relationship obtained in this way for the mean range of protons in air under normal conditions is

$$\bar{R} = \left(\frac{E[MeV]}{9.3}\right)^{1.8} \mathrm{m} \tag{3.7}$$

For the determination of the range of electrons equation refequ:3-6 is not applicable. It only applies if the momentum transfer is so low that the particle continues to fly almost undeflected. This applies to hadrons and nuclei. In this case, the mass difference to electrons is so large that the statistical character of the scattering processes of a monoenergetic beam leads only to a small scattering of the range (*straggling*). In collisions of electrons with electrons, on the other hand, the momentum transfer is large with regard to the total momentum, so that it moves in randomly scattered directions through the absorber.

An important application of the Bethe-Bloch formula has been the identification of particles in nuclear reactions. The stopping power can be written in the hyperbolic range

$$-\frac{\mathrm{d}E}{\mathrm{d}x} = K \cdot z^2 \cdot \frac{m}{E} \tag{3.8}$$

where m is the mass of the decelerated particle, z is the charge, and K is an energy independent constant. For the detection of the particles a semiconductor telescope is used, configured according to the schematics outlined in Fig. 3.3. It consists of a thin absorber of thickness $\mathrm{d}x$ through which the particles pass and a thick detector in which they are stopped. The relation between the energy loss $\mathrm{d}E$ measured in the absorber and the total energy E deposited in the detector is described by Eqn. 3.8. For particles with the same charge, but different masses, the energy loss $\mathrm{d}E$ as a function of the total energy E is a set of hyperbolic curves with the mass as shape parameter. Since the masses are discrete, the hyperbolas that belong to different particles

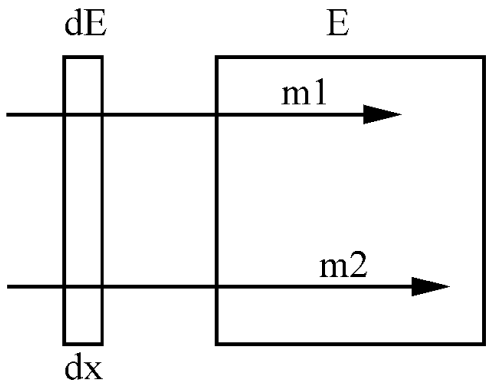

Figure 3.3: Scheme of a telescope to identify particles.

are seperated, if the energy resolution of the telescope is good enough. Apparently, the same is true for particles of same mass but different charge. However, the hyperbolas are further apart from each other, because of the quadratic dependence.

3.1.2 The Bremsstrahlung

In addition to ionization and excitation, there is another possibility of energy loss for charged particles. They can be decelerated in an electric field, such as the Coulomb field of a nucleus, and energy can be converted in the form of electromagnetic radiation, the Bremsstrahlung. The nucleus is necessary to for the conservation of the energy and momentum, but does not take on any excitation energy.

Bremsstrahlung is already known in classical physics. Any acceleration of charges is associated with the emission of electromagnetic radiation. There, as well as in quantum mechanics, the intensity of the bremsstrahlung follows the proportionality

$$I \approx \frac{z^2 \cdot Z^2}{m^2} \tag{3.9}$$

Here, m and z are the mass and charge of the decelerated particle, Z the charge of the decelerating particle. The bremsstrahlung increases quadratically with the charges of both particles and is therefore particularly common in the Coulomb field of heavy nuclei. The mass of the slowed-down particle enters the denominator quadratically, i.e. for light particles, such as electrons, the energy loss due to bremsstrahlung is greatest, for heavy ions it is negligibly small.

The spectrum of bremsstrahlung generated by monoenergetic electrons with an energy of 1.4 MeV in a thick tungsten target is shown in Fig. 3.4. It's a broad, continuous distribution. Most photons take roughly half of the electron's energy with them. Small energies are rare. At energies above $E_{\max}$ the spectrum is truncated. This is the largest energy the bremsstrahlung can take, namely the total kinetic energy of the electron. It is

$$E_{\max}(\text{radiation}) = h\nu_{\max} = E_{\text{kin}}(\text{electron}) \tag{3.10}$$

With this relation, the known energy of the electrons, and the cut-off frequency $\nu_{\max}$ measured with a X-ray spectrometer, it is possible to determine the Planck constant h.

The shape of the bremsstrahlung spectrum is classically and quantum-mechanically the same, although the underlying assumptions are completely different. The classical theory connects with every change of motion of a particle the definite emission of low-energy radiation, whereas after of quantum theory, the emission probability is small, but the energy of the photon is larger.

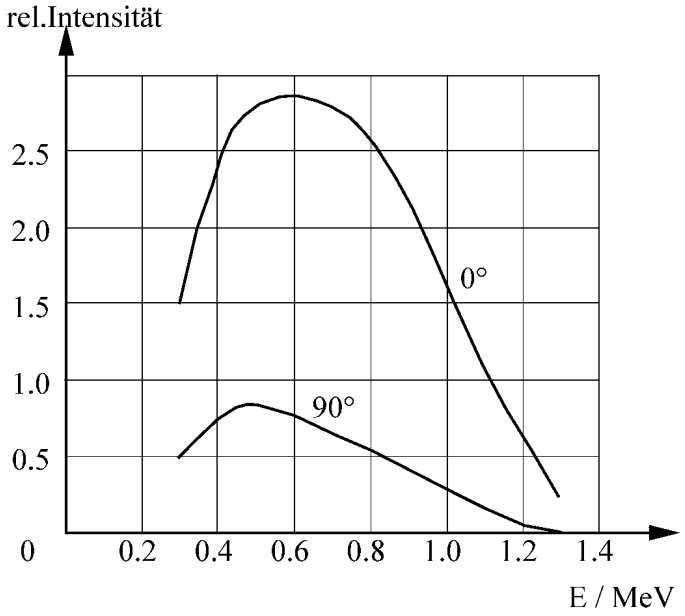

Figure 3.4: Bremsstrahlung spectrum of 1.4 MeV electrons in tungsten.

Averaged over a wide energy range of the incident particles results in both cases in the shape of the photon spectrum shown in Fig. 3.4.

The total effective cross section of the bremsstrahlung of electrons is for non-relativistic energies $E_{\mathrm{kin}} \ll E_0$

$$\sigma_{\mathrm{rad}} = \frac{16}{3} \cdot \alpha \cdot Z^2 \cdot r_0^2 \tag{3.11}$$

α is the Sommerfeld fine structure constant and r_0 the classical electron radius $r_0 = e^2/m_0 \cdot c^2$. This is the form of Eqn. 3.9. It is independent of the electron energy E_i. Near the energy of twice the rest mass E_0 it slowly rises according to the formula

$$\sigma_{\mathrm{rad}} = 8 \cdot \alpha \cdot Z^2 \cdot r_0^2 \cdot \left(\ln \frac{E_i}{E_0} - \frac{1}{6} \right) \tag{3.12}$$

and becomes again independent of the energy in the extreme relativistic range. This behavior is shown in Fig. 3.5 for water and lead by the solid curves. The energy losses due to ionization is shown by the dashed lines. The losses due to bremsstrahlung exceed the ionization losses for the heavy element of lead at about 20 MeV and for the light water molecule above 200 MeV.

A similar effect occurs in circular accelerators (synchrotron), in which electrons are forced into circular motion by strong magnetic fields. The strong increase of the radiation cross section with the energy prevents circular accelerators from accelerating electrons up to arbitrarily high energies. The maximum energy is reached when the radiation losses caused by the so-called synchrotron radiation and the the supplied high-frequency energy compensate each other.

For electron energies above 1 MeV the energy loss by bremsstrahlung in matter with the charge number Z and the mass number M is given by

$$-\left(\frac{\mathrm{d}E}{\mathrm{d}x}\right) = 4\,\alpha\, r_0^2 \cdot \frac{Z_2}{A}\, L \cdot \ln \frac{183}{Z^{1/3}} \cdot E = \frac{E}{X_0} \tag{3.13}$$

L is the Avogadro number. The parameter X_0 is called radiation length. With it this equation can be written as

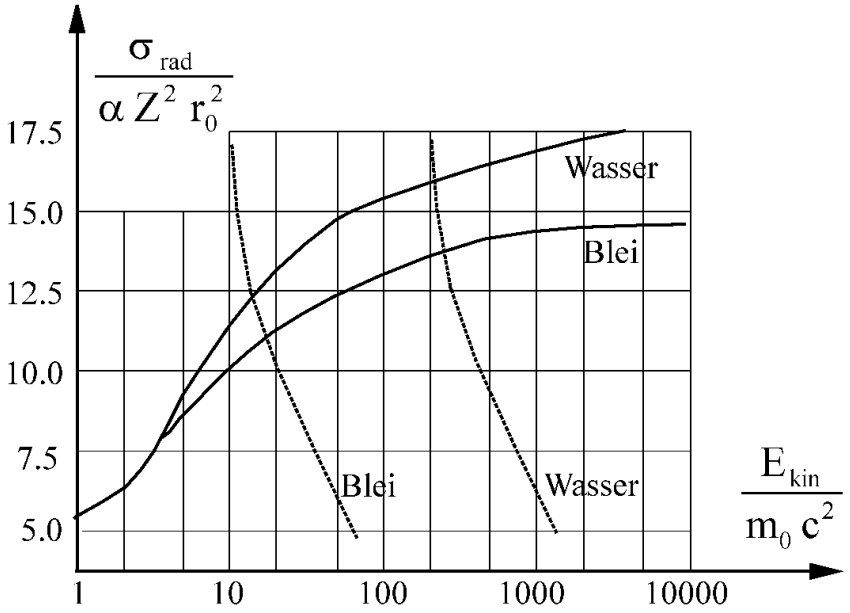

Figure 3.5: Cross sections for bremsstrahlung in lead and water.

$$\frac{\mathrm{d}E}{E} = -\frac{\mathrm{d}x}{X_0} \tag{3.14}$$

with the solution

$$E = E_0 \cdot e^{-\frac{x}{X_0}} \tag{3.15}$$

It describes the decrease of the initial energy E_0 as a function of the distance x traveled in matter. Here the physical significance of the radiation length becomes clear: it is the distance on which the energy is reduced to $1/e$ of its initial value. Measured in g/cm^2, it is, for instance, 24 in Al, 19 in Ar, and 6.3 in Pb. Thus, it decreases with increasing charge number.

3.2 Uncharged particles

Uncharged particles, in this lab course these are neutrons and γ-quanta, are not subject to the Coulomb interaction and can thus not be directly detected through the transfer energy to matter by excitation and ionization. In order to detect them, it is necessary that they interact with charged particles first, which in turn ionize the matter. In general, the secondary particles only receive a part of the kinetic energy of the uncharged primary particle, so that for the determination of the energy additional measurements, e.g. of the scattering angle, are necessary.

3.2.1 The neutron

For the neutron, the interaction with nuclei is the the only cause of the energy loss. The neutron is detected via the strong and not via the electromagnetic interaction. Three types of processes can be distinguished.

3.2.1.1 Elastic scattering of neutrons on nuclei

In the elastic scattering of a neutron, no internal energy is transferred to the nucleus. Due to the conservation of momentum and energy, however, it receives some recoil energy. The energy

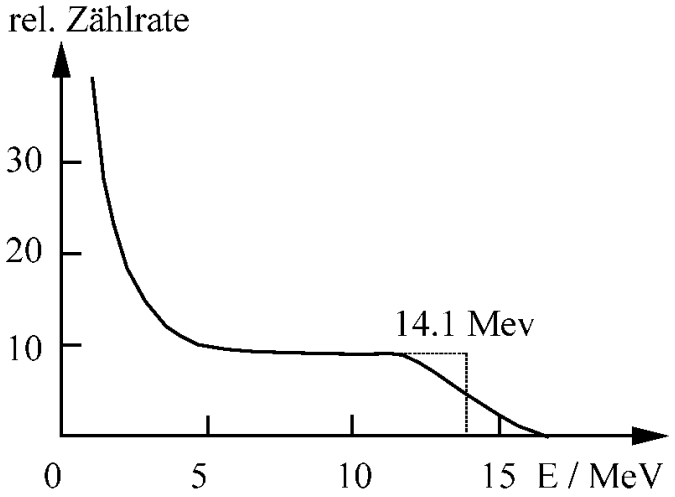

Figure 3.6: The proton spectrum in a recoil detector.

transfer ΔE at the impact of a neutron of energy E_n to the resting nucleus of the mass number A is

$$\Delta E = \frac{4\,A}{(A+1)^2} \cdot E_{\mathrm{n}} \cdot cos^2 \cdot \Theta \tag{3.16}$$

where Θ is the angle between the momenta of the incident neutron and the recoil particle in the laboratory system. The transmitted energy ΔE varies with the recoil angle Θ and takes on all values from zero to the maximum recoil energy at the central impact for $\Theta = 0$. If the neutron's impact partner is a proton (A=1), then the recoil energy of the proton at the central impact is equal to the neutron energy (if the very small mass difference between neutron and proton is neglected).

The high energy transfer in elastic neutron-proton scattering is the basis of the Proton Recoil Detector. It's a scintillator made of a material with a high proportion of hydrogen, so that the sensitivity for neutron detection is high. Plastic is the most common material used. The recoil energy of the protons is measured as the light yield of the scintillator (see 4.2.1.2 The organic scintillator). The spectrum of such a detector for the detection of monoenergetic neutrons is shown in Fig. 3.6. It is continuous from zero to the energy E_{n} of the neutron. The dotted curve represents the ideal distribution where the spectrum breaks off sharply. The actual measured distribution is solid curve. The deviation is caused by the energy straggling of the protons and in the finite energy resolution of the detector. The constant progression for all but the smallest proton energies is a consequence of the isotropic angular distribution of neutron-proton scattering, as observed up to 20 MeV. The energy of neutrons can be determined by the location of the spectrum's decline at high energies, if they are are monoenergetic, because only then the edge corresponds to the energy of the neutrons. If the neutrons have continuous energies, the determination of energy according to Eqn. 3.16 requires in addition to the energy a measurement of the proton's direction of its momentum. The proton recoil detectors can be used at arbitrary neutron energies, but the course of the total scattering cross section in Fig. 3.7 shows that the sensitivity decreases strongly above 1 MeV.

3.2.1.2 Neutron induced nuclear reactions

When a neutron is absorbed by a nucleus, in general an initially excited intermediate nucleus is formed, which goes to the ground state either by emitting a γ-quantum or by the emission of

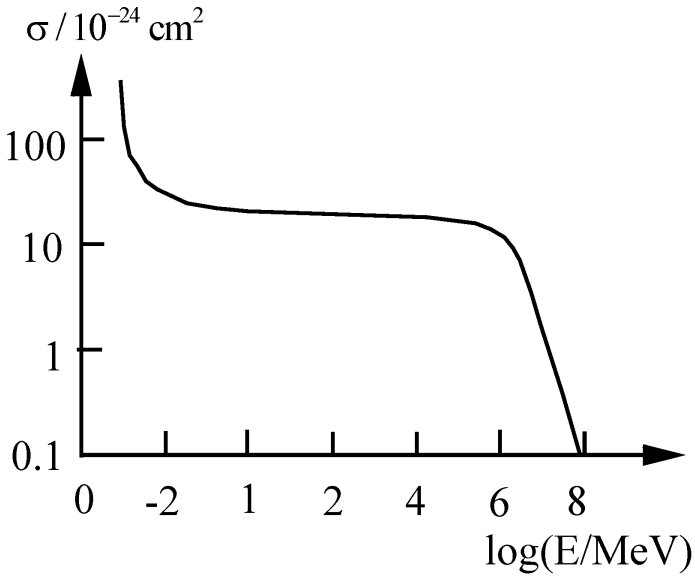

Figure 3.7: The total cross section for neutron-proton scattering.

charged particles or neutrons. The interaction of the γ quantum or the charged particle then allows the detection of the neutron. The most common method is the neutron capture at the boron isotope ^{10}B.

$$\mathrm{n} + {}^{10}\mathrm{B} \;\rightarrow\; {}^{7}\mathrm{Li}^{*} + \alpha + 2.31\,\mathrm{MeV} \tag{3.17}$$

The ^{7}Li nucleus is preferentially formed in an excited state with an excitation energy of 0.48 MeV that goes to the ground state by γ-decay. For thermal neutrons (with an energy of 0.025 eV) it gets a kinetic energy of 0.84 MeV, the α-particle of 1.47 MeV. The Li-nucleus is given a a considerable part of the kinetic energy, in which case the recoil energy of the heavier nucleus can not be neglected.

The above reaction is used for detection in the so-called boron counter tube. This is a proportional counter tube (see section 4.1.1.2) with BF_3 as filling gas. Natural boron can be used, since the abundance of ^{10}B is about 20%. If the α-particles and Li ions, occurring after the neutron capture, release their entire kinetic energy in the ionization process, a line appears that corresponds to a Q-value of 2.31 MeV. This is usually the case, due to their small range in gas. With a lower cross section, the reaction also goes directly to the ground state of ^{7}Li. Therefore, a second line with lower intensity occurs at an energy of $Q = 2.78$ MeV.

The ^{10}B reaction is particularly well suited for neutron detection, because it has a large cross section. For thermal neutrons it is $\sigma = 3837 \cdot 10^{-24}\,\mathrm{cm}^2$. For higher energies up to some keV it drops with $1/v$. It is:

$$\sigma \cdot v = \mathrm{const} = 1.6 \cdot 10^{-16}\,\frac{\mathrm{cm}^3}{\mathrm{s}} \tag{3.18}$$

In this energy range, the boron counter directly measures the neutron flux, which is proportional to $\sigma \cdot isv$. At even higher energies between 1 MeV and 16 MeV the cross section is practically constant with a value of $\sigma = 1.5 \cdot 10^{-34}\,\mathrm{cm}^2$, interrupted only by a resonance at 1.26 MeV.

A similarly high effective cross section for the capture of thermal neutrons, namely $\sigma = 5327 \cdot 1^{-24}\,\mathrm{cm}^2$, has the reaction

$$\mathrm{n} + {}^{3}\mathrm{He} \rightarrow \mathrm{p} + \mathrm{t} + 0.77\mathrm{MeV} \tag{3.19}$$

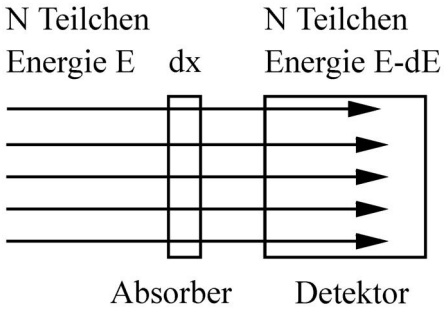

Figure 3.8: Absorption of charged particles in matter.

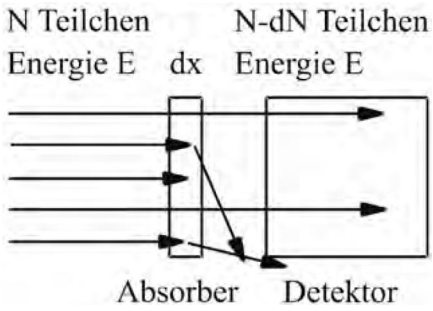

Figure 3.9: Absorption of γ-quanta.

It is used in the ^{3}He-counter, which is also a proportional counter in which the proton and the triton are detected. Here again the $1/v$ law applies for the cross section until energies up to 1 MeV.

3.2.1.3 Neutron induced fission

For very heavy nuclei, such as ^{235}U, the addition of a neutron is sufficient to split the nucleus. Besides a few neutrons, medium-sized core fragments are created, which can be detected in proportional counter tubes, the so-called fission chambers.

3.2.2 The gamma quantum

In contrast to the charged particles, the γ-quanta do not ionize matter directly. It can therefore pass through larger sections of matter undisturbed. It is detected through three processes of the electromagnetic interaction: the photoelectric effect, Compton scattering and pair production. The released or produced electrons and positrons take over kinetic energy, which they lose by ionization, as discussed in section 3.1. Thus, it is the secondary leptons that allow the detection of γ-quanta.

Therefore, the photons behave completely differently in matter than the charged particles. For illustration, think a monoenergetic beam of α-particles flying in parallel, consisting of N particles per second, each of which has the energy E. In quantum mechanics this is called a plane wave. A detector, detecting only particles arriving from the beam direction, measures their energy. In front of the detector there is an absorber of thickness dx (Fig. 3.8). For a thin absorber a particle loses, according to the Bethe-Bloch formula, only a small part dE of its energy, none is absorbed. Even with absorber still N particles per second are registered, but each with the reduced energy $E - \mathrm{d}E$. A charged particle beam loses only energy (in sufficiently thin matter), but not intensity.

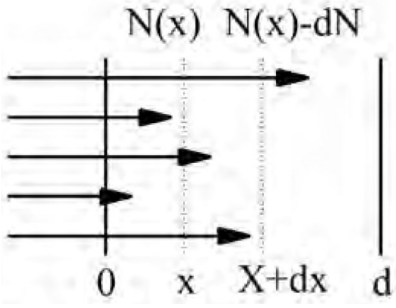

Figure 3.10: Absorption law for γ-quanta.

With γ-quanta the picture is completely different (Fig. 3.9). In matter, photons are absorbed by the photoelectric effect or by pair production, or scattered from their direction of incidence by the Compton effect. Therefore, less photons are detected than without absorber. Those that get into the detector, still have the original energy. A photon beam loses intensity in matter, but the passing photons lose no energy.

The probability of absorption can be determined by the absorption constant. μ which depends on the material and the energy, but not on the penetration depth x of the photons into the matter. When $N(0)$ monochromatic quanta enter an absorber (Fig. 3.10), still $N(x)$ quanta are present after the penetration depth x. The probability P that a quantum is absorbed on the infinitesimal range $\mathrm{d}x$, is

$$P = \mu \cdot \mathrm{d}x \tag{3.20}$$

For the number $\mathrm{d}N$ of the quanta absorbed on the distance $\mathrm{d}x$, the following applies:

$$\mathrm{d}N = -P \cdot N(x) = -\mu \cdot N(x)\mathrm{d}x \tag{3.21}$$

Integrated up to the thickness d this leads to

$$N(d) = N(0) \cdot e^{-\mu d} \tag{3.22}$$

or for the intensities

$$I(d) = I(0) \cdot e^{-\mu d} \tag{3.23}$$

The decrease in intensity of a γ-ray in matter thus obeys an exponential law. This also applies when not only the absorption by photoelectric effect and pair formation, but also the scattering by the Compton effect is considered, as long as the experimental arrangement sketched in Fig. 3.9 is used, which only includes quanta from the direction of the incident plane wave. Thus, no scattered quanta are counted, and the scattering is equivalent to absorption. The absorber only has to be thin enough to avoid double scattering. The detected quanta all have the original energy E, as they do not interact with the absorber. In contrast to charged particles, the intensity of γ-radiation is reduced when passing through matter, but the energy of the quanta is preserved. The γ-radiation cannot be shielded complete, because even after a thick absorbing layer a finite intensity still remains.

In the following, the individual processes of electromagnetic interaction and their reversal processes are discussed, which are important for the detection of positrons.

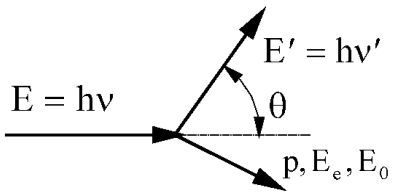

Figure 3.11: Kinematics of the Compton effect.

3.2.2.1 The Compton Effect

The Compton effect is the scattering of γ-quanta off free charged particles. If these are at rest or their kinetic energy is small compared to the energy of the γ-quantum, then the photon loses energy during the scattering. The energy shift is purely kinematic and can be calculated from the momentum and energy theorem. Here we consider the case of scattering on a stationary particle. After the impact the incoming γ-quantum with the energy E has the energy E'. The particle with the rest energy E_0 has after the impact the total energy $\mathrm{E_e}$ and the momentum p. θ is the scattering angle of the γ-quantum. The energy theorem

$$E + E_0 = E_e + E' \tag{3.24}$$

and the momentum theorem

$$c^2\, p^2 = E_e^2 - E_0^2 = E^2 + E'\,2 - 2\,E\,E' \cdot \cos\theta \tag{3.25}$$

yield for the energy of the scattered quantum

$$E' = \frac{E}{1 + \frac{E}{E_0} \cdot (1 - \cos\theta)} \tag{3.26}$$

The kinetic energy E_{kin} of the charged particle is

$$E_{\mathrm{kin}} = E - E' = \frac{\frac{E^2}{E_0} \cdot (1 - \cos\theta)}{1 + \frac{E}{E_0} \cdot (1 - \cos\theta)} \tag{3.27}$$

The energy change of the radiation during scattering, the Compton shift, depends on the scattering angle. It disappears for $\theta \to 0$, in which case the charged particle does not get any recoil energy. It increases with the increasing scattering angle and is at its maximum for $\theta = 180°$. Accordingly, the particle reaches the maximum possible energy E_{max}

$$E_{\mathrm{max}} = \frac{E}{1 + \frac{E_0}{2\,E}} \tag{3.28}$$

It is always less than the initial energy of the γ-quantum, since this keeps a part of its energy when backscattering.

The Compton shift also depends on the energy of the photon. The larger the energy of the γ-quantum in proportion to the rest energy of the particle, the larger the energy shift will be. When scattering with an energy of $E = 1\,\mathrm{MeV}$, the maximum relative Energy transfer $E_{\mathrm{max}}/E = 80\,\%$ for electrons and $E_{\mathrm{max}}/E = 0,2\,\%$ for protons.

The Compton scattering only becomes noticeable when the energy of the photons is comparable with the rest energy of the particles on which they are scattered. So the scattering of γ-quanta from a radioactive decay on protons or nuclei is negligible, as well as the Compton scattering of visible light on electrons. In this case $E_{\mathrm{max}}/E = 5 \cdot 10^{-6}$ for light at electrons.

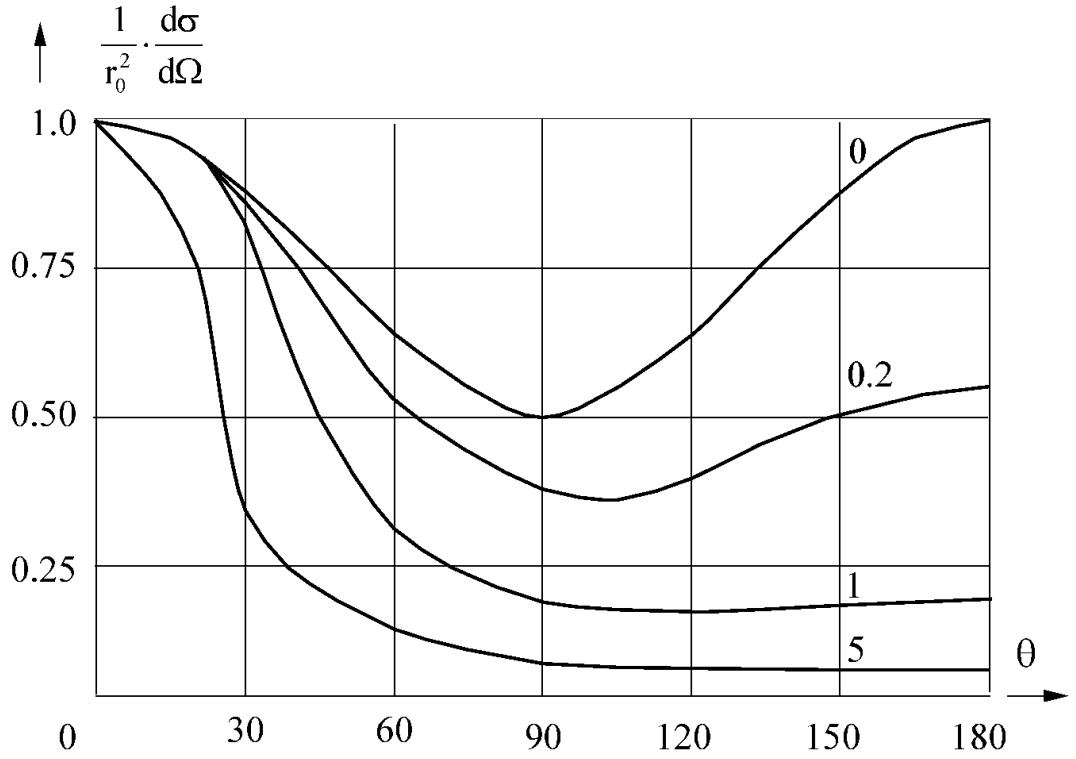

Figure 3.12: The differential cross section of the Compton scattering for different values of E/E_0.

This energy shift lies in the order of magnitude of the line widths of spectral lines. The energy of the scattered Radiation goes for $E/E_0 \ll 1$ against E, independent of the scattering angle. The Compton scattering then goes over into Thomson scattering known from classical physics.

The differential cross section per electron for the scattering of unpolarized γ-quantum on electrons is

$$\frac{\mathrm{d}\sigma}{\mathrm{d}\Omega} = \frac{r_0^2}{2} \cdot \left[1 + \frac{E}{E_0} \cdot (1 - \cos\theta)\right]^{-3} \times \left[-\frac{E}{E_0} \cdot \cos^3\theta + \left(\frac{E^2}{E_0^2} + \frac{E}{E_0} + 1\right) \cdot (1 + \cos^2\theta) - \frac{E}{E_0} \cdot \left(\frac{2\,E}{E_0} + 1\right) \cdot \cos\theta\right] \frac{\mathrm{cm}^2}{\mathrm{sr}} \quad (3.29)$$

with the classical electron radius $r_0 = e^2/(m_0 \cdot c^2)$. For γ energies, which are much smaller than the rest mass of the scattering particle, this turns into the Thomson cross section.

$$\frac{\mathrm{d}\sigma}{\mathrm{d}\Omega} = \frac{r_0^2}{2} \cdot (1 + cos^2\theta) \text{ for } \frac{E}{E_0} << 1 \quad (3.30)$$

In Fig. 3.12 the Klein-Nishina formula and the Thomson formula are plotted qualitatively. The numbers on the curves are the γ-energies in electron rest masses. The Thomson cross section with $E/E_0 = 0$, is symmetric around 90°. Forward and backward scattering have equal probability. The Compton cross section deviates more and more with increasing energy. The bigger the energy gets, the more forward scattering is preferred.

The total scattering cross section per electron for the Compton scattering results from Eqn. 3.26 by integrating over the solid angle

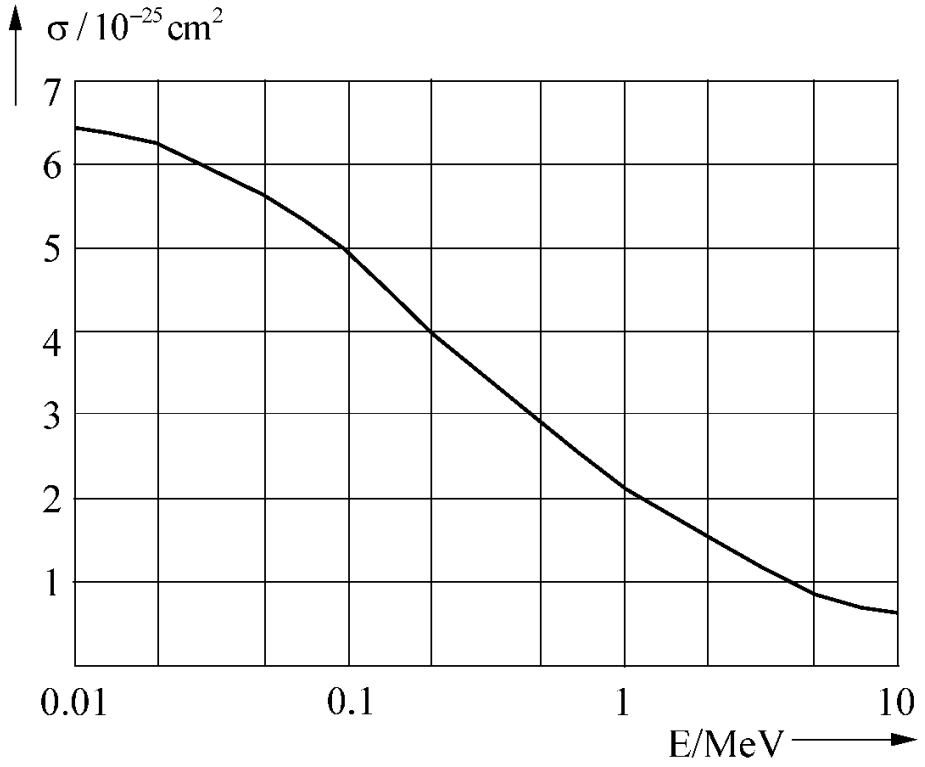

Figure 3.13: The total cross section for Compton scattering as a function of energy.

$$\begin{aligned}\sigma &= 2\pi r_0^2 \cdot \frac{1+\frac{E}{E_0}}{\left(\frac{E}{E_0}\right)^2} \cdot \left[\frac{2\left(1+\frac{E}{E_0}\right)}{1+2\frac{E}{E_0}} - \frac{E_0}{E} \cdot \ln\left(1+2\frac{E}{E_0}\right)\right] \\ &+ \frac{E_0}{2E} \cdot \ln\left(1+2\frac{E}{E_0}\right) - \frac{1+\frac{3E}{E_0}}{\left(1+2\frac{E}{E_0}\right)^2} \end{aligned} \tag{3.31}$$

Its shape depending on the energy is shown in Fig. 3.13. It decreases strongly with increasing photon energy. For the approximation of very small photon energies, this too converges against the total cross-section for the elastic scattering of a light wave on an electron, the Thomson cross-section

$$\sigma_{\mathrm{Th}} = \frac{8\pi}{3} \cdot r_0^2 \tag{3.32}$$

All cross sections given here refer to the scattering off a free, single electron. However, electrons are bound in matter, but their binding energy is very small, at least for the light atoms. It is smaller than those energies for which the Compton effect is of any significance, and they can therefore be considered as free electrons. The cross section σ_a *per atom* for an element with the atomic number Z is therefore in good approximation the sum of cross-sections σ_e *per electron*:

$$\sigma_a = Z \cdot \sigma_e \tag{3.33}$$

Thus, it is proportional to the proton number. For heavy atoms, in which the binding energy of the inner electrons can take on considerable values, this relationship no longer applies.

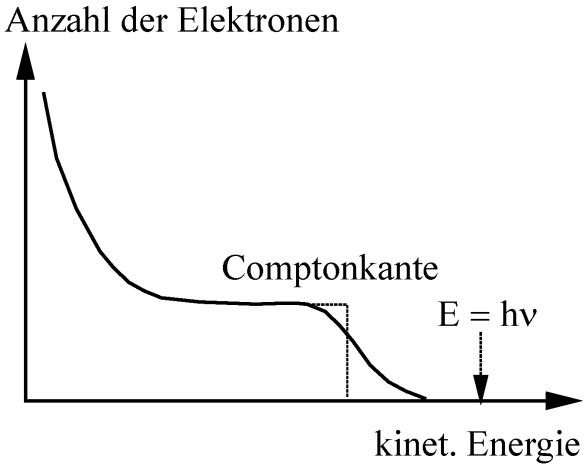

Figure 3.14: Ideal and measured Compton spectrum.

As said before, the Compton effect allows γ-quanta to be detected and their energy to be measured, even though the energy measurement is not very accurate. An energy-sensitive detector is used for this purpose, i.e. a detector, whose output pulse is proportional to the energy of the electrons produced by the photons. The spectrum of recoil electrons, the Compton spectrum, which is derived from monoenergetic γ-quanta with the energy $E = h\,\nu$, has the form shown in Fig. 3.14. The number of electrons is plotted versus their kinetic energy. The spectrum is continuous, although the generating quanta are monochromatic. It starts at energy zero and aborts at the maximum energy E_{max}, given by Eqn. 3.28. Because of the sharp, ideally vertical, termination, this energy is also called the *Compton edge*. The broadening comes from the finite energy resolution of the detector. The worse the energy resolution of the detector, the flatter the edge is. The number of electrons at a given kinetic energy is proportional to the differential cross section at the corresponding scattering angle θ (Eqn. 3.29). The Compton edge corresponds to the backward scattered photons, the small energies correspond to the forward scattered photons. If one assumes the case $E/E_0 = 1$ from Fig. 3.12, then the resulting spectrum from the Compton edge towards lower energies is initially constant and increases rapidly at low energies.

At least in principle, one can determine the energy of the photons with Eqn. 3.28 from the position of the Compton edge. Because the finite energy resolution and the resulting smearing of the edge, this is very inaccurate.

Finally, a remark about the different ways in which the Compton effect is described in the literature either as elastic or inelastic process. Both possibilities are justified, depending on whether the process is considered as a *scattering* of an electromagnetic wave or as *elastic collision* of particles. A collision is elastic, if the total kinetic energy before and after the impact is the same, the inner energy of the involved particles thus remains unchanged. This is the case with the Compton effect. The wave formulation is referred to as elastic scattering only if the frequency of the wave does not change. Compton scattering is inelastic here.

3.2.2.2 The photo effect

The photoelectric effect is the absorption of a photon by an atom with simultaneous emission of a free electron. It is known from atomic physics that the electrons in the atomic shell can only be in certain discrete energy states. One speaks of the shell structure of the atom. The energies of the shells are essentially determined by the principal quantum numbers n. States with $n = 1, 2, 3$ etc. form the K-, L-, M-shell, etc. In addition, the energy of a state also depends on the quantum number J of the total angular momentum, which is vectorially composed of the

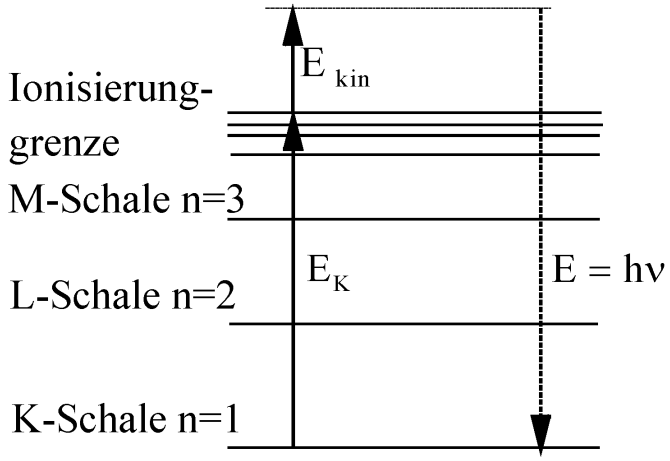

Figure 3.15: Schematic representation of the photo effect.

orbital angular momentum l and the spin s of an electron. Taking into account the total angular momentum J, the shells have a fine structure: they are split according to the values that J can assume in a shell. Since the orbital angular momentum l in a shell with the main quantum number n can assume all values less than n, there are $2n-1$ different total angular momenta. Thus, the K-shell is not split, The L-shell is split three times, the M-shell is split five times, etc.

In an atom with the atomic number Z, the Z states with the lowest energies of electrons are occupied in the ground state. When energy is transferred to an electron, be it by the impact of a charged particle or by absorption of a photon, it can either change into a state with higher energy – the atom is then excited – or into a state beyond the ionization limit – the atom is then ionized. During the excitation, only discrete energies can be absorbed, which are defined by the differences of the state energies, while during ionization any energy greater than the ionization energy can be absorbed.

In Fig. 3.15 the photoelectric effect of a γ-quantum with the energy $E = h\,\nu$ in the K-shell of an atom is schematically depicted. The energy balance can be read as

$$E = h\nu = E_{\text{kin}} + E_{\text{K}} \tag{3.34}$$

In order to ionize the atom, the binding energy has to be provided first. The rest of the γ-energy goes to the released electron as kinetic energy. The very small recoil energy of the atom is neglected in this balance. Of course, analogous relations are valid for the higher shells, at which the fine structure splitting, not depicted here, must also be taken into account.

In the photoelectric effect it is the kinetic energy of the electron that is measured by an energy sensitive detector. It is always, and especially so for heavy atoms, smaller than the photon energy. At first sight it looks like the energy of the photon can not be determined. If the photo effects of successive quanta take place in different shells, the kinetic energies of the emitted photoelectrons can even for monochromatic quanta assume many discrete values, and there is no longer a clear relationship between the energies of photons and electrons. However, it turns out that as a result of secondary processes, the binding energy of the shells is converted into kinetic energy of electrons, so that in the end the entire photon energy is detectable as kinetic energy.

An atom that lacks an electron in a normally occupied shell is in an unstable, excited state, whose excitation energy is just the binding energy of this shell. The lifetime of such excited states is about 10^{-8} s for the outer ones and much shorter, namely in the order of 10^{-12} s, for the inner shells. The atom is going into the ground state by capturing an electron from a higher shell or from the continuum and the excitation energy is released as radiation. This radiation is visible or ultraviolet light when a hole is filled in an external shell, and characteristic X-ray

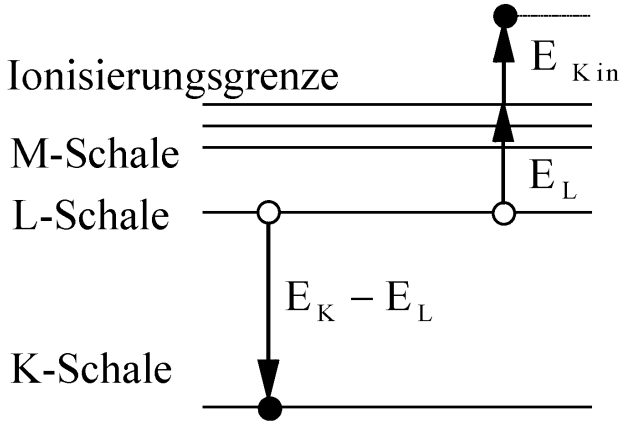

Figure 3.16: Schematic representation of the Auger effect.

radiation, if it is filled in an inner shell. (Characteristic means that for each element this radiation has different, specific values that only depends on the atomic number. The occurrence of this radiation is indicative of an element and can therefore be used for chemical analysis). This is the inverse process to the photoelectric effect: an electron moves from an excited, bound state into a deeper state or from the continuum into a bound state, at which the energy difference is emitted as radiation.

For the energy measurement with the photoelectric effect it is essential that the characteristic X-rays in the matter in which they are generated, have only a short mean free path. It is easily absorbed by other photoelectric effects in the higher shells and thus produces secondary electrons. In a sequence of processes, the original excitation energy is transformed into kinetic, detectable energy.

This also happens directly in the Auger effect, where the excitation energy is transfered directly to an electron. For example, an electron of the L-shell can transfer the energy $E_\mathrm{K} - E_\mathrm{L}$, which is released at its transition into the K-shell, to another electron of the L-shell, if it is greater than the binding energy E_L (fig. 3.16). This so-called Auger electron then leaves the atom with the energy $E_\mathrm{kin} = E_\mathrm{K} - 2E_\mathrm{L}$. The Auger effect can thus be understood as a second order inner recoil, after which excitation energy occurs as kinetic energy. The atom, which now lacks two electrons in the L-shell, goes through radiation emission or further Auger effects into the ground state. In general, these are competing processes, with the Auger effect more likely for low atomic numbers and radiation emission more likely for high atomic numbers.

In the ideal case, the energy of a γ-quantum is transformed through the secondary processes completely into kinetic energy of electrons, which can be measured in energy sensitive detectors. These processes occur in a time of the order of 10^{-8} s, which is comparable to the response time of a detector to an event. That means, the detector integrates across all secondary events and provides a signal that is proportional to the photon energy. The photoelectric effect therefore produces in the energy spectrum a line at the γ-energy, the photo line, as shown in Fig. 3.17. Ideally, it is symmetric, is at the energy of the γ-quantum and has a finite width caused by the limited energy resolution of the detector and which is wider the worse the resolution is. The dotted line of the unsymmetrical broadening towards lower energies is caused by events, in which not all of the energy is detected, be it X-rays escaping from the detector, or secondary electrons that are not completely absorbed in the sensitive part of the detector. It can be observed in the spectra of high-resolution semi-conducting detectors, where the line width is smaller than the energy of the characteristic X-ray radiation.

The calculation of the cross section for the photoelectric effect is not easy to perform. Since the wave functions of the electrons in the bound states are not exactly known and those of the

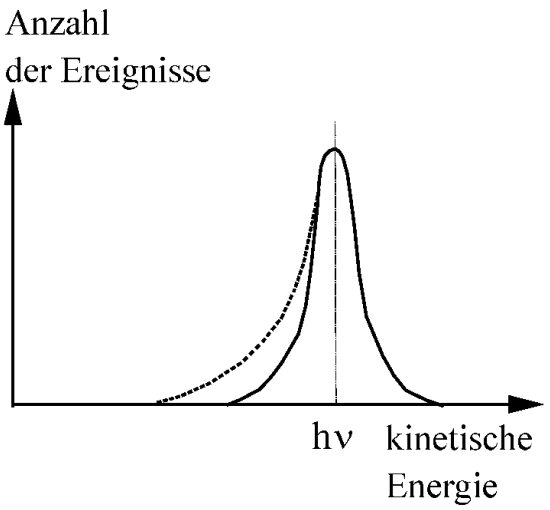

Figure 3.17: The photo peak.

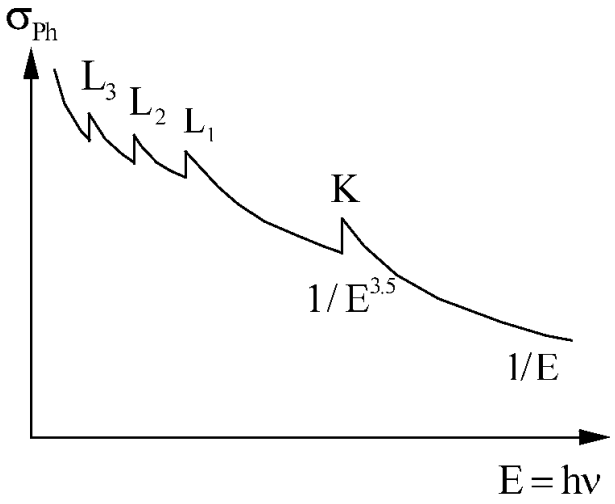

Figure 3.18: Schematic representation of the cross section for the photoelectric effect.

free electron are available as an infinite series, simplifying assumptions are necessary, in order to to arrive at least at approximate solutions for in certain cases [11]. In most cases, only the photoelectric effect in the K-shell is taken into account, which is much more likely than in the higher shells. More than 80% of the photons are absorbed in the K-shell. The explanation lies with the kinematics of the photo effect. The energy and momentum transfer to the atom, required by the conservation laws, is simplest when the photon is absorbed by strongly bound electrons.

In the Fig. 3.18 the shape of the cross section is shown as a function of the energy (not to scale). The general tendency is: it decreases with increasing energy. In the low-energy range, however, structures can be seen, the absorption edges. Here, the drop is always interrupted by a steep ascent, when the photon energy reaches the ionization energy of a shell or subshell. At these energies, the ionization of new shell becomes possible, which leads to a jump in the cross section. Also indicated is the fine structure splitting of the shells: while the K-shell has only one absorption edge, the L-shell shows a triple splitting. Even higher shells are no longer marked.

In the region above the sawtooth structure, the cross section decreases monotonically, initially with $E^{-3.5}$ and eventually with E^{-1}.

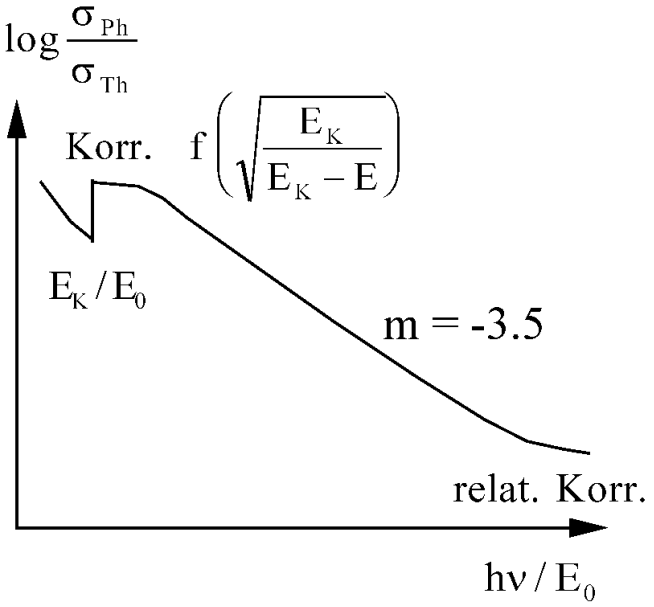

Figure 3.19: Semi-logarithmic application of the total cross section for the photoelectric effect.

This behaviour is shown somewhat more quantitatively in Fig. 3.19. In a non-relativistic approximation with plane waves for the wave function of the electrons, which is the so-called Bornian approximation, Heitler found for the total absorption cross-section of a photon on both K-electrons:

$$\sigma_{\mathrm{Ph}} = \alpha^4 \cdot Z^5 \cdot \sqrt{32 \cdot \left(\frac{E_0}{E}\right)^7} \cdot \sigma_{\mathrm{Th}} \tag{3.35}$$

where α is the fine structure constant, Z the atomic number of the absorbing atom, E_0 the the rest energy of the electron, E the energy of the absorbed photon and σ_{Th} the classic Thomson cross section. In the semi-logarithmic representation, its dependence on energy is represented by a straight line with a gradient of 3.5. For photon energies near the binding energy of the K-shell, this relationship is no longer valid. It must be multiplied by an expression of the form given in Fig. 3.19, which takes into account the resonance character of the absorption in the K-shell. Also at the highly energetic end of the representation, in the relativistic range, it is also no longer valid. It then changes to

$$\sigma_{\mathrm{Ph}} = 1.5\,\alpha^4 \cdot Z^5 \cdot \frac{E_0}{E} \cdot \sigma_{\mathrm{Th}} \tag{3.36}$$

As you can see, both corrections flatten the slope. Essential for the photoelectric effect is its strong dependence on the atomic number. In both equations it is included with the 5th power. Even for more precise calculations the exponent is between four and five, depending on the energy.

About the angular distribution is can be noted that with increasing energy the photoelectrons are emitted more and more in forward direction, i.e. in the direction of the incident quantum. At 100 keV, the distribution very broad, a considerable number of electrons is still emitted perpendicular to the photon, the most likely Angle is 45°. At 0,5 MeV the maximum is already at 20°, and there is practically nothing left at angles greater than 45°.

3.2.2.3 The pair production and pair annihilation

In the possible types of interactions of γ-radiation with matter discussed so far, the photon energy was completely or partly transfered to a charged particle of the matter. Pair production is a completely different process: particles are created. The γ-quantum disappears and its energy prevails as rest energy and kinetic energy of a particle-antiparticle pair.

Dirac was the first with a very descriptive explanation of pair production, as well as the nature of antiparticles. Meanwhile, it has been supplemented or replaced by Feynman's quantum electrodynamics. According to the Dirac equation, the energy states of the electron are given by

$$E = \pm\sqrt{p^2c^2 + E_0^2} \tag{3.37}$$

With the positive sign, this is the equation for the total energy of a free, relativistic electron with the rest energy E_0 and the momentum p. However, Dirac took also the minus sign seriously and concluded that in addition to an electron with a known positive energy range of $E \geq E_0$ a second, negative range with $E \leq E_0$ can exist. The two areas are separated by an energy gap $2E_0$. Having to assign negative energy states to electrons was against all experience. He sidestepped the difficulty by postulating that all negative states are occupied according to the Pauli principle. It was called the Dirac Sea. The electrons bound in the atoms or molecules occupy in this image discrete states in the (for free electrons) forbidden area below the area boundary.

A transition of an electron from the positive to the negative energy range is not possible, since there are no free sites. On the other hand, an electron can be lifted out of the sea into an unoccupied state of the positive range. In a process comparable to the photoelectric effect, a γ-quantum with an energy of at least $2E_0$ can lift an electron from the sea into the range of positive energy. In the real world, one has a normal, free, *negative* electron and a hole in the sea. One can show that this hole behaves exactly like a *positive* electron with *positive* energy. The hole is called Positron, the process is pair production.

The resulting hole or positron is obviously a very unstable state in the presence of electrons. The transition of an electron from the positive to the negative energy range is now possible. Both the the electron as well as the hole disappear. the transition energy is released as electromagnetic radiation. This radiation is called annihilation radiation, the process is pair annihilation.

Fig. 3.20 shows the possible processes. During pair production, a γ-quantum with an energy greater than the forbidden zone disappears, and an electron-positron pair is created. From the γ-energy, a fraction of $2\,E_0$ is used up in order to lift the electron across the forbidden zone, the rest occurs as kinetic energy of the pair. During annihilation, a hole that was originally range of negative energy, is filled by an electron from the positive range. The figure shows the most common case, where both the positron and the electron are at rest. In this case, the entire released radiation energy is equal to the energy gap. It can be distributed among one or more quanta, depending on whether the process takes place in the field of a charged particle or in vacuum. Not included in these simple considerations are possible recoil-energies, which will be discussed further below.

The positron is also called the anti-particle of the electron. In the Dirac picture it is clear what is meant by this. It has the properties of a *missing* electron and in this sense it is complementary to an electron, as it can dissolve into pure energy together with the electron. In quantum mechanical terms, this means that the additive quantum numbers of electron and positron cancel each other out.

The energy and momentum balance shows that the pair production with a single γ-quantum in a vacuum is not possible. A photon with the energy E_γ and the momentum $p_\gamma = E_\gamma/c$ cannot simultaneously transfer its entire momentum and energy to a particle with a finite rest mass. The energy E of an electron-positron pair is

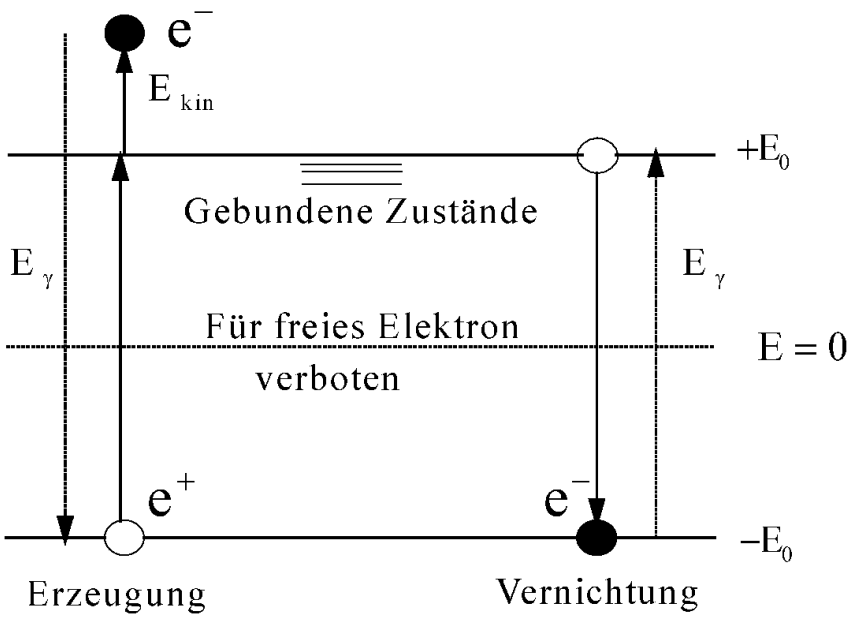

Figure 3.20: Schematic representation of pair production and pair annihilation.

$$E = \sqrt{p^2c^2 + E_i^2} \tag{3.38}$$

E_i is the inner energy and p the momentum of the pair. If the photon transmits its entire energy, i.e. $E = E_\gamma$, then the result for the momentum of the pair with the center of gravity velocity v is:

$$p = \frac{E}{c^2} \cdot v = \frac{E_\gamma}{c^2} \cdot v = \frac{v}{c} \cdot p_\gamma \tag{3.39}$$

For a complete energy transfer, the pair's momentum is less than that of the γ-quantum. However, in the field of a charged particle the excess momentum of the photon can pass over to this particle. There is a minimum energy E_γ of the quantum, the threshold energy, at which pair production begins. This is

$$E_\gamma = 2E_0 \cdot \left(1 + \frac{E_0}{M_0\, c^2}\right) \tag{3.40}$$

M_0 is the rest mass of the particle in whose field the pair production takes place, and E_0 is, as before, the rest energy of an electron. During pair production in the field of heavy nuclei, the threshold energy is virtually equal to the rest energy of the electron-positron pair, because in this case the second term in the parentheses can be neglected. The recoil energy is infinitesimally small and the photon energy is distributed between the pair. In the Coulomb field of an electron, on the other hand, the threshold energy is four times the rest energy of an electron. A considerable recoil energy is transferred to the electron, which is just as large as the rest energy of the pair, which is why this process is also known as inelastic pair production.

The calculation of the angular distribution and the effective cross section for the pair production is very complex and leads to complicated terms, which can only be simplified under specific conditions. Such an approximate expression for the total cross-section of interactions in heavy elements, which applies to high energies, but does not take into account the charge shielding in the inner shells, is in Born's approximation:

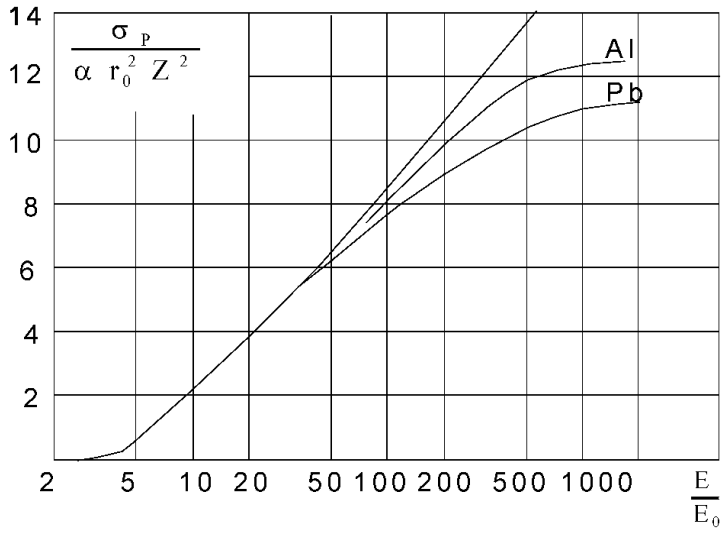

Figure 3.21: The cross section for pair production.

$$\sigma_P = \alpha \cdot r_0^2 \cdot Z^2 \cdot \left(\frac{28}{9} \cdot \log \frac{2E}{E_0} - \frac{218}{27} - 1,027 \right) \text{ pro Atom} \tag{3.41}$$

α is the fine structure constant, r_0 is the classical electron radius, and Z is the atomic number of the elements. It strongly depends on the atomic number, with which it rises quadratically. It depends only slightly on the energy, increasing logarithmically. However, since the cross sections for both the Compton effect and the photoelectric effect become smaller with increasing energy, pair formation far outweighs all other interactions at high energies. A more detailed discussion of the calculation that leads to Eqn. 3.41 and the range of the validity is found in [11]. The course as a function of the energy is shown in Fig. 3.21. The linear curve represents Eqn. 3.41. The flattening of the curve is caused by taking into account the charge shielding. In this approximation, the cross section converges towards an asymptotic limit. The curve should be the same for all elements, independent of the atomic number. This is actually the case in the approximation without charge shielding. But if it is taken into account, deviations occur at high energies. In Fig. 3.21 the values for aluminum and lead are drawn.

Also for the pair annihilation the occurrence of a single quantum in vacuum is forbidden by the conservation laws. The Eqn. 3.39 says in this case that the momentum of the quantum is greater than that of the pair. This becomes immediately clear, when the pair is at rest before the annihilation. Then, the initial momentum is zero, the outgoing momentum of the γ-quant is $2E_0/c$.

The annihilation in two or more quanta, on the other hand, is permitted without further recoil partners by the conservation laws. With the energies E_- and E_+, and the momenta p_- and p_+ in the center of gravity system for the electron and the positron, the total energy E and the total momentum p of the pair in the laboratory system, and the energies $E_{\gamma i}$ and momenta $p_{\gamma i}$ of the γ-quanta, the energy theorem for the annihilation with the emission of two quanta is:

$$E = \sqrt{p^2c^2 + \epsilon_0^2} = E_{\gamma 1} + E_{\gamma 2} \tag{3.42}$$

with

$$\epsilon_0 = E_+ + E_-, \quad E_+ = \sqrt{p_+^2 c^2 + E_0^2}, \quad E_- = \sqrt{p_-^2 c^2 + E_0^2} \quad \text{with} \quad \vec{p}_+ = \vec{p}_- \tag{3.43}$$

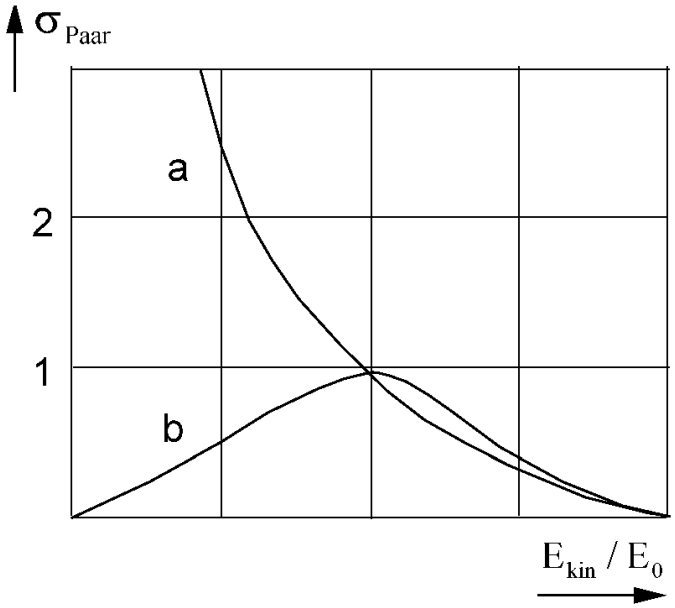

Figure 3.22: Cross section for the $e^+ e^-$ annihilation: a) in two quanta, b) in one quantum.

The momentum theorem is

$$\vec{p} = \vec{p}_{\gamma 1} + \vec{p}_{\gamma 2} \tag{3.44}$$

If the center of gravity of the pair is at rest ($\vec{p} = 0$), it is

$$\vec{p}_{\gamma 1} = -\vec{p}_{\gamma 2} \quad \text{and} \quad E_{\gamma 1} = E_{\gamma 2} = E_+ + E_- \tag{3.45}$$

The γ-quanta move apart in exactly opposite directions. They both have the same energy, each with the total energy of one particle of the pair. If the particles of the pair also have vanishing kinetic energy in the center of gravity system, i.e. if $p_+ = p_- = 0$, this energy is reduced to the rest energy of a lepton. In the two-quanta annihilation of a pair at rest, each of the quanta has the energy $E_\gamma = 0.511\,\text{MeV}$.

This is no longer the case if the center of gravity of the pair is moving, e.g. if the positron is moving with the velocity v_+ towards a resting electron. Then the energies of the γ-quanta are different and there is a deviation from the 180° correlation. For non-relativistic velocities of the positron the angle ε of the maximum deviation (c = speed of light) is:

$$\varepsilon = \sqrt{\frac{v_+}{2c}} \tag{3.46}$$

The angular correlation is broadening and the speed of the positron can be inferred from its width. The conservation laws also allow the decay into more than two quanta. Energy and momentum are then arbitrarily distributed.

The cross sections for the one and two quantum radiation in Born's approximation are shown in Fig. 3.22 as a function of the reduced kinetic energy of the positron, with the electron at rest. For single quantum radiation, it is given in units of $\pi \cdot \alpha^4 \cdot r_0^2 \cdot Z^5$, for the dual quantum radiation in units of $\pi \cdot r_0^2 \cdot Z$, where Z is the atomic number of atoms in the material, r_0 is the electron radius and α is the fine structure constant. It can be seen that for light nuclei the two-quanta decay is far more likely, especially at low positron energies. The probability decreases monotonously with increasing energy. The single quantum decay passes through a maximum for a positron kinetic energy of 0.5 MeV.

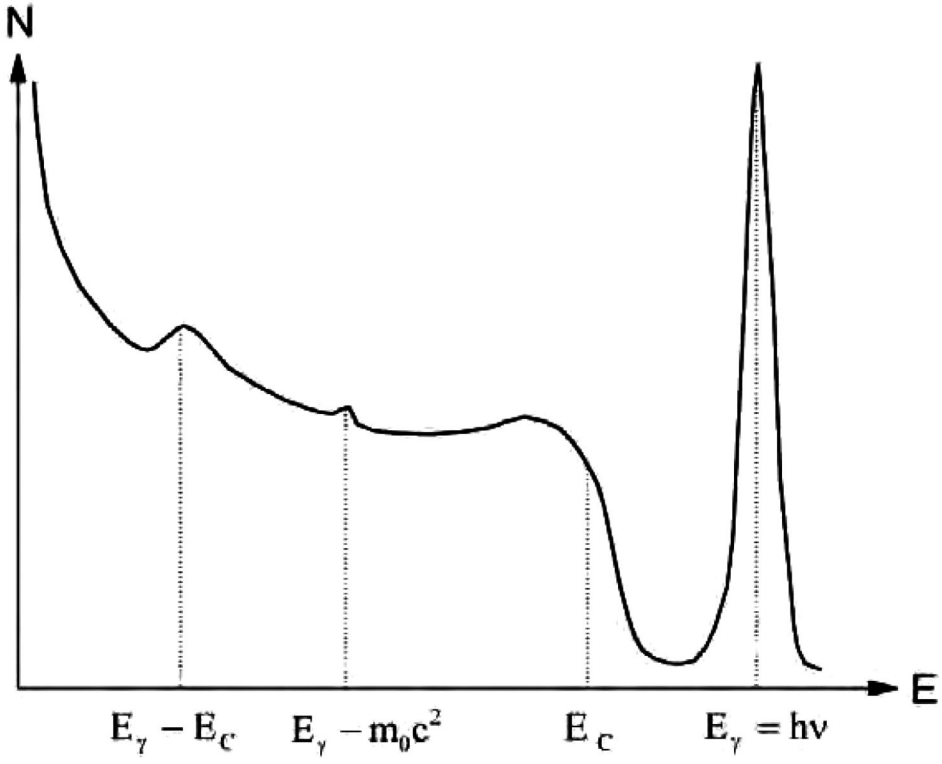

Figure 3.23: γ-spectrum.

The annihilation radiation has practical implications for the detection of positrons in matter. Two coincident γ-quanta, each with an energy of 0.511 MeV, flying in opposite directions, are an unambiguous sign of the annihilation of an electron-positron pair. Even the appearance of a line at this energy is sufficient, if it is ensured that no quanta from other processes occur in this region.

What does the spectrum of an event look like that was triggered by a pair production in an energy-sensitive detector? This is a question of the energy transferred to the electrons. For this, one must take a closer look at the processes that take place during pair production. First, the generated pair receives the remaining γ-energy, exceeding the rest mass, as kinetic energy. Within picoseconds, the time needed for the deceleration of the leptons, the kinetic energy is transformed into excitation energy of the surrounding matter. After a few nanoseconds, the positron at rest almost always annihilates into two γ-quanta, each of which has an energy of 0.511 MeV. (More details can be found in the experiment Positronium). If both annihilation quanta are now absorbed in the detector by the photoelectric effect, the total energy of the original γ-quantum occurs as excitation energy in the detector and the event occurs at the photo-peak. But if one or both quanta escape the sensitive volume of the detector without interaction, then further lines appear in the spectrum, which are one or two rest energies below the photo-peak. These lines are called escape peaks.

Fig. 3.23 shows the complete spectrum of a monochromatic γ-source. You can see the photo line at the γ-energy E_γ and the continuous Compton distribution rising from the edge E_C to lower energies. It is assumed that the γ-energy is slightly larger than the threshold of pair production. Therefore an escape line appears at the distance of an electron rest mass. It has the width of the photo line, but is much weaker, as the cross section for pair production just above the threshold is much smaller than that for the photoelectric effect. Depending on the geometry of the detector arrangement, a secondary process leads to another line, the backscatter line. It is created when the quantum initially passes through the detector without interaction, and then is

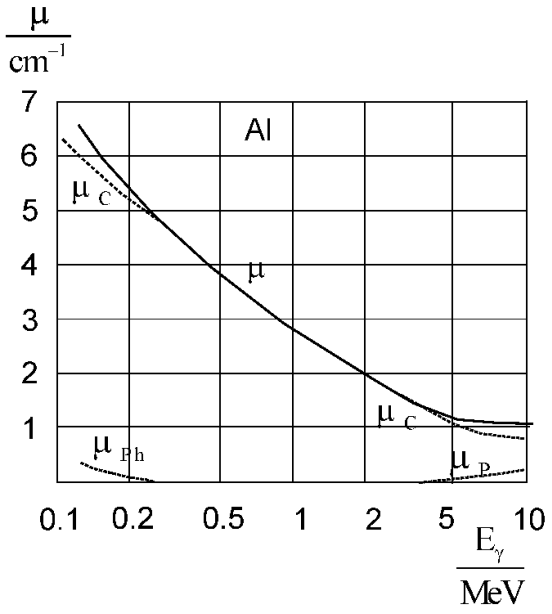

Figure 3.24: The linear absorption coefficients of aluminum.

scattered back by the matter behind it into the detector, where it interacts in the photoelectric effect. It has lost the energy of the Compton edge during the scattering and therefore occurs at an energy, which corresponds to the distance between the photo line and the Compton edge. Since the backscattering is not always exactly at 180°but within a certain angular range, the backscatter line is broader compared to the photo line.

3.2.2.4 The total absorption coefficient for electromagnetic radiation in matter

The decrease of the intensity of electromagnetic radiation by the absorption in matter is determined by the previously derived relation

$$I = I_0 \cdot e^{-\mu d} \tag{3.47}$$

The parameter μ, which describes the probability of absorption, has the dimension of a reciprocal length and is called the total linear absorption coefficient. The quantity

$$\lambda = \frac{1}{\mu} \tag{3.48}$$

is the mean free path of radiation in matter, i.e. the mean distance covered by a quantum, before it is absorbed. Absorption can essentially be attributed to the three processes discussed above, which are the photoelectric effect, pair production and with the previously discussed limitation the Compton effect. The total linear absorption coefficient is therefore the sum of the partial absorption coefficients of the individual processes, i.e.

$$\mu = \mu_C + \mu_{\mathrm{Ph}} + \mu_{\mathrm{P}} \tag{3.49}$$

The absorption coefficients are linked with the cross sections of the relevant processes by the particle density N, which is the number of atoms per unit volume.

$$\mu = N \cdot (\sigma_{\mathrm{C}} + \sigma_{\mathrm{Ph}} + \sigma_{\mathrm{P}}) \tag{3.50}$$

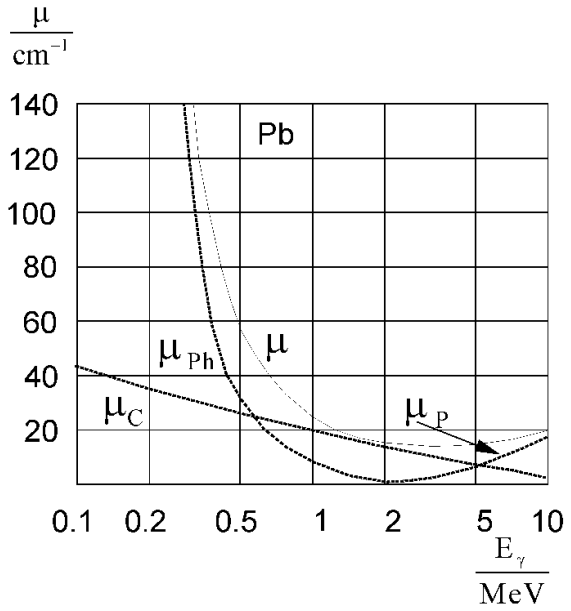

Figure 3.25: The linear absorption coefficients of lead.

Fig. 3.24 shows the linear absorption coefficients for aluminum as a function of energy up to 10 MeV. It's obvious that for this light element the absorption is almost entirely caused by the Compton effect. The photoelectric effect is only noticeable at low energies below 200 keV. Pair production is only detected at a noticeable rate at energies greater than 5 MeV. The reason for this behavior lies in the Z-dependence of the cross sections. The photoelectric effect is only significant at higher atomic numbers, and predominates in the case of heavy elements. This can be seen from Fig. 3.25 in which the absorption coefficients are plotted at the same energies for lead. Here the photoelectric effect dominates at low energies. Only above 600 keV the Compton effect is more likely. It is also noteworthy that the absolute values of absorption are much higher than those of aluminum. The total absorption has a minimum that lies at about 3 MeV for lead, for aluminum at about 10 MeV beyond the plotted range.

Fig. 3.26 shows the ranges of the atomic numbers and the energy in which one of the three effects is dominant. They are separated by two curves. On the left curve the linear absorption coefficients for the Compton effect and the photoelectric effect are the same and on the right curve the Compton effect and the pair production are the same. Roughly speaking, at low energies the photoelectric effect, at medium energies the Compton effect, and at large energies the pair production predominate.

One learns from this graph that at energies around 1 MeV and slightly below, where most of the radioactive sources are located, the predominant interaction in plastic scintillators is practically only the Compton effect. This is also seen in the spectra, where not even the slightest trace of a photo line can be seen. Starting from the chemical composition CH_2, plastic scintillators have an average atomic number of 2.7. Other detectors used in the lab course, such as Ge and NaJ, both have $Z = 32$ and therefore a considerable fraction of the photo peak.

In table 3.1 this behavior is summarized again in the last column. Also, the dependence of the electromagnetic effects on the energy of the quanta and the atomic number of the material is listed.

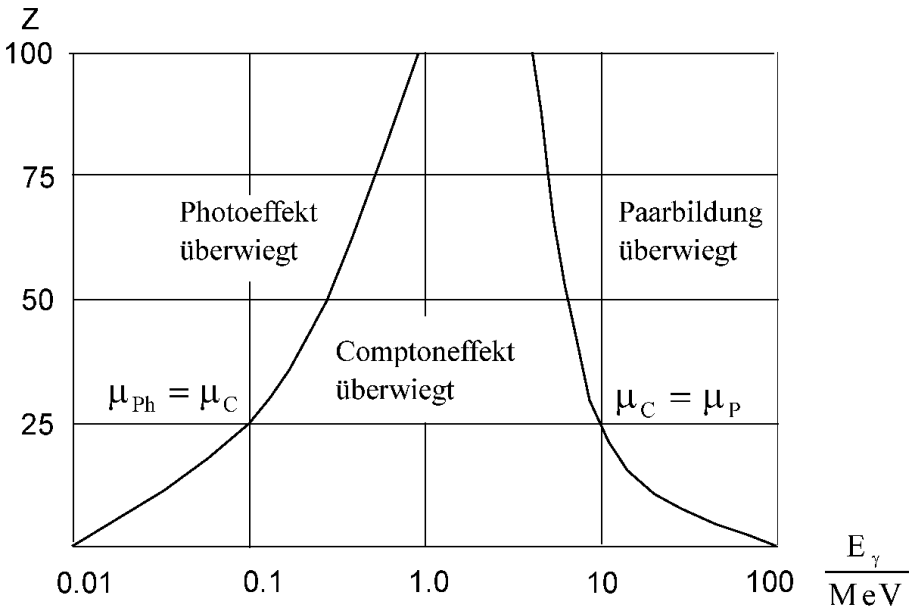

Figure 3.26: Comparison of the linear absorption coefficients.

Table 3.1: Energy and Z-dependence of electromagnetic effects.

	Energy	Z	predominant at
Photo Effect	$1/E^3$	$Z^4 - Z^5$	E small Z large
Compton effect	$1/E^2$ coarse	Z	E medium (1 MeV) Z small
Pair production	$\ln E$ over the threshold	Z^2	E large Z large

Chapter 4

Radiation detectors

In the previous section, the interactions of radiation with matter were discussed, i.e. how the energy is transferred to matter. It was shown that the charged particles transmit their energy in a direct way by excitation or ionization, while the uncharged particles first produce charged particles in a primary process in which their energy is transferred completely or partially and then the charged particles interact with matter.

In this section we discuss the methods by which excitation or ionization can be detected, quantitatively measured, and the detectors in which these measurement principles are realized. In addition to those which are used in the lab course and which will therefore be treated in detail, a few others will be briefly discussed which are important for other applications.

4.1 Detectors for direct detection of ionization.

The oldest principle used in radiation detectors is the direct detection of ionization by observing the change in conductivity of the irradiated matter. In the early days of nuclear physics, electrometers that discharged upon irradiation, or ionization chambers, a type of gas-filled capacitor that became conductive by ionization, were used. From that the gas and proportional counters, still used today, have been developed. They are much more sensitive than their predecessors because of the internal amplification of the originally weak signals. Not only in gases, but also in solids, electrical resistance is affected by the ionizing radiation. This has led to the development of semiconductor detectors.

4.1.1 The gas counter

All gas counters work in a similar way. The particle ionizes the gas inside a capacitor. The electrons and positive ions thus created, migrate to the electrodes in the applied electric field. The electric current created during their migration is measured. Usually the positive ions are single-charged. Therefore, cations with more than +1 charge are not considered further, nor are the anions which are formed with low probability by electron accumulation.

The mode of operation of the various counters is determined by the processes to which electrons, ions, atoms, and molecules are subjected in electric fields. It is therefore useful to first introduce the most important terms and definitions in gas electronics. More details can be found in [16].

As long as the charged and uncharged particles are in thermal equilibrium, the same temperature T can be attributed to them. A particle with mass M_i then has a mean thermal velocity

$$v_i = \sqrt{\frac{3 \cdot k \cdot T}{M_i}} \tag{4.1}$$

where k is the Boltzmann constant. On average, the particles move freely in the gas with this velocity until they collide with another particle. The distance they travel between two collisions is called the mean free path and is [17]

$$L = \frac{1}{\sqrt{2}\pi \cdot a^2 \cdot N} \quad \text{for ions, atoms, molecules} \tag{4.2}$$

$$\lambda = \frac{1}{\pi \cdot \left(\frac{a}{2}\right)^2 \cdot N} \quad \text{for electrons} \tag{4.3}$$

The quantity a, with the dimension of length, depends on the size of molecules and is called the impact parameter. It is not known precisely, but in any case, it is a measure of the smallest distance between the colliding particles. In Eqn. 4.2, it is assumed to be the same for the ions and for the neutral particles. Therefore, they have the same mean free path. The electrons are much smaller and can be considered as point-like in comparison. Therefore, in Eqn. 4.3 only half of the impact parameter is included. N describes the density of the heavy particles. The mean free path of electrons in gases is therefore inversely proportional to the gas pressure and follows the rule of thumb

$$\lambda = \frac{1.3}{p}\,\text{mm} \qquad \text{for } p \text{ in hectoPascal} \tag{4.4}$$

and is of the order of $10^{-4}\,$cm at atmospheric pressure.

If an electric field with strength E is applied in the gas, then the charged particles absorb energy from the field. If they were in a vacuum, they would be accelerated uniformly, and their kinetic energy would increase linearly. In gases, however, they transfer part of the gained energy to the gas molecules with each collision. After some time, as a steady state is established in which the average velocity is higher than the thermal velocity of the molecules. Its magnitude is determined by the energy balance, according to which the energy absorbed from the field between two impacts is on average equal to that released during one impact. The increase of the mean velocities from the charged field results in an increased of the temperatures.

$$T_i = \frac{T}{2} + \frac{1}{2} \cdot \sqrt{T^2 + \frac{16 \cdot e^2 \cdot E^2 \cdot L^2}{9 \cdot k^2}} \quad \text{ions temperature} \tag{4.5}$$

$$T_e = \frac{T}{2} + \frac{1}{2} \cdot \sqrt{T^2 + \frac{4 \cdot e^2 \cdot E^2 \cdot \lambda^2}{9 \cdot k^2} \cdot \frac{M_i}{M_e}} \quad \text{electrons temperature} \tag{4.6}$$

For small field strengths, the temperatures are practically equal to the temperature T of thermal equilibrium, but for larger field strengths, at least the electron temperature is considerably higher because of the large ratio of the ion mass M_i to the electron mass Me.

The electric field causes the electrons and ions to migrate along the field lines superimposed on the thermal movement - this is called drift - with average velocities called drift velocities . These are

$$\bar{u}_i = b_i \cdot E = \sqrt{\frac{6}{\pi}} \cdot \frac{L \cdot e}{M_i \cdot v_i} \cdot E \quad \text{for ions} \tag{4.7}$$

$$\bar{u}_c = b_c \cdot E = \sqrt{\frac{6}{\pi}} \cdot \frac{\lambda \cdot e}{M_e \cdot v_e} \cdot E \quad \text{for electrons} \tag{4.8}$$

According to Eqn. 4.1, v_i or v_e are the average velocities calculated for the ions or electrons at a set temperature and b_i or b_e are their mobility . For weak fields they are independent of the field.

$$b_i = \frac{e \cdot L}{\sqrt{3 \cdot k \cdot T \cdot M_i}} \quad \text{ion mobility} \tag{4.9}$$

$$b_e = \frac{e \cdot \lambda}{\sqrt{3 \cdot k \cdot T \cdot M_e}} \quad \text{electron mobility} \tag{4.10}$$

Their ratio is

$$\frac{b_e}{b_i} = \frac{\lambda}{L} \cdot \sqrt{\frac{M_i}{M_e}} = 4\sqrt{2} \cdot \sqrt{\frac{M_i}{M_e}} \tag{4.11}$$

The mobility of the electrons and thus their drift speed is around three orders of magnitude greater than that of the ions. As example, in nitrogen under normal conditions and a field strength of 1000 V/cm, the drift speed of the ions is

$$\bar{u}_i = 13 \, \frac{\mathrm{m}}{\mathrm{s}} \tag{4.12}$$

It is superimposed on the thermal movement of the ions, for which results from Eqn. 4.1

$$\bar{v}_i = 490 \, \frac{\mathrm{m}}{\mathrm{s}} \tag{4.13}$$

where the drift speed of the electrons, under the same conditions is

$$\bar{u}_e = 17 \, \frac{\mathrm{km}}{\mathrm{s}} \tag{4.14}$$

From this, it can be seen that the ions mostly remain where they were created, while the electrons fly through the entire gas counter.

If the electron and ion temperatures differ from the gas temperature, energy is transferred via collisions as the systems move toward a new thermal equilibrium. For small differences, collisions are predominantly elastic, because only in a few cases the energy of the colliding partners is sufficiently high for internal excitation of a particle. In an elastic collision with a molecule of mass M, an electron loses the energy ΔE_e.

$$\Delta E_e = \frac{2 \cdot M \cdot M_e}{(M + M_e)^2} \cdot \left(E_e - \bar{E}\right) \approx \frac{2 \cdot M_e}{M} \cdot \left(E_e - \bar{E}\right) \tag{4.15}$$

and, if the masses of the ion and the molecule are considered to be equal

$$\Delta E_i \approx \frac{1}{2} \cdot \left(E_i - \bar{E}\right) \tag{4.16}$$

where E_e and E_i are the energies of the electron and ion, respectively, and $\bar{E}$ is the energy at thermal equilibrium. Because of the large mass difference, an electron must collide frequently to lose its excess energy, whereas an ion transfers half of its energy in just one collision. For this reason, the electron temperature can become considerably larger than the ion or gas temperature, as expressed in Eqn. 4.5 and Eqn. 4.6.

In strong electric fields, the electron temperature reaches values at which internal excitation and also ionization of the collision partner become more and more frequent. These two processes are important for the charge balance in the gas, since they both generate charges. In the ionization process a new electron-ion pair is created in a direct way, whereas during an excitation the new charge is created indirectly via a photon. The transition to the ground state does not always happen without radiation, but there is a certain probability for the emission of a photon, which can in turn release an electron via the photoelectric effect.

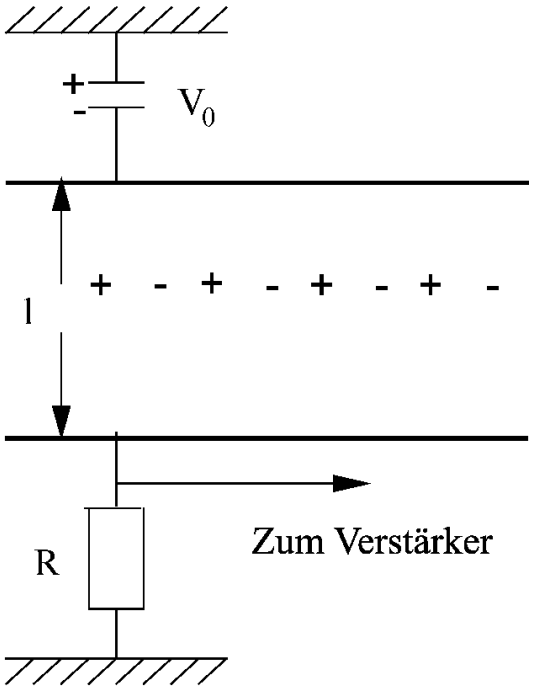

Figure 4.1: The ionization chamber.

In collisions between the ions and the gas molecules the energy is not sufficient for ionization or excitation, because first, the ions do not reach the high temperatures of the electrons, and second, because of the high kinetic energy of the center of mass only a small part of the energy is available for excitation. The heavy particles make almost exclusively elastic collisions.

In case of collisions of electrons with ions another process is possible: recombination. It is responsible for the loss of charges in the gas. The electron and the ion combine to form an electrically neutral molecule. The binding energy of the electron is transferred in the so-called triple collision to a third collision partner or leads to the dissociation of the molecule. Another, but less probable possibility is the release of energy by photons in a process called radiative recombination.

4.1.1.1 The ionization chamber

The ionization chamber consists of a plate capacitor filled with gas. The distance between the plates is defined by l, the capacitance by C, and a voltage V_0 is applied (Fig. 4.1).

A charged particle flying through the ionization chamber will ionize the gas. Each charged pair needs an average ionization energy W, for example, for air it is 35 eV. If the particle loses the total energy ΔE in the chamber, then n ion pairs are generated.

$$n = \frac{\Delta E}{W} \tag{4.17}$$

The total charge Q of the released electrons is

$$Q = -n \cdot e \tag{4.18}$$

It is of course equal to the *negative* total charge of the positive ions. In an electric field, the ions are attracted to the negatively charged plate, whereas the electrons to the positively charged plate. If the capacitor is isolated, then the voltage changes by the value

$$\Delta V = \frac{Q}{C} = \frac{n \cdot e}{C} \tag{4.19}$$

The voltage change can be directly measured. With Eqn. 4.17 the primary energy loss of the radiation can be obtained. The prerequisite for this, however, is that essentially the entire charge is collected and no charged particles are lost by recombination. This is the case if a sufficiently high voltage is applied, because then the particles reach the electrodes quickly.

This method of measurement is used in radiation dosimeters. It measures the voltage drop of a charged capacitor exposed to radiation. This is a direct measure of the dose of radiation.

In pulse mode, the chamber is connected as in Fig. 4.1. A constant and stabilized voltage V_0 is applied to a chamber with a capacitance C and a load resistor R. Without ionization the chamber has an infinite resistance, and no current flows. If the gas is ionized then it becomes conductive and a current flows as long as long as the charges are moving and have not yet reached the electrodes. A voltage pulse is thus generated at the resistor, which begins with the ionization and ends with the neutralization of the charge carriers at the electrodes.

The temporal pulse shape is describe by

$$V(t) = \frac{n \cdot e}{l \cdot C} \cdot (\bar{u}_e + \bar{u}_i) \cdot t \tag{4.20}$$

and depends on the mean drift velocities of electrons $\bar{u}_e$ and ions $\bar{u}_i$. If we assume that the ionization takes place at the distance x_0 from the positive electrode, and taking into account that ion mobility is small, then the total momentum can be decomposed into a rapidly increasing fraction $V_e(t)$, which originates from the motion of the electrons and the slowly increasing part caused by the ions $V_i(t)$. The electron fraction increases linearly up to the maximum value $V_{\mathrm{e\,max}}$

$$V_{\mathrm{e\,max}} = \frac{n \cdot e \cdot x_0}{l \cdot C} \tag{4.21}$$

when the electron collection time

$$T_e = \int_0^{x_0} \frac{\mathrm{d}x}{\bar{u}_e} = \frac{x_0 \cdot l}{b_e \cdot V_0} \tag{4.22}$$

is reached. After about 10^{-6} s all electrons have arrived at the positive electrode. The pulse now continues to grow by the ionic fraction up to the value

$$V_{i\ max} = \frac{n \cdot e \cdot (l - x_0)}{l \cdot C} \tag{4.23}$$

It is reached after an ion collection time

$$T_i = \int_{x_0}^{1} \frac{\mathrm{d}x}{\bar{u}_i} = \frac{(x_0 - l)l}{b_i V_0} \tag{4.24}$$

within about 10^{-3} s when all ions have reached the negative electrode. After the collection of all charges, the total magnitude of the pulse is

$$V_{\mathrm{max}} = V_{\mathrm{e\,max}} + V_{\mathrm{i\,max}} = \frac{n \cdot e}{C} \tag{4.25}$$

This is the same value as in Eqn. 4.19.

Unlike the individual components, it is independent of the location where the primary ionization occurs. Therefore, if we want to determine the energy deposited by the ionizing particle, the amplitude of the total pulse must be measured. This is only possible if the charges dissipate so slowly that no significant losses occur. This in turn requires a resistance R so large that the time constant $T = RC$ for the change of charge of the capacitor is small compared to the

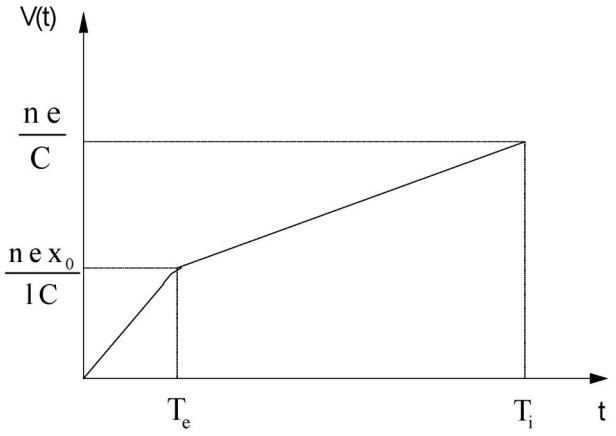

Figure 4.2: Schematic representation of the pulse shape in an ionization chamber.

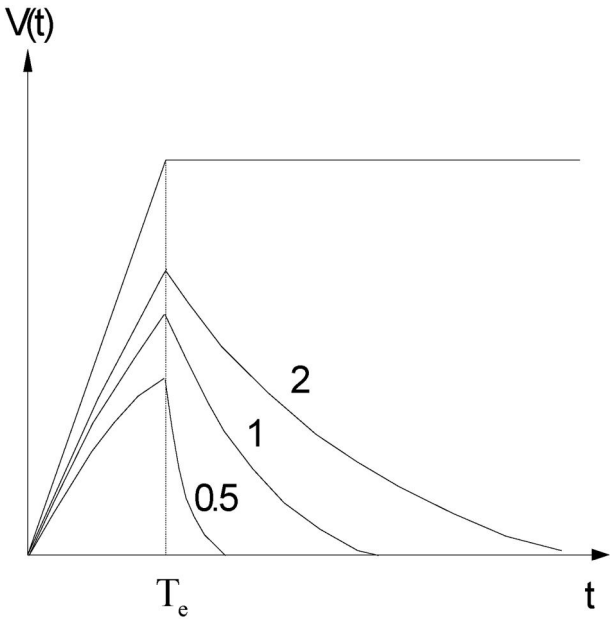

Figure 4.3: Pulse shape for different values of T/T_e.

ion collection time. This approximation is given in Eqn. 4.21, 4.23, and 4.25 and is shown, not to scale, in Fig. 4.2. It also states that the maximum pulse height remains constant for times greater than that of the ion collection time.

In practice, however, such large time constants are not possible, since they would require to measure a pulse in the order of milliseconds. Only small count rates can be processed with such a gas counter. Therefore, one chooses time constants that are much smaller than the ion collection time. Then only the electron component is measured and Eqn. 4.20 becomes [18]:

$$V(t) = \frac{T}{T_e} \cdot V_{\mathrm{e\,max}} \cdot \left(1 - e^{-\frac{t}{T}}\right) \quad \text{für } 0 \leq t \leq T_e \tag{4.26}$$

$$V(t) = \frac{T}{T_e} \cdot V_{\mathrm{e\,max}} \cdot \left(1 - e^{-\frac{T_e}{T}}\right) \cdot e^{-\frac{t}{T}} \quad \text{für } T_e \leq t \tag{4.27}$$

These pulse shapes are shown in Fig. 4.3 for different time constants T. The pulses are short with their maximum at $t = T_e$, however T_e depends on the origin. The curves increase linearly up to

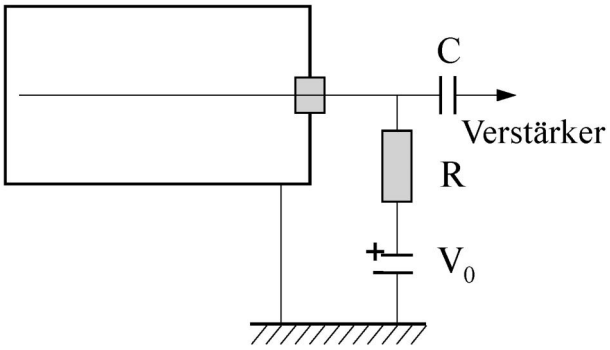

Figure 4.4: Cylindrical gas counter.

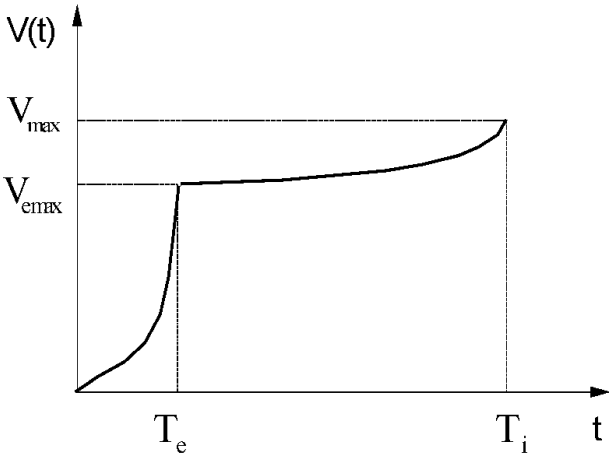

Figure 4.5: Pulse shape in a cylindrical counter.

T_e and the subsequent constant trend, shown in this representation, is the known approximation for very large time constants.

More advantageous than the flat ionization chambers in the form of a plate capacitor is the cylindrical arrangement of the electrodes. Along the axis of a metal cylinder on ground potential with the (inner) radius r_a a counting wire with the radius r_i is located. The counting wire together with the input stage of the amplifier has the capacitance C. A positive voltage V_0 is applied to the wire (see Fig. 4.4).

The field strength inside the gas counter is no longer homogeneous, but increases sharply in the vicinity of the wire

$$E = \frac{V_0}{r} \cdot \ln \frac{r_a}{r_i} \tag{4.28}$$

This results in a maximum height of the electron pulse when the primary ionization takes place at a distance r from the counting wire

$$V_{\mathrm{e\,max}} = \frac{n \cdot e}{C} \cdot \ln\left(\frac{r}{r_i}\right) / \ln\left(\frac{r_a}{r_i}\right) \tag{4.29}$$

The inhomogeneity of the potential means that the pulse shape over time is no longer linear as in Fig. 4.2, but increases slowly at first, then faster, as shown in Fig. 4.5. Compared to the plate capacitor, the cylindrical set-up has the advantage that the pulse height is less dependent on the location of the ionization; it is logarithmic instead of linear.

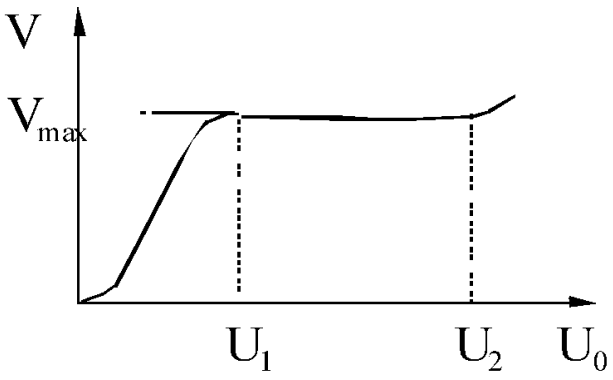

Figure 4.6: Pulse height as a function of the applied voltage.

As already mentioned, the prerequisite for measuring the energy of the particle is the complete collection of the charges generated during the ionization. This requirement can be checked by measuring the maximum pulse heights as a function of the gas counter voltage. The result is shown in Fig. **??**. The height V of the total pulse or similarly of the electron component, initially increases from zero until it reaches its maximum value V_{max} at a voltage U_1. In this region not all charge carriers reach the electrodes, but a small part is lost through recombination. The faster the charges are separated, i.e. the higher the applied voltage is, the smaller the losses are. This is followed by a region in which the pulse height remains constant up to the voltage U_2. All charges are collected in this region; increasing the voltage only shortens the collection time, but no longer increases the number of charges. The ionization chamber should be operated in this area.

4.1.1.2 The proportional counter

In Fig. 4.6, one could already see that the pulse height increases again at voltages that are greater than U_2. At that point, in addition to the primary ionization, additional charges are generated. The reason for this is that the electric field strength E in the immediate vicinity of the counting wire is so high that an electron within its mean free path λ is accelerated to energies sufficiently large to ionize the gas. Let U_i be the ionization potential of the gas, then the condition is

$$\lambda \cdot E \geq U_i \tag{4.30}$$

The electron has generated a second electron, both are accelerated again and can ionize further. The process can repeat itself over and over again. This is how an electron avalanche occurs and then the total charge of the electrons is no longer given by Eqn. 4.18, but by

$$Q = -n \cdot e \cdot A(U_0) \tag{4.31}$$

where A is the gas amplification factor and indicates how many secondary electrons are generated by a single primary electron through ionizing collisions. There is a range of voltage where A is independent of the number n of electrons. As in the ionization chamber, the resulting pulse is proportional to n (hence the name), but increased by the factor A. This range is called the true proportional range.

The gas amplification factor is different for each gas and depends very much on the applied voltage. For gas with small gains, the relationship is almost exponential

$$A \approx e^{U_0} \tag{4.32}$$

therefore, A can reach considerable values. For mono-atomic and diatomic gases there is still true proportionality until around $A = 100$, for polyatomic gases such as methane, even at $A = 10^5$.

The true proportionality ends with higher gains. The collisions with the electrons not only ionize the molecules, but also with a certain probability, which varies from gas to gas, excite the molecule which will then emit a photon. That photon can in turn release an electron through photoelectric effect with the gas or with the wall of the tube. If one uses γ to describe this probability, then one can write A_{tot} for the total gain, which takes into account both the direct ionization and the photoelectric effect.

$$A_{tot} = \frac{A}{1 - \gamma\, A} \tag{4.33}$$

This expression results from adding up the electrons that are created during the successive processes. The first electron creates A electrons via ionization and γA via the photoelectric effect. These latter generate $(\gamma A) \cdot A$ electrons directly and another $(\gamma A) \cdot (\gamma A)$ photoelectrons, which further increase the avalanche. The total number of electrons is then

$$A_{tot} = A + \gamma A^2 + \gamma^2 A^3 + ... \tag{4.34}$$

This is a geometric series with the sum shown above. If γA is very small compared to one, i.e. for small gas amplifications or vanishing probability of the photo-processes, the gas amplification is only determined by the ionization collisions, and therefore has true proportionality. If γA can no longer be neglected, which is always the case with sufficiently high gains, regardless of the γ value, then the photo-processes are important and the detector is operated in the range of limited proportionality. Amplification up to 10^8 are possible in this area.

The desired small values for γ are achieved by adding polyatomic molecules to the counting gas, which are characterized by large cross-sections for the absorption of photons. The energy is ultimately converted into heat via the excitation of vibrations and rotations. The use of a cathode material with a high work function for the photoelectrons also reduces the number of photo-processes.

The shape of the pulses is calculated exactly like the ionization chamber, except that the logarithmic potential of the cylinder geometry is used. Since the avalanches occur close to the wire, the electrons only have to traverse a small section of the total applied voltage before they are collected. In contrast, the ions need to drift through the entire counting tube. The rapidly increasing proportion of electrons in the total pulse is therefore only a few percent and can in good approximation be neglected. The pulse consists of the ion component, which is given for large time constants by

$$V_i(t) = \frac{n \cdot e \cdot A}{C \cdot \ln \frac{r_a}{r_i}} \cdot \ln\left(1 + \frac{r_a^2}{r^2} \cdot \frac{t}{T_i}\right) \tag{4.35}$$

Here r is the distance between the place where the avalanches occurs and the gas counter axis, and T_i is the ion collection time .

$$T_i = \frac{\ln \frac{r_a}{r_i}}{2 \cdot V_0 \cdot b_i} \cdot \left(r_a^2 - r^2\right) \tag{4.36}$$

The avalanches occur during the drift of the electrons, i.e. within the electron collection time. This happens, when compared to T_i, instantly. They arise within a range of a few free path lengths around the counting wire, so that the distance is about the same for all electrons and can be set equal to r_i. In this approximation, the ion component of the pulse is independent of the spatial position of the ionization track of the primary particle. Therefore, the energy of the particle can be determined by measuring the pulse height.

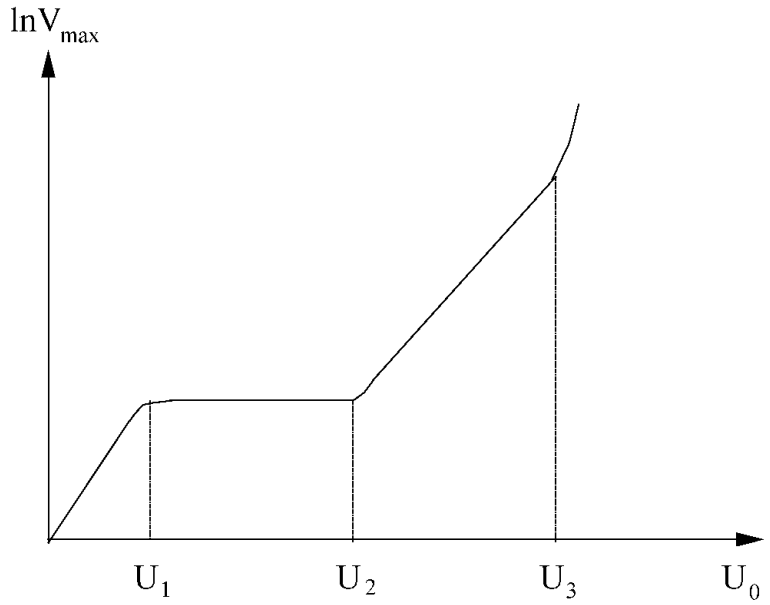

Figure 4.7: Pulse height of a proportional counter as a function of the voltage.

The timing of the pulses increases rapidly up to the maximum level of

$$V_{i\ max} = \frac{n \cdot e \cdot A}{C} \tag{4.37}$$

which is reached after the ion collection time. At halfway to the max, the time is

$$t_{1/2} = \frac{r_i}{r_a} \cdot T_i \tag{4.38}$$

which is already much shorter because $r_i \ll r_a$. This is why you can also work with small time constants, since you don't lose much of the pulse height.

The maximum pulse height increases by the gas amplification factor compared to a gas counter operated as an ionization chamber under identical conditions. It is around 10 to 100 mV. The size of the pulses and their independence from the location of the primary ionization distinguish the proportional counter from the ionization chamber.

Of course, the electron component can also be used in the proportional counter by choosing sufficiently small time constants as in the ionization chamber for detection and, under the conditions discussed there, also for energy measurement of the particles. The pulses are then roughly as long as the electron collection time. Since the space charge of the positive ions is too low to influence the potential curve, the gas counter is again sensitive to the detection of a further pulse after the electrons have been collected. There is practically no dead time (that is the time in which a subsequent pulse can not be detected), thus high counting rates can be achieved without losses.

The accuracy with which the time of arrival of an ionizing particle is determined depends on the collection time of the electrons. It is possible to determine from the rise time of the electron avalanche to nanosecond accuracy by applying high voltages or by using a thin counting wire, but if the primary electron did not originate at the counting wire, the transit time from the point of origin to the wire adds to this. The inaccuracy of the time determination is therefore always as great as the drift times of the electrons, which are microseconds. Counting tubes are therefore not suitable for exact time determination.

The dependence of the pulse height on the gas counter voltage is shown in Fig. 4.7. The logarithm of the pulse height is plotted. The gas counter acts as an ionization chamber up to

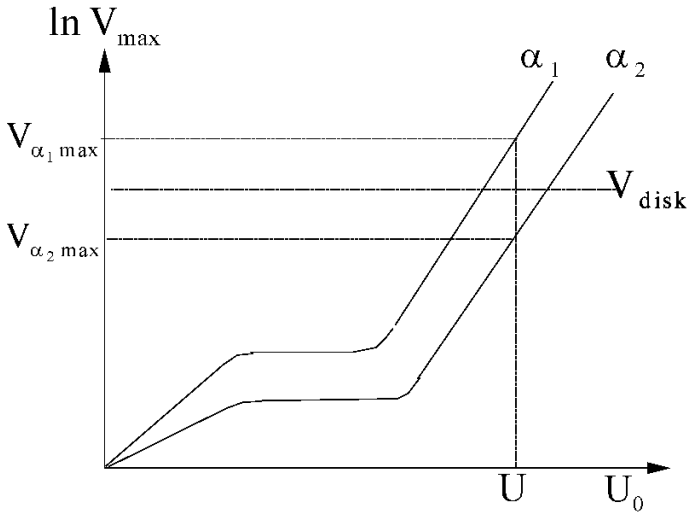

Figure 4.8: Energy discrimination with a proportional counter.

the voltage U_2, above which the gas amplification begins. The pulse height initially increases linearly in the logarithmic plot with increasing voltage up to voltage U_3. This is the region of true proportionality. Above this voltage, in the area of limited proportionality, the photoelectrons let the pulse height increase even faster.

Since the pulse heights of the ionization chamber and the proportional counter depend linearly on the number of primarily produced ion pairs and these, according to Eqn. 4.17, on the deposited energy, it is possible to detect particles of different types or energies separately. In Fig. 4.8 the maximum pulse heights are shown as a function of the gas counter voltage for two groups of mono-energetic α particles. If the gas counter is operated at voltage U, a spectrum is obtained that consists of two lines at $V_{\alpha_1\ max}$ and $V_{\alpha_2\ max}$. The low-energy line can be completely ignored by a pulse height discriminator that only lets through pulses that are larger than V_{disc}.

4.1.1.3 The trigger counter or Geiger-Müller counter

For the proportional counter it was found that with increasing voltage, in addition to the electrons generated by ionization, photons also appear in increasing numbers, and the electron density in the avalanches increases more and more. Since these photons release more electrons via the photoelectric effect in the gas and/or on the walls, the working principle of the gas counter changes.

Formally, this behavior can already be seen from Eqn. 4.33. If the probability γA approaches one, i.e. if every electron generates another through photoelectric effect, the total gas amplification factor , and with it the gas counter's pulse height, approach infinity. The voltage range in which this phenomenon occurs is called the trigger range. The gas counter is in a new state: no more individual, separate avalanches migrate to the wire, but a corona discharge spreads throughout the entire space.

The creation of the discharge should be considered a little more closely. The lateral expansion of the avalanches is tightly limited in the trigger and proportional counters, as it is determined by the diffusion speed of the electrons, which is much smaller than their drift speed in the field. Thus, the electrons of an avalanche move in a narrow conduit. As long as *one* electron only generates *one* avalanche, the different avalanches do not spatially overlap one another. This is precisely the criterion of true proportionality. In contrast, the area of limited proportionality is characterized by the fact that *some* of the primary electrons, in addition to the collision avalanche, trigger another avalanche by a photo-electron. The resulting photo avalanches are

statistically distributed over the volume of the gas counter and can overlap with others as they migrate. In the triggering area, *every* primary electron produces a photo-avalanche and every avalanche a new one. This creates a chain of spatially statistically distributed avalanches that spread over the entire volume.

With the trigger counter, a single electron is sufficient to ignite a discharge in the entire gas volume. In addition to the type of gas, the total charge that occurs depends only on the applied voltage and the geometry of the gas counter and is many times greater than when the same gas counter is operated in the proportional region. It is independent of the size of the primary ionization. Therefore the trigger gas counter is only suitable for **detection** of the particles, but no longer for energy measurement or for particle identification.

In contrast to the proportional range, the positive ions play a role in the electron balance for the triggering range, since the temperature and spatial density of the ions are significantly higher due to the higher voltage.

The high ion densities arise in the vicinity of the wire and influence the path of the electric field in the gas counter. The discharge develops within a few electron collection times. Since the avalanche formation takes place close to the wire, a high positive space charge quickly accumulates there, because the electrons are continuously collected by the anode wire, while the ions only marginally drift away due to their low mobility. The space charge acts as if the radius of the wire had increased in Eqn. 4.28 and strongly reduces the field on the counting wire. As a result, new avalanches no longer form and the discharge ends. This happens after a few microseconds.

Now the positive ions drift to the cathode, where they arrive after the ion collection time in the order of milliseconds. If the ion temperature is high enough, electrons can be generated, which start a new discharges, since they find the counting wire unshielded. The result is a permanent pulsed discharge, an operating state unsuitable for counting that must be inhibited.

The easiest way to terminate the discharge is to measure with a high time constant. Then the voltage drop at the load resistor (Fig. 4.4) after the ions have been collected is still so large that the effective voltage is no longer in the triggering range. However, high count rates cannot be processed in this way. In this case, it is better to reduce or reverse the gas counter voltage at a sufficient pulse height with an external electronic circuit, until the ions have been collected.

The best way of quenching is to prevent the emission of secondary electrons at the cathode. This is how the self-quenching gas counter operates. Small amounts of polyatomic molecules such as alcohols or hydrocarbons are added to the counting gas. The cations of the counting gas collide with these molecules on their way to the cathode and are neutralized by electron captures. The now ionized quenched gas molecules in turn migrate to the cathode, but can no longer release electrons there because of their lower temperature due to their greater mass. The discharge is contained.

The quenching gas has yet another effect. If it is selected so that its ionization energy is smaller than the excitation energy of the counting gas, it will be ionized by the photons emitted by the counting gas. The probability of this can be so high that the photons only have a mean free path of the order of millimeters and can no longer reach the cathode, but rather produce new avalanches in the immediate vicinity of their origin. The discharge spreads along the counting wire at a constant speed (typical value $1\,\mathrm{cm}/\mu\mathrm{s}$). When it has reached the ends, the electrons are already collected. Because of the high space charge, new avalanches no longer form, and the ions eventually migrate to the cathode.

The pulse shape of the self-quenching trigger counter is determined by the avalanche pulses from Eqn. 4.35, which already occurred in the proportional domain. It is calculated by summing up the individual propagating avalanches. If we assume for simplicity that the first avalanche occurs at one end of the counting wire ($z = 0$), and if we neglect the electron component, we get

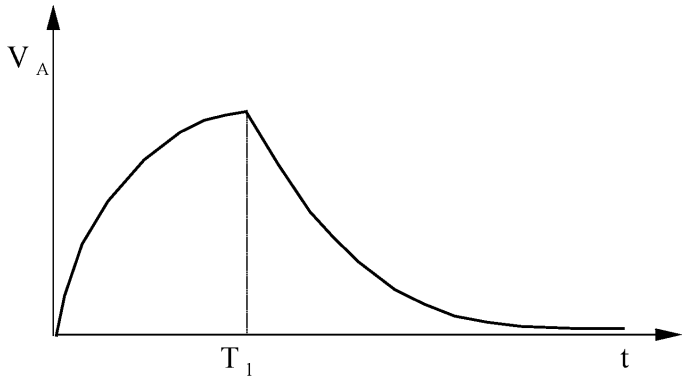

Figure 4.9: Pulse shape of the Geiger-Müller counter

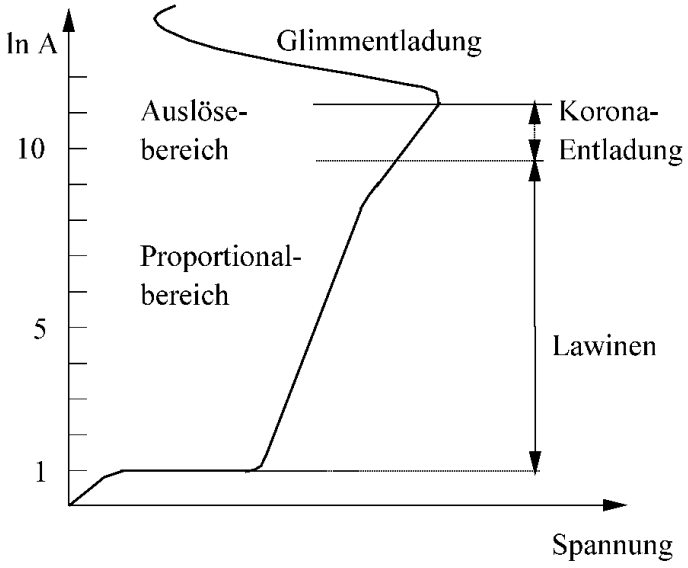

Figure 4.10: Characteristic curve of a gas counter.

$$V_A = \int_0^1 V_i \cdot \left(t - \frac{z}{v}\right) \cdot \frac{\mathrm{d}z}{l} = \int_0^{T_i} V_i \cdot (t - \tau) \cdot \frac{\mathrm{d}\tau}{T_1} \tag{4.39}$$

where v is the avalanche propagation velocity (approximately $1\,\mathrm{cm}/\mu\mathrm{s}$), l is the length of the counting wire, $V_i(t)$ from Eqn. 4.35 is the ion pulse, and $T_l = l/v$ the propagation time of the discharge, which is on the order of microseconds. If the time constant T of the gas counter circuit is equal to or less than the propagation time T_l, the pulse has the shape drawn in Fig. 4.9. It reaches its maximum value at T_l and then decreases with the time constant T.

In reality, the ion pulse is superimposed by the electron component, which can no longer be neglected in the trigger counter. The space charge around the wire prevents large gradients of the electric field. Therefore, the avalanches no longer occur only near the wire, but also at greater distances. Thus, the electrons travel longer distances and absorb noticeable energies from the field. For each individual avalanche there is a very short electron pulse, which is added to the ion pulse.

The gas amplification of the trigger counter can take values up to 10^{11}, which correspond to pulse heights up to 100 V. Such pulses can be counted without complex electronics. This is an advantage in comparison to other gas counters. However, this comes with the disadvantage that the energies of the particles can no longer be measured and different particles can no longer

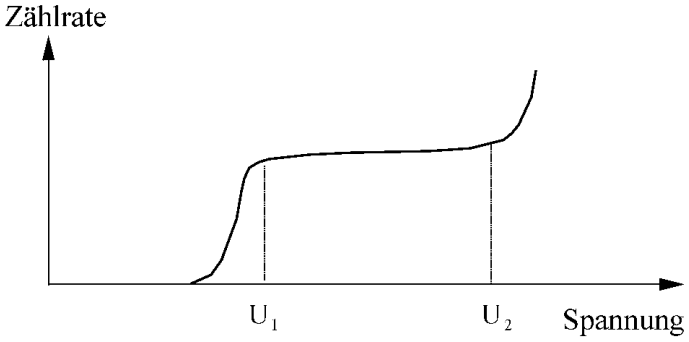

Figure 4.11: Gas counter characteristics.

be distinguished from one another, since the pulse heights are not proportional to the primary ionization.

The complete characteristic curve of a gas counter and its different working ranges are shown in Fig. 4.10. The pulse height increases with the voltage. In the proportional range the gas amplification factor can reach up to about 10^8 and in the triggering range up to 10^{11}. At such high currents, the corona discharge changes into a permanent glow discharge, which is characterized by a negative resistance. In the limited proportional region (and in the trigger region) the slope of the characteristic curve is shallower than in the true proportional region, although, according to Eqn. 4.33, the opposite is to be expected. This behavior occurs especially for strongly ionizing particles and is a consequence of the shielding of the field at the wire by the high positive space charges.

The working range of a gas counter can be selected on the basis of the characteristic curve. Unfortunately, it is usually not known, so that one must use another method to find the optimum operating voltage. It consists in measuring the counting rate as a function of the voltage, where of course the rate of the ionizing particles entering the counting tube must remain constant over time. The curve obtained in this way is called gas counter characteristics and behaves as shown in Fig. 4.11. It can be understood, if one considers that the electronic counting circuit has a threshold for pulse heights, below which no pulse is registered. The pulse height at the trigger threshold corresponds to a minimum operating voltage U_1, the threshold voltage, at which the counting process starts. In the ideal case, where all pulses have exactly the same height, the slope of the counter characteristics should be infinitely steep. In reality, the magnitude of the primary ionization and thus the pulse heights varies statistically. Therefore, the rise of the count rates around the threshold voltage flattens out, especially for low ionization rates. Above the threshold voltage, one expects a constant count rate up to a voltage U_2, at which the corona discharge begins. A slight increase is observed, which can be explained by after pulses caused by single electrons released at the cathode, whose number increases with the voltage.

The space charge of the ions that accumulates around the counting wire during the formation of a pulse, prevents two pulses to be detected in close succession. It reduces the effective voltage to values that are below the threshold voltage of the gas counter. The voltage returns to the original value after the migration of the ions. As long as the threshold voltage is not reached, newly arriving particles do not trigger any more avalanches. The gas counter has a dead time.

In Fig. 4.12 the time behavior of the voltage (a) and the corresponding pulses (b) are sketched. The voltage decreases from U_0 to a minimum that occurs after the electron collection time. If, as assumed here, this is measured with a small time constant, this is approximately the same time in which the pulse reaches its maximum. During the increase of the voltage the threshold voltage U_1 is reached again after a time t_1. This time t_1 is the dead time of the gas counter. If another particle arrives immediately after the dead time, the pulse it generates does not reach

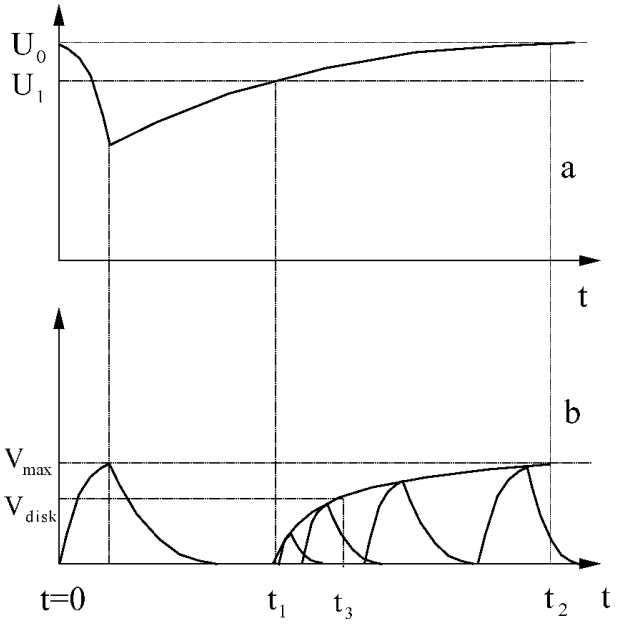

Figure 4.12: Dead time of a gas counter.

the full height V_{max}. A full pulse can only be generated again by particles that arrive after a time t_2, when again the full voltage takes effect. The time between t_1 and t_2 is called recovery time, after which the gas counter is back in its nominal operating state. The graph shows three pulses registered at different times and the envelope of the pulse heights.

With an oscilloscope the pulses in Fig. 4.12,b can be observed directly, without the envelope of course. The trigger threshold is set to the maximum pulse height, the sweep time approximately to the ion collection time (a few milliseconds). The count rate must be large enough so that there is a certain probability that a second particle arrives during this time. After the triggering pulse of the initial particle at full pulse height, one observes no other particles for a certain range of time, followed at later times by other pulses at statistically fluctuating times. The earlier the particles arrive, the smaller the pulse hight; after a certain time they have their full height again. If the observed range is long enough, the dead and recovery times can be estimated.

The sketch also shows that the dead time of a gas counter depends on the threshold of the detection electronics. If it is not zero, but at V_{disk}, then the dead time is prolonged to the value t_3, and the recovery time is shortened accordingly.

For the determination of the time of arrival of the radiation, the same applies as for the proportional counter. Here, too, the fluctuations of the drift times of the electrons prevent an exact time measurement. The time resolution, which is the minimum time interval between two pulses at which they can be detected separately, is even worse because of the dead time. It is of the order of milliseconds.

4.1.1.4 Overview of properties of gas counters

In table 4.1 the properties of the different gas counters are compiled. The numerical values are typical magnitudes and vary depending on the design of the gas counter or the type of detection electronics. The pulse heights in the different modes differ by several orders of magnitude because of the different gas amplification. They are typically in the range of millivolts for the ionization chamber, and even smaller for weaker ionization. Even if the pulses are highly amplified and optimally shaped to improve the signal-to-noise ratio, there is a lower limit to the number of ion pairs that can be detected. The sensitivity is around 300-500 pairs. On the other hand, in the

Table 4.1: Properties of different gas counters

	Pulse height [volt]	Sensitivity for ion pairs	Energy measure-ment	Time resolution [s]	count rate per sec. [Hz]
Ionization chamber	$< 10^{-3}$	300 -500	yes	$< 10^{-6}$	10^6
Proportional counter	≈ 1	1	yes	$< 10^{-6}$	10^6
Geiger counter	10 - 100	1	no	$\approx 10^{-3}$	10^3

proportional range, and even more so in the trigger range, a single ion pair is sufficient to induce a pulse.

As long as events are only counted, without discrimination or energy measurement, it is best to use Geiger counters, otherwise one has to go back to proportional counters. You cannot do without these when high counting rates have to be processed. In this case, the Geiger-Müller counter is inferior because of its dead time.

The accuracy with which one can determine the point in time at which a particle arrives is determined for all gas counters by the electron collection time. It is bad compared to other detectors. Gas counters are therefore only of limited use for coincidence experiments.

4.1.2 The semi-conductor detectors

A semi-conductor detector works similar to an ionization chamber. In both, the detection of ionizing particles and the measurement of the energy is based on the movement and collection of the charges released in an electric field. In the ionization chamber the electric field is generated by an external voltage applied to the capacitor, and the entire volume is sensitive to detection. The semi-conductor detectors that comes closest to this, is the simplest type, the intrinsically conductive crystal counter. It, too, has a homogeneous field over the entire volume. The most frequently used detectors are not intrinsically conductive, but doped. It is the type and strength of the doping that determines the field and the charge transport, which distinguish the detectors from each other. The materials used for semi-conductor detectors are almost exclusively germanium and silicon crystals, which can be produced inexpensively in the necessary size, homogeneity and purity.

4.1.3 The crystal detector

It is the simplest semi-conductor detector, but it is no longer in use. Nevertheless, it is discussed here because it has great similarity with the ionization chamber. It consists of an intrinsically conducting, homogeneous single crystal of high purity. On two opposite sides of the rectangular crystal, metal layers are vapor deposited as electrodes.

In the band model of solids, intrinsic conduction is caused by thermal excitation of electrons. They are emitted from the occupied valence band across the forbidden zone, which is for germanium 0.7 eV and for silicon 1.1 eV wide, into the conduction band. In the valence band, this results in the same number of positively charged holes or defect electrons. The charge carriers can move freely within the bands.

The occupation probability of the allowed energy values depends on the temperature and is described by the Fermi distribution $f(E)$

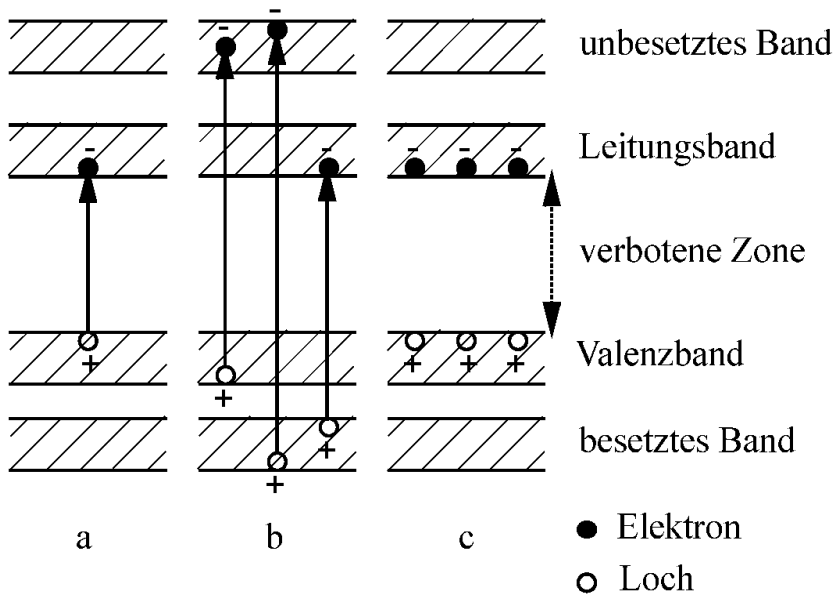

Figure 4.13: Excitation of a crystal in the band model.

$$f(E) = \frac{1}{1 + \exp(E - F)/kT} \tag{4.40}$$

F is the Fermi energy. At the absolute zero point the distribution breaks off steeply, only up to this so-called Fermi edge the states are occupied. In semi-conductors, it lies below the conduction band. Therefore, at the zero point it contains no electrons and the conductivity is zero. At finite temperatures the transition between the occupied and the unoccupied states is no longer abrupt, it becomes more and more smoothed out with increasing temperature. There are more and more electrons with higher energies, so that the conduction band is partially occupied and the crystal is slightly conductive.

When an external DC voltage is applied, the electrons in the conduction band and the holes in the valence band drift according to their mobility – $1500\,\mathrm{cm^2 s^{-1} V^{-1}}$ for the electrons, one third smaller for the holes – with constant velocity to the electrodes, and a current flows, the so-called dark current. In silicon at room temperature, it is of the order of μA. Germanium must be cooled to the temperature of liquid nitrogen, because of its smaller band gap, if such small values should be maintained. In the ideal crystal, the dark current disappears when the temperature goes towards absolute zero. In reality, there is still a residual conductivity even in this case, which is caused by the unavoidable impurities and defects. Therefore, there is always a part of dark current which is independent of the temperature.

The working principle of a semi-conductor crystal as a detector of ionizing particles is based on the generation of additional electron-hole pairs. In contrast to the thermal excitation, where electrons are lifted from the top edge of the valence band to the bottom edge of the conduction band (Fig. 4.13.a), the Coulomb excitation causes electrons from the entire width of the valence band and the occupied bands below to enter the conduction band and the unoccupied bands above(Fig. 4.13.b). Therefore, the average energy required to generate a pair is about three times larger than the width of the forbidden zone. One measures 2.8 eV for germanium and 3.55 eV for silicon. Immediately after primary ionization, the crystal is highly excited for a very short time (10^{-13} s). After this time, the electrons have collected at the bottom of the conduction band and the holes at the top of the valence band (Fig. 4.13.c). The energy they give off in the process is consumed to generate more electron-hole pairs (secondary ionization) or to excite phonons. In this state, the charge carriers live for quite a long time - the average lifetime is

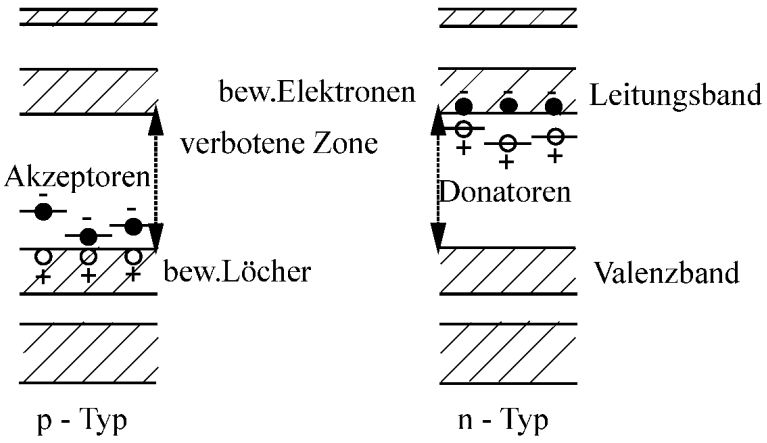

Figure 4.14: Band model of a doped semi-conductor.

microseconds - before they recombine or are trapped. This is sufficient for most to survive the journey to the electrodes. The collection time for the charges, which is inversely proportional to the external voltage, usually has a comparable value.

The concentration of charge carriers generated by ionization is much greater than in the case of thermal excitation. In an external field, therefore, a current flows which exceeds the dark current multiple times. It is proportional to the number of electron-hole pairs generated and therefore, because of Eqn. 4.17, proportional to the energy deposited by the ionizing particle in the sensitive volume. The crystal detector is therefore suitable for the determination of the energy of ionizing particles. For this purpose, the height of the pulses formed during the collection time of the charges is measured. It is essentially an ionization counter with a solid medium. As with the ionization chamber, the entire volume is sensitive and the field generated by an external voltage is homogeneous.

4.1.3.1 The p-n junction detector

Doped semi-conductors are used for this type of detector. The ionizing radiation is detected in the junction layers of the semi-conductors.

In the band model of such semi-conductors (Fig. 4.14), besides the allowed zones, there are additional *discrete* energy states. When they are doped with acceptors (p-type) just above the valence band, which accept and bind electrons from the valence band, they have negatively charged centers in the doped region and freely movable positive holes in the valence band. The same applies to doping with donors (n-type). Below the conduction band, centers are created that donate electrons to the conduction band, resulting in positively charged centers and free electrons in the conduction band. Since the energy distances of the acceptors and donors to the corresponding bands are much smaller than the forbidden zone, the doping increases the concentration of free charge carriers multiple times compared to thermal excitation. The conductivity of doped semi-conductors is therefore orders of magnitude higher than that of pure semi-conductor crystals. At high doping levels, it can reach that of metals.

Transitions between n- and p-doped layers can be used as detectors for ionizing particles. They are produced, for example, by allowing donor atoms to diffuse into a p-type semi-conductor at one end in such a high concentration that an n-conducting layer is formed there.

The properties of such an n-p layer are described in good approximation by the band model. For simplicity, it is assumed that in the p-layer the density of the conductive electrons and in the n-layer the density of the holes can be neglected. Furthermore, it is assumed that the transition from the p- to the n-layer is sharp, and that the concentrations of the acceptor- and donor layers

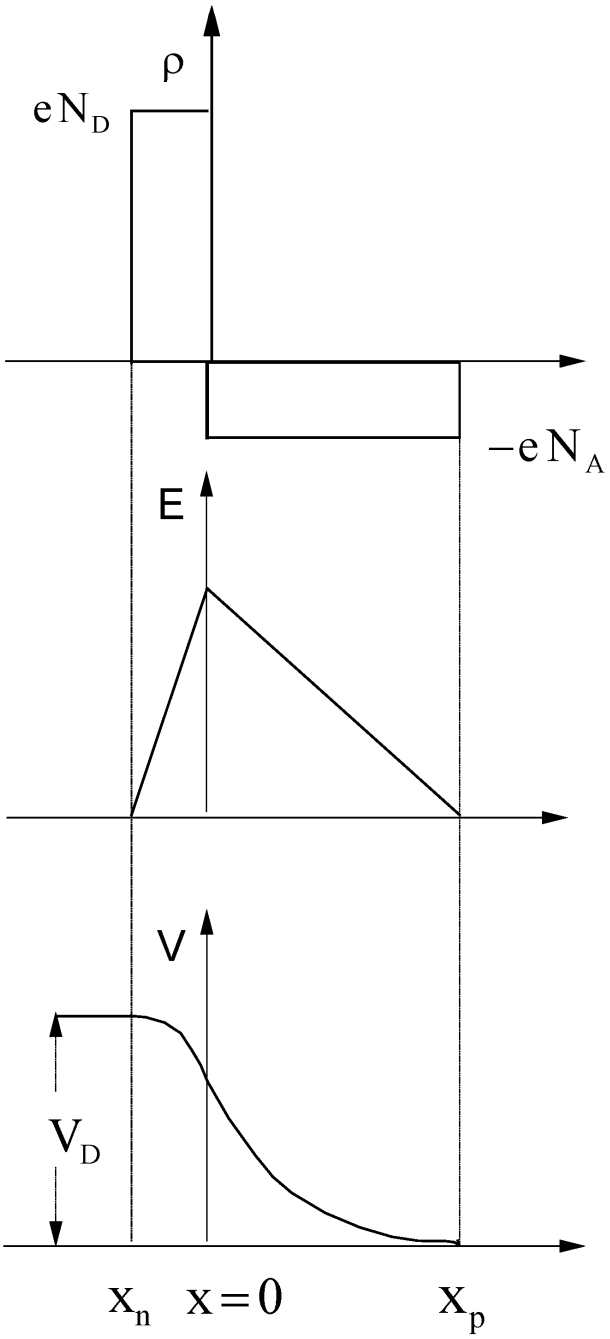

Figure 4.15: Course of the space charge. Field strength and voltage at an n-p junction.

are constant in their respective regions. In addition, the donor states should be as close to the conduction band and the acceptor states only so slightly above the valence band that in the n-region all donors are ionized in the n-region and all acceptors in the p-region are occupied by electrons.

At the transition point of the dopants, a junction is formed, which is characterized by a lower concentration of free charge carriers than in the regions of pure p- or n-conduction. The reason for this is that the mobile charges do not follow the sudden change in concentration at the junction. The electrons from the n-region diffuse over into the p-region, while in the opposite direction the holes diffuse into the n-region. In doing so, they enter a region where the concentration of charge carriers of the opposite sign is high. They recombine, the junction (also called depletion region) becomes depleted of free charges and acquires high electrical resistance, ideally that of an intrinsic (pure) conductor.

Due to diffusion, a space charge is formed on both sides of the boundary layer. It consists of the ionized positive donors in the n-region and the occupied negative acceptors in the p-region. A potential difference builds up, the diffusion voltage, whose level increases with the concentration of the free charge carriers. The space charges, in turn, generate an electric field, which causes a field current in the opposite direction of the diffusion current. In equilibrium, no current flows through the junction: the diffusion current is then equal to the field current.

With the above mentioned assumptions for the box model, the space charge ϱ, the field strength E, and the potential V in the transition zones have the shape drawn in Fig. 4.15. With the additional, only approximately true assumption that the junction is free of mobile charge carriers, the space charge has a box-shaped distribution, from which the name of the model is derived. It is zero at the transition point ($x = 0$) of the dopants, positive and constant up to a point x_n in the n-region, negative and constant up to to x_p in the p-region. The width of the transition or field zone is $d = |x_n| + |x_p|$. After integration over the space charge, the field strength depends linearly, the voltage quadratically on the location, and in equilibrium it is equal to the diffusion voltage $\mathrm{V_D}$, which is

$$V_D = \frac{kT}{e} \cdot \ln\left(\frac{N_D \cdot N_A}{n_i^2}\right) \tag{4.41}$$

where N_D and N_A are the donor and acceptor concentrations, respectively, n_i is a constant, k is the Boltzmann constant, e is the elementary charge, and T is the temperature. Here it can be seen that the diffusion voltage increases, albeit only logarithmically, with doping. It is typically 0.4 - 0.7 V for silicon. The drawn transition is asymmetric: the doping on the n-side is higher than on the p-side. Therefore, the thickness x_n of the positively charged layer is larger than the thickness x_p of the negatively charged one. Since the crystal as a whole is electrically neutral, there is the relation

$$x_n \cdot N_D = x_P \cdot N_A \tag{4.42}$$

The depth of the field zone also depends on the doping

$$d = \sqrt{\frac{2\epsilon\epsilon_0 \cdot V_D}{e} \cdot \left(\frac{1}{N_D} + \frac{1}{N_A}\right)} \tag{4.43}$$

For an asymmetric p-n junction in originally n-type silicon, which has, for instance, a donor concentration of $5.2 \cdot 10^{11}\,\mathrm{cm}^{-3}$ and a diffusion voltage of 0.5 V, the junction is approximately 40 μm thick. In the calculation, the thickness of the p-layer has been neglected. Thus, it is a strongly asymmetric junction ($N_A \gg N_D$).

The thickness of the junction (depletion zone) can be considerably increased if an external voltage is applied to the junction so that the positive pole is connected to the n-type junction

(reverse-biasing). Then not only the diffusion voltage but also the much larger external voltage drops off across the junction. It is built up by an increase of the space charge. Since all acceptors are occupied and all donors are ionized, this can only happen by an expansion of the junction. The width is still given by Eqn. 4.43, only now instead of the diffusion voltage the total voltage or in good approximation the externally applied one is used. For 300 V and the above doping, the junction is then 0.9 mm wide.

If the p-n junction is operated in conducting direction (forward bias), the space charge dissipates by reducing the thickness of the junction. At sufficiently high voltages, it disappears completely and the junction becomes conductive.

A reverse-biased p-n junction is suitable for detecting and determining the energy of ionizing particles. In principle, it works like a crystal counter. Normally, only a very small dark current flows across the junction, since it contains almost no free charge carriers. A charged particle lifts, as shown in Fig. 4.13, electrons into the conduction band, which are detected together with the holes as a short current pulse. The difference to the crystal counter lies in the smaller thickness of the sensitive layer and the higher resistivity.

On the one hand this is an advantage, since due to the shorter drift range the charge collection times are much shorter and due to the smaller resistance a higher bias voltage can be applied. Shorter drift times lead to a better energy resolution (see chapter 4.1.3.3). On the other hand the small volume of the detector is a disadvantage. For instance, in the mentioned thickness of the p-n junction of 0.9 mm, protons are only stopped up to an energy of 10 MeV. Protons with higher energies pass the depletion zone (impinging perpendicularly). They deposit only a fraction of their energy, thus evading the determination of their total energy.

4.1.3.2 The lithium drift detector

An enlargement of the junction by increasing the reverse voltage is limited due to the exponentially increasing reverse current. Therefore, other methods must be used to produce detectors with a large sensitive volumes. The goal is to create a thick, intrinsically conductive layer with the properties of a crystal counter without the expense that purity and homogeneity require. The solution is to grow an intrinsically conducting zone in which the acceptor (donor) centers of a weakly doped material are compensated by diffused donor (acceptor) centers. It will be discussed in more detail for the Li-driven detector.

The starting material is weakly p-doped silicon or germanium, into which lithium is diffused at one end at temperatures between 300 °C and 600 °C by the usual methods. The lithium has a donor character in Si and Ge. This results in a n-conducting zone at the surface, since the acceptor concentration is overcompensated. The Li concentration decreases sharply with increasing distance from the surface, and an n-p junction is formed. The concentration of Li in the n-layer is thereby higher than the concentration of the acceptors in the p-layer, so that the n-conducting zone is thin compared to the junction layer and the junction is strongly asymmetric. One has a junction detector with a diffused n-p junction.

In Si and Ge, the Li atoms are not firmly incorporated into the lattice, they are located on interstitial sites and therefore have a high mobility. This is exploited to create an intrinsically conductive zone. An external voltage is applied to the n-p junction in the reverse direction. The field across the junction forces the Li-ions to drift into the p-region. In this way, an intrinsically conductive zone is formed between the n- and p-regions, whose thickness d depends only on the reverse voltage U, the drift time t and the mobility of the Li ions b_i.

$$d = \sqrt{2\, b_i \cdot U \cdot t} \tag{4.44}$$

thickness d can be as large as 1 cm for Ge-Li detectors. In the drift zone, the concentration of Li donors is just the same as that of acceptors, because space charge cannot form due to the high mobility of Li ions.

After completion of the drift process, which occurs at much lower temperatures (100 - 200 °C) than diffusion, the crystal is cooled to room temperature. In this process, the Li-ions lose their large mobility and the drift zone remains stable. It has the properties of a crystal counter: the applied voltage drops linearly, the resistivity and consequently the dark current are very small.

With the Li-driven detector, much higher particle energies can be measured than with the junction counter. In a 1 cm Ge-Li detector, for example, protons of 60 MeV are stopped. However, the time resolution is worse because of the long drift distance. It is on the order of microseconds.

4.1.3.3 The energy and time resolution

The semiconductor counters have the best energy resolution of all detectors. Therefore, the conditions which enable a good resolution shall be discussed here. They apply directly or accordingly modified also to other detectors, in particular to the ionization chambers and the proportional counters, whose mode of operation is also based on the collection of electric charges.

In order for the signal emitted by the detector to be proportional to the energy of the particle, some conditions must be met.

First, the entire kinetic energy of the particle must be deposited in the sensitive volume of the detector. In practice, this means that the insensitive region – the window – of the detector must be sufficiently thin. Then, the unavoidable losses are negligible compared to the energy. This is the case for the junction counter with strongly asymmetric transition and in particular for a special version of it, the surface junction counter.

Second, the sensitive layer must be thick enough to stop the particle to be detected in it. Therefore, it cannot measure arbitrarily high energies, but there is a maximum measurable energy for each type of detector. For protons, for example, it is 10 MeV in a junction counter and 85 MeV in a Li-driven Ge detector.

Third, the number of charge carriers must remain proportional to the deposited energy even during collection. This is always guaranteed if complete collection can be achieved. In semiconductors, the charge carriers have a finite average lifetime until they recombine and are lost to detection. It depends strongly on the purity of the material. In crystals of highest purity, it can take values up to 10^{-4} s. Since collection times are two to four orders of magnitude smaller, complete collection appears to be no problem. In reality, this is not true. In the case of strong ionization, the times deviate from the given values. So-called plasma tubes with high charge density are formed, in which the electric field collapses. The lifetimes are then shorter and the collection times longer. The inhomogeneous spatial distribution of the recombination centers also contributes to a scattering of the lifetimes and deterioration of the energy resolution. In short, good resolution is achieved with homogeneous and pure semiconductors and high operating voltages.

A certain scattering of the collection times is unavoidable due to the different paths that the charges travel in the detector. Nevertheless, the energy proportionality can be maintained to a certain extent by a suitable circuit. During the rise time, a part of the charge already flows off via the working resistor. If the rise time is the same for all pulses, then this is always the same fraction of the total charge and the pulse height is proportional to the energy. With a large time constant in the electronic counting circuit of the detector the fall time of the pulse can be made large compared to the rise time. Then the loss of charge is so low that different rise times do not have any effect

In principle, the resolving power is finite even for ideal detectors and best possible circuitry, because both ionization and transport of charge are statistical processes. If $\langle I \rangle$ is the average

ionization energy, then the number n of ion pairs produced during the deceleration of particles with a certain energy E is

$$n = \frac{E}{\langle I \rangle} \tag{4.45}$$

It fluctuates around a mean value n. The magnitude of the fluctuation, assuming Poisson statistics, is equal to $\sqrt{n}$. It entails an uncertainty δE in the energy measurement. The energy resolution is then

$$\frac{\Delta E}{E} = \frac{\sqrt{n}}{n} = \frac{1}{\sqrt{n}} \propto \frac{1}{\sqrt{E}} \tag{4.46}$$

Two things can be deduced from this relationship. The resolution is the better (i.e. this value is the smaller), the more charge carrier pairs are generated at a fixed energy E. This explains the outstanding resolution of semiconductor detectors, where only about 3 eV have to be applied for one ion pair. In the case of the gas counters and the scintillation counters, this value lies between 25-35 eV, correspondingly worse is their energy resolution. For the same reason, the resolution increases with increasing energy.

Statistical processes also occur during the transport of charge carriers, which are summarized under the term electronic noise. The most important component limiting the resolving power is the thermal noise index. It is present even when no current is flowing and is caused by spatial fluctuations of the charge carrier density, which in turn is a consequence of the thermal velocity distribution of the electrons and holes.

Time resolution is the accuracy with which the time of arrival of a particle in the detector can be determined. The statistical processes during the generation of the pulses cause temporal fluctuations of the rise times and thus uncertainties in the time determination. However, the shorter the rise times or, as one says, the faster the pulses, the smaller they are.

For semiconductor detectors, the rise times are determined by the transit times of the charges, similar to gas counters. The collection time t is calculated from the integral

$$t = \int_{x_1}^{x^2} \frac{\mathrm{d}x}{\mu \cdot E} \tag{4.47}$$

E is the electric field strength and μ is the mobility of electrons. For junction counters with a layer thickness which is large compared to the range of the particles, this results in

$$t = \frac{d}{\mu \cdot E_{\max}} \cdot \frac{\ln 10}{2} \tag{4.48}$$

These are values on the order of nanoseconds. For a Li drift counter with a drift distance d at which the voltage U is applied, one has

$$t = \frac{d^2}{\mu \cdot U} \tag{4.49}$$

Here the collection times are much larger, they are in the range of microseconds. Therefore, they are not suitable for measuring small times or fast coincidences.

Good time resolution requires not only short collection times, but also correspondingly small time constants in the electronic counting circuit. Otherwise, the rise time would be extended by the integration. But this is at the expense of the energy resolution, which requires just this integration with a large time constants. Good time resolution and good energy resolution are complementary. One can achieve both at the same time only if one processes the pulses in separate counting circuits.

4.1.3.4 The pulse shape of a semiconductor detector

If the charges are collected undisturbed, i.e., no plasma effects and no recombination occur, the pulse shape is calculated in the same way as for the ionization chamber. Eqn. 4.20 to Eqn. 4.27 as well as Fig. 4.2 and Fig. 4.3 apply. The positive holes in the semiconductor detector correspond to the ions in the ionization chamber. The only difference is that the holes are only 2-3 times slower than the electrons, and not by three orders of magnitude like the ions.

4.2 Detectors for the detection of ionization by the emission of light

In solids, the energy transferred from charged particles by ionization or excitation is partially re-emitted by the emission of photons. Ideally, the intensity of the emitted light is proportional to the particle energy. To detect the photons, secondary electron multipliers (SEM) are used (here the word *photomultiplier* is more common), whose sensitivity can be increased to such an extent that a few photons are sufficient to produce easily measurable current pulses. In the end, as in the case of gas counters, the information about the particles to be detected is available in the form of electrical pulses.

4.2.1 The scintillation detector

The scintillation detector, along with the ionization chamber, is the oldest detector used in nuclear physics. Its mode of operation is based on the principle that certain inorganic substances such as ZnS and NaJ, and organic compounds such as plastics and anthracene are excited by ionizing radiation to emit light. Thus, in studying the scattering of α particles by nuclei, Rutherford and his co-workers observed and counted the flashes of light produced by the α particles when they struck a ZnS screen. The scintillation detector has reached its full potential only since electronic light detectors have been used instead of observation by eye. Photomultipliers are often used, although semiconductor photodiodes (Avalange photo diodes, Si photomultipliers) are now also increasingly being used. Thus, a scintillation detector is the combination of a scintillator, which converts the energy of ionizing radiation into visible light, and a photodetector, transforming it into an electrical pulse with an amplitude or charge that is proportional to the energy deposited in the scintillator. The signal is usually further processed electronically and digitized with an ADC (analog-to-digital converter).

The classical photomultiplier (PMT) consists of several coated metal electrodes placed in a closed, evacuated glass tube (see Fig. 4.16). Light enters one end of the PMT and strikes the photocathode (PK). The photocathode is usually a bi-alkali layer, vapor deposited on the entrance window that is connected to the power supply of the PMT. The scintillator is placed directly in front of the photocathode of the PMT. Only about every third to fourth photon produces a photoelectron by the photoelectric effect, which exits the cathode and is accelerated by electric fields from focusing electrodes onto the first of a series of bent metal electrodes, called dynodes (Dy_i). The dynode sheets are coated with a material from which an impinging electron with sufficient energy can produce multiple secondary electrons. The dynode chain is called a secondary electron multiplier and is the actual amplifier of the photomultiplier. Amplification factors from 10 to 10^8 can be achieved. The amplification factor depends on the number, geometry and coating of the dynodes and especially on the accelerating voltage between the dynodes. At the end of the dynode chain the anode (An) is located, which collects the amplified photoelectron pulse and transmits the signal to the output pin. The photocathode, dynodes and anode are connected through electrical feedthrough pins to the outside world. The different potentials are usually generated by a passive voltage divider consisting of high-resistance resistors, which

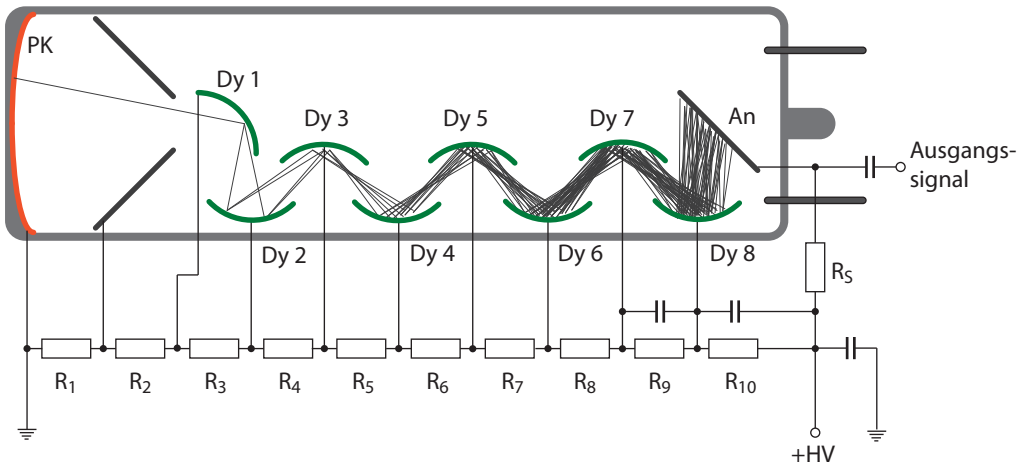

Figure 4.16: Schematic sketch of a photomultiplier. The evacuated glass housing contains the photocathode (PK), the dynodes (Dy n) of the secondary electron multiplier and the anode (An). The schematically shown voltage divider is supplied by a positive high voltage source. The anode signal, which is fed to the measurement electronics, is decoupled from the high voltage via a capacitor.

is connected to a high-voltage (HV) power supply which provides a stabilized DC voltage. The required operating voltage depends on the type of PMT and the required amplification factor. For most PMTs it is between 600 V and 2500 V. A detailed description of photomultipliers can be found e.g. in [20].

A scintillator is characterized by the following quantities:

1. **The absolute scintillation sensitivity** S It indicates the fraction of the energy E deposited in the scintillator, which is released as energy of the fluorescent light. If an average energy E_F is attributed to the light quanta, then it is given by

$$S = N(E) \cdot \frac{E_\mathrm{F}}{E} \tag{4.50}$$

   where $N(E)$ is the number of generated quanta that depends on the particle energy. S should be large because the more photons are generated, the better the energy resolution. The remaining energy deposited in the scintillator is emitted via so-called non-radiative transitions in the form of phonons.

2. **The location of the emission spectrum** . The energy resolution is also determined by the number of electrons released by the fluorescent light on the photocathode. The more electrons emitted, the less their number fluctuates, and the better the energy resolution. The number of electrons is greatest when the emission spectrum is in the range of the maximum sensitivity of the photocathode of the PMT.

3. **light yield or specific light efficiency** The light yield L is defined as the total energy emitted by the scintillator in the form of light

$$L = N(E) \cdot E_\mathrm{F} = S \cdot E \tag{4.51}$$

   The specific light efficiency is the energy emitted along the distance dx in the scintillator.

$$\frac{\mathrm{d}L}{\mathrm{d}E} = S \cdot \frac{\mathrm{d}E}{\mathrm{d}x} \tag{4.52}$$

At first sight, it seems that the light yield is equivalent to the quantity S, because from the above equations we can deduce

$$\frac{\mathrm{d}L}{\mathrm{d}E} = \frac{L}{E} = S = \text{konst.} \tag{4.53}$$

In special cases, namely when the primary ionization is small, as e.g. for electrons, this equation is correct. In this case the size of the primary ionization has no influence on the emission. However, if the primary ionization and thus S is large, emission is suppressed in favor of non-radiative transitions, a process called quenching. For the specific light yield it is described by the expression

$$\frac{\mathrm{d}L}{\mathrm{d}x} = \frac{S \cdot \frac{\mathrm{d}E}{\mathrm{d}x}}{1 + q \cdot B \cdot \frac{\mathrm{d}E}{\mathrm{d}x}} \tag{4.54}$$

S is again the scintillation sensitivity without the quenching caused by ionization, B is a constant, and q is the quenching parameter that quantifies the fraction of non-radiative transitions over the total number of transitions. Thus, the light yield does not always depend linearly on the particle energy; the parameter S depends on the energy and type of the particle.

4. **The decay time of the scintillation** The excited emission centers have a average lifetime or decay time τ. They decay statistically and follow the well known law from radioactivity. The intensity of the fluorescence light at time t after the excitation is

$$I(t) = I_0 \cdot e^{-\frac{t}{\tau}} \tag{4.55}$$

The average lifetime or decay time τ is an important quantity characterizing the scintillator, determining the time resolution. It is around 10^{-9} s for some organic scintillators, and can be as low as 10^{-7} s for the inorganic ones. This component, called the fast one, makes up the main part of the fluorescent light. In addition, there is usually a weaker component, which accounts for about 10% of the intensity that also obeys an exponential decay law, but has a much longer decay constant (up to 10^{-4} s). It arises from the decay of long-lived metastable states. If these metastable states are only slightly below the rapidly decaying ones, a third component can also be observed in the emitted light, which also decays very slowly, but without following an exponential decay law. It is known as the afterglow of a scintillator and is produced by thermal excitation of the metastable states into the higher states with the short decay time. The long-lived and delayed components of luminescence are not wanted in appreciable intensity, because they cause slowly increasing pulses. Further below, the different types of luminescence will be discussed again in more detail.

The quantities listed here, which are characteristic of the scintillators, are determined experimentally. Theoretical predictions can only be approximate because of the large number of processes involved. The physical processes involved in scintillation are discussed below. They are different in organic and inorganic materials.

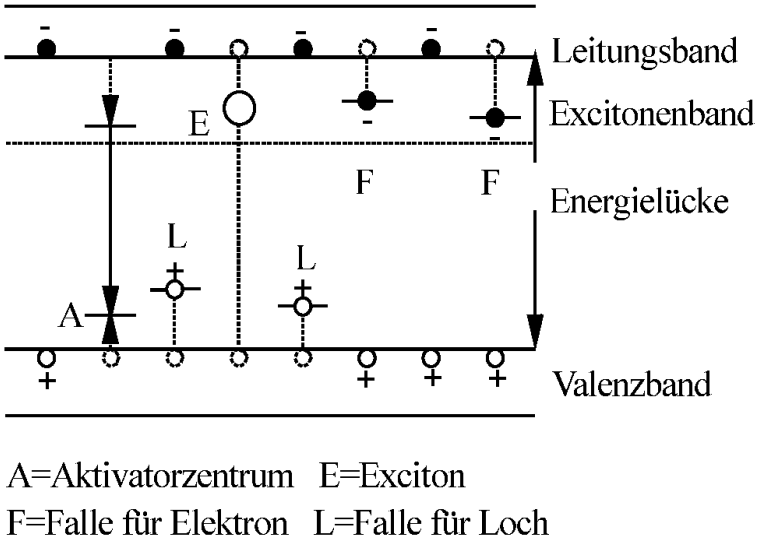

Figure 4.17: Band model of an inorganic scintillator.

4.2.1.1 The inorganic scintillator

The inorganic scintillator is a crystal. Its working principle is described by the band model. The lower bands of a crystal are completely occupied by electrons, the valence band is partially filled. Above the valence band, separated by the energy gap E_g, lies the conduction band. It is unoccupied in the ground state. The pure crystal is therefore electrically non-conductive.

The crystal can be excited by ionizing radiation or by absorption of light. Then, transitions take place from the occupied bands, especially from the valence band to the conduction band. The electrons in the conduction band are free to move, as are the remaining positively charged holes in the valence band: the crystal is electrically conductive.

The free electrons recombine with the holes. The excitation energy is emitted in the process. In the ideal crystal, only phonons can be excited, but no photons can be emitted. The optical transitions are forbidden by the Pauli principle . The electrons in the conduction band lose their kinetic energy very quickly (approx. 10^{-13} s) after the excitation through elastic collisions and are then at the lower band edge, which corresponds to the momentum $k = 0$. However, states with $k = 0$ are occupied in the valence band, a transition is not possible. Ideal crystals are therefore no scintillators.

In reality, however, pure crystals also show luminescence when they are excited. Lattice errors are always present, be it that lattice sites are not occupied, or that there are surpluses on interstitial sites. The latter are intentionally created in crystals that are to be used as detectors by doping them with foreign atoms. An example of this is the doping of a NaI crystal with thallium ions in the most widely used inorganic scintillator, the NaI(Tl). In this way the so-called activator centers are created, which decisively determine the scintillation through the following processes.

1. **The capture of excitons** Excitons are electrically neutral quasi-particles that are created by correlating a free electron with a hole. They can diffuse through the crystal, their energy is just below the conduction band, in the so-called exciton band. The activator centers, the ground states of which are only slightly above the valence band, can capture excitons, whereby they pass into excited states below the edge of the conduction band. It is these excited centers that are essential to scintillation. When returning to the ground state, photons are emitted with a high degree of probability, the fast component of fluorescence . Only a small part of the excitation energy is converted into phonons without radiation.

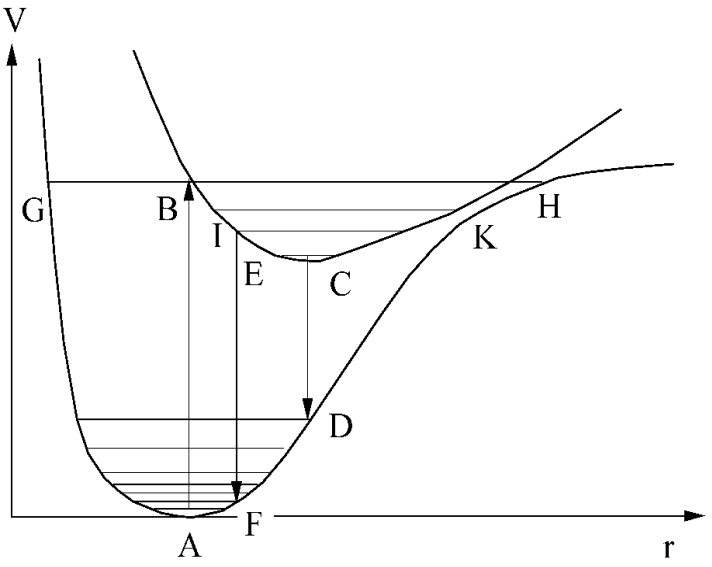

Figure 4.18: Term diagram (Grotrian diagram) of an activator center.

2. **The capture of free electron-hole pairs** Without having previously formed an exciton, diffusing electrons and holes can recombine directly at a center and excite it.

3. **The capture of free charge carriers** The activator centers can trap electrons or holes. They then act as a trap for the load carriers. If they are occupied, their energies are close to the band edges. They remain occupied until they recombine with diffusing charges of the opposite sign or pass into the neighboring bands by absorbing thermal energy from the environment. This thermal excitation of the charges in the traps is the cause of the delayed fluorescence.

An activator center and the processes occurring when an exciton is captured can be described in a model that is closely analogous to molecular physics. In the crystal, too, the centers have discrete states of excitation, as they do not influence each other due to the low concentration. They correspond to the different electronic states of a molecule. A center is bound in the lattice and can oscillate around its equilibrium position. As with the molecule, the electronic states that are far apart are therefore split up into vibrational states that are close to one another. In Fig. 4.18 the potential curves for the ground state and an excited state of a center are shown as a function of the deflection of the oscillation. The lowest oscillation terms are also drawn in for each curve, the lowest of which corresponds to the state of rest. The quantum mechanical probability of stay has a maximum in the middle of the zero point amplitude, so that the rest positions are determined by the minima of the potential curves. The population density of the oscillation states is a function of the temperature and is described by the Boltzmann distribution. Only a few oscillation states are occupied at room temperature.

If an activator center is excited by capturing an exciton, then it goes along the vertical line AB into the higher electron state. The transition is vertical because, according to the Franck-Condon principle, it is fast compared to the vibrational movement of the center, which therefore remains in the same place during the excitation. The excited center is thus also in an excited vibrational state. From here there are three possible ways back to the basic state: firstly, a photon can be emitted spontaneously, and secondly, it can first pass into lower-lying oscillation states without radiation before it emits a photon. The third possibility is the direct, non-radiative transition to the ground state. In all non-radiative transitions, lattice vibrations (phonons) of the crystal are excited. The ratio of the probabilities for the transitions of the first two paths determines the

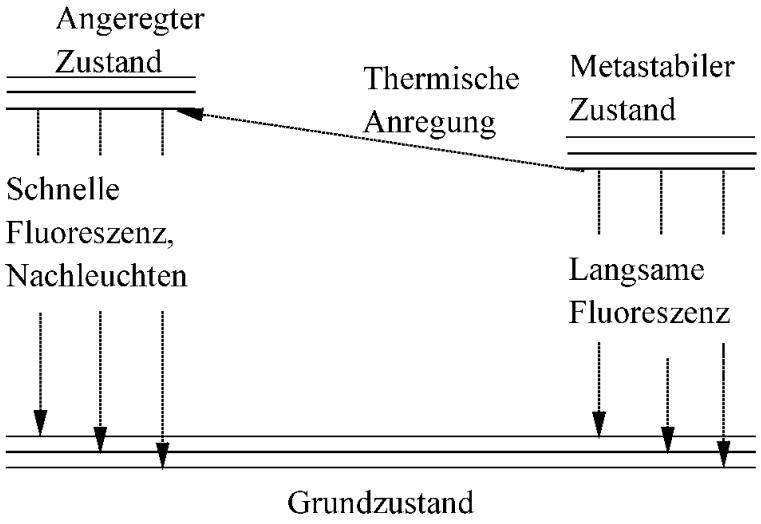

Figure 4.19: The different forms of luminescence

shape of the optical emission spectrum. Most of the time, the optical transitions are slower, so that the spectrum lies at the energy given by the path CD and is strongly shifted in relation to the excitation energy. If, on the other hand, they are fast, they can also take place from excited oscillation states, e.g. along EF, the spectrum is then less shifted and also broadened. Most of the transitions end in oscillation states of the ground state, the energy of which is ultimately also transferred to the grid.

The mean lifetime of the excited states of an activator center is typically 10^{-7} s. In a crystal in which many similar centers are excited at the same time, the intensity of the emitted light decreases over time according to an exponential law of decay with a fixed time constant, the decay time of the scintillation. This process is normal fluorescence.

The third way, the direct non-radiative transition , is particularly likely in areas where the potential curves converge or even intersect. In Fig. 4.18, for example, a transition from the oscillation level IK of the excited electron state to the oscillation level GH of the ground state is possible. Then all of the excitation energy is released to the crystal. This is process is called quenching. It always occurs when the IK level is occupied. If this happens through thermal stimulation of the lower oscillation states, the frequency of quenching increases with increasing temperature. Depending on the position of the potential curves of the activator centers, either the spontaneous emission of light or the non-radiative transitions can dominate. Then, one speaks of luminescence centers or of quenching centers . Each activator center has several excited states. Among them there may be those for whom the optical transition to the ground state is severely hindered by selection rules, such as the forbidden singlet triplet inter-combination. If, in addition, the probability of quenching is also small, then such states can live for a relatively long time. They are therefore called metastable. In Fig. 4.19 such a metastable state is shown schematically in the term diagram of an activator center, together with a normal excited state and the ground state. With exciton or charge capture, both excited states are occupied. After a short time, both are in the lowest oscillation state, if the relaxation of the excited oscillation states is fast. When the excited normal state decays, the already mentioned fast fluorescent light is emitted. Its spectrum is not sharp, but continuous because of the closely spaced oscillation terms of the ground state. There is also another component that arises from the optical decay of the metastable state. Due to the long lifetime of the state, it has a much longer decay time and is shifted towards lower energies. Like the fast one, the slow component also obeys an exponential law of decay.

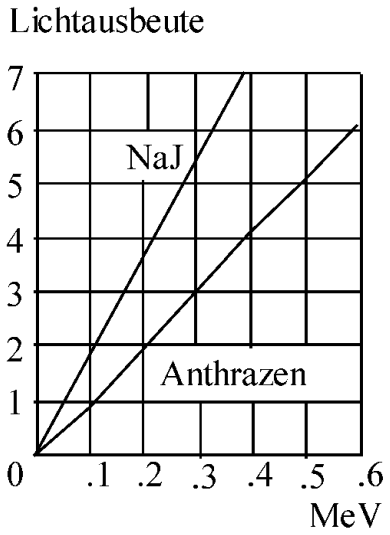

Figure 4.20: Light yield for an electron as a function of the energy.

The third component arises when the metastable state is only slightly below the normal excited state. Then, through thermal excitation, transitions to the upper state can take place, which then decays with the decay time and the spectrum of rapid fluorescence. The time behavior is thus determined by the rate of thermal transitions, it is no longer exponential. This is the afterglow which can last a few seconds.

4.2.1.2 The organic scintillator

There are many organic substances that are stimulated to luminescence by ionizing radiation. They can be divided into three groups.

1. **The molecular crystals** , which consist of nothing but the same molecules without additives. These include, for example, anthracene and stilbene.

2. **The solid solutions.** These are solid substances, mostly plastic or other polymers, which do not show any luminescence themselves and to which other molecules as luminescence centers are mixed in small amounts.

3. **Liquid scintillators.** They are like solid solutions, only the basic component of them is an organic liquid. For example, paraffins or toluene are used. A large number of molecules are now known, which show luminescence in solution when excited. The best known include PPO (2,5-diphenyloxazole) and POPOP (1,4-to 2 (phenyloxazolyl) benzene).

The organic scintillators are not described by the band model. The interaction of the molecules in the molecular crystals with each other and also that of the centers with molecules of the solutions are so weak that their energy states are not or only slightly influenced by the neighbors. They posses discrete electron states on which oscillation states are superimposed. The term scheme is analogous to that of the activator centers in Fig. 4.18, as well as and the physical processes that take place during scintillation. Only the excitation of the centers is somewhat different. It takes place either through photons or without radiation through excitons from the ionization channel.

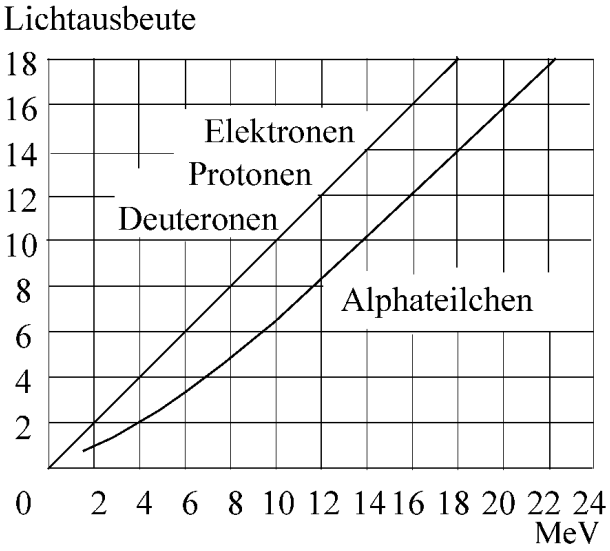

Figure 4.21: Light yield from a NaI(Tl) for different particles as a function of the energy.

4.2.1.3 Comparison of inorganic and organic scintillators

Inorganic and organic scintillators differ in their properties and are therefore not equally suited for certain applications. In the following, the two types are compared with each other, with NaI(Tl) representing the inorganic scintillators and anthracene for the organic ones.

The light yield of the inorganic scintillators is considerably higher than that of the organic ones. This can be seen from Fig. 4.20, in which the light yield is plotted in arbitrary units for electrons up to 600 keV. In NaI(Tl) it runs completely linearly with the energy, while in anthracene it is slightly non-linear at low energies and only approximately half as large over the entire range. It also depends on the type of particle, as shown in Fig. 4.21 for different particles in NaI(Tl): it is the same for electrons, protons and deuterons, for α particles it has smaller values. Here, too, the dependence on the energy is linear for the lighter particles. For the heavier and doubly charged α particles, a deviation from the linearity can be seen. This deviation is even more pronounced in anthracene; here it can also be observed for the other heavy particles. From the Fig. 4.22 it can be seen that there is a straight line only for the electrons. The very strong decrease in the light yield with increasing mass and charge of the particles is also remarkable. Both phenomena can be explained with the Bethe-Bloch formula (Eqn. 3.4 and Eqn. 3.8). According to it, the ionization density increases linearly with the mass and quadratically with the charge of the particles and goes through a maximum at low energies for all particles. At high ionization densities, some of the charge carriers recombine before the energy is transferred to the luminescence centers, i.e. the non-radiative processes increase at the expense of the quantum yield, the more the higher the ionization density. Therefore, the light yield at a certain energy decreases, the greater the mass and the charge. It only goes linearly with the energy if there is no recombination. Thus, the deviation from linearity is particularly evident at low energies.

In order to measure the energy of particles, NaI(Tl) is better suited than anthracene for two reasons. On the one hand, a single calibration measurement with particles of known energy is sufficient to determine the energies of electrons, protons and deuterons in the entire specified range, cause of its linearity. In the case of anthracene, a separate calibration curve must be determined for each class of particles. On the other hand, the overall light yield is greater. Therefore, more photons reach the photocathode of the photomultiplier and also release more electrons there.

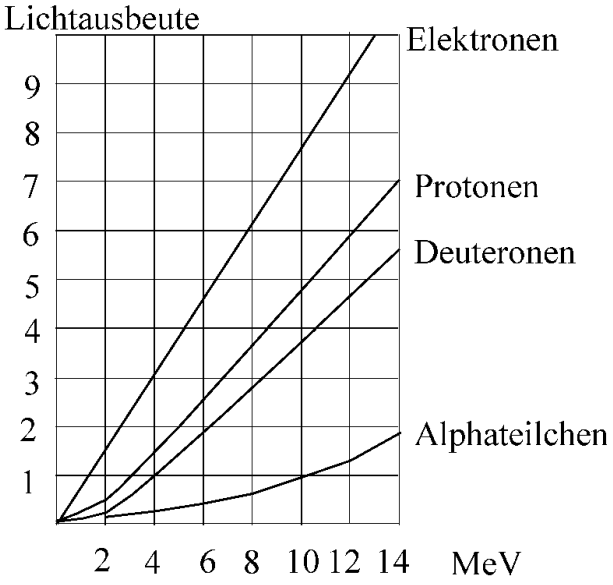

Figure 4.22: Light yield of Anthracene for different particles as function of energy.

Table 4.2: Comparison of the properties of organic and inorganic scintillators. ε is the sensitivity.

	Pulse decay time	Energy resolution	Time resolution	ε for charged particles	ε for γ	ε for n
NaI(Tl)	$2,5 \cdot 10^{-7}$ s	good	bad	near 1	10-30% by 1 MeV and 5 mm	none
plastic	$8 \cdot 10^{-9}$ s	bad	good	near 1	2-5% by 1 MeV and 5 mm	proton-recoil

The statistical fluctuations in the electron current are therefore smaller, improving the energy resolution of the detector.

In contrast, the organic scintillators are better suited for fast coincidence measurements (this means those with resolution times of nanoseconds) and for precise time measurements, due to the short decay times of the fluorescence. They are $3 \cdot 10^{-8}$ s in anthracene, $8 \cdot 10^{-9}$ s in plastic, but $2.5 \cdot 10^{-7}$ s in NaI(Tl). In organic substances, light emission is up to two orders of magnitude faster. The rise times of the electron pulses in the PMT are correspondingly short, which is the prerequisite for fast time measurements. The sensitivity, i.e. the ratio of the number of particles detected to the number of arriving particles, is the same for charged particles in both scintillators. It is practically one. For the detection of γ quanta, however, the inorganic crystals are preferable because they have a larger mean atomic number ($\bar{Z} = 32$ for NaI(Tl) and therefore the photo effect is more common. In plastic scintillators ($\bar{Z} = 2.7$) the photoelectric effect can no longer be observed. On the other hand, the organic compounds are well suited for the detection of neutrons, since they contain protons to which the neutrons transfer considerable energy during scattering (recoil counter see chapter 3.2.1.1) The inorganic scintillators are insensitive to neutrons.

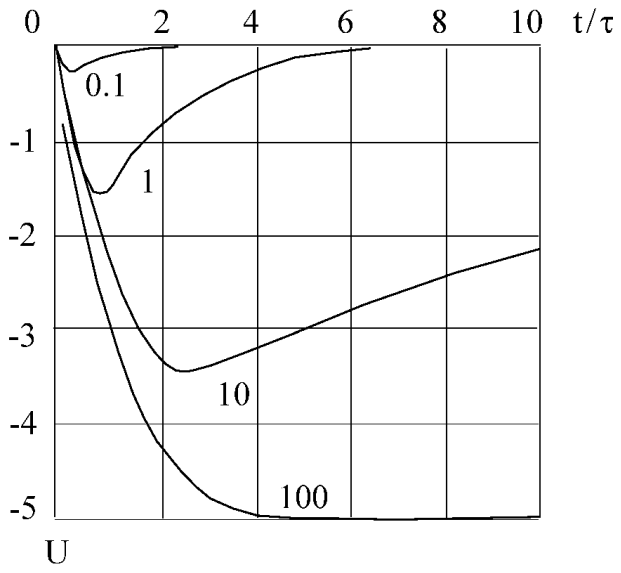

Figure 4.23: Pulse shape of a scintillator for different integration parameters $K = RC/\tau$.

4.2.1.4 The pulse shape of the scintillator

In general, the anode of the PMT is connected to the working resistance R and parallel to it the capacitance C (including the stray capacitances of the setup). The decrease in scintillation is described by the exponential law Eqn. 4.55. The voltage curve across the resistor is then

$$U(t) = \frac{Q_0}{C} \cdot \frac{RC}{RC - \tau} \cdot \left(e^{-t/\tau} - e^{-t/RC} \right) \tag{4.56}$$

Q_0 is the total charge that reaches the cathode. When deriving this equation, it is assumed that the current pulse generated at the anode by a single photo-electron from the cathode has a Gaussian shape with a width that is small compared to τ.

Fig. 4.23 shows the pulses as a function of time for various integration time constants $T = RC$ in arbitrary units. The parameter of the curves is $K = RC/\tau$. It turns out that with fast integration (K small) the pulses increase quickly, but are small, since a large part of the charge already flows off during the integration. For the exact measurement of the pulse heights and thus of Q_0, long integration is required (large K). In this case, the pulses rise more slowly than with a small K. They are also very long, which is why you can only measure with limited count rates in order to avoid cumulative effects (pile-up). This shows again that one cannot easily have good time and energy resolution at the same time.

Chapter 5

The processing of the detector signals

All detectors used in the lab generate electrical pulses that contain all the information about the detected particles. Depending on the detector, this is not always the same. For example, in the case of the trigger counter tube, it consists only of the conclusion that some ionizing particle was present. In general, it includes the magnitude of the energy deposited by the particle and the time at which it entered the detector. For charged particles, the deposited energy is equal to the kinetic energy, provided they are stopped in the detector. In this case, the signal also implicitly contains information about mass and charge via the Bethe Bloch formula and thus about the identity of the particles.

The information about the energy is given in analog form by the magnitude of the electrical pulses, the time of arrival is correlated with the time of occurrence of the pulses. The accuracy with which it is present varies from detector to detector. It depends on the statistical processes involved in the primary ionization and in the subsequent formation of the pulses.

The electrical pulses from the detectors are processed in electronic circuits with the goal of making the analog and temporal information as completely accessible as possible. Ideally, the former means pushing the energy and time resolution so far that they are limited only by the detector itself. The latter means digitizing the analog information. In most cases, a nuclear physics experiment asks for a number. One wants to know how many particles with a certain energy or of a certain kind are detected at a certain time.

The detection electronics can be divided into three parts. Directly from the detector, the pulse reaches the analog section, where it is amplified and suitably shaped for further processing. The optimal pulse shapes vary depending on the experiment. For energy measurement, the pulses usually have to be integrated, while short, differentiated pulses are required for precise time information.

In the next step, the analog pulses are converted into digital ones. This part of the electronics is called analog-to-digital Converter (ADC). As will be discussed later, some information is lost in the process. In most cases, the ADC is a multi-channel analyser (MCA) that records energy or time spectra. In some cases, for example, when only the low-energy part of a spectrum is to be separated, a simple discriminator is sufficient.

In the third part, the digitally measured variables are stored for further processing on a computer. In most of the experiments in this lab course, the MCA electronics is connected to a computer via a standard interface, such as USB or Ethernet, or it resides on a circuit board installed inside the computer, where the data is read out and stored by software.

The individual parts of the detection electronics are discussed in more detail below. Only their function and the main mode of operation will be discussed. Specific electronics circuits and more detailed descriptions can be found in textbooks for electronics.

In a modern data acquisition (DAQ) system the digitization of the signal takes place as early as possible. The temporal course of the pulse shape is digitized with a fine time resolution and

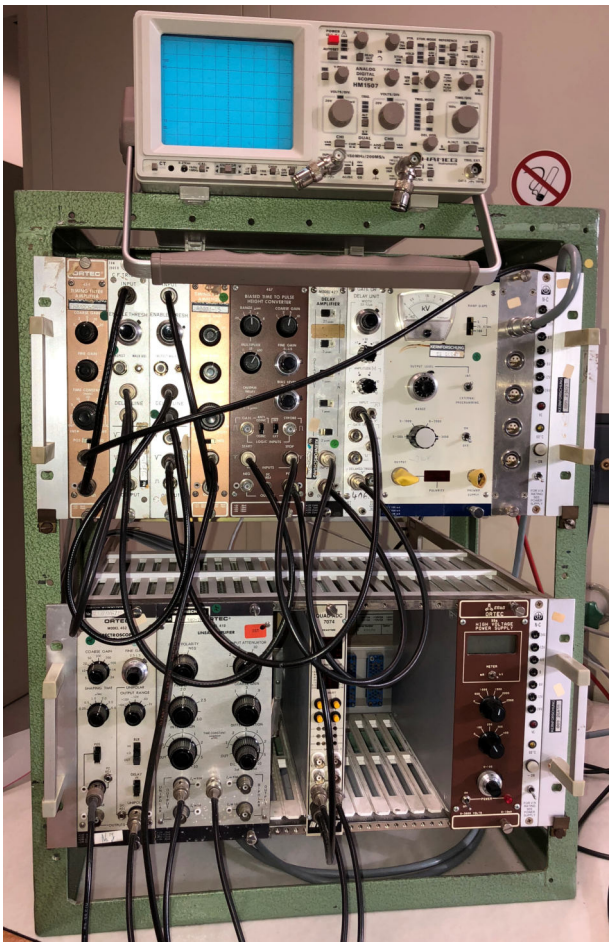

Figure 5.1: NIM-Crate with modules with different functions and BNC cables.

either stored or directly analyzed in a so-called FPGA (field programmable gate array), providing just an energy or time value that is transfered to the computer. The different functional units, which will be described below as individual hardware modules, can be emulated in software. The exchangeable hardware modules, which are still used in some experiments, are plugged in a so-called NIM-crate (see Fig. 5.1), where they are supplied through a plug at their backside with various voltages ($\pm 6\,\mathrm{V}$,$\pm 12\,\mathrm{V}$, $\pm 24\,\mathrm{V}$). The resulting signals are exchanged between the modules through coaxial BNC cables.

5.1 The analog part

The pulses as delivered by the detectors are current pulses of a certain duration. What is measured is ultimately a charge that is proportional to the deposited energy. The current pulses are first converted into voltage pulses, which are then amplified and shaped. This is done for the following reasons:

1. **Improvement of the signal-to-noise ratio.** The current pulse is always accompanied by statistical fluctuations, which arise partly in the detector itself, partly in the resistors and capacitors through which it is coupled to the subsequent electronics. This so-called noise comes from the quantum nature of electric charges and has a white spectrum, i.e. all frequencies are represented in it with equal probability. However, the bandwidth required

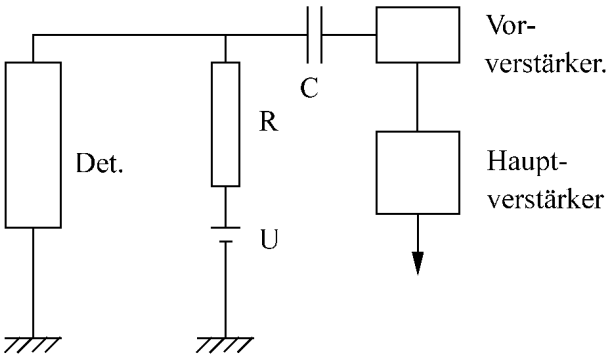

Figure 5.2: The circuit of a detector

for pulse shaping comprises only a part of the entire spectrum. So it is possible to suppress a large frequency portion and in this way improve the signal-to-noise ratio.

2. **Reduction of cumulative effects.** If a certain count rate is to be processed in an experiment, the pulses must be sufficiently short. Otherwise, they overlap, the so-called *pile-up* occurs. In this case, the magnitude of a pulse is no longer proportional to the energy loss of the particle, since it contains a fraction of the immediately preceding one. In extreme cases, two different pulses may not be separated at all. For pulses of one millisecond length, for example, this already occurs at a count rate of one kilohertz. The pile up is prevented by electronically shortening the pulses from the counting tube.

3. **Generation of a pulse shape optimal for further processing** .

   The quantities following the analog section, such as discriminators and multi-channel analyzers, require a certain rise time and length of the pulses to function properly. These are achieved by pulse shaping with the help of differentiation and integration elements in the preceding amplifiers.

4. **Preservation of time information.** The time information of a pulse is contained in its rise time. Its occurrence is defined by the time at which it reaches a certain level. Since every pulse is overlaid by noise, there is an indeterminacy in the definition of this time, which is called *time jitter*. This indeterminacy is smaller the steeper the rise of the pulse. Because the smallest rise time is given by the detector itself, it is sufficient to choose time constants in the detection circuit that do not slow down the rise time of the pulse. Smaller time constants are bad for energy resolution because they increase the bandwidth and degrade the signal-to-noise ratio.

   Another quantity, which brings an uncertainty in the time determination, is the so-called *walk*. This is understood as the time difference with which physically simultaneous pulses, which have the same shape but different amplitudes, reach a predefined height (see Fig. 5.9). There are several ways to keep the *walk* within limits. One of them is to use fast pulses.

5.1.1 The amplification of the signal

First, the current pulse from the detector is converted into a voltage pulse. For this purpose, a resistor R is connected in series to the detector, at which the drop of the applied constant voltage U is measured (Fig. 5.2). The voltage drop is fed to the pre-amplifier via a capacitor C.

The voltage pulse is always superimposed by noise, which has various causes. One part comes from the leakage current of the detector. It is unavoidable, but can be made sufficiently small by the choice of operating conditions. Other noise sources are the working resistor R, the capacitor

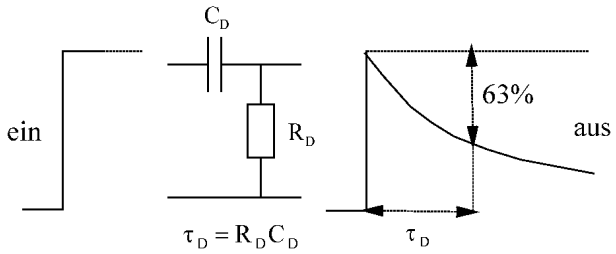

Figure 5.3: Simple RC differentiation.

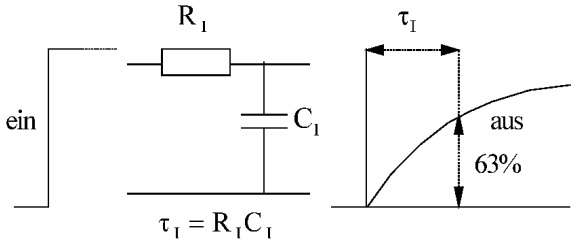

Figure 5.4: RC integration.

C and especially the connecting cables between detector and pre-amplifier. The noise of R can be reduced by suitable dimensioning whereas the noise of C by using low-noise capacitors. The connecting cable is chosen with low capacitance per unit length and kept as short as possible. For this reason, the pre-amplifier is always placed close to the detector.

The pre-amplifiers are usually designed to preserve the (short) rise time of the pulses while limiting the fall to about 50 μs. The pulses are then short enough to make the pile-up tolerable.

The slightly pre-shaped impulses then reach the main amplifier, where they are amplified (or attenuated) and, above all, shaped.

5.1.2 The pulse shaping

The pulses are formed by differentiation and/or integration with passive RC elements or by a delay line and subsequent integration. The different methods are discussed in the following. The input pulse is always regarded in an idealization as an infinitely long step pulse with height one.

5.1.2.1 Simple RC differentiation

A capacitor of capacitance C_D and a resistor R_D are connected, as shown in Fig. 5.3. The capacitor is charged instantaneously to the full magnitude of the step pulse, then discharged through the resistor following an exponential function with time constant $\tau_D = R_D \cdot C_D$. τ_D is the time after which the pulse has dropped to $e^{-1} = 37\,\%$ of its original value. Differentiation shortens the pulse, and the constant plateau drops rapidly. The differentiator acts like a **high-pass filter**, attenuating the low frequency components.

5.1.2.2 RC integration

By swapping the capacitor and the resistor, an integrating element is formed (Fig. 5.4). The capacitor with capacitance C_I is charged via a resistor R_I. Initially, a very high current flows, so that the total voltage drops across the resistor. The voltage at the capacitor slowly increases according to the law

$$U = 1 - e^{-\frac{t}{\tau_I}} \tag{5.1}$$

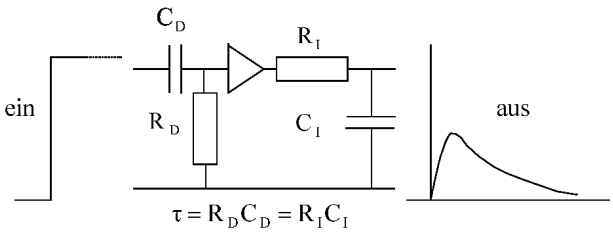

Figure 5.5: Simple RC differentiation with subsequent integration.

with the time constant $\tau_I = R_I \cdot C_I$. The integrator acts like a **low pass filter** attenuating the high frequency components. Pulses formed exclusively by integration are useless because of their infinite length.

5.1.2.3 Simple RC differentiation and subsequent single or multiple integrations

The simple differentiation alone is not useful, because the pulses increase too fast for the analysis. Therefore, it is usually combined with one or more subsequent integrations. Fig. 5.5 shows the shape of the pulse for an integrating stage with the same time constant as for differentiation. It has a rapid rise time and a slower decay time. Each additional integration increases the decay time. The pulses become more symmetrical but also smaller, as shown in Fig. **??**. The latter is disadvantageous, but is accepted, because the signal-to-noise ratio improves with an increasing number of integrations. It is best if the time constants for differentiation and integration are the same.

5.1.2.4 Double differentiation and subsequent multiple integrations

Completely different pulse shapes are obtained by connecting two differentiation elements in series, which can be followed by several integration stages. They are shown in Fig. 5.6. From a positive step pulse, bipolar pulses are obtained, which consist of a positive and a negative part. Without integration (n=0) the pulse is strongly asymmetric, the positive part is fast, short and high, the negative is smaller and long. The integrations cause the positive pulse to become longer and smaller, so that the shapes of the two parts conform to each other. The areas above and below the zero line always remain the same size.

Based on Fig. 5.6, one can indicate which form the real pulses have. For several reasons, the case of a single differentiation producing unipolar pulses is an unachievable ideal case. On the one hand, the different shaping and amplifying stages of the analog part are coupled by capacitors, since a galvanic coupling is usually very unstable. However, this introduces additional differentiations. On the other hand, the detector or pre-amplifier do not provide the ideal pulse shape assumed so far, the step pulse. The real pulses increase rapidly, but then do not remain constant. Thus, the pulse shape which has to be processed is already slightly differentiated or somewhat equivalent to it, anyway. This means that one always has at least bipolar pulses with a so-called undershot. With n-fold differentiation it becomes a kind of damped oscillation with n-1 zero crossings.

5.1.2.5 Simple delay line

Very short and symmetrical pulses are obtained when shaping with a delay line. The simplest circuit for this is sketched in Fig. 5.7. In a short-circuited delay line, which is usually a coaxial cable, the pulse is reflected under phase inversion and superimposed on the step pulse. If T_D is the delay of the line, the tilted pulse has transit time $2T_D$. As a sum of the incoming and the

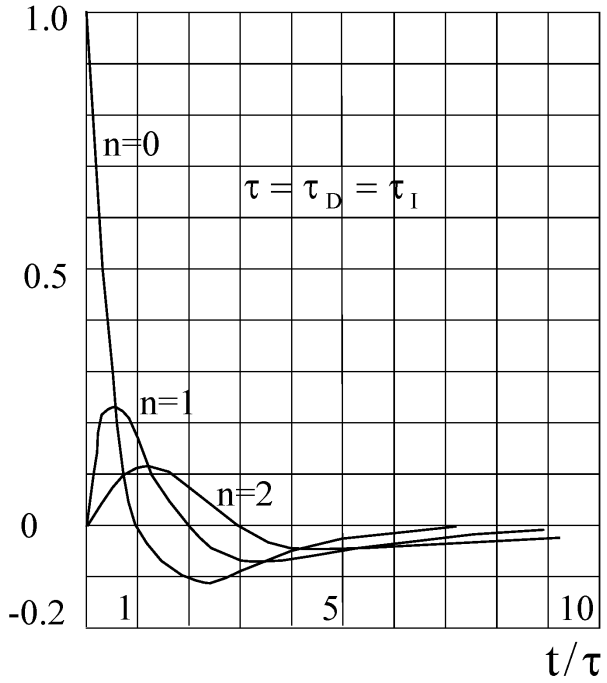

Figure 5.6: Pulse shape with a double differentiation and n-fold integrations.

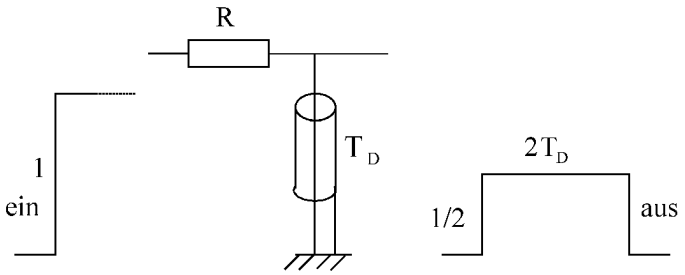

Figure 5.7: Simple delay line

delayed pulse, a pulse of length $2T_D$ is produced whose height is halved because of the series connection of the delay. This method can be used to generate pulses that are a few nanoseconds long. No zero line shift occurs, but the signal-to-noise ratio is smaller than with RC shaping.

Subsequent integration yields the pulse shapes of Fig. 5.8. If the time constant of the integration τ_1 is smaller than the delay time, approximately rectangular pulses are produced, if it is equal or larger, the pulses are almost triangular.

5.2 The Analog-to-Digital Converter (ADC)

At the output of the analog part of the detection electronics, all the information that the detector has about an event is generally still available, i.e. about the energy that has been deposited in the detector by an event and about the time when it occurred. The information about the energy is available in an analog form: the pulse height and its charge integral are proportional to the energy.

In the ADC, the analog information is converted into digital information. In principle, this is done in such a way that a digital conversion is only generated when the analog pulse at the input meets a certain trigger criterion. For example, a digitized value is only generated if the

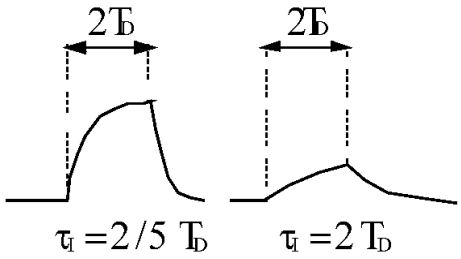

Figure 5.8: Pulse shape with delay and integration.

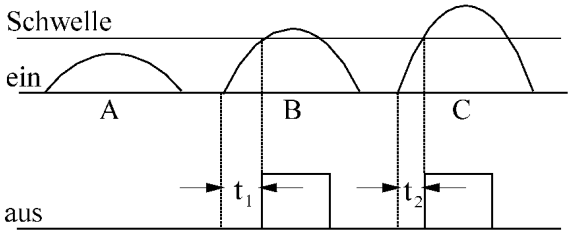

Figure 5.9: Integral discriminator.

input pulse exceeds a certain level (integral discriminator), or if it lies within a certain range (differential discriminator).

In any case, information is lost during the conversion. The analog pulse spectrum is continuous. However, the conversion of the registered pulses into a number is discrete. The pulse height is converted into an integer number $N(U)$ between 0 and $N_{\max} = 2^r - 1$, where r is the number of bits of the ADC. The discrete numbers correspond to a voltage between 0 V and the maximum voltage $U_{\max}$ of the ADC. A 10-bit ADC, for instance, subdivides this range into 1024 equidistant bins, sometimes called ADC-channels. Each bin is $U_{\max}/1024$ wide. There are also ADCs which provide a total range from $-U_{\max}$ to $+U_{\max}$. The distinction of the pulses within the range of a bin is not possible, i.e. the resolution during the conversion is finite.

In practice, however, the loss of information is usually insignificant. As a result of the limited energy resolution of the detectors, the pulse heights corresponding to a certain fixed energy have a certain range of fluctuation. Therefore, it is sufficient to select an ADC with a resolution finer than these fluctuations, so that even after conversion, the resolution is determined by the detector alone. The loss of information does not play a major role then.

5.2.1 The integral discriminator

The integral discriminator delivers a logical pulse at its output only if a pulse at the input exceeds an adjustable level, the threshold. In Fig. 5.9 this is the case for the pulses B and C. The pulses below the threshold are not processed.

5.2.2 The differential discriminator or single-channel analyzer

The single-channel analyzer (SCA) outputs a logic pulse only when the pulse height at the input is between two adjustable values, i.e. for pulse B of Fig. 5.10. The distance between the lower and upper discriminator thresholds is called the window. If the window is made narrower and narrower, the height of the selected pulses can be determined more and more precisely. In practice, however, this cannot be pushed arbitrarily far, because with a window width going towards zero also the counting rate goes towards zero.

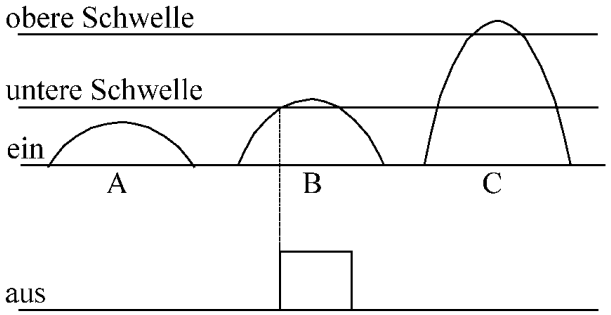

Figure 5.10: Single-channel analyzer.

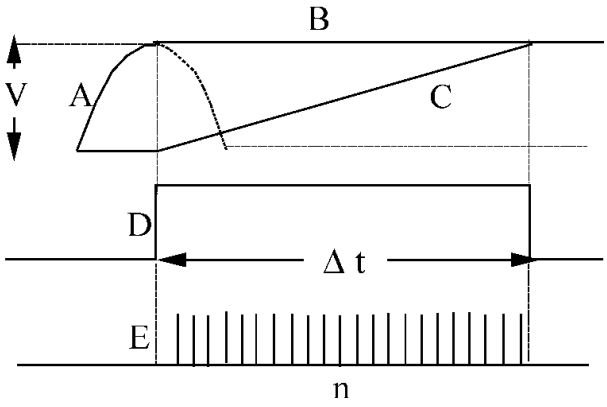

Figure 5.11: Mode of operation of a Wilkinson ADC.

A pulse spectrum can be analyzed with an SCA with an accuracy corresponding to the window width, if the new windows' lower thresholds are successively shifted by the window width and the respective events are counted.

5.2.3 The multi-channel analyzer

An SCA is not really suitable for analyzing a pulse spectrum. It is time-consuming if good resolution is required, or inaccurate if only limited measurement time is available. Therefore, multi-channel analyzers (MCA) are used for this purpose, which employ an ADC for the pulse height analysis and operate in principle as if many SCA were connected in parallel, each with the lower threshold shifted by the window width in such a way that the entire part of the spectrum of interest is covered. The output pulses of each SCA are counted separately. The result are the total number of events registered in each window or channel. In this way, the entire spectrum is measured in one operation. After the corresponding channel of the histogram has been incremented in the MCA the information can no longer be attributed to a specific event.

Such a measurement is a digitization of the pulse height spectrum. Suppose that analog pulses in the range of 0-10 V are to be examined with a MCA which has a thousand channels. Then each of the channels, which all have a width of 0.01 V, is assigned a consecutive number from one to one thousand. Then, in channel 1, the pulses between 0 and 0.01 V are detected, and in channel n the pulses between $0.01 \cdot (n-1)$ and $0.01 \cdot n$ are detected. Then, the numbers of the channels, the channel addresses, correspond to the pulse heights in digital form.

One of several possibilities to realize such an ADC is the Wilkinson converter. Its operation is outlined in Fig. 5.11. The pulse height is first converted to a pulse length, which is then digitized. The incoming pulse A is first stretched, creating a plateau of height V (B). At the time it reaches its maximum height, a constant current source begins to charge a capacitor, whose voltage then

increases linearly with time (C). At the same time, a gate pulse (D) is generated. When the linear ramp has risen to the value V, which is detected with a comparator, the gate pulse resets. Its length Δt is proportional to V. While the gate pulse is applied, the oscillations of a stable oscillator are counted, whose number n is proportional to Δt. The number of oscillations is thus proportional to V and is the digitized value of the pulse. During conversion, the VKA is not ready to process new pulses, it has a dead time. It is measured and subtracted from the real time. The count rates of a MCA are therefore always already corrected to the dead time.

This type of ADS digitizes only the pulse height and is relatively slow. Modern data acquisition systems (DAQ) use more and more flash-ADCs, containing a large number of comparators, which digitize the present height of the input voltage in one step. With digitization times of a few nanoseconds down to several hundred of picoseconds they can digitize the entire shape of the pulse over time. Afterwards the digitized information is often analyzed electronically by fast programmable logic arrays (FPGA = field programmable gate array),and the required information is determined, such as the energy or time of an event. In this way, the data rate can be reduced to a manageable amount and recorded on a storage device. If the event rate is not too large, the entire digitized pulse shape can be recorded to be analyzed by a computer at a later time (offline analysis). These fast DAQ systems allow a event-wise offline analysis that can take into account correlations between different event parameters, which are otherwise lost in a standard MCA spectrum.

5.3 The time information of the discriminator

There are two classes of experiments in which time information is essential. The first class is the coincidence experiments, which determine whether two or more events occur within a very short time. They play an important role in γ spectroscopy, since they allow to determine the energy states of a nucleus in a gamma cascade.

The second class includes experiments in which the time between two events is measured, for instance the determination of the lifetimes of particles or states.

The time at which a pulse occurs at the output of the amplifier is correlated with the time of its trigger in the detector. Although the pulse is delayed on its way through the pre-amplifier and amplifier, this delay is the same for all pulses. It is subject only to the unavoidable statistical fluctuations caused, for example, by the variation of the collection times of the charges in a counting tube or a semi-conductor detector, by the fluctuation of the decay times in a scintillator, or by transit time fluctuations of the electrons in a photomultiplier. Until then, the time information remains within the uncertainty given by the statistics.

In general, this is no longer the case for the pulse height analysis in the discriminators. In Fig. 5.9 an example is shown. There, a logic signal is generated when the input pulse exceeds the threshold. Then the times between the occurrence of the pulses and the triggering – t_1 for B and t_2 for C – are not the same, but differ for different pulse heights. The time difference $t_1 - t_2$ is called *walk*. It depends on the rise time of the pulses and is smaller the faster they are.

Discriminators that trigger on the threshold crossing can only be used in experiments where timing information is important, if the rise time is less than the temporal uncertainty that can be accepted in time measurement.

The *walk* becomes smaller the lower the threshold is, and disappears completely when triggering on zero height. In discriminators operating on this principle, the pulse height discrimination and the timing discrimination are performed separately. The first one still occurs at the predefined threshold, the latter one at the zero crossing. In order to prevent the noise from also generating timing signals, a coincidence circuit is used, which only emits signals when the triggering pulse has also crossed the threshold. The process is simplified when the time sequence is reversed. Bipolar pulses are used, where the zero crossing is at the same time regardless of the

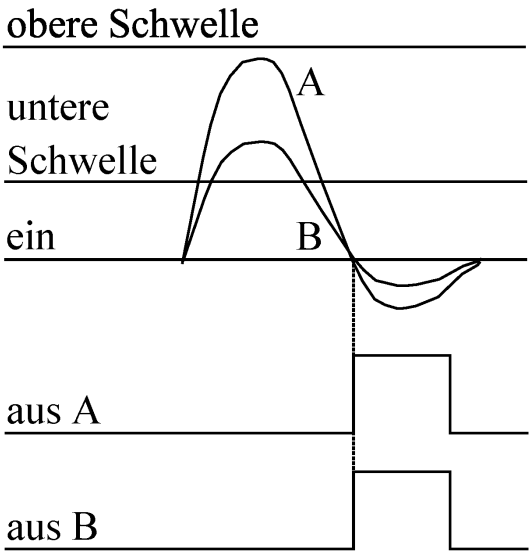

Figure 5.12: Zero crossing trigger.

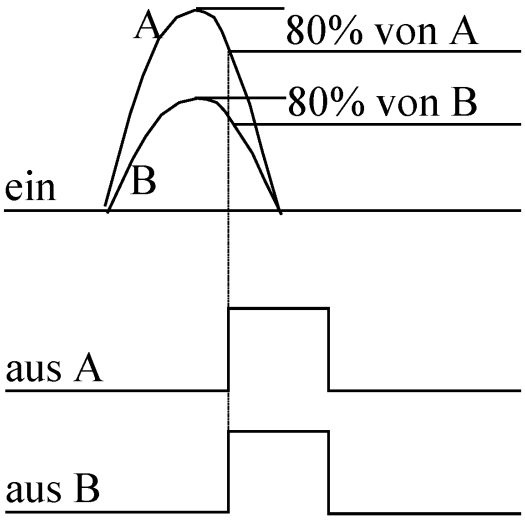

Figure 5.13: Constant-fraction trigger.

height. In Fig. 5.12 the operation of an SCA as a zero-crossing trigger is sketched. For the pulses that are in the window, standardized output pulses are generated that both appear at the same time, at the zero crossing. If the lower threshold is sufficiently high, no noise pulses will appear.

This method is a special case of the most accurate method of time determination known, the triggering on a constant fraction of the pulse amplitude. This method takes advantage of the fact that for all RC-shaped pulses of different heights not only the maximum height and the zero crossing are reached at the same time, but also each constant fraction of the amplitude (Fig. 5.13). The advantage of a constant-fraction trigger (CFT) over the zero-crossing trigger is that no bipolar pulses are needed, which have a worse signal-to-noise ratio than the unipolar ones.

5.3.1 The coincidences

A coincidence unit generates a logical pulse if two or more pulses arrive at the input within a certain time, the coincidence resolution time. The mode of operation can be explained for an

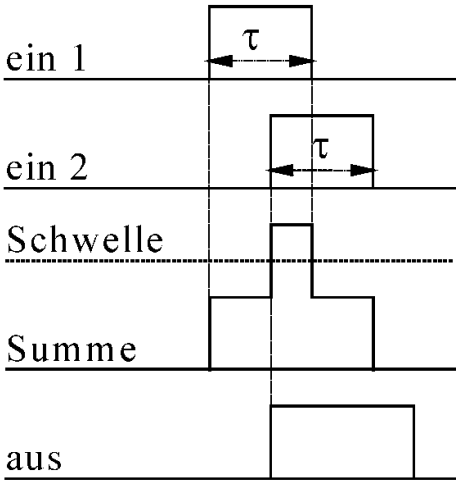

Figure 5.14: overlap coincidence.

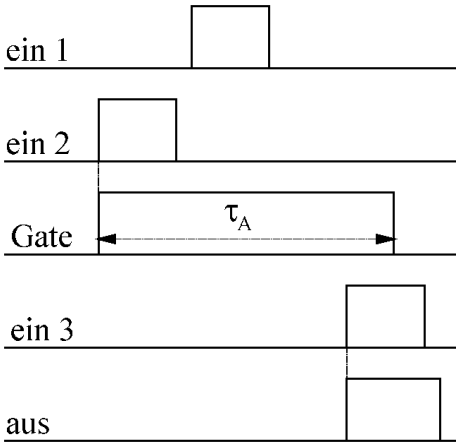

Figure 5.15: Variable coincidence.

overlap coincidence with the help of Fig. 5.14. Norm pulses of length τ arrive at the two inputs from the discriminators. In the coincidence stage the pulses are added. Provided that they overlap in time, a sum pulse with twice the height of the input pulses is produced. This can be detected by discrimination with a threshold which lies between the single and double pulse height. Thus, an output pulse is generated only when the input pulses overlap, hence the name. This is the case for all pulses whose distance is less than τ. Since either pulse can be the first, the resolution time of the coincidence is 2τ, thus determined only by the length of the individual pulses.

Another type of coincidence stage is shown for a triple coincidence in Fig. 3.16. The first arriving pulse, here the one at the second input, generates with its rising edge a gate pulse with variable, adjustable length τ_A. This opens the other inputs of the coincidence. The last of the pulses passing the gate, here the third, triggers an output pulse. If a pulse does not arrive at each input during the opening time, there is no output pulse. The resolution time is therefore equal to the length of the gate pulse.

5.3.1.1 The time-to-pulse-height converter

A coincidence experiment determines whether two or more events have occurred within a certain time. However, the time itself is not measured. The information of such an experiment is there-

fore somewhat analogous to that obtained about the energy of events by means of a differential discriminator. The resolution time of the coincidence corresponds to the channel width of the SCA.

In the same way, the measurement of the time between two events corresponds to the analysis of an energy spectrum with a multichannel analyzer. In the two-step working principle, first an analog pulse is generated in a time-to-pulse-height converter (TPC from Time-to-Pulse-height Converter, sometimes also TAC from Time-to-Amplitude Converter) whose height is proportional to the time difference between the first arriving pulse that starts the converter (start input) and the subsequent pulse that stops the conversion (stop input). Afterwards, the pulse height is digitized in the usual way with an ADC (see 5.2.3) and added to a spectrum in an MCA or stored as en event, possibly together with the energies, on a storage device for offline analysis.

There are two methods for time-to-pulse-height conversion. In the first one, the start pulse closes an electronic switch that connects a capacitor to a constant current source. The stop pulse opens the switch again. The charge and thus the voltage on the capacitor is then proportional to the time between the two pulses. In the second one, the overlap method, the start pulse generates a standard pulse of a certain length and the stop pulse generates the same pulse again, only with negative amplitude. The two pulses are added electronically, producing a positive pulse whose length is equal to the time difference between start and stop. Finally, the length of this pulse is converted into a pulse height by integration.

Direct digitization without the detour via a pulse height is also possible. In this case, a gate is opened by the start pulse through which pulses of an oscillator with a constant frequency reach a counter. The stop pulse closes the gate. The number of counted oscillations is proportional to the time between the two pulses. It provides the time difference in digital form. The higher the frequency of the oscillator, the more accurate the digitization.

5.4 The digital part

The digitally available information must be collected and recorded. In single-channel discriminators, the logic pulses are registered with a pulse counter for this purpose. In this case, the threshold that may be present at the counter input must be lower than the height of the pulses. The counter has a gate input via which it is opened by a clock (timer) only for a pre-set time. In this way the measuring time is set. With some counters it is possible to count a predefined number of pulses. This operating mode is preferable if measurements are to be made with a specified statistical accuracy. In this case, the measured quantity is the time in which the pulses were registered.

When using multichannel analysers, the measured data are added to a histogram and read out and stored by a computer (usually a table with the channel number and channel content) for further *offline* analysis. Data from several detectors and ththeir timing information can also be stored directly as individual events. In the *offline* analysis one can apply different cuts on the energies and time differences of the recorded detector signals.

5.5 The structure of the experiments in block diagrams

After the functionality of the individual components has been explained in the previous sections, the complete set-up of the experiments will be discussed in the following. At first glance, it may seem that the large number of experiments can only be handled with an equally large number of different experimental setups. Fortunately, this is not the case; one can get by with only a few standard methods. There are two reasons for this.

1. The measured data in nuclear physics are mostly count rates in specified energy or momentum intervals obtained under certain conditions that will be discussed below.

2. The processing of the electrical signals from the detectors is largely standardized. (Of course, this only applies to detectors that provide electrical signals. Only those are used in the lab course).

The electronic components and circuits described below are constructed from modular plug-in units which are inserted into NIM module frames with a power supply unit and whose input and output signals are distributed to the subsequent modules with coaxial cables. At the end, the resulting signal is either counted electronically, analysed with a multichannel analyser (ADC followed by a storage unit for the pulse height histogram), or stored as individual events for the *offline* analysis. The multichannel analyser provides a spectrum (histogram) of an energy, momentum, or time distribution, depending on the input signal.

In modern experiments, the detector signal is digitized at the earliest possible stage with a fast ADC and the signal logic of the electronic modules described below is emulated with the aid of software. For example, trigger thresholds are no longer generated with discriminator modules, but by a simple "if" query of the pulse height in the analysis code. Currently, the data acquisition of many experiments in the lab is being modernized so that the pulse processing and trigger logic specified in the experiment description is no longer wired but programmed. This results in large amounts of data. For processing we use either software from the manufacturer in combination with code in the programming language PYTHON or so-called JUPYTER notebooks, in which the Python code and the results are in the same document. Which method, software or hardware is used will be explained at the experiment by the supervisor. Experiment descriptions will be updated over time to reflect updated data analysis. Have a USB flash drive (recommended: 16 GB or more) or free cloud storage area available for the data. We continue to use the modular NIM technology for some experiments, as it is still used in some simple lab experiments, despite the growing digitization.

5.6 The measurand

It measures the number of events per unit time caused by:

1. particles of a certain type,

2. particles of a certain energy, which may be

3. in a temporal relation with other events, or

4. detected with additional conditions.

5.6.1 The identification and discrimination of particles

In order to identify particles, it is necessary to determine their charge and mass. The charge is obtained by observing the orbits in electric and magnetic fields, where the magnitude and direction of the deflection depends on the magnitude and sign of the charge.

There are several methods for mass determination, all of which require knowledge of the kinetic energy. Its measurement is therefore always the first step. For this purpose, another quantity is measured, e.g.:

the momentum by deflection in a magnetic field,

the velocity by measuring the time of flight over a known distance,

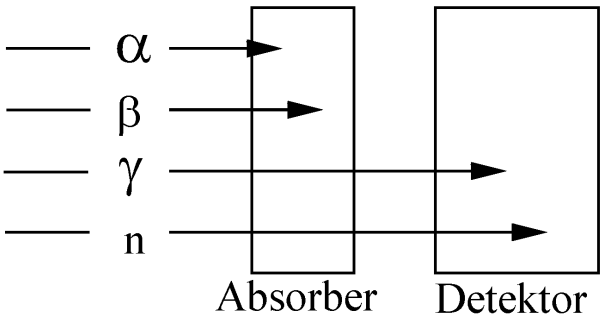

Figure 5.16: Schematics of an absorption experiment.

the specific energy loss of charged particles.

In many cases, also in the lab course, in which one knows from the start that only few kinds of particles can occur, the measurement of the energy is sufficient, possibly together with the observation of the absorption behavior in matter. In the lab course the following particles occur:

Charged particles: electrons, positrons, α-particles and muons.

Neutral particles: γ-quanta and neutrons.

Except for muons, which come from cosmic rays, the charged particles all come from radioactive decays. As it is known, the leptons have continuous energy spectra, while the α particles have discrete energies. The γ energies are discrete in radioactive decay, whereas they are continuous in bremsstrahlung. The neutrons from the α-n sources also have a continuous spectrum.

It is very easy to distinguish the charged particles from the neutral ones. For this purpose, one only needs to perform an absorption experiment, where absorbers of variable thickness are placed between the source and the detector (Fig. 5.16). This takes advantage of the fact that charged particles have a finite range in matter and are stopped when the absorber is sufficiently thick. The γ rays, on the other hand, are only attenuated in intensity while retaining their original energy. The neutrons show a similar behavior i.e. their intensity also decreases. In addition, as a result of the deceleration, a shift of the spectrum towards small energies can be observed, but only for very thick absorbers. For a thickness, which is already sufficient to stop α-particles and electrons, neither a noticeable decrease of the intensity nor a change of the spectrum of the neutral particles occurs.

If one knows from the absorption experiment that charged particles are present, then one can identify the α-particles and electrons by a more precise measurement of the absorption and/or by observing the shape of the spectrum. In the first case, the fact is exploited that the α particles have much shorter ranges than leptons of the same energy, because the specific ionization is much (about 4000 times) larger. In the second case, the fact that the α spectrum is discrete is used. The leptons are distinguished by deflection in electric or magnetic fields or more simply by looking for the annihilation radiation of a positron of 0.511 MeV.

If, on the other hand, the investigated radiation consists of uncharged particles, it is best to observe the shape of the spectrum. γ radiation with a discrete energy has the typical spectrum described in section 3.2.2, and bremsstrahlung is distinguished from continuous neutron spectra by the use of special γ- or neutron-sensitive detectors.

These methods of particle discrimination are also used in such cases where several particles are detected in a detector at the same time, but only one species is to be counted. Here, too, it is usually sufficient to measure the energy, especially if one has only two species. First, the measured spectrum is interpreted with the methods of particle discrimination. If it is possible in

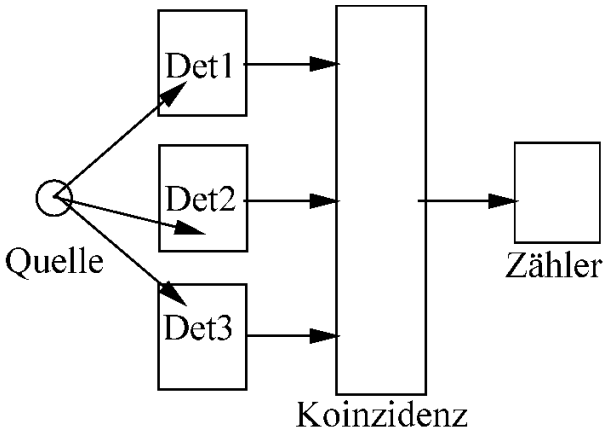

Figure 5.17: Scheme of a coincidence.

this way to assign parts of the spectrum to a single species, then only the events in the relevant region need to be counted for discrimination. This method can always be applied if the particles have different energies. In order to separate the charged and uncharged particles, one applies a difference method. In a first step, the entire superimposed spectrum is measured. In a second measurement, only the rate of the uncharged particles is determined after the charged ones are filtered out by an absorber. The difference of the measured values then gives the rate of the charged particles.

5.6.2 The energy discrimination

Energy discrimination is a special case of particle discrimination. The goal is to detect particles of the same kind but with different energies separately from each other. For this purpose, the entire spectrum is measured and only the region of interest is utilized.

5.6.3 The temporal correlation of the radiation

In addition to the identity and the energy, the temporal correlation between the time of detection of a particle and a reference time, which is usually determined by the detection of another particle, is another important measurand. Temporal correlation means that either the simultaneity of two events is detected, or the time interval between the events is measured.

5.6.3.1 The coincidence measurement

Coincidence measurement means the detection that two or more events have occurred within a certain predetermined time, the coincidence resolution time (see also section refsec:5-3-1). By coincident detection of different particles in multiple detectors (Fig. 5.17), it is possible to infer that the particles were created simultaneously. Examples of such experiments are the simultaneous detection of two γ quanta following a β decay, allowing to study the energy states of the daughter nucleus, or the detection of the airshowers in the interaction of cosmic rays with matter.

Another group of coincidence experiments are those in which a single particle is seen simultaneously by several detectors (Fig. 5.18). They are used to determine trajectories and thus, for example, the place of origin. Combined with an absorber, particles can also be identified in such an arrangement.

If the telescope is provided with suitable apertures, only particles from a defined opening angle are transmitted. It can then be used to define the directionality of the radiation intensity.

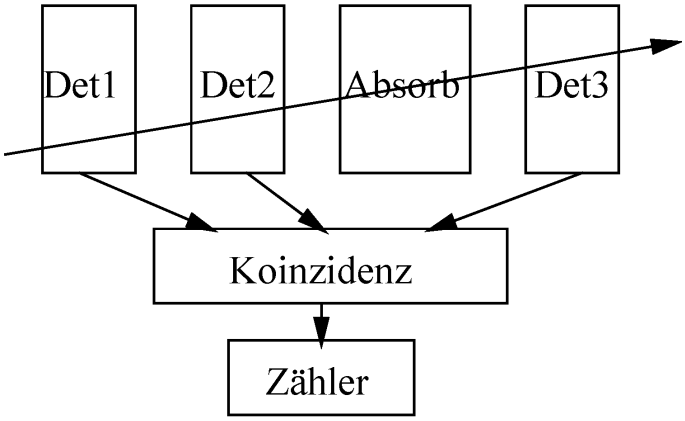

Figure 5.18: Scheme of a telescope.

It is also used in such cases where particles from different directions are to be detected only if they have passed through the full length of a target or absorber.

In addition to the physically correlated events, the *true* coincidences, counted in a coincidence setup, there are also counts which arise from randomly occurring events during the coincidence resolution time that are not from correlated particles and are therefore called *random* coincidences. For a two-fold coincidence the number of random events can be determined as follows. Let us assume an overlap coincidence with pulse length τ in each branch, a total measurement time T, and the count rates N_1 and N_2 in the corresponding branches. The number Z_1, of particles arrived in the counter 1 during the measuring time T, is

$$Z_1 = N_1 \cdot T \tag{5.2}$$

If in the same time in the counter 2

$$Z_2 = N_2 \cdot T \tag{5.3}$$

particles arrive, the number Z_R of coincidences randomly registered during the fraction $Z_1 \cdot \tau/T$ of the total time T is

$$Z_R = Z_1 \cdot \frac{\tau}{T} \cdot Z_2 \tag{5.4}$$

Since the same consideration applies to the second branch, we finally obtain for the rate N_R of random coincidences

$$N_R = \frac{Z_R}{T} = 2 \cdot \tau \cdot N_1 \cdot N_2 \tag{5.5}$$

The time resolution of the coincidence is $2 \cdot \tau$, twice the width of the single pulses. It can be seen that for given count rates in the two branches, the number of random coincidences can be decreased only by shortening the resolution time.

For a triple coincidence the corresponding formula is

$$N_R = 3 \cdot \tau^2 \cdot N_1 \cdot N_2 \cdot N_3 \tag{5.6}$$

5.6.3.2 The time measurement

Time measurements are performed on the one hand to determine the time of flight of particles. In an arrangement as shown in Fig. 5.18, the time is measured that is needed by the particle to

cover the known distance between two detectors. The time signal from the first detector is the start signal, and that from the second one is the stop signal for the time-to-amplitude converter (TPC). The time of flight and the flight path result in the velocity of the particle. The additional measurement of its kinetic energy allows the identification.

On the other hand, time measurements are also performed to obtain the lifetimes of particles or states. For this purpose, it is necessary to measure the time difference between events associated with the formation and decay of the particles or states. Decay is determined by detecting the decay products, i.e. it is also necessary to identify the particles formed during the decay. If the generation of the states is associated with the emission of particles, the same applies. In other cases, other quantities, e.g., the coincidences in a telescope, must be used to determine the reference time. In general, it is sufficient to measure the time of decay with respect to a time when the particle existed with certainty.

5.6.4 Other methods

The methods discussed so far are characterized by a simple basic design. The radiation to be examined is detected in time and energy sensitive detectors. The information about time and energy is obtained by electronic processing of the signals.

There are experiments which cannot be described by this simple scheme. It may be that the information reached in this way is not precise enough or not sufficient, since other properties of the radiation are also of interest. Therefore, another experimental apparatus is added, with which the radiation interacts according to its properties, and which has the task to investigate just these properties.

The simplest example of this has already been mentioned. It is an absorber which is placed in the trajectory of the charged particles. Due to the electromagnetic interaction, which causes a deceleration depending on charge, mass and energy, the particles can be discriminated with respect to these properties. Thus, energy and particle discrimination are possible.

Another example is the magnetic spectrometer, which only passes particles with a certain charge and a defined momentum and is therefore suitable for identification and energy measurement.

Finally, the polarization of γ beams can be determined. For this purpose, the γ quanta are scattered on polarized (i.e. spin-aligned) electrons before their detection. The effective cross section of Compton scattering depends on the orientation of the spin of the γ quanta with respect to the electron spin. If the γ count rate is measured for opposite directions of the electron spin, a count rate difference is found from which the polarization of the γ beam can be determined.

In summary, the following can be said: The most important issue in nuclear physics experiments is the measurement of the energy and the determination of the time behavior of the radiation, because they allow the determination of the essential properties, namely the identity and the energy. In many cases this information is sufficient to answer the open questions of the experiment. Even in experiments where additional properties are investigated, they represent an essential property. For this reason, the experimental methods of measuring energy and time will be discussed in detail in the next section.

5.7 The block diagrams

The block diagram of an experiment is useful in two ways. On the one hand, it unifies the individual functions discussed above for a particular experiment and therefore provides a schematic of the logical experimental setup. On the other hand, it is at the same time a representation of the actual setup. Still today, commercially available nuclear electronics realizes the individual functions in separate units, which are suitably assembled according to the respective requirements.

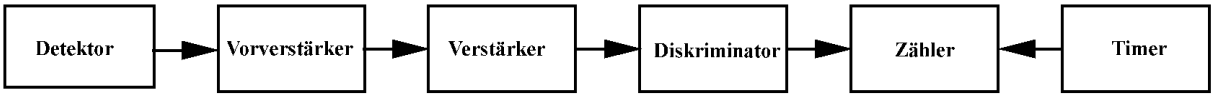

Figure 5.19: Counting of selected events.

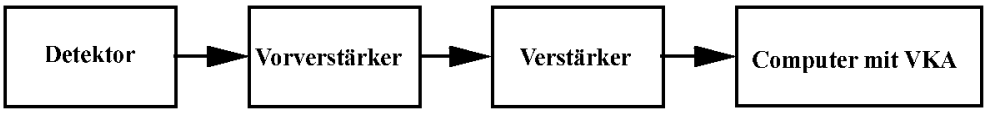

Figure 5.20: Energy measurement with a multi-channel analyser.

With this so-called plug-in technique standardized setups can be composed, which are listed in the following section in the order of increasing information, which they are able to provide about energy and time behavior.

5.7.1 Determination of the count rate of selected events

The signal from the detector passes through the pre-amplifier and the spectroscopy amplifier for pulse shaping to the discriminator, which selects the events with respect to their energy. In scintillation detectors, the pre-amplifier is usually already integrated in the voltage divider of the photomultiplier. For each selected event, a standard pulse is generated in the discriminator, which is passed on to the counter. An adjustable clock, the timer, determines the length of the measuring time of the counter. This arrangement is used e.g. for particle discrimination, possibly in connection with an absorber and for energy discrimination.

A single-channel analyser is usually used as a discriminator. With this, the energy spectrum is first recorded and then either a threshold is set above which all events are counted, or a window is set so that only one region of interest, e.g. a line, is selected from the entire spectrum. The step-by-step recording of the energy spectrum is time consuming if a good resolution is needed, because many steps with small count rates are required. Today it is more likely that a MCA with an ADC is used for the energy measurement and the discriminator is only used to suppress low-energy noise events.

The arrangement is simplified if only counting is required, i.e. if particle and energy discrimination are omitted, either because they are unnecessary, as in dosimetry, or because they are done outside the detector. In such cases, a trigger counter can be used whose pulses are energy-independent and large enough to be counted without amplification and discrimination.

5.7.2 Determination of the energy spectrum with a multi-channel analyser

This method is an extension of the one described above. Here, the entire energy spectrum, i.e. the count rate as a function of energy, is recorded in one step. It is the standard method of energy measurement.

The signal processing is the same as before until the gain shaping. Then the pulses are fed to a MCA, where they are sorted according to their pulse height and stored. After the measurement is finished, the data is printed or stored on a computer for further processing. The spectrum can be observed on the screen of the MCA (or computer) during and after the measurement.

5.7.3 Measurement of the energy spectrum of selected events

In this method of measurement only energies of such events are analysed, which have been selected by additional conditions. The setup consists of a branch for energy measurement as

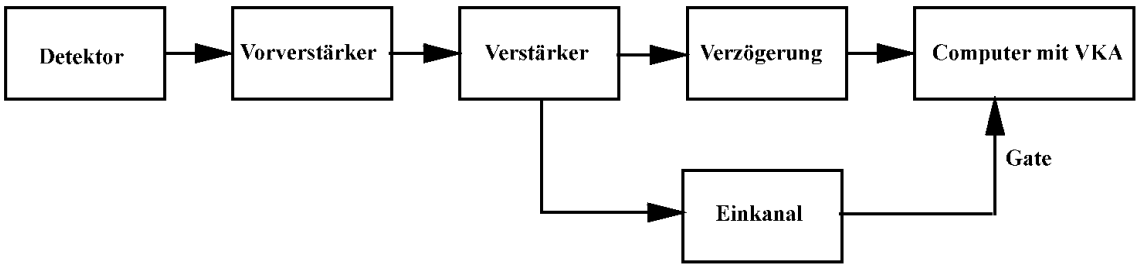

Figure 5.21: Energy measurement of selected events.

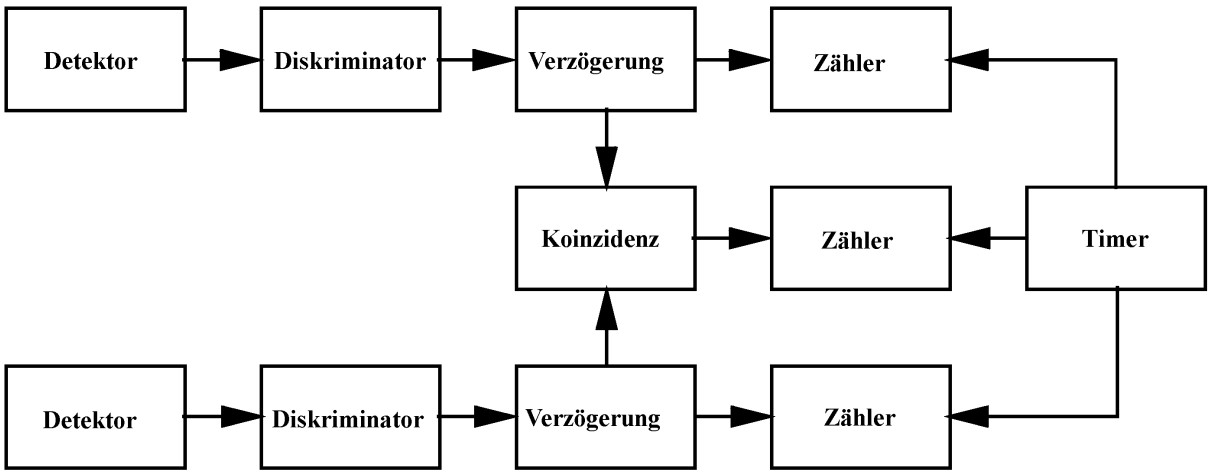

Figure 5.22: Coincidence measurement.

described in section 5.7.2. The selection is made by a digital pulse from an SCA connected to a parallel output of the amplifier in the example outlined here. The SMA provides a standard pulse only for adjustable ranges of the spectrum. This pulse opens a gate at the MCA for the analog pulses arriving at the input. In this way, only those pulses that originate from the selected range enter the MCA. In addition, the analog signal passes through a delay unit so that it arrives at the MCA only *after* the gate and finds it ready for recording. The gate works like a garage door: it must be open when the signal arrives, and it must remain open while it is present. Specifically, this means that the gate pulse must arrive 0.5-1 μs earlier than the signal and be 2-5 μs long. Usually the standard pulse from the SCA is shorter Therefore, it is extended by another unit (gate generator) not drawn here.

The described circuit is a special case of a coincidence. The MCA accepts the signal only if it arrives within a certain time span in the time window determined by the gate pulse. This time span is the resolution time of the coincidence.

The setup, as shown in Fig. 5.21, is used for fast and accurate energy calibration of the discriminator. This is done by comparing the total calibrated spectrum, recorded with the threshold lowered or the window fully open, with the partial spectrum that remains when the discriminator is set. The lower and upper limits of the partial spectrum are the energies of the thresholds.

5.7.4 The coincidence measurement

The block diagram in Fig. 5.22 shows the typical setup of an experiment to measure the coincidence of two events in different detectors. Pre-amplifier and amplifier are omitted, which is always done when scintillators are used as detectors and time information is essentially what

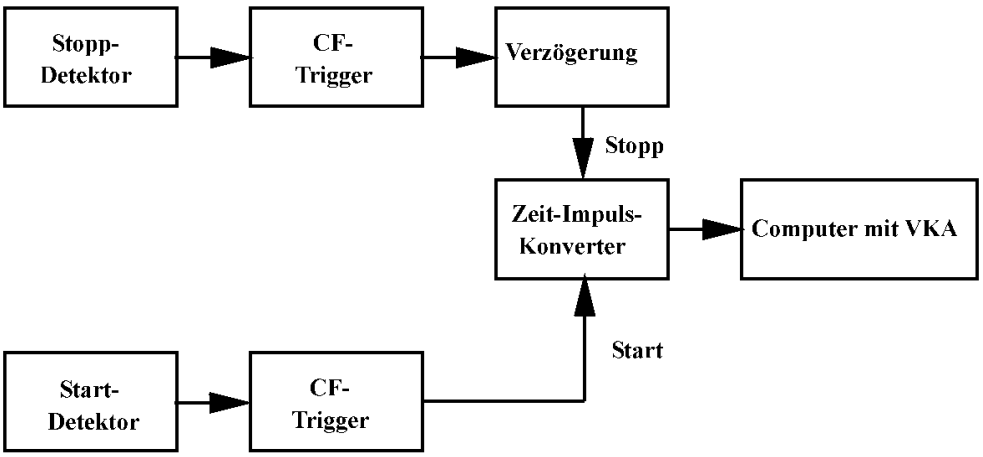

Figure 5.23: Time measurement.

matters. The timing signal is then taken directly from the anode of the photomultiplier, which is very fast. This makes the energy resolution poor, but that is not what matters here. The discriminators are chosen, based on the required time resolution. The signals are discriminated, and the digital pulses are passed through delay units for coincidence. The variable delays compensate for any transit time differences in the two lines, so that the signals of physically simultaneous events also reach the coincidence at the same time. They are also used to determine the coincidence resolution time.

In addition to the coincidence rate, the single count rates of the two branches are measured to estimate the rate of random coincidences (see Eq. 5.5).

5.7.5 The time measurement

Also in this arrangement one gets by without pre-amplifier and amplifier for the same reasons as with the coincidence measurement. If times in the range of nanoseconds are to be measured, constant-fraction triggers are used as discriminators. The signals reach the TPC and generate a pulse spectrum which is converted by the ADC of the MCA. The stop signal passes through a variable delay element that has two functions. First, the stop can be delayed by a certain amount of time. This is necessary because, for circuit reasons, the TAC needs a few nanoseconds after being started before it can process a stop signal. (There is also the logical reason: you cannot analyze a pulse with zero height). Secondly, this is used to calibrate the time scale of the TPC. For this, one measures real coincident events with the (physical) time difference zero. According to the chosen delay, a single pulse height occurs after the TPC, which appears in the ADC as a line, the prompt curve. If one now increases the delay by a defined value, the pulse height of the TPC increases and the prompt curve in the ADC shifts. The size of the shift corresponds to the additional delay.

This calibration method is independent of transit time differences in the two branches and is therefore used when measuring very small times (a few nanoseconds). For large times (microseconds) the difference in transit times is negligible and a simpler method can be used. The inputs of the TPC are directly connected to a pulse generator, which provides pulse pairs with adjustable spacing.

A time measurement then proceeds as follows. In the start branch, an event is selected which is linked to the start of the time measurement. In the ideal case one would discriminate events in the stop branch in such a way that only signals occur which designate the end of the time to be measured and originate from the same event as the start. Unfortunately, this is not possible as the following example illustrates. Let the beginning be the lifetime of a particle characterized

by the emission of a γ quantum with energy E_1 and the end, the appearance of a second photon with energy E_2. Accordingly, the start branch is set to E_1, the stop branch to E_2. Now the TPC is started by an event with E_1, the clock runs, and one knows: the particle whose lifetime is to be measured exists. The clock is stopped by the first signal with E_2 in the stop branch. If this signal comes from the same particle that caused the start, then the lifetime was measured. If, on the other hand, it comes from a different particle, then the time between two temporally uncorrelated events has been determined. In this case, the occurrence of the stop is equally probable at any time, i.e. random. Therefore, in the measured time spectrum there are not only the desired, true, temporally correlated events, but also a time-independent, constant background of random ones. As long as the random coincidences do not get out of hand – they can be kept low by limiting the activity of the source – they can be separated during the evaluation without damage.

Chapter 6

Data analysis and error calculation

This chapter deals with the last step of an experiment, the determination of the measurement results with their uncertainties and the interpretation of the measurement results in comparison to theoretical expectations.

Based on the analysis of the recorded detector signals, models are typically fitted to the measured data and an evaluation of the fitting quality is performed. Then the determination of the uncertainties of the model parameters obtained in this process of parameter estimation is performed. The most important and final step is the interpretation as a physical result.

6.1 Importance of statistical data evaluation and existing basics

You have already been able to gain extensive experience in data analysis in the beginner's lab courses, on which you can build on for the advanced lab courses. Extensive documentation exists, e.g. the lecture "Computer Assisted Data Analysis (CgDA)" and summaries of the content [50], a script on fitting models to measured data [51], and tutorials with Jupyter notebooks containing explanations and example code in the programming language *Python* on statistics and error calculation and on fitting models to measured data [52]. In the beginner's lab courses, uncertainties were mostly assumed to be subject to a Gaussian distribution. As a procedure for fitting models to measured data, you learned about the "least squares error" method proposed by Carl Friedrich Gauss and applied it in many places. As future scientists you now need to extend this knowledge in order to be able to deal with more complex applications on the one hand, and on the other hand to meet the constantly evolving scientific standards in the documentation of results.

Physics as a "theory-guided empirical science" lives from the interaction of theoretical hypothesis formation and their stringent verification in experiments. Thus, when interpreting the measurement data you have recorded, the first question is whether they correspond to an expected model. Only if you can answer this question with "yes", the extraction of model parameters makes sense at all [1].

In order to meet these challenges, the use of your own program code, ideally in the programming language *Python* in a Jupyter notebook, is unavoidable, since most tools for statistical data analysis, often controlled through a graphical user interface, do not or only partially meet the typical requirements in physics. As additional help and preparation for the challenges in statistical data analysis, which are clearly greater in the advanced lab courses, there is a special tutorial, *advancedFitting.ipynb* [53] as a Juptyer Notebook. Another basic tutorial introduces the method of the adjustment of parameters with the Maximum-Likelihood method [54].

The important points for the determination of parameters of models are:

[1] Unfortunately, most of the frequently used tools do not take this requirement into account in the default setting, but aim at a parameterization of the data as exact as possible. If unsuitable models are specified, the parameter errors are increased to such an extent that the parameterization fits as exactly as possible

- All uncertainties of the measurement should be considered directly during model fitting and modeled accordingly to propagate them completely and correctly to the uncertainties of the parameters. The error propagation performed later by hand is laborious and works only in the simplest cases.

  The tools used must be able to handle uncertainties in the abscissa direction in addition to uncertainties in the ordinate direction. The support of correlated uncertainties is also necessary in order to be able to represent typical uncertainties of measuring instruments - i.e. independent digitization uncertainties and noise contributions as well as correlated calibration uncertainties.

- Relative uncertainties also frequently occur, e.g. in the case of calibration uncertainties which appear as a fraction of the true measured value. The correct treatment of such uncertainties with the least squares method is only an approximation. Exact parameter estimates are based on the maximum likelihood method ("MLE", Maximum Likelihood Estimation).

- In quantum, nuclear and particle physics, count rates are usually represented as a frequency distribution (histogram) as a function of energy, scattering angle or other quantities. However, the entries in an interval of a histogram (so called "bin") are not Gaussian but Poisson distributed. Even approximately, bins with zero entries cannot be taken into account with an - still often used - adapted least squares method. Thus, to fit models to histograms, again maximum-likelihood methods must be used.

- When analyzing very small count rates for infrequently occurring events, the very need to split the data into bins can lead to a loss of information and a bias in the result. In such cases, an unbinned maximum likelihood fit should be applied.

Unfortunately, there are hardly any customization tools that fulfill all of the above requirements at the same time. Therefore, an open source customization tool, *kafe* or *kafe2* [**?**] in the latest version, was developed at ETP in numerous bachelor theses, which covers the previously mentioned aspects. The package *PhyPraKit.phyFit* [56] includes a very lean Python interface for fitting with the tool *iminuit* [57] that provides advanced methods for parameter fitting and for the analysis of uncertainties.

Examples are presented in the above mentioned Jupyter tutorial that can be used as a template for your own applications. For an introduction to the functions of the meanwhile very powerful tool *kafe2* there is a separate Jupyter tutorial as well as an extensive collection of examples which are packaged together with the *kafe2* package[2].

6.2 Theoretical foundation

Unlike in previous courses, we start at this point with a top-down approach. Starting from the maximum likelihood principle, we establish the connection to well-known methods. In a concrete application we have to consider which simplifications are possible for a given problem.

The starting point is the formalism for the parameter estimation of probability densities, which are the basis of measurement results. Sometimes the parameters of the probability density are interesting themselves, e.g. for the lifetime distribution of quantum mechanical states or of (elementary) particles. Often, however, parameters of probability densities appear only as "perturbations" describing statistical fluctuations around an assumed true value. The treatment of measurement uncertainties is an example of this.

[2] kafe2 is under constant development. If you find bugs, have suggestions for improvements or enhancements, please use the official web page given in the reference and enter an "Issue".

6.2.1 Basics of the maximum likelihood method: Estimation of the parameters of a probability density function

We assume a probability density function $\mathrm{pdf}(x, \vec{p})$ that depends on a number of parameters p_j. A data set $\vec{x}$ consists of n_d independent individual measurements x_i. According to the maximum likelihood principle, the best estimate of the parameters, $\hat{\vec{p}}$, is given by the values that maximize the so-called "likelihood", the product of the values of the pdf for the individual measurements, $\mathrm{pdf}(x_i, \vec{p})$:

$$\mathcal{L}(\vec{x}, \vec{p}) = \prod_{i=1}^{n_d} \mathrm{pdf}(x_i, \vec{p}) \,. \tag{6.1}$$

To avoid unmanageably small values of the product, for numerical stability and also for mathematical reasons (see "Fisher information"), one uses the negative logarithm of $\mathcal{L}$, the "negative log-likelihood" $nl\mathcal{L}$, given by

$$nl\mathcal{L}(\vec{x}, \vec{p}) = -\sum_{i=1}^{n_d} \ln\left(\mathrm{pdf}(x_i, \vec{p})\right) \,. \tag{6.2}$$

The negative log-likelihood function is then taken as a function of the parameters and minimized with respect to the parameters. Usually it is used as a cost function in numerical optimization methods.

It can be shown that the log-likelihood method is optimal among all methods for parameter estimation, i.e. it provides the smallest variance of the parameter values. This is another reason to give preference to the likelihood method if one wants to gain maximum information from sometimes extremely expensive experiments.

6.2.2 Determination of parameter uncertainties and interval estimation

Besides the best values of all parameters, their uncertainties are also significant. The variance of the parameters, or better the covariance matrix of the uncertainties of all parameters, can be determined from the course of the log-likelihood at the minimum. Clearly, the "sharper" the minimum, the more precisely a parameter is determined. This can be quantified via the second derivatives of the log-likelihood according to the parameters:

$${V_{ij}}^{-1} = \left.\frac{\partial^2 \ln \mathcal{L}()}{\partial p_i \, \partial dp_j}\right|_{\hat{p}_i \hat{p}_j} \,. \tag{6.3}$$

Correlations between parameters are very common, even with uncorrelated measured values. If correlations are particularly large, this indicates an improper parameterization of the problem. Correlations larger than 10 % should be communicated as part of the result, because the shape of the parameter ranges still allowed within a given confidence level depends on it.

In non-linear problems, which already occur when uncertainties in the abscissa direction or model-related relative uncertainties are taken into account, the course of the log-likelihood is not parabolic at the minimum. In such cases, the specification of a symmetric interval for the uncertainties is not correct. To assess possible problems, a graphical representation of the course of the likelihood at the minimum should be considered in every case.

The profile likelihood is a suitable quantity for this purpose. In this procedure, a number of points near the minimum are considered for each parameter and the log-likelihood is minimized with respect to all other parameters - in this way, correlations with other parameters are taken into account. The confidence interval, which corresponds to the range of plus-minus one standard deviation of a Gaussian distribution around the parameter value, i.e. a confidence level of 68.3 %,

is obtained at the points where the log-likelihood is larger than at the minimum by the value $\frac{1}{2}$. For non-parabolic distributions, the analysis of the profile likelihood yields an asymmetric confidence interval around the parameter value at the minimum, which in such cases should be given in place of the standard deviations of the parameters determined from the second derivatives.

The profile likelihood procedure can also be performed in two dimensions, i.e. for pairs of parameters. One then obtains contour lines which correspond to confidence intervals analogous to one- or also two-sigma contours of Gaussian distributions. In case of strong deviation of the contours from the elliptical shape, they should be reported together with the result, because the allowed parameter range depends on it.

Profile likelihood curves and confidence contours can be easily generated with the above mentioned packages *kafe2* or *phyFit*, if desired.

An example is shown in Fig. 6.1 and 6.2. It is taken from the Jupyter tutorial *advancedFitting.ipynb* (Example 4.2). The data are lifetimes of stopped cosmic muons detected in a water Cherenkov detector (in this case a coffee pot with photomultiplier). As the muons pass through the water, they produce a light signal; when they are stopped in the water or in the soil below, electrons from the decaying muons can re-enter the detector and be detected. The data correspond to the time differences (in μs) of such double pulses. Randomly arriving muons and detector background produce random double pulses, but in contrast to the lifetimes, they are flatly distributed.

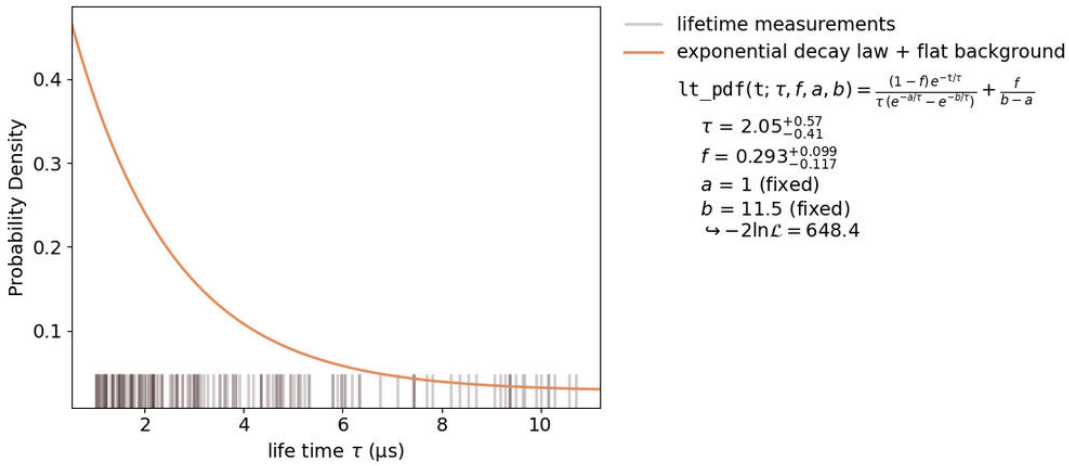

Figure 6.1: Result of fitting an exponential function with flat background for the measurement of the muon lifetime, generated with the program package *kafe2*.

6.2.3 Fitting probability densities to histograms

Another typical example for the application of the log-likelihood method is the treatment of problems involving Poisson distributed quantities. These are e.g. the numbers of entries in individual intervals of frequency distributions (histograms).

The Poisson distribution of numbers n_i with the expected values μ_i is given by

$$P(n_i;\mu_i) = \frac{{\mu_i}^{n_i}}{n_i\,!}\,\mathrm{e}^{-\mu_i}\,. \tag{6.4}$$

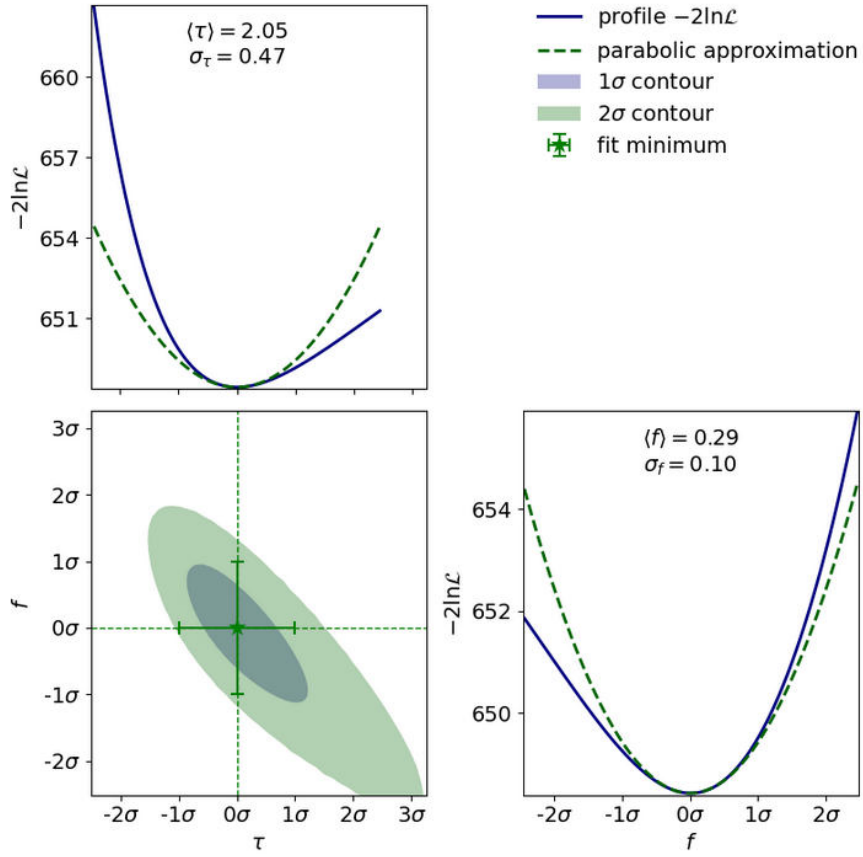

Figure 6.2: Profile likelihood and confidence contours of the fit from Fig. **??**.

By forming the product over all bins (assumed to be statistically independent) of a histogram, we obtain the likelihood

$$\mathcal{L}_{Poisson} = \prod_{i=1}^{N} \mathrm{P}\left(n_i; \mu_i(\vec{p})\right) \,, \tag{6.5}$$

and finally by taking the logarithm we obtain the log-likelihood of the Poisson-distributed numbers of entries in the bins of a histogram

$$nl\mathcal{L}_{Poisson} = -\ln \mathcal{L}_{Poisson} = \sum_{i=1}^{N} -n_i \cdot \ln(\mu_i(\vec{p})) \, + \, \mu_i(\vec{p}) \,. \tag{6.6}$$

Using this cost function in the minimization process, adjustments of probability densities to histograms can thus be performed quite analogously to the use of the above mentioned likelihood function for measurement data. Only this time, the data are available as histograms. The computational expense in this example depends on the number of bins and not - as in the first example - on the size of the data set.

6.2.4 Maximum Likelihood and Least Squares Method

The least squares method for fitting models is a special case of the maximum likelihood method.

Let us first derive a method based on the log-likelihood fitting of model functions on measurement data. We denote the random deviation of a measured value from the true value with the letter z, which is described by a probability density f_z. In the case of measurement uncertainties,

f_z is often the normal distribution $\mathcal{N}(z;\sigma)$ with an expectation value of zero and the standard deviation σ. In the multidimensional case for n_d, not necessarily independent, data points, the multivariate Gaussian distribution $\mathcal{N}(\vec{z};V)$ with the covariance matrix V is relevant,

$$\mathcal{N}\left(\vec{z},V)\right) = \frac{1}{\sqrt{(2\pi)^{n_d}\det(V)}} \cdot \exp\left(-\frac{1}{2}\vec{z}^T V^{-1}\vec{z}\right) . \tag{6.7}$$

The random variable z corresponds to the fluctuations around the true value; if there is an exact theoretical expectation for this in the form of a parameter-based model $f_i(\vec{p})$ with a set of parameters $\vec{p}$, a measured value y_i can be written as

$$y_i = f_i(\vec{p}) + z_i \, . \tag{6.8}$$

Usually, to test parameter-based models described by functions, several measurements are taken at different sampling points x_i, thus considering a model function $f(\vec{x};\vec{p})$. The probability density, which describes all measurements, looks like this:

$$\mathcal{N}\left(\vec{y},V,f(\vec{x},\vec{p})\right) = \frac{1}{\sqrt{(2\pi)^{n_d}\det(V)}} \cdot exp\left(-\frac{1}{2}(\vec{y}-\vec{f})^T V^{-1}(\vec{y}-\vec{f})\right) . \tag{6.9}$$

According to the maximum likelihood principle, the best parameter set is given by the point $\hat{\vec{p}}$ in the parameter space for which the likelihood is maximum. As above, the negative natural logarithm of the likelihood is used, $nl\mathcal{L}_{\text{Gauss}}$, which is then minimized.

$$-2\,\ln\mathcal{L}_{\text{Gauss}}\left(\vec{y},V,\vec{f}(\vec{x},\vec{p})\right) \;=\; \left(\vec{y}-\vec{f}(\vec{x};\vec{p})\right)^T V^{-1}\left(\vec{y}-\vec{f}(\vec{x};\vec{p})\right) + \ln(\det(V)) + n_d\,\ln(2\pi)\,. \tag{6.10}$$

Under very special conditions, the minimization of the log-likelihood and the quadratic sum of the residuals, S, are equivalent. However, this simple case is no longer valid when model-related uncertainties are involved, or when there are uncertainties in the abscissa direction that are transformed to an uncertainty of the ordinate with the help of a first-order Taylor expansion. In this case they depend from the derivative of the model with respect to x and therefore also on the parameter values. The practical rule is to always use the likelihood as far as possible, and to resort to the least squares method only in well-founded, justified cases. However, one is severely limited in the choice of the numerical tools available, when implementing this recommendation.

If problems with **non-Gaussian distributions** are treated, the use of log-likelihood methods is inevitable. Today, the construction of appropriate likelihood functions for the treatment of special problems belongs to the standard methods in the scientific practice. Thanks to very powerful algorithms for numerical minimization in high-dimensional parameter spaces and also thanks to modern computer technology, the use of correct likelihood methods is no longer an insurmountable problem.

6.3 Practical information

In practice, the methods described above are only feasible in combination with numerical methods for minimizing scalar functions in multi- or even high-dimensional spaces and program code for managing the data and their uncertainties. Although analytical solutions also exist in rare cases, in practice one almost exclusively uses program packages for parameter fitting. Analytical (partial) solutions only have to be used when time-critical problems are involved.

6.3.1 Construction of the Covariance Matrix

The covariance matrix of the data fully represents the uncertainties of the input data. If it is taken into account during the fitting, all uncertainties independent and correlated between the data are propagated into the final result - a classical error calculation by hand is then no longer necessary.

Let us first briefly summarize the main properties of the covariance matrix $\mathbf{V}$:

- $\mathbf{V} = (\mathrm{V}_{ij})$ is a symmetric matrix;
- it has dimension n_d corresponding to the number of measured values;
- for independent measured values the matrix is diagonal;
- the off-diagonal elements V_{ij}, $i \neq j$ can be understood as the product of the joint uncertainties σ_i^g and σ_j^g of measurements i and j;
- the covariance matrix elements for independent uncertainties are added.

Especially the last point is of crucial importance, because it allows to build up the complete covariance matrix successively from individual contributions to the uncertainty, with the construction rule:

- Uncertainties of measured values are broken down by different independent sources.
- Independent uncertainties of each individual measurement are added up quadratically in the diagonal elements.
- Absolute or relative uncertainties common to all measured values or groups of measurements are added up quadratically in the relevant diagonal and off-diagonal elements V_{ii}, V_{ji} and V_{ij}.

Uncertainties in the abscissa direction, given by a covariance matrix $\mathbf{V}^x$, can be taken into account by using the model prediction $f(\vec{x}, \vec{p})$ transformed by first-order Taylor expansion in the y-direction and then added to the covariance matrix of the data points in the y-direction, $\mathbf{V}^y$:

$$V_{ij} = (V^y)_{ij} + \frac{\partial f}{\partial x_i}\frac{\partial f}{\partial x_j}(V^x)_{ij} \tag{6.11}$$

In total, this results in eight types of uncertainties, namely independent and / or correlated absolute and / or relative uncertainties in the x- and / or y-direction.

For the construction of the covariance matrix one uses ideally programmed code. Very few common fitting programs provide options for this directly. Normally, the full covariance matrix must be provided as a parameter. The package *kafe2* contains the method

```
add_error(err_val, axis=?, correlation=?, relative=?, reference=?)
```

which can be used to add individual components of uncertainty. The interfaces to various fitting programs in the *PhyPraKit* package also accept the specification of individual components of the uncertainty as parameters, if the corresponding fitting packages support this. All eight types of uncertainties can be handled directly only with *kafe2* and *PhyPraKit.phyFit*.

6.3.2 Consideration of external and constrained parameters

Often, model functions depend on external parameters that are subject to uncertainties, e.g. determined in an auxiliary measurement or taken from the literature. These can be the results from calibration measurements, or from natural or apparatus constants. Instead of propagating

the effects of the parameter uncertainties to the final result by means of a manual error calculation, they can also be taken into account directly in the fit as constrained parameters. For this purpose, such parameters are introduced simultaneously as free parameters in the fit and as measured variables - i.e. a corresponding term is added to the log-likelihood. For this purpose, the *kafe2* package contains the method

`add_parameter_constraint(name, value, uncertainty, relative=False)`.

There is also the method

`fix_parameter(name, value=None)` with the help of which parameters can be fixed to a constant values. With this the influence of external parameters can also be investigated by fixing them successively to their expected value and the respective upper and lower limits of their confidence range, observing the changes in the fitting result. Temporarily fixing and releasing parameters again, using the method

`release_parameter(name)`

can also be helpful when a complex fit does not converge to the global minimum. In this case, one can fix one or more parameters near the expected value and perform a minimization with respect to the remaining parameters. After releasing the fixed parameters at this temporary minimum, the fit should converge to the appropriate minimum.

A problem during the fitting process is sometimes posed by parameters that temporarily assume values in mathematically undefined region or in non-physical ranges (negative values in square roots, negative masses, etc.). The method

`limit_parameter(name, lower=None, upper=None)`

can be used to exclude such parameter ranges.

In non-linear problems, often further secondary minima exist in addition to the global minimum - or even several or many equivalent solutions. In such cases initial values for the parameters are needed close to a "'reasonable"' solution. *kafe2* provides the function

`set_parameter_values(name1=val1, ...)`

for this purpose.

Since in the course of better understanding some simple problems become nonlinear problems later on, it is a good practice to always define initial values as a matter of principle. If no initial values are given by the user, *kafe2* uses the default values of the parameters in the model function; so these should also be set - with care - when defining the model.

6.3.3 Determining exclusion limits and significance levels

Another application of the profile likelihood is to determine the significance of a parameter that differs only slightly from zero or to determine an upper limit for a parameter value at a given significance level. In this case, it is not the central area of the profile likelihood near the minimum that is of interest, but rather the border.

A common example is the search for a signal peak above a background or the existence of an additional signal feature such as a weak periodic modulation of a smooth curve. To do this, one selects a parameterization of the model function in which an additional parameter s defines the size of the signal sought. For $s = 0$ the model then changes to one where there is no signal. Ultimately, this question is a hypothesis test in which the value of s distinguishes between the null hypothesis and the alternative. In the case of smaller signals, the question can be clarified as to whether they are "significant" at all or whether they could merely result from a fluctuation of the null hypothesis.

A frequently used measure of the significance S of a signal strength s is the distance of the signal parameter from zero normalized to its uncertainty σ_s - this corresponds to the statement: "We have observed a signal with a significance of z sigma". The bigger this distance, the more improbable is a statistical fluctuation of the background as a cause for a non-zero value of s,

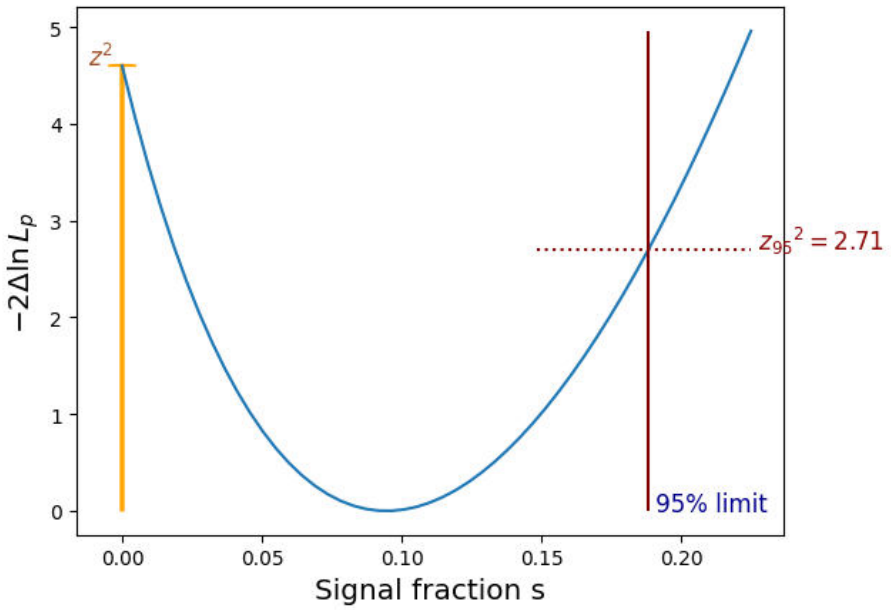

Figure 6.3: Evaluation of the profile likelihood for the calculation of exclusion limits and the significance.

misinterpreted as a signal. However, if the course of the negative logarithm of the likelihood at the minimum deviates greatly from the parabolic form, this is no longer a good measure.

In mathematical stochastics, there is a clear statement about the optimal test statistic to be used in the form of the "Neyman-Pearson lemma", if no other parameters than s play a role (so-called "simple hypothesis test"). In this case the ratio $Q = \frac{\mathcal{L}(s=s)}{\mathcal{L}(s)}$ of the likelihood functions or, equivalently, the negative difference of the logarithms of the likelihood, $-\ln Q$, is the optimal test statistic. If further parameters are present, the profile likelihood $\mathcal{L}_p(s)$ with respect to s is used. Because of the relationship between χ^2 and likelihood, in practice one often chooses $-2\ln Q = -2(\ln \mathcal{L}_p(0) - \ln \mathcal{L}_{\surd}(\hat{f}))$ as a measure of the difference between the null and alternative hypotheses, where $\hat{s}$ represents the optimal value of s found in the fit at the minimum.

The square root of $-2\ln Q$ represents the so-called z value, which we introduced above and which expresses the equivalent number of standard deviations of a Gaussian distribution by which the expected value deviates from zero. It is

$$z^2 = -2\ln Q = (-2\ln \mathcal{L}_p(s=0)) - (-2\ln \mathcal{L}_p(s=\hat{s})) \tag{6.12}$$

$S = z$ is then the significance in "Number of σs", as we expressed it somewhat imprecisely above. The term $-2\ln \mathcal{L}_p$ is the cost function commonly used in fitting programs and in some simple cases corresponds to the χ^2 value.

It is better and more generally understandable if, instead of the z value, one gives the corresponding p value, which can be obtained by calculating the corresponding value of the cumulative distribution density of the standard normal distribution, $\mathcal{N}(x) = 1/\sqrt{2\pi} \cdot \exp(-x^2/2)$: p_s = *scipy.stats.norm.cdf*(z). Usually one chooses the p value with respect to the null hypothesis, $p_0 = 1 - p_s$, which quantifies the agreement of the observation with the null hypothesis. The smaller the value of p_0, the worse the null hypothesis fits and the more secure is the existence of the observed deviation, referred to as a signal.

If the signal is not sufficiently significant, one should specify an upper limit for the magnitude of the signal. An exclusion limit with a confidence level of $cl = 95\,\%$ is commonly used here. Translated into a change in the profile likelihood relative to its value at the optimum, this limit

is again determined by using the corresponding quantile of the standard normal distribution, which can be calculated via the function z_{cl} = *scipy.statsnorm.ppf(cl)* (ppf = percent point function, the inverse of the cumulative distribution function cdf). The corresponding change in the logarithm of the profile likelihood is z_{cl}^2, which is 2.71 for $cl = 95\,\%$.

Figure 6.3 shows graphically these relationships described above. In the example shown, the signal component s has a significance of $z = \sqrt{4.58} = 2.14$, which corresponds to a p value of 0.016. The signal is less than 0.19 at the 95 % confidence level.

Chapter 7

The Experiments

The description of the experiments in the following chapters is not complete. It assumes that the previous chapters, describing some basic principles, have been worked through. Some tables and graphs (for instance the decay schemes of radioactive isotopes used in the experiments) are located in the appendix and are required for the preparation and analysis of some experiments. The complete experiment is divided into three parts:

Preparation: Before the experiment, the necessary theoretical foundations for the understanding of the experiment and required measuring procedures must be elaborated. The written preparation is part of the protocol.

Measurement: A measurement log will be written during the experiment in the lab. It contains the actual measurement data (can be a computer file), a sketch of the experimental setup and brief description of the experimental procedure, including the set parameters of the measuring apparatus. The measurement protocol can be either written by hand or directly into a text file on the Laptop.

Analysis: The evaluation of the measured data includes data analysis and the calculation of errors. All procedures are described with the relevant formulas, so that intermediate results and final results can be traced using the data in the measurement protocol and the description. The results and associated errors are discussed.

Before each experiment, a discussion of the supervisor with the group takes place. The aim is to determine whether the group is sufficiently prepared and has the necessary understanding of the basic principles for carrying out the experiment.

The protocol should be structured as follows:

1. topsheet with name of the experiment, names of the students, group number, and date
2. objective of the experiment, short theoretical foundations
3. description of the experimental setup
4. experimental procedure
5. Evaluation with formulas, error analysis, discussion of results
6. original measurement protocol

Not required are detailed derivations of formulae and excerpts from literature. However, if text segments or pictures have been taken from textbooks, journals or the internet, they must be sufficiently indicated and the source has to be cited. Also example protocols, which were used as a template of the protocol must be cited.

7.1 Experiment (B): Drift velocity of electrons in gases

7.1.1 Tasks

1. Measurement of drift velocities of three different argon-methane mixtures (including argon-methane 90:10).

2. Confirmation of the E/p dependence of the drift velocity at three different pressures with pure methane.

3. Comparison of the results with the theoretically calculated values.

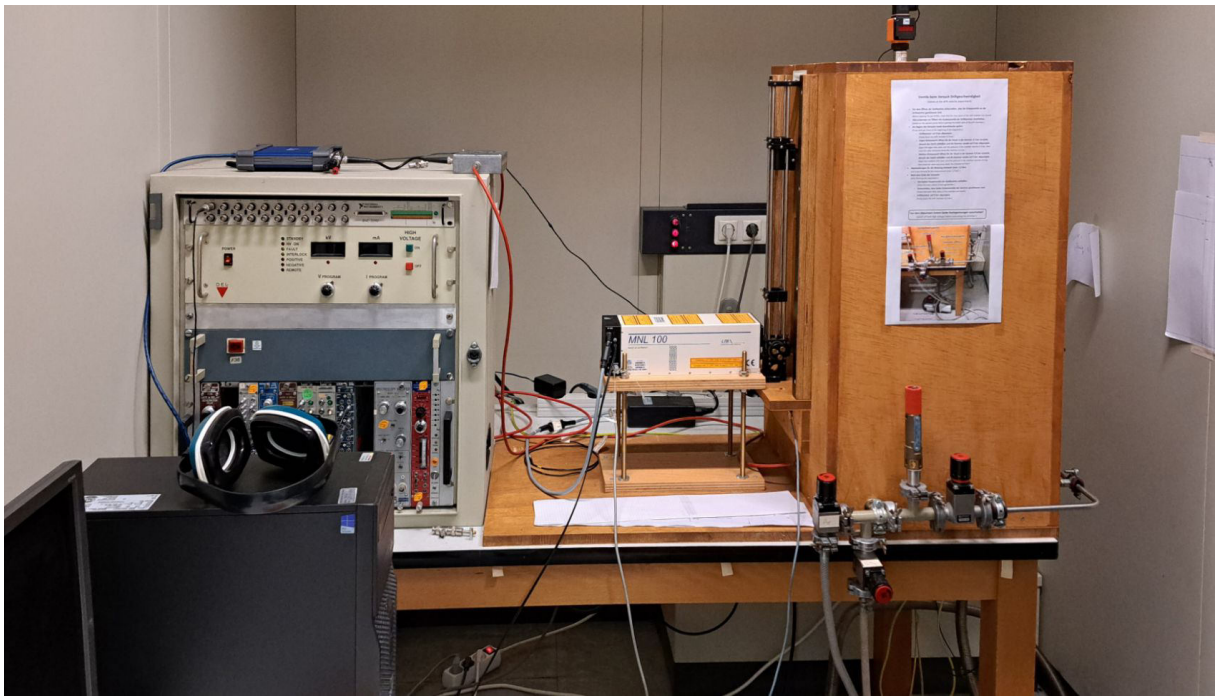

Figure 7.1: Setup of the drift velocity experiment.

7.1.2 Introduction

In this experiment, the transport processes of electrons in gases will be investigated in more detail. The transport of electrons in a gas under the influence of an electric field is a superimposed process of non-directional diffusion motion and directional motion along the field lines. In a homogeneous electric field, a constant drift velocity is obtained whose value depends strongly on the gas composition. The dependence of the drift velocity on various parameters such as pressure, field strength and quenching gas fraction will be investigated in more detail.

7.1.2.1 Diffusion

Electrons in a gas of temperature T, which have been produced, for example, by the passage of a charged particle through the gas or ionization by a high-energy laser beam, rapidly lose part of their energy by collision processes with the surrounding gas molecules until they are thermalized. The energy of the electrons in this case can be described by a Maxwell-Boltzmann distribution function $F(\varepsilon)$:

$$F(\varepsilon) \cdot \mathrm{d}\varepsilon = C \cdot \sqrt{\varepsilon} \cdot \mathrm{e}^{-\varepsilon/kT} \cdot \mathrm{d}\varepsilon \tag{7.1}$$

This results in an average kinetic energy ('thermal energy') of

$$\langle \varepsilon \rangle = \int_0^\infty \varepsilon \cdot F(\varepsilon) \cdot \mathrm{d}\varepsilon \tag{7.2}$$

which, according to the equipartition theorem, corresponds to an energy of $(3/2)\,kT$. At room temperature, this would be about 40 meV.

Due to this non-directional motion, the "Brownian molecular motion", a charge distribution now diffuses into the surrounding space, while its center of charge is preserved.

The number density N of the charge carriers is described by a deliquescent Gaussian distribution, which in one-dimensional representation at time t is of the following shape:

$$\frac{\mathrm{d}N}{\mathrm{d}x} = \frac{N_0}{\sqrt{4\,\pi \cdot D \cdot t}} \cdot \mathrm{e}^{-x^2/4\,D\,t} \tag{7.3}$$

N_0 denotes the total number of charge carriers, x the distance from the origin and D the so-called *diffusion coefficient*. This is related to the mean free path length λ and the mean thermal particle velocity $\bar{v} = \sqrt{8\,kT/\pi\,m}$ via

$$D = \frac{1}{3} \cdot \lambda \cdot \bar{v} \tag{7.4}$$

The mean free path can be interpreted as the radius of a sphere on whose surface the particles collide with a gas molecule for the first time after their generation. For electrons, the mean free path is about four times as larger than for ions. It also depends on the scattering cross section $\sigma(\varepsilon)$ of the particles in question, which is generally energy-dependent, and the number density N_g of the gas molecules in the volume in question:

$$\lambda(\varepsilon) = \frac{1}{N_g \cdot \sigma(\varepsilon)}, \qquad N_g = \frac{N_L \cdot \rho}{A} \tag{7.5}$$

Here N_L stands for the Loschmidt constant, A for the molar mass and ρ for the density of the gas in question. For noble gases at normal conditions, $N_g = 2{,}69 \cdot 10^{19}\,\mathrm{molecules/cm^3}$.

7.1.2.2 Ramsauer-Townsend effect

The scattering cross section for collisions between electrons and noble gas atoms is far below the classically expected gas kinetic value, depending on the electron energy. This is due to the fact that at certain electron energies the wavelength of the electrons is in the range of the dimensions of the atomic potential, and the atoms thus become practically "transparent" for the colliding electrons, based on a quantum mechanical interference effect. The scattering cross section consequently decreases by up to two orders of magnitude. The effect is called *Ramsauer effect* after its discoverer, who demonstrated this for the first time in 1921 by scattering slow electrons from noble gas atoms. Fig. 7.2 shows the course of the elastic scattering cross section of electrons for the three noble gases helium, argon and xenon as a function of their kinetic energy. As can be seen, helium has no Ramsauer minimum in the energy range shown, while the two minima for argon and xenon are clearly visible.

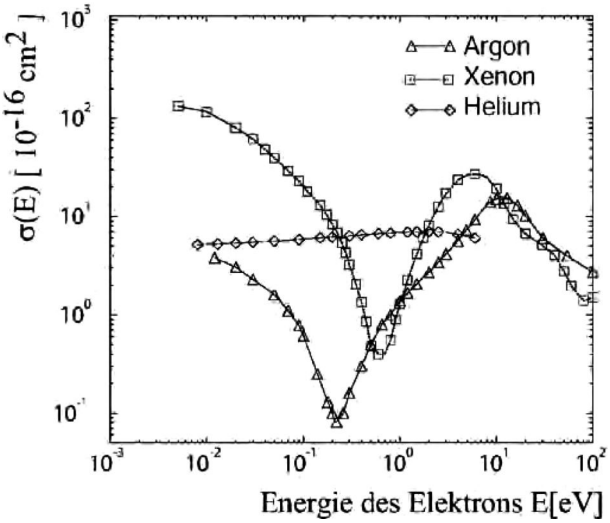

Figure 7.2: Dependence of the elastic scattering cross section on the kinetic energy of the electrons for the three noble gases helium, argon and xenon.

7.1.2.3 Drift and mobility

Under the influence of electric fields, a superposition of disordered diffusion motion and ordered motion in the direction of the applied field (or opposite, depending on the sign of the charge) results. The following considerations all refer to electrons, but can easily be applied to ions as well.

In a simple model and without the presence of an external magnetic field, the number of collisions $\mathrm{d}n$ that an electron experiences while travelling the distance $\mathrm{d}x$ can be described by

$$\mathrm{d}n = \frac{1}{\bar{v}_\mathrm{D} \cdot \tau} \cdot \mathrm{d}x \tag{7.6}$$

where $\bar{v}_\mathrm{D}$ denotes the mean drift velocity and τ the mean time between two collisions. The so-called collision rate $1/\tau$ is related to the particle number density N_g, the scattering cross section σ and the instantaneous electron velocity ω via the following relation:

$$\frac{1}{\tau} = N_g \cdot \sigma \cdot \omega \tag{7.7}$$

The differential probability $\mathrm{d}P$ that an electron will suffer its next collision in the time interval between t and $t + \mathrm{d}t$ is defined as

$$\mathrm{d}P = \frac{1}{\tau} \cdot \mathrm{e}^{-t/\tau} \cdot \mathrm{d}t \tag{7.8}$$

The electron is now moves between two collisions according to the equation of motion

$$m \cdot \frac{\mathrm{d}v}{\mathrm{d}t} = e \cdot E \tag{7.9}$$

accelerated by the electric field E. Thus, the mean distance traveled is obtained by averaging $x(t)$ over time and using the collision probability (Eqn. 7.8) to give

$$\langle x \rangle = \frac{e}{2\,m} \cdot E \cdot \int_0^\infty \frac{t^2}{\tau} \cdot \mathrm{e}^{-t/\tau} \cdot \mathrm{d}t = \frac{e}{m} \cdot E \cdot \tau^2 \tag{7.10}$$

The averaged drift velocity is then

$$\bar{v}_{\mathrm{D}} = \frac{\langle x \rangle}{\tau} = \frac{e}{m} \cdot E \cdot \tau = \mu \cdot E \tag{7.11}$$

where μ stands for the mobility of the electrons. Because τ is inversely proportional to the density of the gas, it follows for the drift velocity:

$$\bar{v}_{\mathrm{D}} \propto \frac{E}{N_g} \qquad \text{bzw.} \qquad \bar{v}_{\mathrm{D}} \propto \frac{E}{p} \qquad \text{für} \quad T = \text{konst.} \tag{7.12}$$

with the pressure p. Therefore, the drift velocity is often plotted against the so-called "reduced electric field" E/p (unit: $\mathrm{V\,cm^{-1}\,hPa^{-1}}$) or also against E/N_g (unit: 1 Td (Townsend) $= 10^{-17}\,\mathrm{V\,cm^2}$), since it scales with these quantities. The total energy ε of an electron, which depends on the instantaneous electron velocity ω, is composed of its thermal energy and the energy gain ε_{E} in the electric field:

$$\varepsilon = \frac{1}{2} \cdot m \cdot \omega^2 = \varepsilon_{\mathrm{E}} + \frac{3}{2} \cdot k\,T \tag{7.13}$$

If there is a balance between the energy loss of the electrons by collisions with the gas atoms and their energy gained in the electric field, it results in a constant drift velocity if the field strength and pressure are constant.

7.1.2.4 Counting gases and quencher

The chemical composition of a gas determines its usability as a counting gas. Commonly used mixtures consist of a mono-atomic noble gas and an addition of a polyatomic organic gas from the hydrocarbon group such as CH_4, C_3H_8, C_4H_{10} (isobutane) or also C_2H_6. The noble gas component is predominantly responsible for the charge multiplication, whereas the organic component absorbs photons from the gas amplification process due to its non-radiative rotational and vibrational levels present over a wide energy range, which could otherwise lead to secondary emission of electrons and thus to permanent gas discharge. This poly-atomic component of the gas mixture is therefore also called quenching gas or quencher. The organic additive should be as non-polar as possible so that no electrons are lost through trapping processes. Even a small proportion of such a gas decisively changes the behavior of the detector. A counting tube operated with pure argon, for example, allows a gas amplification of only 10^3 to 10^4 before permanent discharge occurs. If, however, an approximately ten percent share of methane is added, amplification factors of 10^6 and above can be achieved.

7.1.2.5 Influence of the quenching gas content on the drift velocity

However, the addition of a quenching gas also affects the drift velocity of the electrons, which can be considerably increased as a result. Fig. 7.3(right) shows, for example, the drift velocities of various argon-methane mixtures. As can be seen, pure argon has a very low drift velocity over the whole depicted range of the reduced field. This is due to the fact that for argon already at values of $E/p > 0.2\,\mathrm{V\,cm^{-1}\,Torr^{-1}}$ the average electron energies are above 2 eV (Fig. 7.3, Left) and thus the effective cross sections, when compared to value in Fig. 7.2, are not in the Ramsauer minimum of the noble gas. Therefore, the electrons interact with the argon atoms in a purely elastic collisions, thus retaining their high energy, which in turn results in the low drift velocity. The pattern of the drift velocity changes dramatically with the addition of a molecular gas, such as CH_4, $C0_2$, CF_4, or N_2, which reduce the average electron energies compared to argon over a larger range of the field strength. The electrons collide inelastically with the gas molecules, losing a large fraction of their kinetic energy. This is converted by the molecules into rotational and vibrational energy. As a result, the average electron energy is reduced to such an extent

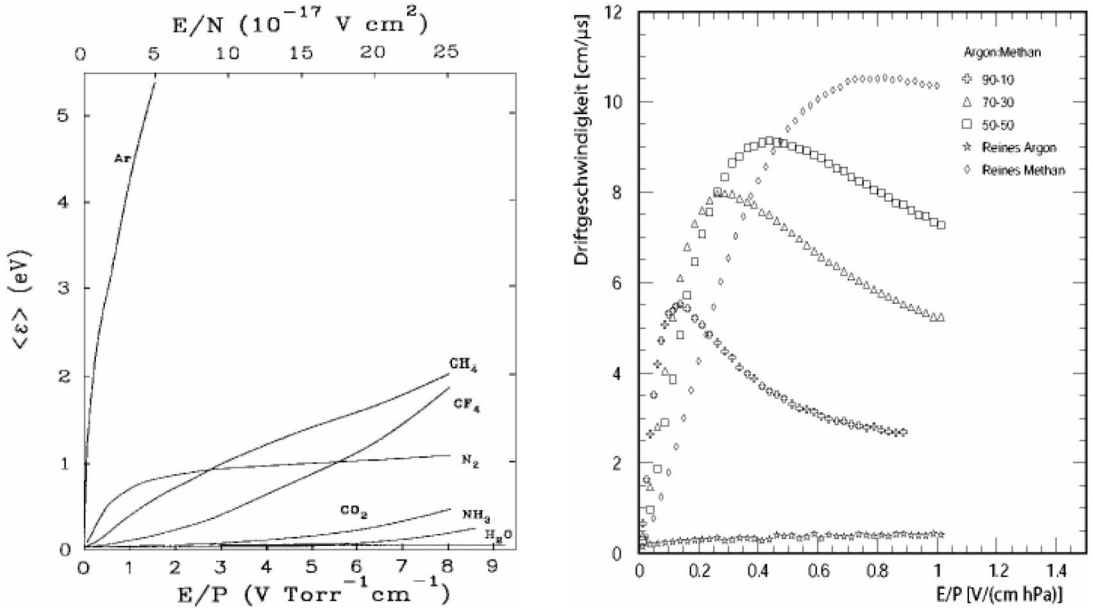

Figure 7.3: Left: Mean electron energy of some gases as a function of the reduced field. Right: Change of the drift velocity in an argon-methane mixture with increasing methane content.

that it reaches the region of the Ramsauer minimum of the respective noble gas. Due to the much smaller scattering cross section at these electron energies, this results in a much higher drift velocity. The absolute value of the drift velocity also depends on the strength of the electric field by which the electrons are accelerated. The higher the electric field strength, the higher the kinetic energy of the electrons. At a low field strengths of about 0.4 kV/cm, the average electron energy is located in the region of the Ramsauer minimum of argon, resulting in a maximum drift velocity. With increasing field strength, the energy distribution of the drifting electrons shifts toward higher energies, which correspond to a higher inelastic cross section of argon. For this reason, the drift velocity decreases despite the stronger electric field, accelerating the electrons.

Argon is also called a "hot gas" because here the associated electron energy is dominated by the electric field ($\varepsilon \approx \varepsilon_{\mathrm{E}} \gg 3/2 \cdot kT$), while e.g. CO_2 is a "cold gas" ($\varepsilon \approx 3/2 \cdot kT$).

7.1.3 Principle of the measurements

In this experiment, the drift velocity of the electrons is measured by measuring the difference in the drift times of two charge clouds generated at different locations in a drift chamber. The free charge carriers are generated by ionization of the gas in the drift chamber, using a pulsed nitrogen UV laser (λ = 337,1 nm, pulse duration = 500 ps). However, the quantum energy of the laser is much lower than the ionization energies of typical counting gas atoms or molecules, which are around 20-30 eV. Various investigations have shown that it is primarily impurities in the gas mixture that are ionized, which originate from outgassing of the chamber materials or admixtures in the counting gases themselves. Especially with the commonly used organic quenchers such as methane, ethane or isobutane, impurities with different hydrocarbons are often unavoidable. Some of these admixtures have ionization energies in the range of 7 eV, which means that they can be ionized via so-called two-photon processes. In this process, the molecule is excited by one photon and ionized by a second photon, which must strike the molecule within the lifetime of the excited state. In order to guide the laser beam into the chamber, it is split into two approximately equally intense beams by means of a beam splitter cube. The beams are focused directly into the center of the drift chamber through two UV lenses with a focal

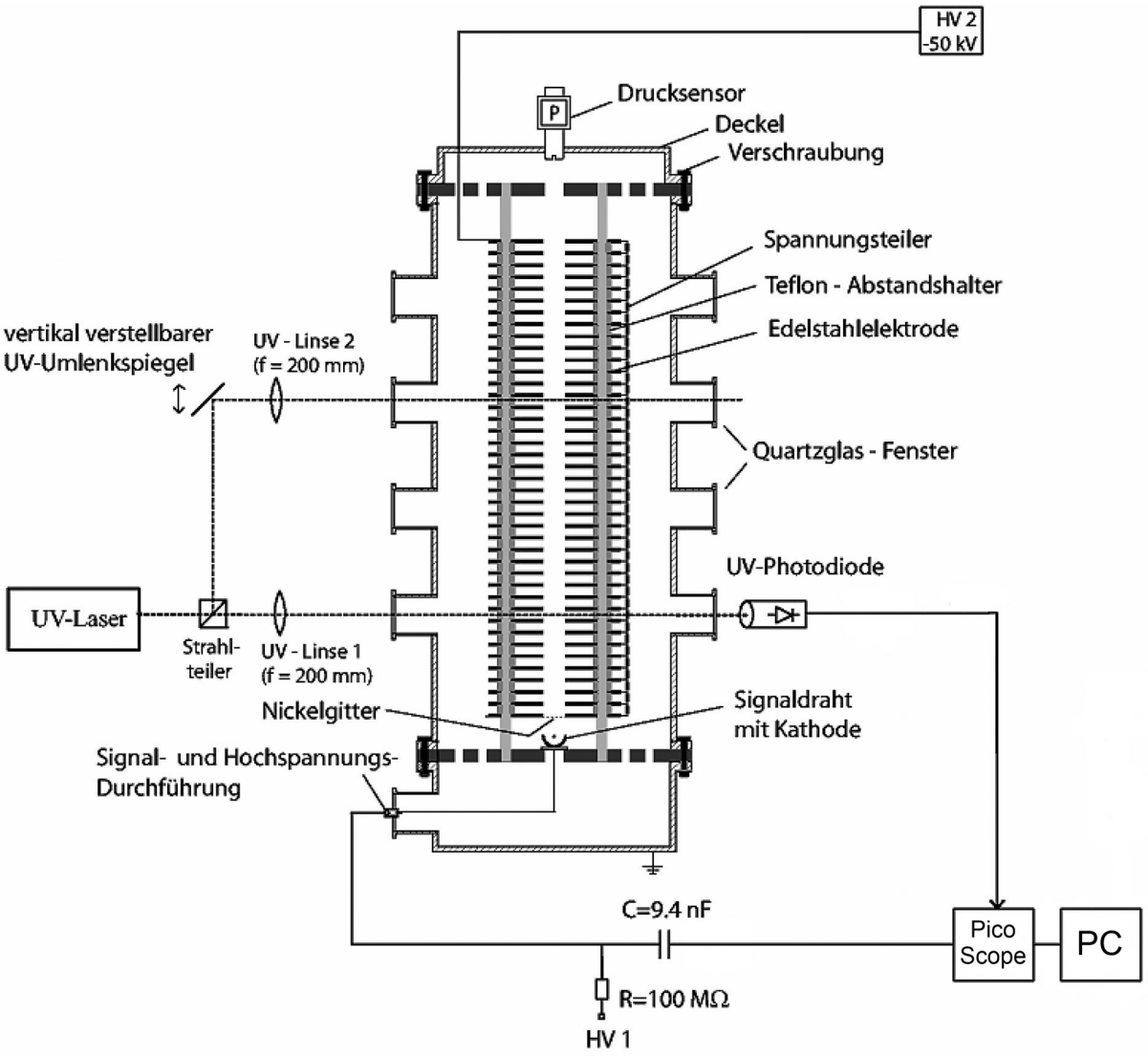

Figure 7.4: Schematic of the experimental set-up.

length of 200 mm, one directly, the other one after deflection with a UV mirror. A UV-sensitive photodiode is attached to the lowest exit window of the chamber, which is used to trigger the data acquisition. The drift field is generated by a total of 40 stainless steel electrodes with a diameter of 120 mm and a thickness of 3 mm. These have a hole in their center with a diameter of 25 mm, through which the electrons drift to a proportional chamber at the end of the drift path and are detected there. The electrodes are insulated from each other by Teflon rings, which also ensure a constant spacing of the plate pairs of 10 ± 0.1 mm. The wire for high voltage is soldered to the top electrode, while the bottom electrode is grounded. The electrodes are connected by a precision voltage divider to achieve a homogeneous drift field. The high voltage is provided by a power supply from *Del Electronics*, which can generate a maximum output voltage of 50 kV. The drift velocity of the electrons at a fixed field strength can be assumed to be constant due to the homogeneous field. It can therefore be determined directly as the quotient of the distance Δx of the two partial laser beams, i.e. the effective drift distance, and the time difference Δt of the two charge clouds arriving at the anode wire:

$$\bar{v}_{\mathrm{D}} = \frac{\Delta x}{\Delta t} \tag{7.14}$$

The pulses from the two electron clouds are decoupled from the high-voltage supply of the signal wire outside the chamber via an RC element. In the original version of the experiment, they then passed through a spectroscopy amplifier for pulse shaping and amplification, and then through a discriminator to generate logic pulses for the logic unit that followed. These served to reduce unavoidable false triggers. After both pulses passed the logic unit, the first pulse started a time-to-amplitude converter (TAC), and the second one stopped it. The TAC then provided an analog square wave signal at its output whose amplitude was proportional to the time interval between the start and stop pulses. The amplitude was then read and digitized by an analog-to-digital converter (ADC) in a PC and converted to a time difference. The readout software averaged over 100 laser pulses and calculated the mean drift time and the standard deviation of the mean. The electronics with the necessary module frame and power supply (NIM-Crate) weighed 20 – 30 kg and cost a five-digit amount.

Today, data acquisition is performed by a USB oscilloscope (Picoscope 3404D), which digitizes the pulses from the counting wire of the proportional chamber and transfers them to the analysis PC (Linux). The pulse shape is analyzed by a Python program on the PC in parallel with the running measurement and the time difference of the two signals is determined. The software is explained to you on site by the tutor of the experiment. From a large number of laser pulses, the mean value and the standard deviation from the mean value are again determined. In contrast to the original electronics, the USB oscilloscope weighs only a few hundred grams, costs a fraction of the NIM electronics and consumes hardly any power compared to a 2 kW NIM crate.

7.1.4 Performing the experiment

The experiment includes the measuring of drift velocities of at least three different argon-methane mixtures, as well as pure methane and in addition the confirmation of the E/P dependence of the drift velocity by measuring a mixture at different pressures. The mixture Ar-CH4 90-10 (10 vol% methane) should be measured in any case, the other two mixtures are freely selectable in 10% methane fraction steps. The various mixtures are produced directly in the drift chamber. Two gas cylinders with the pure gases methane and argon are available for this purpose. Assuming that these behave like ideal gases, the ideal gas equation ($pV = nRT$) can be used to determine the partial pressures of the two components to produce a specific mixing ratio. Calculate the partial pressures for your chosen mixing ratios. However, an absolute pressure in the chamber of 1500 hPa should not be exceeded.

Before the first gas mixture is generated, the supply hoses must be purged to ensure that the desired gas from the gas cylinders is actually in the chamber. For this purpose, the chamber is evacuated and then filled with the first gas (e.g. Ar) up to a pressure of about 400 mbar. Then it is evacuated again and filled with the second gas to 400 mbar. After evacuating again, the desired gas mixture can now be prepared. For all further gas mixtures it is sufficient to evacuate the chamber completely and to prepare the new mixture. The hoses do not need to be purged for the rest of the day.

The positive high voltage (Fig. 7.4, HV 1) for the proportional chamber is set so that the pulse height of the chamber signals are clearly visible on the USB oscilloscope. To do this, use the photodiode signal as a trigger for the oscilloscope and display the capacitively decoupled signal of the counting wire on the other channel. Since the time constant of the RC element, with which the signal is coupled out, is much larger than the pulse length and the distance of the two pulses, you will see on the oscilloscope no pulses, but steps, whose heights correspond to the integrated charge of the pulses on the capacitor and thus to the pulse height. The time difference between the two steps thus corresponds to the time difference of the two charge clouds. Watch the relative position of the two chamber pulses when the drift voltage is slowly increased (HV 2).

Measure the drift times for the respective gas mixture for both drift paths available (24 cm and 36 cm). Before the first measurement, the parallelism of the laser beams with the electrodes in the chamber must be checked and the optics re-adjusted if necessary. The exact length of the drift paths is also measured. For this purpose, the laser is switched to continuous pulse mode (repetition rate 10 Hz) and the protective cover (insert interlock bridge into laser) is removed. **Attention, wear laser safety goggles when the laser cover is open!**

For the measurement of a drift time, typically 100 laser pulses are averaged at a fixed value of the reduced field E/P. For this purpose, the laser is set to pulse mode with a specified number of shots (usually 200). The pressure in the chamber and the voltage of the counting wire remain constant. The variation of E/P is done by changing the accelerating voltage HV 2. The step size of the reduced field should be about 0.02 V/(cm·hPa). At a total pressure of 1000 mbar, this corresponds to an increase of the drift voltage in 1 kV steps from 1 kV to 21 kV.

Compare your results with the theoretical values for the particular mixture of table 7.1.

Then measure the drift velocities of one argon-methane mixture with both drift paths at least for three different pressures. These should be approximately in the range of 500-1500 hPa. Adjust the partial pressures of the gases and the step size of the high voltage supply for the drift field accordingly to obtain equal values for the reduced field.

ATTENTION! OBSERVE THE SAFETY INSTRUCTIONS!

- The safety instructions for handling a class 3b UV laser, which are available at the experiment, must be observed!
- A maximum current of 0.15 mA (21 kV) at the high-voltage power supply should generally not be exceeded, otherwise permanent gas discharge may occur in the drift chamber, which could damage the apparatus!
- When the laser beam path is open, the laser safety goggles provided at the experiment must be worn and the curtain of the experimental room must be closed! The beam path may only be opened after consulting with the responsible tutor!
- Dangerous high voltages up to 50 000 V are used to generate the drift field!
- No changes may be made to the test apparatus!

7.1.5 Literature

Electrons drift: [6], [7], [8], [9]

Table 7.1: Drift velocity$v$ (cm/μs) as a function of the reduced electric field E/p (V/(cm·hPa)) for different argon-methane mix at T = 20 °C.

v (Ar:CH_4)										
E / p	**0:100**	**10:90**	**20:80**	**30:70**	**40:60**	**50:50**	**60:40**	**70:30**	**80:20**	**90:10**
0.025	0.348	0.384	0.418	0.467	0.525	0.627	0.712	0.899	1.166	1.583
0.050	0.772	0.838	0.936	1.063	1.199	1.448	1.692	2.164	2.816	3.417
0.075	1.248	1.387	1.543	1.754	2.025	2.410	2.839	3.548	4.375	4.639
0.100	1.794	1.982	2.225	2.534	2.917	3.431	3.990	4.819	5.546	5.247
0.125	2.365	2.622	2.951	3.335	3.803	4.428	5.013	5.849	6.300	5.472
0.150	2.992	3.319	3.683	4.132	4.667	5.361	5.923	6.636	6.745	5.454
0.175	3.617	3.994	4.403	4.934	5.492	6.189	6.652	7.191	6.968	5.356
0.200	4.256	4.648	5.110	5.619	6.202	6.882	7.247	7.571	7.047	5.188
0.225	4.847	5.267	5.767	6.304	6.820	7.459	7.682	7.806	7.041	4.989
0.250	5.452	5.882	6.426	6.922	7.348	7.932	8.053	7.937	6.965	4.822
0.275	6.010	6.482	7.007	7.432	7.853	8.303	8.285	7.995	6.857	4.614
0.300	6.529	6.982	7.446	7.866	8.251	8.591	8.453	7.995	6.726	4.428
0.325	7.025	7.481	7.869	8.269	8.603	8.811	8.548	7.949	6.581	4.287
0.350	7.455	7.880	8.287	8.624	8.855	8.964	8.551	7.880	6.429	4.113
0.375	7.902	8.251	8.648	8.911	9.060	9.073	8.615	7.789	6.275	3.983
0.400	8.243	8.630	8.928	9.127	9.193	9.140	8.584	7.681	6.124	3.840
0.425	8.550	8.902	9.160	9.340	9.322	9.176	8.535	7.566	5.976	3.707
0.450	8.899	9.151	9.413	9.465	9.417	9.177	8.478	7.441	5.832	3.635
0.475	9.132	9.441	9.566	9.568	9.461	9.160	8.377	7.316	5.687	3.555
0.500	9.395	9.569	9.700	9.687	9.513	9.124	8.275	7.190	5.556	3.439
0.525	9.568	9.769	9.840	9.769	9.484	9.075	8.179	7.063	5.435	3.307
0.550	9.780	9.884	9.892	9.790	9.488	9.012	8.083	6.939	5.307	3.261
0.575	9.921	9.981	9.957	9.782	9.490	8.939	7.987	6.812	5.195	3.170
0.600	10.049	10.058	10.044	9.826	9.392	8.862	7.850	6.691	5.082	3.109
0.625	10.155	10.175	10.056	9.775	9.361	8.777	7.758	6.572	4.982	3.075
0.650	10.253	10.200	10.089	9.771	9.304	8.687	7.645	6.456	4.884	2.994
0.675	10.323	10.252	10.087	9.778	9.231	8.599	7.517	6.346	4.787	2.946
0.700	10.445	10.283	10.101	9.697	9.142	8.502	7.444	6.238	4.697	2.890
0.725	10.495	10.350	10.038	9.652	9.075	8.407	7.343	6.135	4.613	2.827
0.750	10.504	10.354	10.014	9.615	8.984	8.310	7.203	6.036	4.534	2.859
0.775	10.498	10.299	10.002	9.543	8.904	8.211	7.089	5.939	4.457	2.798
0.800	10.509	10.296	9.952	9.457	8.822	8.118	6.980	5.846	4.395	2.789
0.825	10.532	10.249	9.954	9.368	8.735	8.018	6.907	5.754	4.323	2.745
0.850	10.486	10.246	9.835	9.341	8.656	7.926	6.864	5.673	4.258	2.703
0.875	10.510	10.209	9.790	9.241	8.567	7.832	6.713	5.589	4.194	2.656
0.900	10.436	10.114	9.758	9.136	8.485	7.738	6.634	5.505	4.137	2.644
0.925	10.459	10.102	9.664	9.089	8.375	7.648	6.560	5.429	4.083	2.657
0.950	10.380	10.075	9.618	9.058	8.328	7.557	6.479	5.360	4.031	2.616
0.975	10.369	10.011	9.536	8.982	8.227	7.469	6.410	5.291	3.986	2.581
1.000	10.354	9.919	9.483	8.852	8.150	7.384	6.345	5.221	3.934	2.561

7.2 Experiment (B): Parity violation at β decay

7.2.1 Tasks

1. Energy calibration with a ^{22}Na source.
2. Confirmation of parity violation in β decay.
3. Estimation of the degree of polarization of the bremsstrahlung produced by the β particles.
4. Estimation of the longitudinal polarization of the electrons emitted in the β decay.

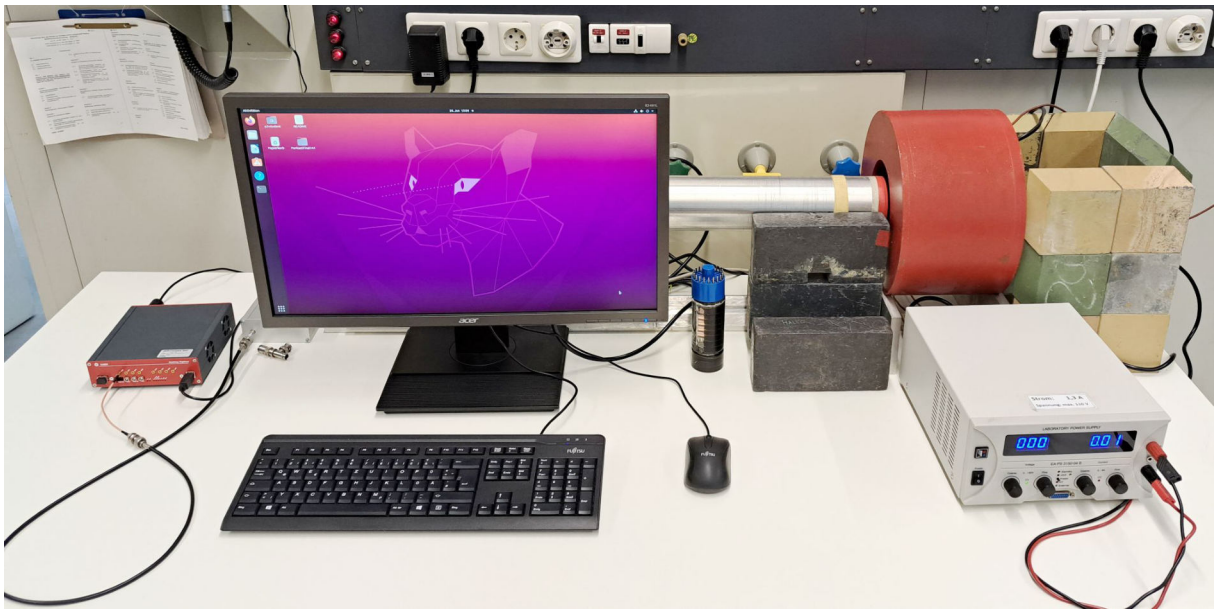

Figure 7.5: Setup of the parity violation experiment.

7.2.2 Introduction

In this experiment, an important conservation law is tested with the simplest of means. Before the experiment, however, some theoretical effort is necessary. Namely, from the measured circular polarization of the γ quanta, the longitudinal one of the electrons has to be inferred unambiguously. For this purpose it is necessary to calculate the corresponding Feynman diagrams. It turns out that the uniqueness is given only for large energies. For this reason only bremsstrahlung-quanta with energies larger than 1 MeV are counted. In principle even simpler is the Wu experiment, because the recourse to theory is not necessary. The parity violation follows directly from the measured asymmetry of the electrons. However, the experiment itself requires a little more effort because of the low temperatures and the high magnetic fields.

7.2.2.1 The parity

The parity operation is the inversion of coordinates. For a state with the wave function $\Psi(\vec{r})$ in the spatial representation is valid

$$P \cdot \Psi(\vec{r}) = \Psi(-\vec{r}) \tag{7.15}$$

The parity operation is equivalent to the spatial reflection in a plane, since it can be represented as the product of this reflection S and a subsequent rotation by 180°, $D(180°)$.

$$P = S \cdot D(180°) \tag{7.16}$$

The equivalence is a consequence of the invariance of the quantum mechanical expectation values at rotations (conservation of angular momentum).

For an arbitrary state $|a\rangle$ with defined parity, the eigenvalue equation is

$$P\,|a\rangle = \pi_a\,|a\rangle \tag{7.17}$$

and, since the inversion twice leads back to the initial state

$$P^2\,|a\rangle = |a\rangle \tag{7.18}$$

Therefore applies

$$P^2 = 1, \qquad P = P^{-1}, \qquad \pi_a = \pm 1 \tag{7.19}$$

The eigenvalues of the parity operator are +1 and -1. In the first case we speak of even parity or symmetric state, in the second of odd parity or asymmetric state.

The expected value of an operator with defined parity transforms under the parity operation as follows.

$$POP^{-1} = \pi_0\,O \tag{7.20}$$

examples are the operators of location $\vec{r}$, momentum $\vec{p}$, spin $\vec{\sigma}$ and angular momentum $\vec{\ell}$.

$$\begin{aligned} P\vec{r}P^{-1} &= -\vec{r} \\ P\vec{p}P^{-1} &= -\vec{p} \\ P\vec{\sigma}P^{-1} &= +\vec{\sigma} \\ P\vec{\ell}P^{-1} &= +\vec{\ell} \end{aligned} \tag{7.21}$$

Here you can see that there are operators which change their sign under the parity transformation.

An operator is invariant under a transformation if its expectation value does not change. If an operator is invariant, the physical quantity for which it stands obeys a conservation law. Examples include the law of conservation of momentum, which follows from invariance with respect to translations, and the law of conservation of angular momentum, which follows from invariance with respect to space-*rotations*. Similarly, parity is said to be preserved if the expectation value of an operator is invariant with respect to space-*mirroring*.

If one wants to check whether a theory is parity-preserving, one must measure the expectation values of such operators which are sensitive to the mirroring: these are the so-called pseudoscalars. They are quantities which are scalar, i.e., rotationally invariant, but change sign upon mirroring. According to Eq. 7.21 such quantities can be formed as the scalar product of a polar and an axial vector. Exactly such expectation values, the products of one momentum and one angular momentum, have been measured when parity conservation was tested in the weak interaction. Pseudoscalars must necessarily be zero in a parity-preserving theory. Conversely, the observation of a non-zero expectation value is sufficient for the violation of parity.

In Wu's experiment, the β^- emission from polarized ^{60}Co nuclei was measured. The ^{60}Co was aligned by cooling to very low temperatures in a strong magnetic field. This makes the energy difference of states with different magnetic quantum numbers large compared to the energy of thermal motion. Therefore, only the lower states are occupied, which have large

magnetic quantum numbers and describe nuclei aligned in the direction of the magnetic field. In the ideal case ($T = 0$ or $B = \infty$), all nuclei are in the lowest state, which corresponds to complete polarization. The result of Wu's measurement was: the β decay of polarized nuclei is not isotropic, the β^- particles are emitted preferentially *anti-parallel* to the nuclear spin (which is parallel to the magnetic field) of the ^{60}Co.

This result is not compatible with a parity-preserving theory, in which the world is mirror-invariant. In this case, exactly as many particles should have been emitted parallel to the field. From theory the angular distribution of the electron should be,

$$W\left(\vec{p}_\mathrm{e}, \vec{J}\right) = 1 + \frac{v}{c} \cdot P \cdot A \cdot \frac{\vec{p}_\mathrm{e} \cdot \vec{J}}{|\vec{p}_\mathrm{e}| \cdot \left|\vec{J}\right|} \tag{7.22}$$

where P is the degree of polarization of the ^{60}Co, A is the asymmetry parameter containing the matrix elements and the coupling constants of the weak interaction, $\vec{p}_\mathrm{e}$ is the momentum of the electron and $\vec{J}$ is the spin of the nucleus. As can be seen, the pseudoscalar $\left(\vec{p}_\mathrm{e} \cdot \vec{J}\right)$ is responsible for the occurrence of an asymmetry. Note also that in a parity preserving theory the angular distribution must be *necessarily* isotropic. However, this condition is not *sufficient*, because the asymmetry parameter A can be zero by chance.

In this experiment, another, equally simple pseudoscalar is measured, the scalar product of the spin and momentum of the β-particle.

$$H = \frac{\vec{\sigma} \cdot \vec{p}}{|\vec{\sigma}| \cdot |\vec{p}|} \tag{7.23}$$

This is the projection of the electron spin onto the direction of flight and is called longitudinal polarization or helicity. If a finite value is measured for the helicity of a β-particle, the parity is violated.

7.2.2.2 The polarization of particles and photons

For a particle with spin $\vec{S}$, the polarization P with respect to a distinct direction (z-axis) is defined as the ratio of the expected value of the spin operator along this direction to the magnitude of the spin

$$P = \frac{\langle \vec{S}_z \rangle}{S} \tag{7.24}$$

In it $\vec{S}_z$ is the z-component of the spin operator $\vec{S}$. The spin space of a particle with spin S has $2S + 1$ dimensions. As basis vectors in this space can be chosen the $2S + 1$ orthonormal states $|S, S_z\rangle$, which are at the same time eigenstates of $\vec{S}^2$ and $\vec{S}_z$, for which thus holds

$$\begin{aligned} \vec{S}^2 |S, S_z\rangle &= S(S+1) |S, S_z\rangle \\ \vec{S}_z |S, S_z\rangle &= S_z |S, S_z\rangle \\ -S \leq \; S_z &\leq +S \end{aligned} \tag{7.25}$$

For a particle with $S = 1/2$, the representation of the spin operator $\vec{S}$ by the Pauli matrices $\vec{\sigma}$ is common. It is

$$\vec{S} = \frac{1}{2}\vec{\sigma} = \frac{1}{2}(\sigma_x, \sigma_y, \sigma_z) \tag{7.26}$$

with

$$\sigma_x = \begin{pmatrix} 0 & 1 \\ 1 & 0 \end{pmatrix}, \quad \sigma_y = \begin{pmatrix} 0 & -i \\ i & 0 \end{pmatrix}, \quad \sigma_z = \begin{pmatrix} 1 & 0 \\ 0 & -1 \end{pmatrix} \tag{7.27}$$

In this representation, the base states $|S, S_z\rangle$ are.

$$|1/2, +1/2\rangle = \begin{pmatrix} 1 \\ 0 \end{pmatrix} \text{ und } |1/2, -1/2\rangle = \begin{pmatrix} 0 \\ 1 \end{pmatrix} \tag{7.28}$$

These states describe the alignment parallel and anti-parallel to the z-axis, respectively. The general state is a superposition of the two basic states

$$\Psi = \begin{pmatrix} a_+ \\ a_- \end{pmatrix} = a_+ \cdot \begin{pmatrix} 1 \\ 0 \end{pmatrix} + a_- \cdot \begin{pmatrix} 0 \\ 1 \end{pmatrix} \qquad \text{mit} \qquad a_+^2 + a_-^2 = 1 \tag{7.29}$$

a_+^2, a_-^2 are the probabilities of the states with parallel or anti-parallel orientation. The polarization of this state is

$$P = \frac{\langle S_z \rangle}{S} = \langle \sigma_z \rangle = \langle \Psi | \sigma_z | \Psi \rangle = a_+^2 - a_-^2 \qquad \text{mit} \qquad -1 \leq P \leq +1 \tag{7.30}$$

The maximum values belong to parallel ($a_- = 0, P = +1$) and anti-parallel ($a_+ = 0, P = -1$) configuration to the z-axis, respectively. These are the cases of complete polarization *with respect to the z-axis.* For any *other* state, a direction can be found in which the particle is completely polarized.

This is valid for *one* particle. For a entirety of *many* particles, e.g. a particle beam, the polarization is still defined by Eq. 7.24, but now the averaging goes also over the total number of all particles. In this case there is not any more a pure state, so the expectation value is no longer given by Eq. 7.30, but by

$$P = \langle \bar{\sigma_z} \rangle \sum_{S_z=-1/2}^{S_z=+1/2} p_{S_z} \langle S, S_z | \sigma_z | S, S_z \rangle \tag{7.31}$$

Here, p_{S_z} is the probability of the occurrence of a pure state with a given S_z and it is

$$p_{+1/2} + p_{-1/2} \equiv p_+ + p_- = 1 \tag{7.32}$$

Inserting Eq. 7.27 and Eq. 7.28, we obtain for the polarization

$$p = p_+ - p_- \tag{7.33}$$

The probabilities p_+ and p_- can be determined by measuring the relative number of particles N_+ and $N-$ in the pure states, respectively. Finally, one obtains for the polarization

$$P = \frac{N_+}{N_+ + N_-} - \frac{N_-}{N_+ + N_-} = \frac{N_+ - N_-}{N_+ + N_-} \tag{7.34}$$

Absolute polarization exists when all particles are oriented parallel ($N_- = 0$, $P = +1$) or anti-parallel ($N_+ = 0$, $P = -1$) to the z-axis. The polarization vanishes if there are equal numbers pointing in each direction ($N_+ = N_-$). If it is not totally polarized ($|P| < 1$), no other direction can be found with respect to which the polarization is absolute.

These considerations are valid in the non-relativistic regime, where the direction of the momentum and the direction of the spin are not coupled. Therefore, the z-direction can be chosen arbitrarily with respect to the momentum direction, so that a purely transverse polarization is

possible for the single electron as well as for the electrons at large. In relativistic Dirac theory, on the other hand, the electron always has a spin component in the direction of momentum, i.e. longitudinal polarization, whose magnitude depends on the velocity. It goes down to zero with the velocity and becomes absolute when the velocity approaches the speed of light.

The situation is somewhat different for the γ quantum, which has spin 1. In general, according to Eq. 7.25, three states are necessary for such a particle to describe the polarization. In the chosen representation, these are the projections along the z-axis with $S_z = -1, 0, +1$. For the γ quantum, which has the rest mass zero and therefore moves with the speed of light, this is not valid. In this case, there is no transverse spin. There are only two alignments, either in the direction of the momentum or in the opposite direction. These alignments correspond to the circular polarization in classical optics. A *single* γ quantum is always fully circularly polarized and if the spin is in the direction of momentum, the polarization is right-circular.

$$P_{\mathrm{C}} = \frac{N_+ - N_-}{N_+ + N_-} \tag{7.35}$$

N_+ and N_- are the numbers of right and left circularly polarized quanta in the beam, respectively. $P_{\mathrm{C}} = 1$ means that all quanta are right circularly polarized.

Linear polarization of a *single* γ-quantum does not exist. However, for the *whole number of quanta*, it is possible if there are fixed phase relations between the circular polarizations of the quanta. This is also in analogy to classical optics.

7.2.3 Principle of the measurement

7.2.3.1 The polarization of Bremsstrahlung

In this experiment, the longitudinal polarization of electrons emitted during β-decays is determined by measuring the polarization of the bremsstrahlung produced when the electrons decelerate in matter. In this process, the polarization of the electrons is partially transferred to the photons, and the polarization state of the bremsstrahlung is determined by the electrons. There are three cases to distinguish.

a) The electrons are unpolarized: then the bremsstrahlung is linearly polarized. The polarization is largest at the low energy end of the bremsstrahlung spectrum. As the energy increases, the linear polarization decreases and disappears at the high end.

b) The electrons are transversely polarized: In this case, the polarization is elliptical, since a circular component is added to the linear one. This is also energy dependent and largest at low energies. It goes towards zero when the photon energy goes towards the endpoint energy of the β-spectrum.

c) The electrons are longitudinally polarized: The bremsstrahlung is circularly polarized. The polarization is always larger than that in b) and shows the opposite behaviour. It increases sharply with increasing energy of the photons, and takes the highest values at the endpoint energy. This is shown in Fig. 7.6 for the bremsstrahlung of electrons emitted by ^{90}Y. At the endpoint energy, the bremsstrahlung is practically completely polarized.

The circular polarization has the same sign as the helicity. Thus, for β^--particles which have negative helicity, the bremsstrahlung is left circularly polarized. This suggests that during deceleration, helicity is transferred. The magnitude of the transfer depends only slightly on the energy of the electron, but strongly on the energy of the γ quantum, as can be seen from Fig. 7.7. The transfer is plotted as a function of the relative photon energy for two very different electron

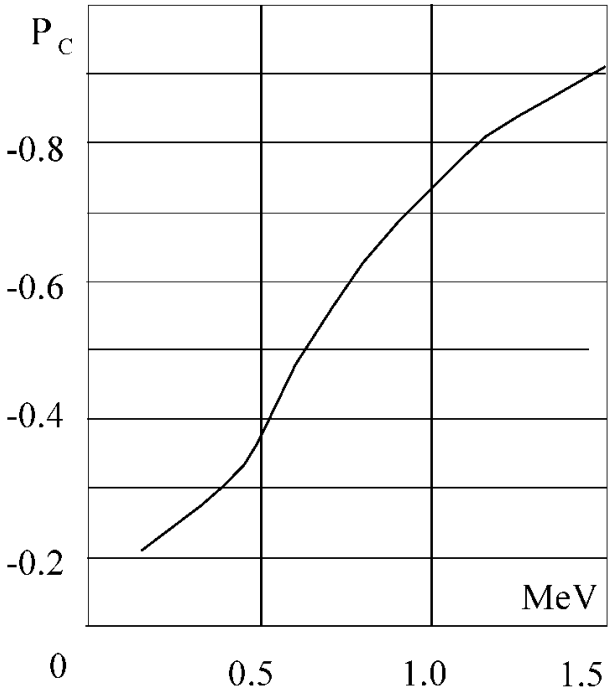

Figure 7.6: Circular polarisation of bremsstrahlung of ^{90}Y.

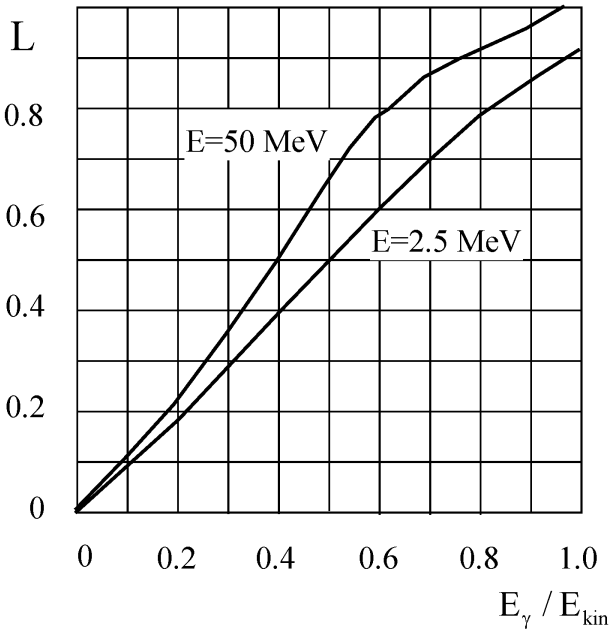

Figure 7.7: Helicity transfer as a function of the energy of the photon.

energies. The two curves are not very different, but both increase sharply with photon energy. At the upper end of the bremsstrahlung spectrum, the transfer is complete.

The reason for this is the conservation of angular momentum. At energies in the range of a few 100 keV, the spin of the electron is completely opposite to the momentum before the collision. At the endpoint energy, the brems-quantum is preferentially emitted forward in the momentum direction, with the electron coming to rest and flipping the spin. The angular momentum changes by a whole unit in the process. The photon carries away this angular momentum.

An aggregate of β-particles emitted into a certain solid angle cannot be transversely polarized. Although every single electron has a transversal component (except in the extreme relativistic case), the directions are statistically distributed in space, so that the average value of all electrons vanishes. This is not true for the longitudinal component, for which there is always a finite value in a limited solid angle.

7.2.3.2 The measurements of the circular polarization of the γ-quanta

The longitudinal polarization of γ quanta is experimentally determined by Compton scattering from polarized electrons. This is possible because the effective cross section contains a term that depends on the alignment of the spins of the scattering particles. The polarization dependent Compton cross section is

$$\frac{\mathrm{d}\sigma}{\mathrm{d}\Omega} = \frac{r_0^2}{2} \cdot \frac{k^2}{k_0^2} \cdot (\Phi_0 + f \cdot P_\mathrm{C} \cdot \Phi_\mathrm{C}) \tag{7.36}$$

r_0 is the classical electron radius, k_0 the momentum of the incident and k that of the scattered photon, P_C the circular polarization and f the degree of polarization of the electrons. In the experiment, magnetized iron is used as the scatterer. Thus, $f = 2/26$ is the proportion of aligned electrons to the total number of electrons.

$$\Phi_0 = 1 + \cos^2\theta + (k_0 - k) \cdot (1 - \cos\theta) \tag{7.37}$$

contains the dependence of the effective cross section on the scattering angle θ without taking the spins into account and leads to the Klein-Nishima formula.

$$\Phi_\mathrm{C} = -(1 - \cos\theta) \cdot [(k_0 + k) \cdot \cos\theta \cdot \cos\psi + k \cdot \sin\theta \cdot \sin\psi \cdot \cos\phi] \tag{7.38}$$

is the polarization dependent part. Where ψ is the angle between $\vec{k}_0$ and the electron spin $\vec{S}$ and ϕ between the $\left(\vec{k}_0 \cdot \vec{S}\right)$ plane and the $\left(\vec{k}_0 \cdot \vec{k}\right)$ plane.

It can be seen that Φ_C changes the sign when the electron spin flips, because then ψ changes into $\psi + \pi$. In the experiment, the magnetization direction of the stray magnet is reversed (pole reversal). Let N_+ be the number of scattered photons when the electron spin is approximately parallel to the incident quantum ($0 \leq \psi < \pi/2$), N_- the corresponding number for anti-parallel alignment ($\pi \leq \psi < 3\pi/2$), then the relative count rate difference when the spin is reversed is

$$E = \frac{N_- - N_+}{N_- + N_+} = f \cdot P_\mathrm{C} \cdot \frac{\Phi_\mathrm{C}^-}{\Phi_0} \tag{7.39}$$

here Φ_C^- is Φ_C for $(\pi \leq \psi < 3\pi/2)$. An asymmetry E occurs only when both electron polarization and circular polarization of photons are different from zero. The factor Φ_C^-/Φ_0 depends on the photon energy and on the geometry of the arrangement and can therefore be made large by clever arrangement.

In Fig. 7.8 Φ_C^-/Φ_0 is plotted as a function of the scattering angle θ for different γ energies (in units of electron rest mass). The curves are valid for $\psi = 0$. It is seen that the magnitude of Φ_C^-/Ψ_0 increases with photon energy. That is why it is convenient to use only the high-energy

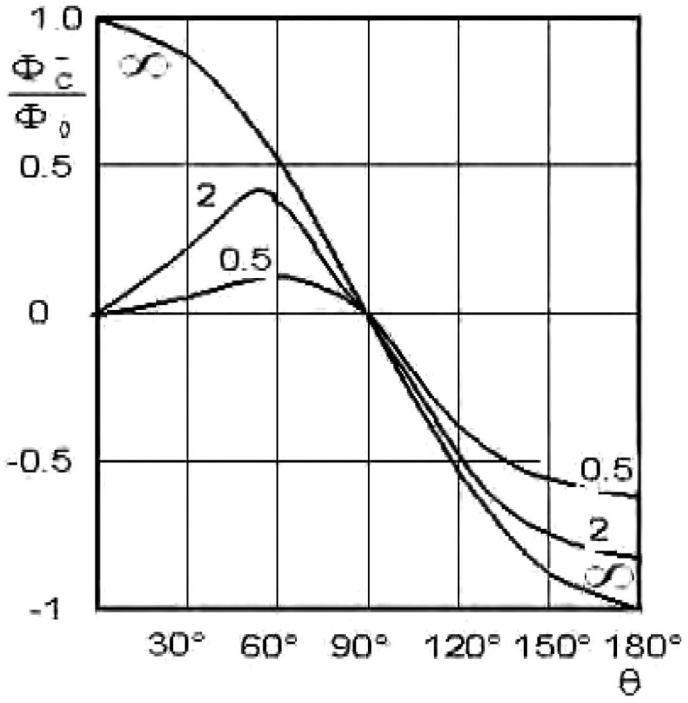

Figure 7.8: Φ_C^-/Φ_0 as function of the scattering angle for different photon energies.

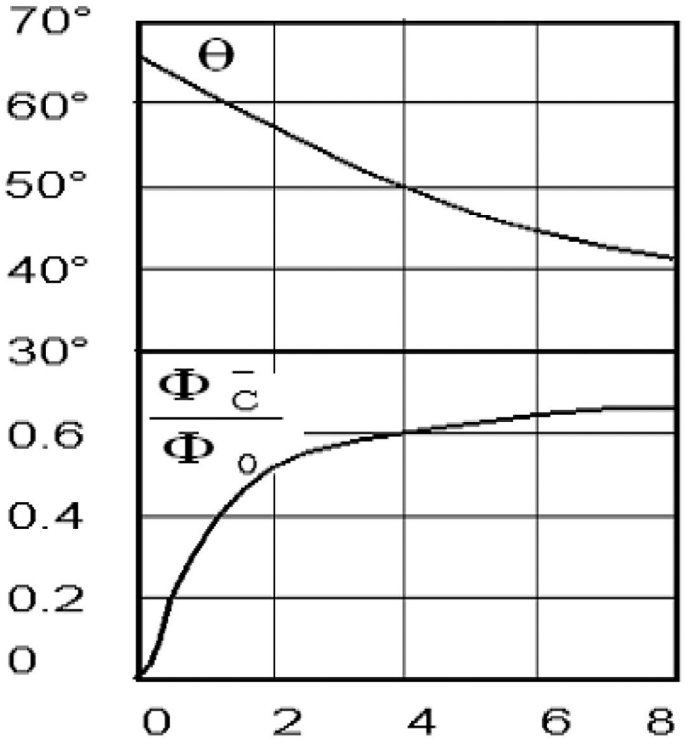

Figure 7.9: The optimal scattering angle and the corresponding ratio Φ_C^-/Φ_0 versus the photon energy in units of the electron rest mass (511 keV).

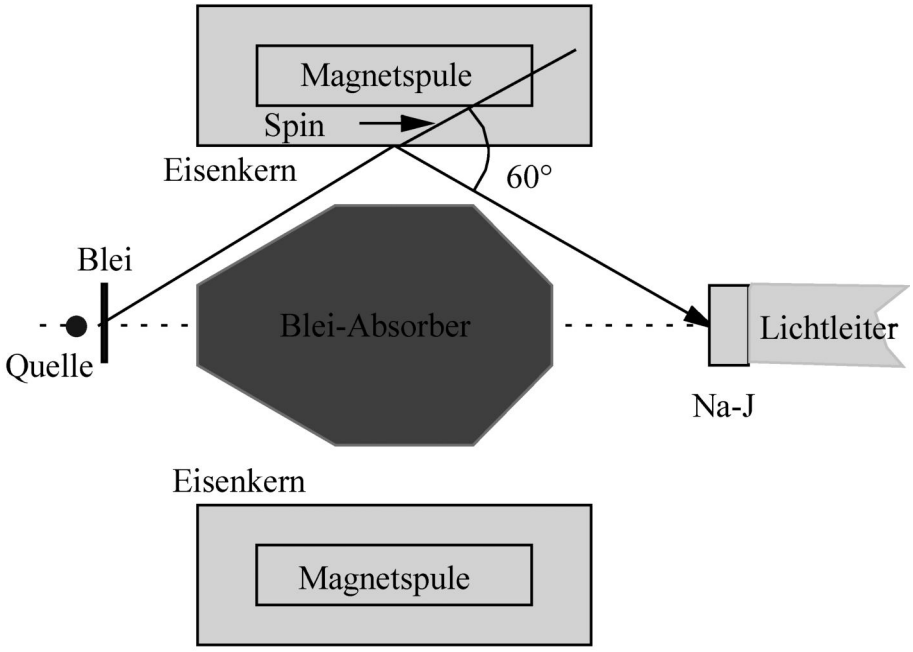

Figure 7.10: Sketch of the apparatus.

part of the spectrum. For the radioactive source $^{90}\mathrm{Sr} + {}^{90}\mathrm{Y}$ used in the experiment, this is the region above 1 MeV ($k_\gamma = 2$). At this energy Φ_C^-/Φ_0 is largest for backward scattering ($\theta \to 180°$) and in forward scattering in the neighbourhood of $\theta = 60°$. Backward scattering is eliminated because it has a too small effective cross section. Regarding the angle ψ it is not necessary to optimize, because its influence on the magnitude of Φ_C^-/Φ_0 is only small.

The optimal scattering angle θ as a function of photon energy (in electron rest masses) is drawn in Fig. 7.9 together with the corresponding maximum values of Φ_C^-/Φ_0. In the experiment, the mean scattering angle is 60°. The corresponding value of Φ_C^-/Φ_0 is

$$\Phi_C^-/\Phi_0 = 0,52 \pm 0,05 \qquad \text{at} \qquad \theta = 60° \tag{7.40}$$

With the asymmetry E in Eq. 7.39 the circular polarization including the sign can be determined. Since Φ_C^-/Φ_0 is positive for forward scattering, P_C has the same sign as E. The asymmetry is positive when, for most scatterings, the electron spin is opposite to the direction of the photon incidence, i.e. pointing toward the source. In this case, since the iron has a negative magnetic moment, the magnetic field is directed away from the source.

7.2.4 Setup and implementation

Fig. 7.10 shows a drawing with a cut along the symmetry axis of the apparatus. Electrons emitted from a $^{90}\mathrm{Sr} + {}^{90}\mathrm{Y}$ source generate bremsstrahlung quanta in a Pb layer surrounding the source. These are first scattered in the iron core of a cylindrical magnet, whose axis is alligned in the source-detector direction, before entering the NaJ detector. The crystal is connected to a photomultiplier tube (PMT) via a long light guide so that the PMT is outside the magnetic field. This avoids false asymmetries that can occur due to the influence of opposing magnetic fields on the pulse heights. An absorber made of lead is placed in the center of the magnet to prevent unscattered quanta from travelling directly from the source to the detector. The geometry is chosen so that the average scattering angle is 60°. The photomultiplier signal is digitized by a fast ADC (CAEN Digitizer DT5725, 8x 250 MSPS). The data of the individual events are transferred to a PC (Linux) and stored in a file. Afterwards the pulses are analyzed with a Python script

that determines the pulse heights. Each pulse height is converted into energy units by an energy calibration. The Python code is executed in a Jupyter notebook.

In the discussion of the curves for the optimization of Φ_C^-/Φ_0 an ideal geometry has been assumed, where the finite dimensions of source, magnet and crystal have been neglected. In reality, one cannot assume fixed values for the angles, but has to take the average over a finite range. Therefore, the given value for Φ_C^-/Φ_0 is only an approximation. For the *proof* of parity violation with $|E| > 0$, however, this is of no importance, since only the *size* of the measured polarization is influenced by it.

The measurement method is counting selected events (see Sec. 5.7.1). Only bremsstrahlung quanta whose original energy before Compton scattering are greater than 1 MeV shall be counted. Therefore, an energy calibration of the measurement system has to be performed first. For this purpose, a ^{22}Na source is available. The number of scattered quanta is measured for the two orientations of the magnetic field. One measures data runs with short measurement times, always inverting the field between the runs. The counts of two neighboring runs belong together to determine E. In this way one can notice possible fluctuations. The measuring time per run should be at least 30 s. At least 30 run pairs should be measured.

CAUTION: Before reversing the polarity of the magnetic field by swapping the banana plugs, it is essential to regulate the coil current to zero.

7.2.5 Evaluation and error calculation

All measured values belonging to one magnetic field direction are added. The asymmetry E is calculated with the sums. The error of the asymmetry is determined by assuming Poisson statistics for the counts and Gaussian error propagation to determine σ_E. The squareroot of the sums is used as the error of the summed up counts. This method yields the pure statistical error.

In a second analysis, the asymmetry is calculated for each run pair individually. Then the mean value $\langle E \rangle$ and the standard deviation of the distribution are determined. This gives the mean error of a *single measurement*. The mean error of the *mean value* is obtained by dividing by the squareroot of the number of individual measurements. Compare this error with the statistical error from the previous analysis.

7.2.6 Literature

Introduction chapters 1 – 6 in this script
β-decay: [1], [11], [27], [28], [40]
Polarization: [41], [42]
Detectors: [19]
Electronics: [21], [22]

7.3 Experiment (B): The Compton effect

7.3.1 Tasks

1. Energy calibration of the data acquisition system and determination of the detection efficiency of the detector.

2. Measurement of the differential effective cross section for Compton scattering of γ quanta by electrons as a function of the scattering angle.

3. Measurement of the energy shift of the scattered γ-quanta as a function of the scattering angle and estimation of the rest energy of the electron.

4. Measurement of the dependence of the effective cross section of Compton scattering on the atomic number of the scattering target.

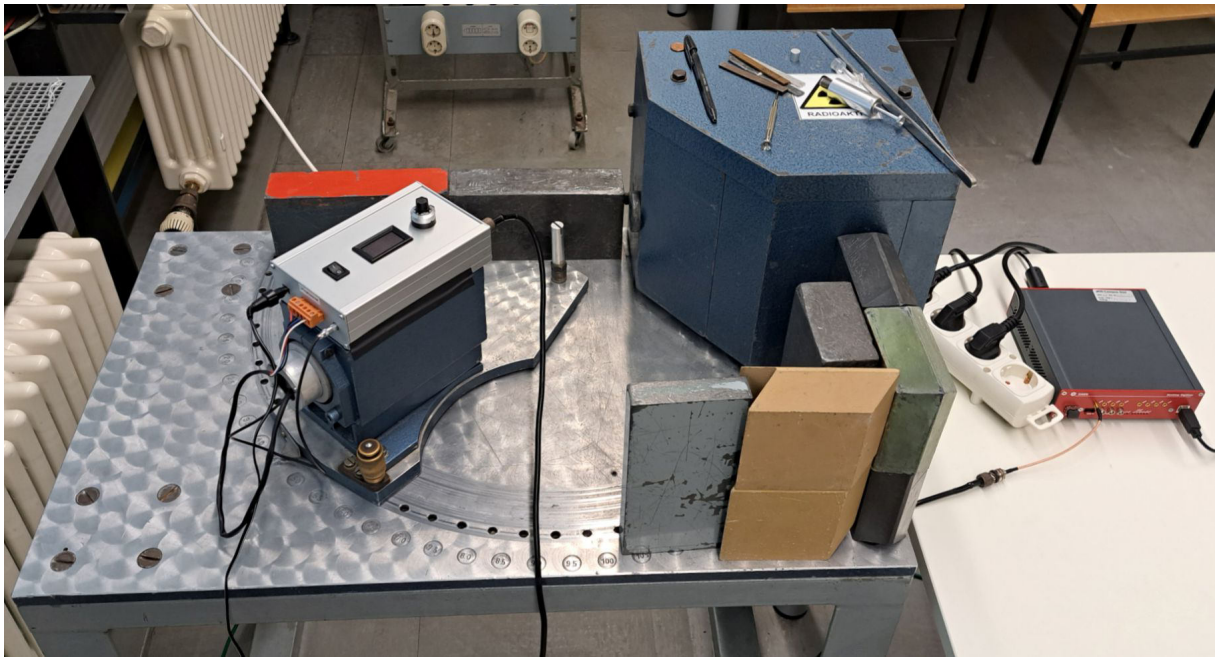

Figure 7.11: Setup of the Compton experiment. On the left side the NaI-detector can be seen, which can be rotated around the scattering target. The blue shielding on the right side contains the ^{137}Cs source.

7.3.2 Introduction

This experiment is an example of the most common experiments performed in nuclear physics: the scattering experiments. The aim is to study the interaction of particles and photons with each other. There are certain types of reactions. If a projectile particle a hits a (mostly) resting target particle b in the input channel, the simplest case is the one where the same particles are also present in the output channel.

	a + b	$\rightarrow$	a + b	elastic scattering
Example:	$\gamma + e^-$	$\rightarrow$	$\gamma + e^-$	Compton effect

It is an elastic scattering if the internal state of the involved particles does not change. If a particle, e.g. b, takes up excitation energy,

	a + b	$\rightarrow$	a + b*	inelastic scattering
Example:	d + ^{12}C	$\rightarrow$	d + ^{12}C*	

then one speaks of inelastic scattering. In this case, the carbon has been excited by deuterons. It releases its excitation energy by emitting other particles or γ quanta.

In the most general type of reactions, the particles in the output channel are not the same as in input channel.

	a + b	$\rightarrow$	c +d + (e)	conversion
Examples:	d + ^{12}C	$\rightarrow$	^{13}C + p	Kernreaktion
	d + ^{12}C	$\rightarrow$	^{12}C + p + n	Aufbruch

This group includes the actual nuclear reactions, in which new nuclei are created by rearrangement of nucleons, or the breakup reactions, in which particles decay into lighter ones. For example, if a deuteron with some MeV energy hits a ^{12}C, then besides elastic scattering there is also the possibility that the neutron from the deuteron attaches to the ^{12}C nucleus, which thereby changes into the isotope ^{13}C, while the proton continues alone. However, the deuteron can also be broken up so that three particles appear in the output channel.

Transformation reactions that leads to the creation of new particles that were not present in the input channel,

$\pi^- + p$	$\rightarrow$	$\pi^0 + n$	charge exchange
$p + p$	$\rightarrow$	$p + p + \pi^0$	pion production

are also possible. Thus, when pions scatter from nucleons, charge can be exchanged. In this process, the charge state of both the pion and the nucleon changes. The total number of charge in the input and output channels is conserved (**law of conservation of charge**), as is the number of nucleons (**law of conservation of baryons**). When two protons with sufficiently high energy scatter, a pion can be produced. Because of the baryon conservation only two protons appear in the output channel and because of the charge conservation the pion is uncharged.

The probability with which a certain output channel occurs for a given input channel in a reaction is given by the cross section, the determination of which is therefore one of the essential tasks in nuclear physics experiments. The measurand is the frequency with which a certain particle occurs in the output channel. Energy and particle discrimination are necessary to separate the different reaction channels.

7.3.3 The cross section

In all impact processes, not only in nuclear physics, the probability of occurrence is described by the impact cross section. It is a hypothetical surface σ associated with the target particle perpendicular to the direction of flight of the projectile particle (see Fig. 7.12). If the projectile hits this surface, the reaction takes place, otherwise it does not. If a projectile particle flies perpendicularly through a macroscopic surface F in which the target particle is located, the probability P_1 for the occurrence of the reaction is given by

$$P_1 = \frac{\sigma}{F} \tag{7.41}$$

If there are n target particles within the area, the probability for an impact is

$$P_n = \sigma \cdot \frac{n}{F} \tag{7.42}$$

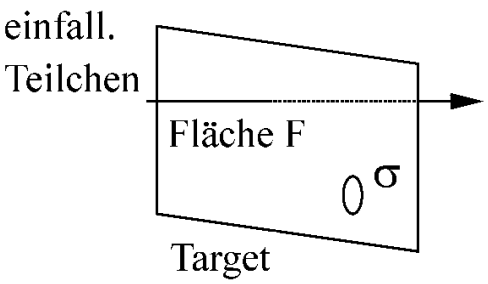

Figure 7.12: Definition of the cross section.

It can be determined by observing the frequency of the reaction when very many projectile particles pass through the surface in a statistically distributed manner. If Φ_0 is the flux of projectiles - the jet then contains Φ_0 particles per unit area and per unit time - then the rate of projectiles passing through the surface is $\Phi_0 F$. The rate R of total reactions occurring is the probability of *one* event times the number of trials per unit time, which is

$$R = P_n \cdot \Phi_0 \cdot F \tag{7.43}$$

which gives the cross section with equations 7.42 and 7.43.

$$\sigma = \frac{R}{n \cdot \Phi_0} \tag{7.44}$$

There are a number of other notations for this formula. Thus, the rate R can be given by the flux Φ_R by which the incident flux has become smaller

$$\sigma = \frac{\Phi_R \cdot F}{\Phi_0 \cdot n} = \frac{\Phi_R}{\Phi_0} \cdot \frac{1}{n/F} \ . \tag{7.45}$$

Here F is again the macroscopic area in which the hit target particles are located. If the beam is spatially more extended than the target, then F is the target area, if the target is larger, then F is the beam cross section.

The effective cross section is expressed here as the ratio of particle fluxes. More generally, it can be represented as the ratio of incoming and absorbed energy fluxes. It then also describes such reactions where the incoming and outgoing radiations are given in the wave image. The general definition is

$$\sigma = \frac{\begin{array}{l}\text{energy (particle) flux,}\\ \text{by which the incident flux decreases}\end{array}}{\begin{array}{l}\text{incident energy (particle) flux}\\ \otimes \text{ number of target particles per unit area}\end{array}} \tag{7.46}$$

This is the *total* cross-section, which takes into account *all* reactions of a given output channel, regardless of the directions of the outgoing reaction products. It is often measured in units of *barn*. A barn is $10^{-28}\,\mathrm{m}^2$.

More information about a reaction is obtained if it is not only established that it has taken place at all, but also the direction of the outgoing reaction products with respect to the incoming radiation is measured. For this purpose, the differential cross section is defined analogously to Eq. 7.46.

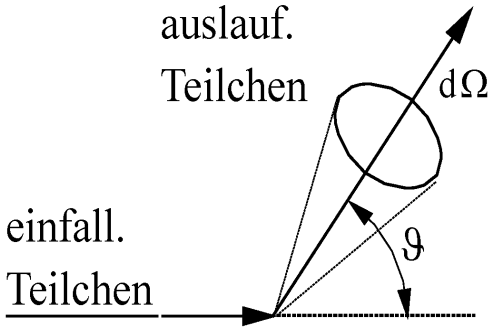

Figure 7.13: Definition of the differential cross section.

$$\sigma = \frac{\begin{array}{l}\text{energy (particle) flux per solid angle d}\Omega \\ \text{by which the incident energy (particle)} \\ \text{flux is reduced by products falling in d}\Omega\end{array}}{\begin{array}{l}\text{incident energy (particle) flux} \\ \otimes \text{ number of target particles per unit area}\end{array}} \tag{7.47}$$

The differential cross section depends not only on the energy of the incoming particle but also on the scattering angle ϑ (see Fig. 7.13). If it is integrated over the whole space, with the mostly correct assumption that $\mathrm{d}\sigma/\mathrm{d}\Omega$ is independent of the azimuthal angle φ, which means that the reaction is rotationally symmetric about the direction of incidence, one obtains the total effective cross section.

$$\sigma = \int_0^{2\pi} d\varphi \cdot \int_0^{\pi} \frac{\mathrm{d}\sigma(\vartheta)}{\mathrm{d}\Omega} \cdot \sin\vartheta \cdot \mathrm{d}\vartheta = 2\pi \cdot \int_0^{\pi} \frac{\mathrm{d}\sigma(\vartheta)}{\mathrm{d}\Omega} \cdot \mathrm{d}(\cos\vartheta) \tag{7.48}$$

In the definition of the differential effective cross section, the solid angle element is a differential quantity, while in the actual measurement the solid angle is given by the aperture angle $\Delta\Omega$ of the detector. For the effective cross section in $\Delta\Omega$ to be considered constant, one must make the detector or the solid angle aperture sufficiently small.

7.3.4 Setup and execution

The detector consists of a photomultiplier and a $CeBr_3$ scintillator[1] mounted in a rotatable housing. The aluminum scattering target is mounted above the rotation axis. The pulse shape of the photomultiplier signal is digitized by a fast ADC (CAEN Digitizer DT5725, 8x 250 MSPS). The data of the individual events are transferred to a PC (Linux) and stored in a file. Afterwards, the pulses are analyzed with the help of a Python script, determining the pulse height. The pulse height is converted into energy units by an energy calibration. The Python code is executed in a Jupyter notebook.

After the energy and efficiency calibration for the detector setup, the monoenergetic γ quanta of a ^{137}Cs source are scattered by the electrons of a cylindrical Al-Targt for task 1. The detector is seen from the target at a solid angle $\Delta\Omega$ with a mean scattering angle ϑ. It can be rotated on a circular path around the target and fixed at different angles ϑ in 5° steps. The measured quantity is the rate $R(\Delta\Omega, \vartheta)$ of quanta detected in the crystal. For each scattering angle, two measurements are taken: i) the rate $R_T(\Delta\Omega, \vartheta)$ with the Al target in front of the source and ii)

[1] This new inorganic scintillator crystal replaces the previously used NaJ crystal, which is often used in scintillation detectors. Compared to NaJ, the new crystal has better energy resolution and an approximately 10-fold shorter pulse length, giving it an advantage for high count rates and accurate timing measurements

the background rate $R_B(\Delta\Omega, \vartheta)$ without Al target. The actual rate scattered in the Al target is $R_{\mathrm{Al}}(\Delta\Omega, \vartheta) = R_T(\Delta\Omega, \vartheta) - R_B(\Delta\Omega, \vartheta)$. With the flux of ^{137}Cs quanta Φ_0 and the number of electrons of the target n follows with Eq. 7.47

$$\frac{\mathrm{d}\sigma}{\mathrm{d}\Omega} = \frac{R(\Delta\Omega)}{\Delta\Omega} \cdot \frac{1}{\Phi_0 \cdot n} \cdot \frac{1}{\varepsilon} \tag{7.49}$$

Here Eq. 7.44 has been used, which is also valid for the differential cross section. The right-hand side of this equation contains the dimensionless quantity ε as a correction factor in the denominator, which is the sensitivity of the detector for the detection of the γ quanta. It takes into account that the *detected* rate of quanta is not the actual rate of *scattered* quanta reaching the detector, since some of the quanta entering the detector leave it again without interacting. The sensitivity, which is the ratio of the detected quanta to the incoming quanta, can be determined either by a quantitative calculation, including all individual interaction processes, or experimentally by a calibration measurement. The value depends on the energy of the γ quanta and on the type and geometry of the detector. Here, it will be measured for the scintillation crystal, using different calibration sources whose activity is known. Since the sensitivity or detection efficiency of a detector is energy dependent, several different radioactive isotopes are used. Concentrate on the photopeak for the determination of the sensitivity for γ quanta.

The solid angle $\Delta\Omega$ will be calculated using geometry dataof the experimental setup. The number n of electrons is obtained from the dimensions of the Al target:

$$n = \frac{N_A}{A} \cdot Z \cdot \rho \cdot \pi \cdot \left(\frac{d}{2}\right)^2 \cdot l \tag{7.50}$$

with the Avogadro constant N_A, atomic weight A, atomic number Z, density ρ, diameter d and length l.

For Task 3, Eq. 3.23 gives the energy E' of a γ quantum after Compton scattering as a function of the scattering angle and its initial energy is E. It can be rewritten in the form,

$$\frac{1}{E'} = \frac{1}{E} + \frac{1}{m_0 c^2} \cdot (1 - \cos\vartheta) \tag{7.51}$$

from which you can see that the reciprocal energy E' plotted versus (1 - cosϑ) is a straight line. Determine the rest mass of the electron (m_0c^2) from the slope. Measure the energy E' using the photopeak in the energy spectrum at various scattering angles. Before doing so, calibrate the data acquisition system by recording the known photolines of ^{22}Na, ^{57}Co, ^{60}Co, and ^{137}Cs.

For task 4, the effective cross section in Eq. 3.26 and Eq. 7.49 refers to an *electron,* which is assumed to be free and at rest. However, when comparing different substances with each other, the cross section related to an *atom* is of interest. If all electrons in the atom are independent and the γ-energy is large compared to the binding energies, the following should hold true

$$\left(\frac{\mathrm{d}\sigma}{\mathrm{d}\Omega}\right)_a = Z \cdot \left(\frac{\mathrm{d}\sigma}{\mathrm{d}\Omega}\right)_e \tag{7.52}$$

where a and e stand for atom and electron, respectively. With Eq. 7.49 and Eq. 7.50 it becomes

$$\left(\frac{\mathrm{d}\sigma}{\mathrm{d}\Omega}\right)_e = C \cdot R\frac{A}{\rho \cdot Z} \tag{7.53}$$

All quantities independent of the target material are combined in the constant C. This equation can be verified by measuring the rate of scattered quanta for targets made of different materials but of the same size at a fixed scattering angle. If the conditions for Eq. 7.53 hold, the quantity $R \cdot A/\rho$, plotted versus the atomic number, should be a straight line. Equivalent, but more

sensitive to detecting deviations, is a plot of $(R \cdot A)/(\rho \cdot Z)$ over Z, which should give a straight line parallel to the abscissa.

7.3.5 Literature

Introduction chapters 1 – 6 in this script
Foundation: [1], [26]
Detectors: [18], [19]
Electronics: [18], [21], [22]

7.3.6 Details of the experiment

- The flux of γ-quanta from the ^{137}Cs source ($t_{1/2} = 30,0\,\mathrm{a}$) was measured in June 1971. It was at the location of the target $\Phi_0 = (1.54 \pm 0.09) \cdot 10^6\,\mathrm{cm}^{-2}\mathrm{s}^{-1}$.

- Geometry:
  Distance source-target: 23,9 cm
  Distance target-crystal: 21,5 cm
  Diameter crystal and length: 2,54 cm

7.3.6.1 Cross section for the Compton effect according to Klein-Nishina

ϑ	1 - cosϑ	$d\sigma/d\Omega * 10^{25}$ cm^{-2}
0	0	0,795239
5	0,004	0,784509
10	0,015	0,753576
15	0,034	0,705922
20	0,060	0,646470
25	0,094	0,580592
30	0,134	0,513243
35	0,181	0,448381
40	0,234	0,388742
45	0,293	0,335885
50	0,357	0,290415
55	0,426	0,255242
60	0,5	0,220845
65	0,577	0,195463
70	0,658	0,175277
75	0,741	0,159444
80	0,826	0,147208
85	0,913	0,137893
90	1	0,130924
95	1,087	0,125817
100	1,174	0,122173
105	1,259	0,119966
110	1,342	0,118033
115	1,432	0,117062
120	1,5	0,116583
125	1,574	0,116463
130	1,643	0,116595
135	1,707	0,116893
140	1,766	0,117291
145	1,819	0,117737
150	1,866	0,118190
155	1,906	0,118619
160	1,940	0,118998
165	1,966	0,119310
170	1,985	0,119542
175	1,996	0,119685

7.4 Experiment (B): The lifetime of the positronium

7.4.1 Tasks

1. Recording of the energy spectrum of ^{22}Na and adjustment of the discriminator threshold (see chapter 5.7.3).
2. Time calibration of the measurement setup and determination of the temporal resolution (see chapter 5.7.5).
3. Determination of the mean lifetime of positronium in plexiglass.
4. Determination of the speed of light

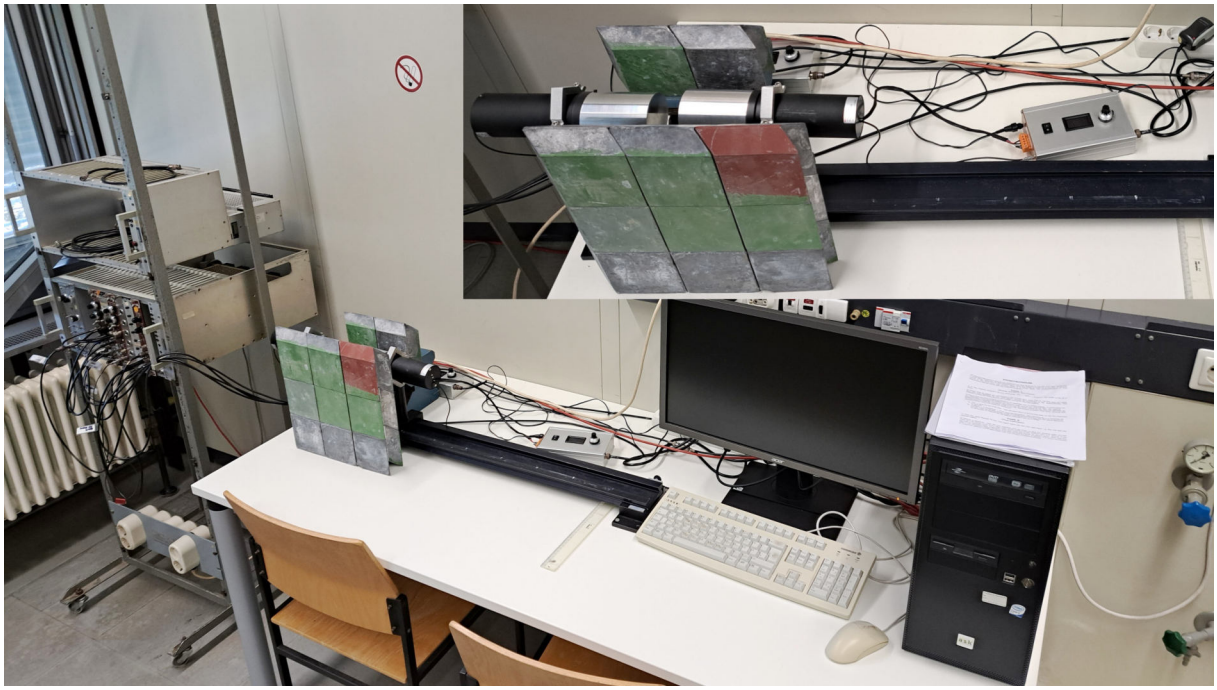

Figure 7.14: Setup of the positronium experiment. The top right corner shows a close-up uf the two photomultipliers.

7.4.2 Introduction

7.4.2.1 Pair annihilation

A positron together with an electron can annihilate into one or more γ quanta (see section 3.2.2.3). Single-quantum annihilation is possible only in matter in which the energy and momentum balance can be satisfied by momentum transfer to a collision partner. In contrast, pair annihilation for two or more quanta is always allowed. In two-quanta decay, provided the electron and positron are at rest, the quanta, each with the energy of an electron rest mass ($511\,\mathrm{keV/c^2}$), are emitted in exactly opposite directions. In three-quanta decay, all emission angles are in one plane and any distribution of decay energies among the individual quanta is possible. The decay into *one* quantum in matter has a much smaller effective cross section than into two, so it is neglected.

The previous discussion of pair annihilation is incomplete because the spin of the leptons has not been included. The leptons have the spin $S = 1/2$. The electron-positron system can

therefore exist (without orbital angular momentum) in two states with total spin $I = 0$ and $I = 1$. In the first case, the spins of the leptons are in opposite direction to each other. It is singular and therefore called singlet state. In the second one, the spins of the leptons are parallel to each other. It is threefold degenerate because of the three possible orientations with respect to a preferred direction. It is called a triplet state.

If the leptons are at rest before the annihilation, or if they have only a small relative velocity, then the relative motion has zero orbital angular momentum, so that the total angular momentum of the pair is solely given by the total spin. Since, in addition to energy and momentum, the total angular momentum is also conserved in the annihilation, an angular momentum of zero must be carried by the γ quanta in the case of singlet annihilation, and an angular momentum of one in the case of triplet annihilation. However, a photon has the spin $I = 1$, which is parallel or antiparallel to the direction of flight. Therefore, two oppositely emitted quanta can only carry a total spin of zero or two. This means that the **singlet state can decay into two quanta, but not the triplet state**. The latter decays into at least three photons. The triplet decay is a process of higher order than the singlet decay and is therefore less probable.

Quantitatively it looks like this. The cross section for the two quantum decay is known from electrodynamics.

$$\sigma_{2\gamma} = \pi \cdot r_0^2 \cdot \frac{c}{v} \tag{7.54}$$

r_0 is the classical electron radius $r_0 = e^2/m_0c^2$, c the velocity of light and v the relative velocity of the leptons. It exhibits the typical $1/v$ law of slow collision processes, so it increases sharply with decreasing velocity. The equation is valid in the approximation of small velocity $v \ll c$. Thus one obtains for the decay probability,

$$\lambda_{2\gamma} = \sigma_{2\gamma} \cdot v \cdot N \tag{7.55}$$

with the electron density N in the medium where the decay takes place. Because of $N = \varrho \cdot Z/A$, it is

$$\lambda_{2\gamma} = \pi \cdot r_0^2 \cdot c \cdot \frac{\rho \cdot Z}{A} = \frac{1}{\tau_{2\gamma}} \tag{7.56}$$

Inserting the values for Plexiglas here, the value for the mean lifetime $\tau_{2\gamma}$ is $4 \cdot 10^{-10}$ s. This is only approximately correct, since in Eq. 7.54 the Coulomb interaction between the particles is not considered. However, it can be seen that the probability for positron annihilation is larger (or the mean lifetime smaller) than that for optical transitions in the atom, which is of the order of 10^7 per s. It is proportional to the electron density of the surrounding matter. This is an important property, because it allows to distinguish the decay of free positrons, from that of positronium, which is independent of density.

In the calculation of the effective cross section in Eq. 7.54 it was averaged over the initial spin states. Since there are a total of four spin states, but the triplet states cannot decay into two quanta, the result for the singlet cross section ${}^1\sigma_{2\gamma}$ with the corresponding probabilities and average lifetimes are

$${}^1\sigma_{2\gamma} = 4 \cdot \sigma_{2\gamma} \qquad {}^1\lambda_{2\gamma} = 4 \cdot \lambda_{2\gamma} \qquad {}^1\tau_{2\gamma} = \frac{1}{4} \cdot \tau_{2\gamma} \tag{7.57}$$

From electrodynamics we know that the cross section for the triplet decay is smaller than the singlet cross section by the order of magnitude of the fine structure constant α ($\alpha = e^2/\hbar c \approx 1/137$), because the probability for the emission or absorption of *one* photon is given by α, the coupling constant of the electromagnetic interaction. The exact calculation results in

$$ {}^3\sigma_{3\gamma} = \frac{\alpha}{8} \cdot {}^1\sigma_{2\gamma} \tag{7.58} $$

Thus the observable ratio of the two decay possibilities is given as

$$ \frac{\sigma_{3\gamma}}{\sigma_{2\gamma}} = \frac{3/4 \cdot {}^3\sigma_{3\gamma}}{1/4 \cdot {}^1\sigma_{2\gamma}} = \frac{3}{8}\alpha = \frac{1}{372} \tag{7.59} $$

The probability of triplet decay is therefore much smaller than for singlet decay, provided that, as has been assumed so far, the lepton pair has freely annihilated, i.e. no positronium has formed.

7.4.2.2 Positronium formation

Free decay is not the only conceivable way for a lepton pair to interact. A hydrogen-like structure, the positronium, can also form, in which a positron replaces the hydrogen nucleus. The energy states are calculated in the same way as for the hydrogen atom. The reduced mass of the atom, which is (almost) equal to the rest mass of the electron, is replaced with the reduced mass of the positronium, which is exactly equal to half the rest mass of the electron. The binding energy is then 6.8 eV, (approximately) half that of hydrogen.

As for a free electron-positron pair, there are two spin states for the positronium, the singlet state and the triplet state. In the first case it is called para-positronium, in the second ortho-positronium. The average lifetimes of these two states can be calculated similar to the free decay, starting from Eq. 7.54. In Eq. 7.55, however, the density of the electron at the location of the nucleus is inserted, instead of the electron density N of the matter. This is known from the hydrogen atom.

$$ |\Psi(0)|^2 = \frac{1}{\pi}\left(\frac{1}{2 \cdot n \cdot a_0}\right)^3 \tag{7.60} $$

Here a_0 is the first Bohr radius and n is the principal quantum number. The lifetime of the singlet state is then

$$ {}^1\tau_{2\gamma} = 2 \cdot \frac{r_0}{c \cdot \alpha^6} \cdot n^3 \tag{7.61} $$

In the ground state, this is $1.25 \cdot 10^{-10}$ s, almost the same value as for free annihilation. The average lifetime of the ortho-positronium is much longer. It is calculated from Eq. 7.58 and Eq. 7.61 and is equal to $1.4 \cdot 10^{-7}$ s, a value comparable to the lifetimes of excited atomic states. Therefore, unlike para-positronium, ortho-positronium almost never decays from excited states because it lives long enough for the excited state to transfer to the ground state before decaying.

The detailed experimental investigation of the positronium decay has led to the following ideas about the formation of positronium in matter. First, the energetic positron is decelerated by predominantly inelastic collisions with electrons, just as fast electrons are. According to the $1/v$ law, the positrons are still too fast to annihilate. Excitation and ionization of the atoms are much more likely. The deceleration is very fast, it takes about 10^{-12} s in solids. After this time, the positron has energies in the eV range, where the annihilation and the formation of positronium become noticeable. There is an energy range where no inelastic processes can take place other than the formation of positronium. The minimum energy that a positron must have in order to release an electron from an atom is $E_{\text{kin}} = V - 6.8\,\text{eV}$, where V is the ionization energy of the atom and 6.8 eV is the binding energy of the positronium, which is released during its formation. The maximum energy of this region is $E_{\text{max}} = E_a$, the lowest excitation energy of the atom (or molecule). Thus:

$$ \Delta E = E_{\text{max}} - E_{\text{min}} = E_a - (V - 6,8\,\text{eV}) \tag{7.62} $$

This energy is called Ore-Gap after its Scandinavian inventor.

7.4.2.3 Positronium detection

For the detection of positronium, it is not sufficient to determine the two- or three-quantum decay. Even if they have the above mentioned lifetimes, they can also come from free decay. There are two possibilities. First, one can determine the ratio of the intensities of the two decays, that is, ratio of the short- and long-lived components of the γ spectrum. For the free decay, it is given by Eq. 7.59. If, on the other hand, positronium is formed, it is determined by the probabilities of the formation of the individual states, and this is

$$\frac{\sigma_{3\gamma}}{\sigma_{2\gamma}} = \frac{3/4}{1/4} = 3 \tag{7.63}$$

The ortho-positronium has three spin states and therefore is formed three times more often than the para-positronium, meaning that there should be three times more decays registered for the former. In reality, the three-quantum decay does not occur as often as indicated by Eq. 7.63, because the formation of positronium is always accompanied by free decay and because interactions with the environment during the long lifetime, which are still to be discussed, can transform the ortho-positronium into para-positronium.

Secondly, in the case of annihilation in gases, the pressure dependence of the lifetimes can be measured. One finds in gases a long-lived component with an average lifetime of about 10^{-7} s and a short-lived one with 10^{-10} s. When the gas pressure is changed, the intensity of the long-lived component remains constant, while that of the short-lived one decreases with increasing pressure. This behavior is expressed in Eq. 7.56, which describes the free annihilation. The long-lived component, on the other hand, comes from ortho-positronium, whose decay probability is independent of pressure according to Eq. 7.58 and Eq. 7.61.

7.4.2.4 Positronium in solids

Soon after the discovery of positronium in gases, it was found that it can also occur in some solids, such as molecular substances. Thus, a long-lived component with an average lifetime between 2-4 ns was found in polymers, with an intensity of 10-30% of all annihilations (ortho-positronium). Two short-lived components were also found. The first, with an probability of 60-80%, has a mean lifetime of about 0.5 ns and is attributed to free decay. The second, weakest (10%), has an even shorter lifetime, which could not be resolved in the first measurements, but is now identified as the decay of para-positronium with an average lifetime of 0.12 ns.

The remarkable difference in comparison with gases is that the long-lived component decays much faster in solids, and that *two* quanta are emitted in the process and not the expected *three* quanta. Accordingly, processes take place in the solid that either destroy the originally formed ortho-positronium or convert it to para-positronium, thereby shortening the lifetime.

The annihilation proceeds via the so-called pick-off processes, in which the positronium interacts with the electrons of the molecules or with inner-molecular magnetic fields. In these cases, a collision partner is present that can absorb momentum and angular momentum, so that the much more probable two-quantum decay also becomes possible for the triplet state. The spectrum of quanta is continuous up to a maximum energy of 0.511 MeV.

The conversion is caused by electron exchange of the positronium with electrons of the matter. Thereby the triplet state changes into the singlet state. The reverse transition can also take place, even with the same probability. However, since this is smaller than the decay probability of the singlet state and larger than that of the triplet state, the conversion destroys more ortho-positronium than it creates. The conservation of angular momentum requires an angular

momentum change of the impact partner opposite to the spin change of the positronium. Thus, in contrast to the pick-off processes, γ quanta with a fixed energy of 511 keV are produced here.

The shortened average lifetime of ortho-positronium has the form

$$\frac{1}{\tau_{Ortho}} = \frac{1}{\tau_0} + \frac{1}{\tau_P} + \frac{1}{\tau_K} \tag{7.64}$$

τ_0 is the unperturbed mean lifetime as would be measured in the absence of the interactions with matter. The probabilities $1/\tau_P$ and $1/\tau_K$ describe the strength of the pick-off and the conversion processes. They can be calculated with appropriate modelling and are determined by the properties of the solid. The measurement of τ_{Ortho} allows the underlying ideas to be tested and thus provides an approach to solid state physics.

7.4.3 Principle of the measurement

For the measurement of the mean lifetime, events must be used, which are temporally connected with the creation or decay of positrons or positronium. In molecular substances, according to the above, (almost) no three-quantum decay occurs. Therefore, during the annihilation of positrons, either quanta appear with the fixed energy of 0.511 MeV, originating from the singlet states, or those with a continuous spectrum up to this maximum energy, originating from the pick-off processes.

The time of the creation of a positron cannot be determined easily. It becomes feasible if simultaneously with the β^+-decay of a nucleus also a γ-quantum is emitted. This is the case for ^{22}Na. Here, the β^+ transition goes preferentially to an excited state of the daughter nucleus ^{22}Ne, whose average lifetime is about 10^{-13} s for the transition to the ground state, and which therefore is instantaneous within the measurement accuracy of the time. In this process, a γ^+ quantum of 1.276 MeV is emitted. Therefore, the appearance of this quantum marks the time of the appearance of the positron, and beyond that also the time of the possible formation of the positronium, since the deceleration time of the positron in matter is also very short, namely approx. 10^{-12} s.

7.4.4 Setup and measurement procedure

The experiment consists of a time measurement between two selected events (see section 5.7.5) marking the beginning and the end of the positron or positronium. ^{22}Na is used as the positron source. The start signal for the TPC (time to pulsheight converter) is derived from the 1.276 MeV γ quantum of ^{22}Ne, which is selected by the method described in section 5.7.3, using a discriminator. One would prefer to use annihilation radiation with energies less than or equal to 0.511 MeV as the stop signal. However, this range cannot be easily cut out from the total spectrum of the source. Therefore, one stops with triggers from the entire energy spectrum, accepting a higher rate of random coincidences than would result in the ideal case. Of course, one has to make sure that the random coincidences do not get out of hand. Therefore, only the possibly occurring electronic noise at the lower end of the spectrum is cut off in the stop branch.

Fast plastic scintillators with photo-multipier tubes (PMT) are used as detectors, which detect the γ quanta essentially via the *Compton effect* due to their low average nuclear charge number (see sections and 4.2).

For the time calibration of the setup, e.g. a ^{60}Co source can be used, which simultaneously emits two γ quanta at 1.173 MeV and 1.332 MeV, both above the set start threshold. The TPC then provides a pulse height spectrum, called the prompt curve, with a Gaussian distribution corresponding to exactly simultaneous events and whose half-width is a measure of the time resolution of the array. By adding various delays in the stop branch, the delay time of the stop

signal is extended by known values and the prompt curve is shifted accordingly. The magnitude of the shift plotted against the difference of the propagation times provides the calibration curve.

If the two detectors are not positioned arbitrarily, but so that the start and stop quanta fly apart at an angle of 180°, the ^{22}Na source does not need to be replaced by ^{60}Co. In this case, the calibratio can be done with the annihilation radiation of ^{22}Na. For this purpose, only the threshold for the start signal has to be lowered accordingly, in order to trigger on as many as possible events from the Compton spectrum of the second annihilation gamma. The threshold should be set just to cut the noise signal of the detector. This method has even the advantage that the prompt curve builds up - almost - with the speed of a *single* decay rate, since the two annihilation gammas are emitted in opposite directions, unlike the (almost) uncorrelated directions of the gammas from the ^{60}Co source. In contrast, the also existing events, delayed by the average lifetimes, which occur with the rate of a *coincidence*, do not matter, since the prompt gammas are emitted in arbitrary directions.

It should be noted that the TPC only works properly if the stop signal arrives a few nanoseconds after the start signal. Therefore, a fixed delay (about 2 ns) is included for all measurements. This corresponds to the minimum delay of the delay box with all switches in the off position.

Due to the good time resolution of the TPC, the setup allows to easily determine the speed of light with which the gamma quanta propagate. For this purpose, the detector for the stop-signal is placed on the aluminum rail, on which the PMT mounts are fixed, at different distances x (0 ... 60 cm) from the start-detector and the time spectrum $\Delta t(x)$ is recorded. This measurement is best made with the lowered start threshold, which is also used for time calibration. The slope of the linear curve $\Delta t(x)$ over x then provides the propagation velocity of the gamma quanta.

For a reasonable measurement time the following sequence is recommended:

1. Record the energy spectrum of the start detector with a low discriminator threshold. To do this, plug the ADC cable into the unipolar output of the spectroscopy amplifier and set the lower threshold of the CF-discriminator to the lowest value. Discuss the observed energy spectrum.

2. While observing the energy spectrum (superposition of the Compton spectra of the two gamma energies), the discriminator threshold is now slowly increased until the Compton spectrum of the 511 keV gammas is completely cut off, so that only 1,276 keV gammas trigger a start signal.

3. The ADC cable is now connected to the output of the TPC in order to record the differential time spectrum (measurement time approx. 1 h).

4. For the time calibration and the measurement of the speed of light, the start threshold is then lowered again so that the discriminator triggers on as many 511 keV gammas as possible, but noise signals are still suppressed. Tip: if double peaks occur in the time spectrum, the trigger threshold is set too low.

5. For time calibration, time spectra can be recorded at different delay times of the delay box. The values should be recorded between 0 and 32 ns with an interval of 4 ns. At 4 ns, the overlap of the individual time peaks is large enough to record all peaks in a single spectrum. The mean value of the peaks at 0 ns delay, at which the lifetime spectrum was also measured, can be used as the zero point of the linear calibration function.

6. For the measurement of the speed of light, the time peaks at different distances of the right detector from the source (0 – 60 cm) are recorded at 0 ns delay. Each time spectrum should be marked in a separate histogram, as otherwise the peaks would overlap too much.

7.4.5 Evaluation

The measured time spectrum theoretically consists of the superposition of three decays. However, the time resolution is not sufficient to separate the two fast decays of the free annihilation and the para-positronium, so only two components are considered. Thus, the spectrum has the form

$$N(t) = A \cdot e^{-\frac{t}{\tau_1}} + B \cdot e^{-\frac{t}{\tau_2}} + C \tag{7.65}$$

C is a constant pedestal, independent of time, on which the exponential functions are superimposed. These are the random coincidences. Random means, after all, equally probable at any time. The height of the pedestal can be seen at sufficiently large times, at which the e-functions have decayed. If, as in the present case, the mean lifetimes are considerably different from each other, this is most easily seen by plotting the logarithm of the count rates versus time. At sufficiently large times, the short-lived component has decayed and no longer contributes anything to the sum. In this range, the curve is a straight line whose slope yields the average lifetime of the long-lived component. With modern fitting methods the free parameters A, B, C, τ_1, and τ_2 of Eq. 7.65 and their respective errors can be directly determined, using for instance appropriate libraries in PYTHON. The intensities A and B correspond to the intercepts of the exponential curves at $t = 0$ (by definition the position of the undelayed prompt curve in the time spectrum). The ratio of the two components of the spectrum $\tau_1 A/\tau_2 B$ is thus obtained by integration over time from 0 to infinity.

As time values Δt for the calibration as well as for the speed of light measurement the peaks of the respective time spectra should be used. The position of the maximum can be determined with a gaussian fit to the time distribution.

7.4.6 Literature

Introduction chapters 1 – 6 in this script
Positrons, Positronium: [1], [13], [23], [24], [25]
Elektronics: [18], [21], [22]
Detectors: [18], [19]

7.5 Experiment (B): Neutron Diffusion

7.5.1 Tasks

1. Determination of the relaxation length of fast neutrons in water.
2. Determination of the diffusions length thermal neutrons in water.

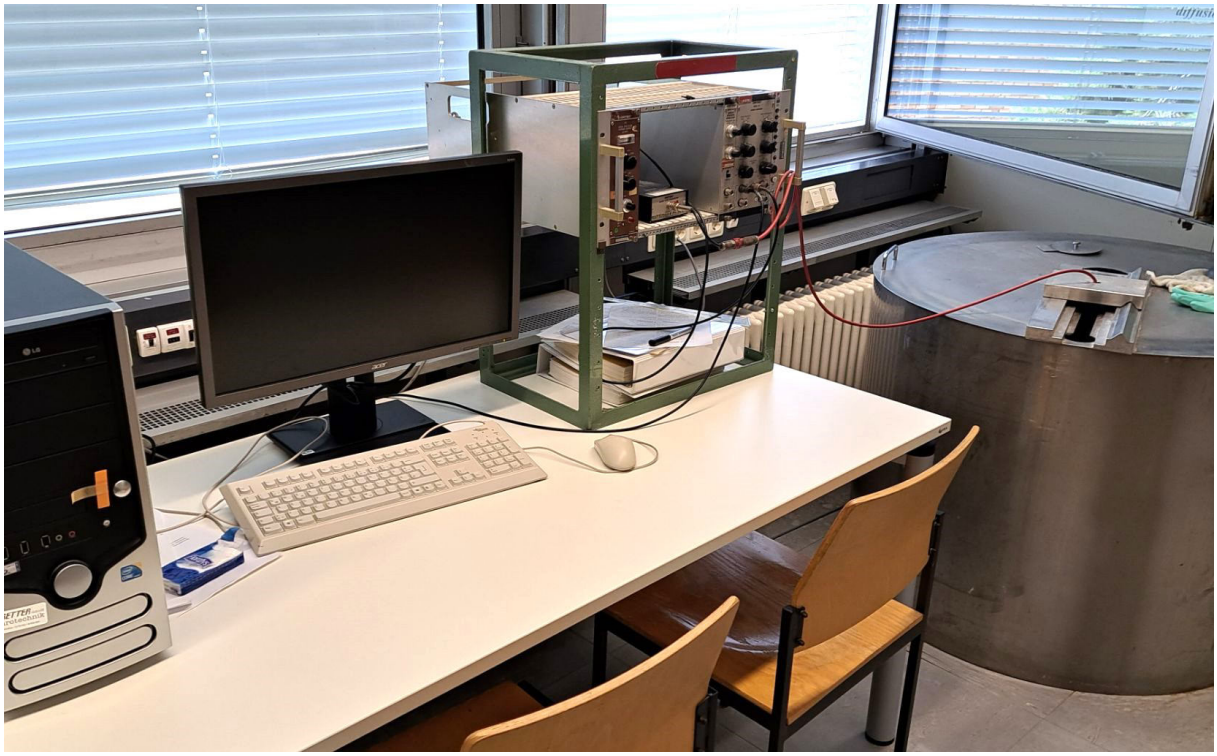

Figure 7.15: Setup of the neutron diffusion experiment. On the right side the water tank with the submerged source and detector are seen.

7.5.2 Introduction

7.5.2.1 Definition of the neutron flux

A neutron field is described by the differential density $n(\vec{r}, \vec{\Omega}, E)$, which is defined as the number of neutrons at the location $\vec{r}$, with energies in the unit energy interval around the energy E and with directions in the unit solid angle around the direction $\vec{\Omega}$. Then $n(\vec{r}, \vec{\Omega}, E)\mathrm{d}V\mathrm{d}\Omega\mathrm{d}E$ is the number of neutrons in the volume element $\mathrm{d}V$ with energies between E and $E + \mathrm{d}E$ lying in the differential solid angle $\mathrm{d}\Omega$ around $\vec{\Omega}$.

The integration over all neutron energies gives the number of neutrons in the volume element with the direction of flight $\vec{\Omega}$.

$$n(\vec{r}, \vec{\Omega}) \cdot \mathrm{d}V \cdot \mathrm{d}\Omega = \int_E n(\vec{r}, \vec{\Omega}, E) \cdot \mathrm{d}E \cdot \mathrm{d}V \cdot \mathrm{d}\Omega \tag{7.66}$$

$n(\vec{r}, \vec{\Omega})$ is the vector density. Integration over all directions in space yields the number of all neutrons in the volume element of any energy and direction:

$$n(\vec{r}) \cdot \mathrm{d}V = \int_\Omega n(\vec{r}, \vec{\Omega}) \cdot \mathrm{d}V \cdot \mathrm{d}\Omega = \int_E \int_\Omega n(\vec{r}, \vec{\Omega}, E) \cdot \mathrm{d}E \cdot \mathrm{d}V \cdot \mathrm{d}\Omega \tag{7.67}$$

Here $n(\vec{r})$ is the neutron density.

Another important quantity, especially for the neutron transport, is the neutron flux $\Phi(\vec{r})$ which is defined as

$$\Phi(\vec{r}) = \int_E \int_\Omega n(\vec{r}, \vec{\Omega}, E) \cdot v(E) \cdot \mathrm{d}E \cdot \mathrm{d}\Omega \tag{7.68}$$

$v(E)$ is the magnitude of the velocity of the neutrons, which of course depends on the energy. The integrand gives the number of neutrons passing through the unit surface perpendicular to $\vec{\Omega}$ in the unit time, having energies between E and $E + \mathrm{d}E$ and whose directions of flight are at the differential angle about $\mathrm{d}\Omega$. An average speed $\bar{v}$ can be calculated by

$$\bar{v} = \frac{\int_E \int_\Omega n(\vec{r}, \vec{\Omega}, E) \cdot v(E) \cdot \mathrm{d}E \cdot \mathrm{d}\Omega}{\int_E \int_\Omega n(\vec{r}, \vec{\Omega}, E) \cdot \mathrm{d}E \cdot \mathrm{d}\Omega} \tag{7.69}$$

With this, Eq. 7.67 and Eq. 7.68 the flux can also be written as

$$\Phi(r) = n(r) \cdot \bar{v} \tag{7.70}$$

It has the dimension of neutrons per area and per time. For neutrons with uniform direction of flight, a beam gives the number of neutrons passing through the unit area in the unit time. For isotropic (and nearly isotropic) neutron fields, the number of neutrons traversing the unit area per unit time *from all directions* is equal to $\Phi/2$. The factor of 2 is obtained by integrating over all spatial directions [33].

7.5.2.2 The propagation of fast neutrons in matter

The propagation of fast neutrons in matter has great similarity with the transport of γ-quanta. As uncharged particles, they do not lose their energy continuously, but in single discrete elementary processes, mainly in reactions with nuclei. The most common ones are:

Elastic scattering: Here the sum of the energies of the collision partners is constant. However, since the nuclei are at rest before the collision, the neutrons lose energy in the process. They are also deflected from their original direction. The energy transfer during the collision (Eq. 3.16) depends on the mass of the nucleus and is largest for the proton. The effective cross section for elastic collisions increases strongly with decreasing neutron energy.

Absorption: The neutron is captured by the nucleus, which emits γ quanta or other particles in the process. Examples are the reactions in Eq. 3.18 and Eq. 3.19. Also for absorption, the effective cross sections are largest at small energies.

The inelastic scattering: In this process, excitation energy is transferred to the nucleus. The neutrons therefore lose more energy than in the elastic collision. However, the effective cross sections are smaller.

The spatial flux distribution of neutrons emitted from a point source is derived exactly as the intensity distribution of γ quanta (Eq. 3.23, Eq. 3.43). If the source is point-like, the flux is given by

$$\Phi(r) = \frac{Q_0}{4\pi \cdot r^2} \cdot \exp(-\Sigma_t \cdot r) \tag{7.71}$$

Where Q_0 is the number of neutrons emitted by the source per unit time, the source intensity. The $1/r^2$ decrease is the usual intensity distribution around a point source in a non-absorbing medium, which follows from the fact that the rate of particles passing through any closed area

around the source is equal to the rate of particles emitted by it. In a medium with absorption, an exponential decay is superimposed on this distribution. The exponential function describes the probability that a neutron will travel the distance r without a reaction with matter.

The quantity Σ_t with the dimension of a reciprocal length is the total linear absorption coefficient, which is composed of the contributions from the possible processes,

$$\Sigma_t = \Sigma_{el} + \Sigma_a = N \cdot \sigma_t = N \cdot (\sigma_{el} + \sigma_a) \tag{7.72}$$

in this case the elastic scattering and absorption. It is associated with the respective effective cross sections σ, where N is the density of the nuclei. The quantity

$$\lambda = \frac{1}{\Sigma_t} \tag{7.73}$$

with the dimension of a length is called **relaxation length** and is the average distance that the neutrons travel in matter before they are scattered or absorbed.

The flux in Eq. 7.71 gives the distribution of those neutrons which have not yet made a reaction and therefore still have the original energy. They are called primary neutrons. The actual flux at the position r contains also the secondary neutrons which have already lost energy and therefore deviates from the given equation.

A deviation can also be expected if the source is not monochromatic but has a continuous spectrum, since the total linear absorption coefficient is energy dependent.

7.5.2.3 The thermalization of neutrons

As long as the kinetic energy of the neutrons is greater than that of the collision partners, they give off energy when interacting with the nuclei of matter. Therefore, after a series of collisions, the excess kinetic energy is completely transferred to the matter. The neutrons are then in thermal equilibrium with their environment: they are said to be thermalized. Their velocities then obey the Maxwellian velocity distribution at the ambient temperature T. If one looks more closely, this is not quite true, since during thermalization neutrons are lost by absorption and others leave the interaction region. However, the deviations are not significant.

The most probable velocity of the Maxwell distribution is

$$v_T = \sqrt{\frac{2 \cdot k \cdot T}{m}} \tag{7.74}$$

where m is the mass of the neutron, k is the Boltzmann constant. The corresponding energy of the neutrons is

$$E = \frac{1}{2} \cdot m \cdot v_T^2 = k \cdot T \tag{7.75}$$

At room temperature (T=273 K) it is 0,025 eV.

7.5.2.4 Propagation of thermal neutrons: Diffusion theory

The goal of neutron transport theory is to find the energetic and spatial distribution of neutrons for a given arrangement of source and matter. The differential neutron density $n(\vec{r}, \vec{\Omega}, E)$ is sought, from which the further quantities, for example the flux, can be derived. This task is solved by the transport or Boltzmann equation. It is nothing else than a continuity equation, which expresses the neutron balance for the differential neutron density. This increases with the emission from the source and with neutrons scattered from other (higher) energies and directions. It decreases with absorption and scattering towards lower energies and other angles. The

Boltzmann equation is an integro-differential equation, which in general has no closed solution. There are several approximate solutions, all starting with simplifying assumptions. One of them leads to the elementary diffusion theory.

In this steady state theory, i.e. time independent, solutions are sought, which do not depend on the energy. Only absorption and scattering are allowed. The effective cross sections for these processes, the absorption cross section Σ_a and the scattering cross section Σ_s, are assumed to be energy independent. It is clear that such a theory cannot describe the process of thermalization itself, which is characterized by the very fact that the neutrons change their energy. It describes only systems in which no more energy is exchanged, i.e. monoenergetic groups. Therefore the diffusion theory can be applied to thermal neutrons.

Under these preconditions and the additional condition of weak absorption ($\Sigma_a \ll \Sigma_s$), the Boltzmann equation for a point source reduces to the elementary diffusion equation

$$D \cdot \nabla^2 \Phi(r) - \Sigma_a \Phi(r) + S(r) = 0 \tag{7.76}$$

Thereby

$$D = \frac{1}{3 \cdot \Sigma_s} \tag{7.77}$$

the diffusion constant and $S(r)$ the source density of neutrons, which is the number of neutrons emitted at location r per unit volume and time. By introducing the length L

$$L = \sqrt{\frac{D}{\Sigma_a}} \tag{7.78}$$

this equation can also be written

$$\nabla^2 \Phi(r) - \frac{1}{L^2} \Phi(r) + \frac{S(r)}{D} = 0 \tag{7.79}$$

The first term describes the change of the flux by diffusion or scattering, the second the decrease by absorption and the third the increase by emission from the source. This equation applies exactly only to a homogeneous infinitely extended medium and not in the vicinity of the source. However, it is a very good approximation also for finite media in such regions which are more than two free path lengths away from the boundary and from the source.

Under the boundary condition that the flux vanishes at infinity, the general solution is

$$\Phi(r) = A \cdot \frac{e^{-r/L}}{r} \tag{7.80}$$

With the additional condition that the total number of neutrons emitted per unit time, which is given by the source strength Q, must be absorbed somewhere in the medium at the same time in the stationary state

$$Q = \int_V \Sigma_a \Phi(r) \cdot \mathrm{d}V = 4\pi \cdot A \cdot \Sigma_a L^2 \tag{7.81}$$

, the constant A can be determined, and one finally has

$$\Phi(r) = \frac{Q}{4\pi \cdot D} \cdot \frac{e^{-r/L}}{r} \tag{7.82}$$

The main difference from Eq. 7.71, which describes the transport of fast neutrons, is the decay with $1/r$, which is characteristic for diffusive fields. The flux of thermal neutrons decays more slowly with distance from the source than the flux of fast ones. The length L introduced in Eq. 7.78 is called **diffusion length**. It describes the absorption behavior of the medium and has

a descriptive physical meaning. It is a measure of the average distance $\bar{r}$ from the source where a neutron is absorbed.

$$\bar{r} = \frac{\int_0^\infty r \cdot \Sigma_a \Phi(r) \cdot 4\pi \cdot r^2 \cdot \mathrm{d}r}{\int_0^\infty \Sigma_a \Phi(r) \cdot 4\pi \cdot r^2 \cdot \mathrm{d}r} = 2L \tag{7.83}$$

This mean distance is not to be confused with the distance a thermal neutron actually travels between creation and absorption. This is longer because of the zigzag motion.

7.5.3 Principle of the measurement

7.5.3.1 Relaxation length

A measurement rule for the relaxation length follows directly from Eq. 7.71. One measures the flux of a monochromatic neutron source as a function of the distance from the source and carries it in the equation

$$\ln\left[r^2 \cdot \Phi(r)\right] = -\frac{r}{\lambda} + \text{konst.} \tag{7.84}$$

which is obtained by logarithmizing Eq. 7.71. This is a straight line with the slope of the reciprocal relaxation length. Only the primary neutrons may be detected. This method of measurement is not applicable for two reasons:

1. It is difficult to separate the primary neutrons from the secondary ones, whose energies are, after all, continuously distributed up to the maximum value of the primary energy. When measuring, for instance, with a proton recoil detector, only the high energy end of the spectrum can be used (see Fig. 3.7). Since the spectrum decreases at the high end, one has small count rates and can only measure inaccurately.

2. There is no source of monoenergetic neutrons in the laboratory. These can only be generated in nuclear reactions at an accelerator.

In the available experiment an Am-Be source with continuous spectrum is used (see section 2.5). The neutrons are detected with the ^{10}B reaction (Eq. 3.17), which is only sensitive to thermal and slow neutrons. Therefore, the flux is not expected to have a shape as in Eq. 7.84.

Thus, the experimental fact is at first surprising that the flux measured in water under these conditions obeys this equation. The distribution of slow and thermal neutrons follows the distribution of fast primary neutrons. A physical reason can be given for this. The neutrons are mainly scattered by the protons of the water. The effective cross section increases sharply with decreasing neutron energy (see section 3.2.1.1). Since the energy transfer per collision is large, the neutrons are soon in the region of high effective cross section and therefore have small mean free path length. They are thermalized close to the site of the first collision. Also, as thermalized neutrons, they do not move far away on average. An estimate using Eq. 7.80 shows that the probability for thermal neutrons in water to move more than 3 cm away from the site of their origin is less than 10%. Therefore, it is an acceptable approximation to measure only the thermal flux to determine the relaxation length of fast neutrons in water.

Nevertheless, the relation in Eq. 7.80 can be considered only as a phenomenological interpretation of the measured data determined by the special experimental conditions. The relaxation length obtained from it does not have the exact meaning of the definition. It changes with the spectrum of the source, the spectral sensitivity of the detector, and with the geometry of the experimental setup. Nevertheless, it is useful because it accidentally describes the course of the flux more or less well. It has a certain importance, because with this knowledge the necessary thickness of the shielding against fast neutrons can be estimated.

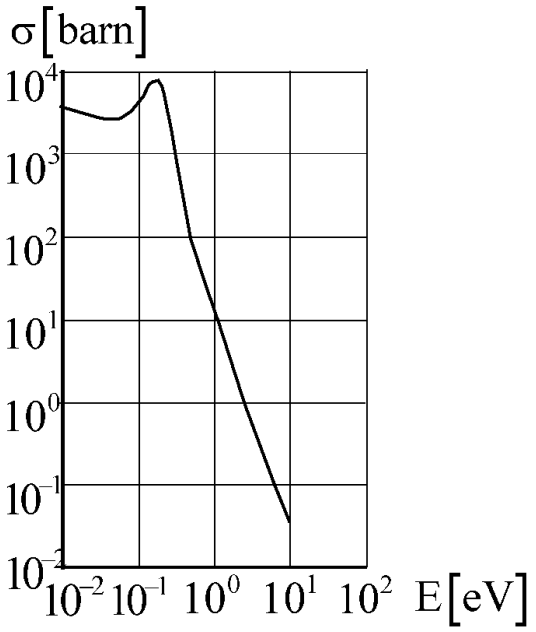

Figure 7.16: Absorption cross section of cadmium.

7.5.3.2 Diffusion length. Cd-difference method

According to Eq. 7.82, the diffusion length can be determined as follows: take a point source of thermal neutrons, measure the flux as a function of the distance from the source, plot the measured values with

$$\ln\left[r \cdot \Phi(r)\right] = -\frac{r}{L} + \text{konst.} \tag{7.85}$$

and determine L from the slope. One cannot proceed in this way, because there is no point source of thermal neutrons. The source provides fast neutrons, and they are thermalized at all locations in the water. Therefore, the distribution of thermal neutrons is anything but point-like.

Nevertheless, a thermal source can be realized by an experimental trick, the Cd-difference method. In a first measurement, the flux $\Phi_0(r)$ caused by the fast neutrons from the source is measured as a function of the distance from the source. Since the proportional counter tube is sensitive only up to a few 100 keV, it does not include all neutrons that are emitted, but only those that have already lost some energy due to collisions, including those that have been thermalized somewhere in the water and diffuse into the counter tube. No thermal neutrons come from the source itself. Now a spherical shell of cadmium a few centimeters in diameter and 1 mm thick is placed around the source. Cd has the property of strongly absorbing thermal and slow neutrons up to about 0.5 eV. From Fig. 7.16, where the absorption cross section is plotted as a function of energy, it can be seen that the cross section for thermal neutrons is about $2.5 \cdot 10^3$ barn. The probability for these neutrons to penetrate a Cd layer of 1 mm thickness is 10^{-6}, practically zero. If in a second measurement the flux $\Phi_m(r)$ is determined with Cd, then as in the first measurement the fast neutrons' contribution remains unchanged. But the ones which have been decelerated within the shielding to energies below 0.5 eV, i.e. the thermal and epithermal ones (which are not distinguished anymore) are now missing. Taking the difference of the two measurements, one obtains the flux of neutrons which have been thermalized inside the Cd sphere, and thus has a virtual source of thermal neutrons, which is considered to be point-like at a sufficient distance. This flux is now plotted according to Eq. 7.85 and then the diffusion length can be determined.

7.5.4 Setup and execution

The Am-Be source is located in the center of a cylindrical water tank with 100 cm diameter and 80 cm height. The BF_3 counting tube is movable in radial direction. The count rate is measured with and without Cd shielding at different distances. From the values without shielding the relaxation length can be determined and from the different distance of the measurements the diffusion length can be determined. Because of the approximation of a point source, it is not useful to measure at distances smaller than 14 cm.

In the spectrum of the counting tube, a threshold must be set at the low-energy end to cut off the electronic noise and the still noticeable fraction of γ quanta from the source despite the small sensitivity. The measurement method is therefore the counting of selected events. Here, the spectrum is determined with multichannel analyzer.

7.5.5 Literature

Introduction chapters 1 – 6 in this script
Neutron physics: [1], [33], [34]
Detectors: [18]
Electronics: [21], [22]

7.6 Experiment (B): Measurement of angular correlation of γ radiation

7.6.1 Tasks

1. Measurement of the γ-γ correlation of ^{60}Ni.
2. determination of the anisotropy and the correlation function.
3. determination of the time resolution of the coincidence.

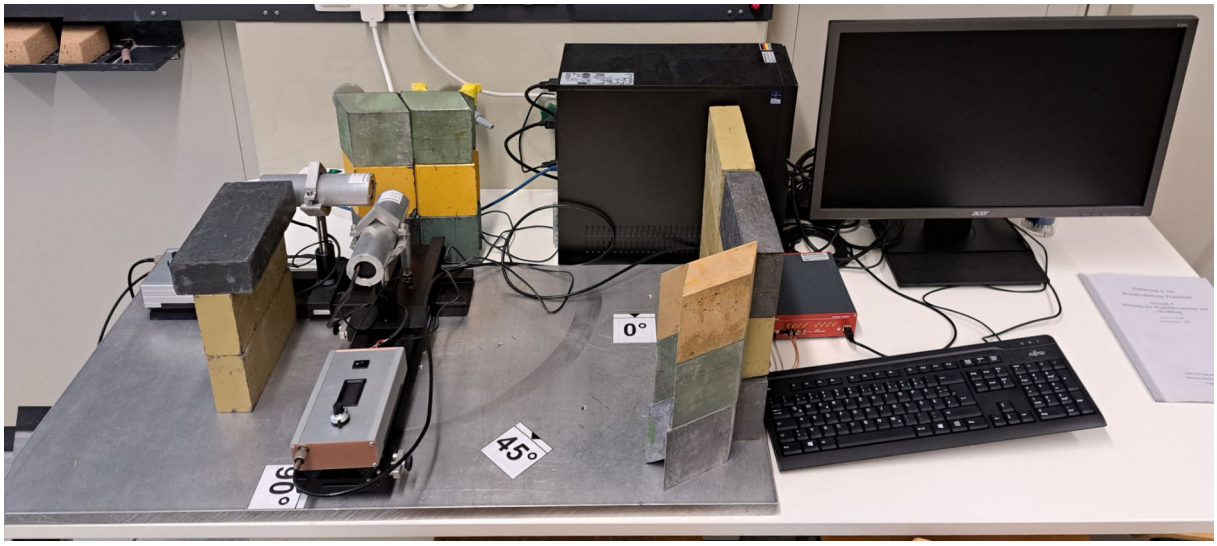

Figure 7.17: Setup of the angular correlation experiment. On the left side of the picture there are two PMTs with NaI detectors. The one in front can be rotated around the vertical axis between the two detectors, where also the ^{60}Co source will be placed.

7.6.2 Introduction

The radiation of an electromagnetic transition between a state with spin J_1 and a state with spin J_2 is isotropic, i.e. the intensity is independent of the emission angle with respect to a certain direction, under two conditions:

- the $2J_1 + 1$ sub-states with different magnetic quantum numbers are equally occupied,
- all transitions possible between the J_1, m_1 and J_2, m_2 states are observed.

This shall be explained in more detail by a simple example. The transition between a state with $J_1 = 1$ and the ground state with $J_2 = 0$ is considered. The upper state is triple degenerate, it has magnetic quantum numbers $m_1 = +1, 0, -1$, the lower state is simple with $m_2 = 0$. Thus, there are three possible dipole transitions with

$$\Delta m = m_1 - m_2 = +1, 0, -1 \tag{7.86}$$

From optics we know the probabilities for these transitions

$$\begin{aligned} W_+ \cdot \mathrm{d}\Omega &= \frac{3}{16} \cdot \pi \cdot \left(1 + \cos^2\theta\right) \cdot \mathrm{d}\Omega \\ W_0 \cdot \mathrm{d}\Omega &= \frac{3}{8} \cdot \pi \cdot \sin^2\theta \cdot \mathrm{d}\Omega \\ W_- \cdot \mathrm{d}\Omega &= \frac{3}{16} \cdot \pi \cdot \left(1 + \cos^2\theta\right) \cdot \mathrm{d}\Omega \end{aligned} \tag{7.87}$$

θ is the angle between the emission direction and the z-axis chosen as the quantization axis.

The probabilities for the individual components are not isotropic, e.g. $W_0 = 0$ for $\theta = 0$. Only the sum of the probabilities is isotropic

$$W_{tot} = \sum_i W_i \cdot \mathrm{d}\Omega = \frac{3}{4} \cdot \pi \cdot \mathrm{d}\Omega \tag{7.88}$$

In the experiment, the intensity I_{tot} of the radiation emitted by an aggregate of very many particles located in the states J_1, m_i is measured. This intensity also depends on the occupation numbers N_i of these states.

$$I_{tot} \cdot \mathrm{d}\Omega = \sum_i N_i \cdot W_i \cdot \mathrm{d}\Omega = (N_+ \cdot W_+ + N_0 \cdot W_0 + N_- \cdot W_-) \cdot \mathrm{d}\Omega \tag{7.89}$$

By substituting Eq. 7.87, the sufficient condition for isotropy is that all states with different magnetic quantum numbers are equally occupied: $N_+ = N_0 = N_-$. It is necessary that all transitions are observed together and none is predominant by special measures.

In atomic physics, such selective observations are known in the Zeeman effect. The three states J_1, m_i are energetically split in a magnetic field as a result of the interaction of the magnetic moment with the field. Therefore, the transitions in Eq. 7.87 have different frequencies. Moreover, each transition has a particular polarization: light with $\Delta m = +1$ and $\Delta m = -1$ is right- or left-circular polarized, respectively. For $\Delta m = 0$ it is linearly polarized parallel to the magnetic field. If polarization sensitive detectors are used or if the intensity is measured at a certain frequency, the components of Eq. 7.89 can be determined individually. In this case there is always anisotropy. For example, the component polarized parallel to the field is not present in the case of longitudinal observation ($\theta = 0$).

When observing the angular distribution of γ quanta, the individual components cannot be resolved due to the insufficient energy resolution of the detectors, so that the total intensity of all transitions is always measured. Anisotropy can then only arise from different occupation numbers of the emitting states. There are two methods to generate such occupation differences: first, the polarization of the nuclei (about polarization see V10 parity violation), second, by the method of angular correlation.

An example of polarization is the famous experiment of Wu [28], [40] to prove parity violation in β-decay. For this purpose, ^{60}Co is polarized with nuclear spin $J = 5$ in a magnetic field. A β^--decay fills the excited state of ^{60}Ni, which is also polarized. When it decays by γ emission, the radiation is anisotropic. The anisotropy is a measure of the polarization of the ^{60}Co nuclei.

The polarization of a nucleus with spin J in a magnetic field B occurs because the degeneracy of the $2J + 1$ sub-states is lifted. The splitting energies are

$$\Delta E_i = -\frac{m_i}{J} \cdot \mu \cdot B \tag{7.90}$$

μ is the magnetic moment of the nucleus and m_i its magnetic quantum number. If the set of nuclei is in thermal equilibrium at a temperature T, then the occupation numbers N_i of the sub-states obey the Boltzmann distribution

$$N_i \approx \exp\left(-\frac{\Delta E_i}{k \cdot T}\right) = \exp\left(\frac{m_i}{J} \cdot \frac{\mu \cdot B}{k \cdot T}\right) \tag{7.91}$$

with k the Boltzmann constant. The level with the lowest energy has $m_i = -J$, above it, at equal intervals, lie the states with $m_i = -(J-1), -(J-2), ... + J$. The relative occupation number of a higher state to the state below is

$$\frac{N_{i+1}}{N_i} = \exp\left(-\frac{1}{J} \cdot \frac{\mu \cdot B}{k \cdot T}\right) \tag{7.92}$$

Under normal circumstances, i.e. at small magnetic fields and at room temperature, the exponent is practically zero. The occupation numbers are then the same for all states regardless of the magnetic quantum numbers. Therefore, the γ radiation is isotropic under these conditions. At high fields and extremely low temperatures ($T = 0.01\,\mathrm{K}$) the exponent takes on considerable values. Then only the lowest states, and in the marginal case only the state $m_i = -J$, are noticeably occupied. Almost all nuclei are aligned parallel to the magnetic field, they are strongly polarized, and in the marginal case, completely polarized.

The anisotropy in this method arises because an ordered state is imposed on the totality of the emitting nuclei from the outside by the field and the low temperature. This is different from the correlation experiments. Here the anisotropy arises with initial uniform distribution by *simultaneous* measurement of *two* transitions. These can be: one β-particle and a subsequent γ-quantum of the daughter nucleus or two γ-quanta, if in the latter case the transition to the ground state occurs via one or more intermediate states. The *simultaneous* observation of two transitions overturns the equal occupation with respect to any quantization axis.

Again, it is best to give an example. Suppose one observes a cascade with $J_1 = 0, J_2 = 1$ and J_3 arbitrary. The probabilities of Eq. 7.89 then apply to the first transition. Since the choice of the quantization axis is arbitrary due to rotational invariance, we place it in the emission direction of the first quantum, i.e. $\theta = 0$. Then

$$\begin{aligned} W_+ \cdot \mathrm{d}\Omega &= W_- \cdot \mathrm{d}\Omega = \frac{3}{8} \cdot \pi \cdot \mathrm{d}\Omega \\ W_0 \cdot \mathrm{d}\Omega &= 0 \end{aligned} \tag{7.93}$$

For all nuclei whose *first* quantum has been detected, the intermediate state $J_2 = 1, m_2 = 0$ is not occupied, and therefore the isotropy is overturned for the *second* quantum of the same cascade. The magnitude of the anisotropy depends, of course, on the spin J_3. By the coincident measurement of both transitions, not all intermediate states contribute with equal weight anymore, but some of them are selected in a defined way.

The differential cross section for the simultaneous emission of two γ quanta of a cascade as a function of the angle θ between the emission directions is

$$\frac{\mathrm{d}\sigma}{\mathrm{d}\Omega} = \sum_{i=1}^{i_{\max}} A_{2i} \cdot P_{2i}(\cos\theta) \qquad i_{\max} = \mathrm{Min}\,(L_1, L_2, J_2) \tag{7.94}$$

if it is pure radiation and not multipole mixing. P_{2i} are the Legendre polynomials of order $2i$. The coefficients A_{2i} can be calculated. They contain the transition matrix elements, the spins of the states between which the transitions occur, and the multipole order of the γ radiation. Since parity is preserved in electromagnetic transitions, only even orders of Legendre polynomials occur. The summation adds up to a maximum value $i_{\max}$, the smallest value of the angular momentum of the radiations and the spin J_2 of the intermediate state.

The size of the cross section is determined by the coefficient A_0. In it and in the higher coefficients, the matrix elements of transitions are included as a factor. To eliminate them, the correlation function $K(\theta)$ is introduced.

$$K(\theta) = \frac{\mathrm{d}\sigma(\theta)}{\mathrm{d}\Omega} / \frac{\mathrm{d}(90°)}{\mathrm{d}\Omega} \tag{7.95}$$

It can also be written

$$K(\theta) = 1 + \sum_{i=1}^{i_{max}} a_{2i} \cdot \cos^{2i}\theta \tag{7.96}$$

The coefficients a_{2i} are now given only by the angular momenta. If they are measured and compared with the values calculated for specific angular momenta, the multipole orders of the radiation and the spins of the nuclear states can be determined.

The γ radiation of ^{60}Co is an electric quadrupole radiation ($L_1 = 2, L_2 = 2$) and the spin of the intermediate state is $J_2 = 2$, so $i_{\max} = 2$. Thus one has

$$K(\theta) = 1 + a_2 \cdot \cos^2\theta + a_4 \cdot \cos^4\theta \tag{7.97}$$

with theoretical values $a_2 = 1/8$ and $a_4 = 1/24$.

The deviation of an angular correlation from an isotropic distribution is the anisotropy

$$An = \frac{\mathrm{d}\sigma(180)/\mathrm{d}\Omega - \mathrm{d}\sigma(90)/\mathrm{d}\Omega}{\mathrm{d}\sigma(90)/\mathrm{d}\Omega} = \frac{K(180) - K(90)}{K(90)} = K(180) - 1 \tag{7.98}$$

7.6.3 Setup and measurement procedure

The measurement method is a coincidence measurement as described in chapter 5.7.4. NaI scintillators with photomultipliers are used as detectors. The pulse shape of the photomultiplier signals is digitized with a fast ADC (CAEN Digitizer DT5725, 8x 250 MSPS). The data of the individual events are transferred to a PC (Linux) and stored in a file. Afterwards the pulses are analyzed with the help of a Python script and the pulse height is determined. The pulse height is converted into energy units by an energy calibration. After the energy cut of single pulses, the coincidence condition is validated and the corresponding counting variables for PMT1, PMT2 and the coincidence are incremented. The Python code is executed in a Jupyter notebook.

Since the anisotropy is small, one is tempted to use a probe with a large activity in order to save measurement time. However, this cannot be pushed as far as one likes, otherwise one will get too many random coincidences. The true coincidences depend linearly on the activity

$$N_k = \epsilon_1 \cdot \epsilon_2 \cdot A \cdot f(\Theta) \tag{7.99}$$

A is the activity. The ε_i are the response probabilities of the detectors including the geometry factor. The function $f(\Theta)$ describes the angular dependence of the coincidences and is close to 1. However, the rate of random coincidences (Eq. 5.5)

$$N_Z = \tau_A \cdot N_1 \cdot N_2 = \tau_A \cdot \epsilon_1 \cdot \epsilon_2 \cdot A^2 \tag{7.100}$$

increases quadratically with A, so the ratio of true to random coincidences is

$$\frac{N_K}{N_Z} \approx \frac{1}{\tau_A \cdot A} \tag{7.101}$$

From this equation, the maximum value A can be taken, assuming a given ratio of true to random coincidences. The resolution time τ_A is always chosen to be as low as possible.

Therefore, the experiment is carried out with the shortest possible coincidence time. To determine the correlation function, it is sufficient to measure the coincidences at three angles. Then two independent equations are available for the calculation of a_2 and a_4.

During the measurement, one detector remains in a fixed position. The other one can be set up at the emission angles 180°, 135°and 90°. NaI scintillation detectors are used, whose time resolution is poorer than that of plastic scintillators, but still sufficient. However, they have the advantage that a large fraction of the γ quanta is detected by the photoelectric effect. Compton scattering from the detectors and equipment produces false coincidences, i.e., the detected quanta did not enter the detectors directly from the source but were originally emitted in other directions. Since the quanta lose energy during scattering, these events could be completely suppressed if only the photopeaks were used for evaluation. Because of poor statistics, this cannot be done. The workaround of using a stronger probe is not possible because of radioactive exposure in the lab. As a compromise, the threshold is set at 60-70% of the photopeak.

To quantify the random coincidences, the time resolution of the coincidence must be determined. This is done by measuring the distribution of the time difference of coincidence events. The width of the resolution curve is used to determine the time slice for selecting true coincidences. Random coincidences can be evaluated by looking for coincidences outside the time window of true coincidences. Check if the time length of the digitized pulses is sufficient for this evaluation or if you have to take a narrower time range whose rate you then scale up to the width of the coincidence time window. If necessary, you can also change the time range of the digitized pulse shape before or after the trigger.

With regard to the evaluation, it is necessary to record at least three series of measurements. Within a series, measurements should be taken twice in immediate succession at each angle to check reproducibility. The measurement time per point should be at least 400 s.

7.6.4 Evaluation

The coincidence rates are divided by the product of the associated individual rates. This ensures that errors due to possibly moving thresholds, inadequate adjustment or different solid angles are reduced or avoided in the various settings. After subtracting the random coincidences, the data are evaluated using two methods.

1. Measuring the statistical error. All coincidence rates belonging to an angle are added and the coefficients a_2, a_4 and the anisotropy are determined with the sums. The errors for these quantities are calculated assuming Poisson distribution for the count rates and using Gaussian error propagation law. They are purely statistical in nature.

2. Measuring the entire error. The series of measurements are viewed as independent and evaluated separately. At the end, averaging is done, the error of a mean value is the standard deviation divided by the square root of the number of measurements.

The comparison of the errors gives an indication of whether you just need to measure longer or whether you need new, more precise equipment.

7.6.5 Literature

Introduction chapters 1 – 6 in this script
Angular correlation [1], [26]
Detectors [18], [19], [26]
Electronics [21], [22]

7.7 Experiment (M): Silicon strip detector properties

7.7.1 Task

This experiment consists of two parts. In the first part, the properties of a Si-strip detector, similar to the type of detector used in the tracking detector of CMS, are investigated. In the second part, signatures of different types of particles are identified in original data from the CMS experiment at the LHC.

1. Investigate the properties of a Si stripe detector using the AliBaVa system.

Figure 7.18: The Si-strip detector, investigated in this experiment is located in the black housing behind the lead shielding.

7.7.2 Introduction

The basis for particle physics experiments is the Standard Model of particle physics, which was introduced in chapter 2.6. Elementary particles and interactions of the standard model of particle physics can be investigated very well in collider experiments. Here, there are two types of accelerators. The linear accelerator is used mainly for electrons and positrons due to its low energy losses by synchrotron radiation. In contrast, the ring accelerator is often used for accelerating protons and ions. To achieve the high beam energies, a whole chain of pre-accelerators is usually installed before the actual storage ring. There, the accelerated particles are brought to collision in certain interaction points.

At the currently largest ring accelerator, the Large Hadron Collider (LHC) experiment[2] at CERN[3] near Geneva, a whole series of pre-accelerators including the storage ring with 27 km circumference accelerate the proton bunches of about $1.15 \cdot 10^{11}$ protons to 7 to 13 TeV center-of-mass energy. The complete acceleration chain including experiments is shown in fig. 7.19. The

[2] The CERN accelerator complex [I]
[3] **C**onseil **E**uropéen pour la **R**echerche **N**ucléaire.

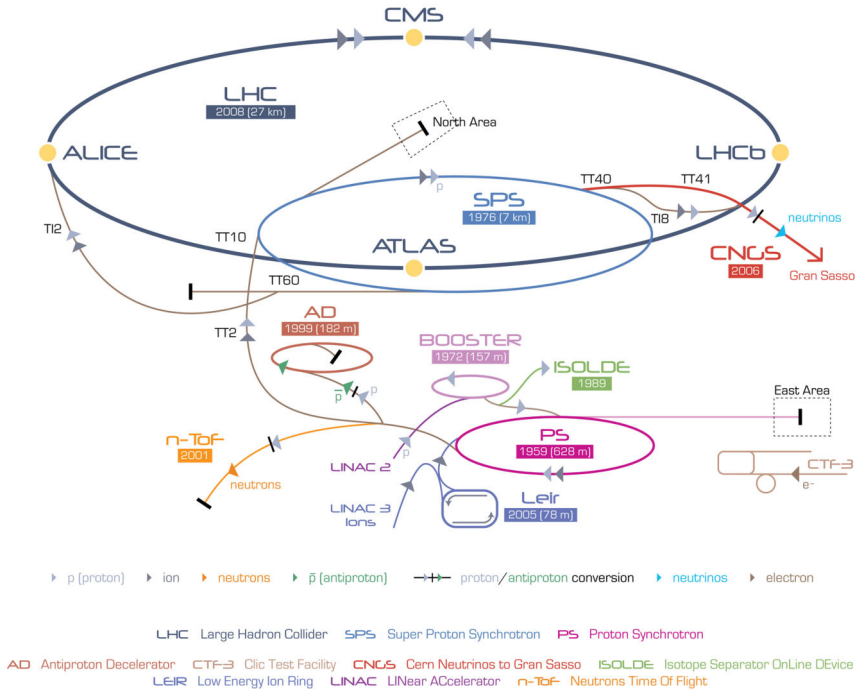

Figure 7.19: The LHC accelerator shown schematically.

main advantage of proton rather than electron acceleration is the much lower energy losses due to synchrotron radiation, which occurs when charged particles are deflected in magnetic fields. In addition, in a proton ring accelerator, the beam can be reused at high collision rates.

The accelerator itself consists of accelerator sections, dipole and quadrupole magnets arranged along a circular path. The vertical magnetic fields of the dipoles ensure that the accelerated particles move in opposite directions on circular paths and gain kinetic energy during each orbit through the accelerator sections. This occurs even after maximum energy is reached to compensate for losses due to synchrotron radiation. By focusing and deflecting with the help of quadrupole magnets, the beams can be prepared and brought to collision.

This is done at the LHC at 4 collision points where the particle detectors – Compact Muon Solenoid (CMS), A Toroidal LHC Apparatus (ATLAS), Large Hadron Collider beauty (LHCb) and A Large Ion Collider Experiment (ALICE) – are ready to measure the collisions.

In a collision, quarks and gluons from two counter-rotating protons interact with each other, which also happens massively in parallel due to the amount of protons per packet. Depending on the invariant mass of the interaction, new particles can be created in different processes. How often collisions occur is determined by the instantaneous luminosity $\mathcal{L}$, which is defined as:

$$\mathcal{L} = \frac{\text{Anzahl der einlaufenden Teilchen}}{\text{Zeiteinheit} \times \text{Fläche}}. \tag{7.102}$$

It is a quantity given by the storage ring and is typically given in units of barn 1b= 10^{-24}cm^2. Here, the LHC achieved an instantaneous luminosity of $\mathcal{L} = 1.75 \cdot 10^{34}\text{cm}^{-2}\ \text{s}^{-1}$. Summing the values over a period of time, we obtain the integrated luminosity L_{int}, which is used as a measure of the number of collisions. In fig. 7.20 the integrated luminosities are shown summed over the whole LHC Run 1 for 2010, whose data are used for this experiment. The number of collisions (events) N that can be detected in the detector is determined by:

$$N = L_{int} \cdot \sigma, \tag{7.103}$$

where $L_{int} = \int \mathcal{L} \cdot \mathrm{d}t$ is the luminosity integrated over time and σ is the effective cross section.

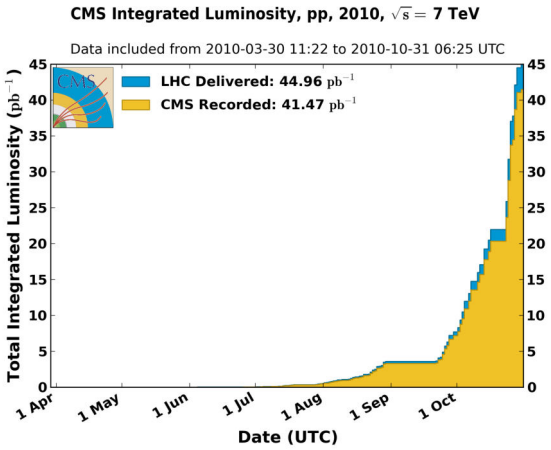

Figure 7.20: Integrated luminosity provided by the LHC and recorded by the CMS experiment cumulatively over Run 1 in 2010.

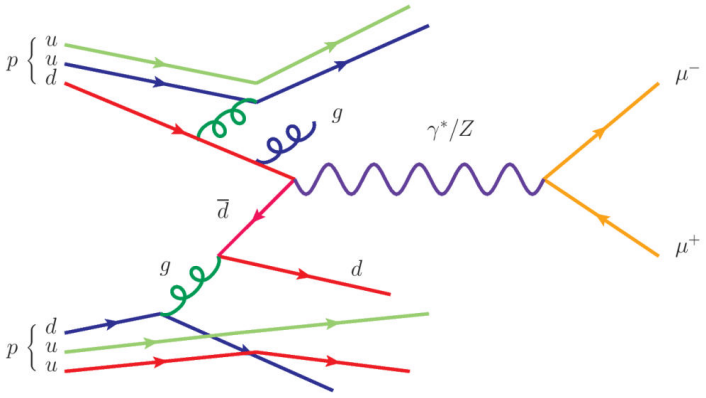

Figure 7.21: Feynman graph of a proton-proton collision producing a virtual Z boson that decays into a muon pair.

The effective cross section determines the collision and decay probabilities, which can be calculated from the Feynman rules of the Standard Model.

These collision processes can be illustrated by Feynman diagrams (see fig. 7.107). The usual convention for Feynman diagrams is that the time axis is plotted to the right. If the arrows are then in the positive time direction, they represent particles, and in the negative time direction, antiparticles. The dots represent interaction points (vertices). Inner lines (those which start and end inside the diagram) represent virtual particles which cannot be observed. Only outer lines (those protruding into or out of the process) represent real (observable) particles. The real particles obey the equation $E^2 = m^2c^4 + p^2c^2$, where E is the total energy, p is the momentum and m is the rest mass of the particle. The virtual particles, on the other hand, exist only for a very short time and thus fall within the range of the Heisenberg uncertainty relation $\Delta E \cdot \Delta t \leq \hbar/2$. So the values of E, p and m do not have to satisfy the above equation.

The more stable particles, such as muons, photons or pions, reach the detector and are registered there. Different particles and their different properties like momentum and energy are measured with the help of different onion-shell subdetectors. Fig. 7.22 shows a cross-sectional photo of the CMS detector with a division of the different subsystems. It also shows which particles can be detected in which detector layer.

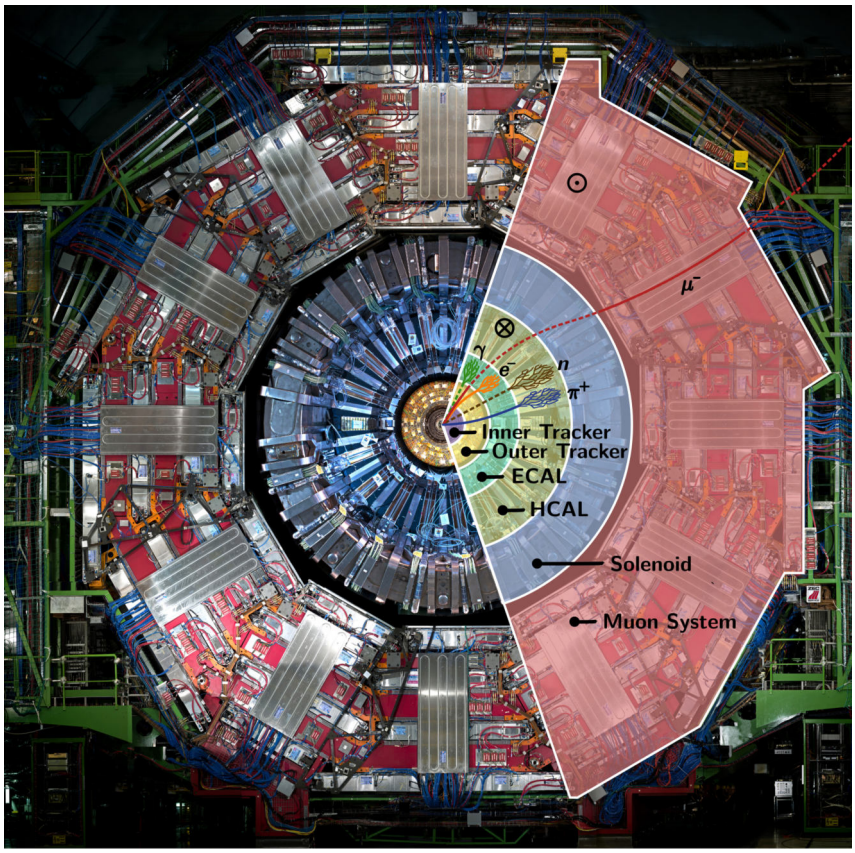

Figure 7.22: A cross-section through the CMS detector shows the different subsystems including the particles that can be detected in each case.

For the CMS detector, these are the following systems from the inside out[4]:

- **silicon-based trace detector**[5]: Immediately around the beamline, the first to be located are the pixel detector and the streak detector. Together, the two are called the tracking detector, or tracker. The task of the tracker is to determine the particle momentum based on the trajectories of charged objects curved in the magnetic field. And the charge sign can also be determined by the direction of deflection, which contributes to particle identification. In addition, the traking detector determines the origin locations of the particles, called vertices. Thus, each particle can be assigned to a specific collision. Only the high accuracy of the tracking detector (partly developed and manufactured in Karlsruhe) thus enables the reconstruction of different events, some of which overlap 100-fold.

- **Electromagnetic Calorimeter**[6]: This system measures the energies of electrons and photons by electromagnetic showering. This is often described by the (highly simplified) Heitler model. Here, the primary particle generates a cascade of secondary particles by pair formation and bremsstrahlung. By Compton scattering and photoelectric effect, the complete energy of the primary particle is deposited in the scintillation material of the calorimeter and measured with the help of photomultipliers (PMTs). Thus – assuming that a shower is completely contained in the calorimeter – a measurement of the energy of the primary particles becomes possible. For hadrons, this condition is usually not met because the electromagnetic calorimeter does not provide enough interaction lengths of material. Therefore, it is enclosed by a second calorimeter.

- **hadronic calorimeter**: The hadronic calorimeter works on the same principle. However, the hadronic shower formation is by far more complicated to describe. Unlike the electromagnetic calorimeter, it consists of several alternating layers of absorber and scintillator material and is not homogeneous. This design is often referred to as a sandwich calorimeter. Nuclear processes in the absorber material produce secondary particles that trigger both a hadronic and electromagnetic cascade. Analogous scintillation light is produced in the scintillation material behind, which is collected by PMTs. In this way, the energy of hadrons is determined analogously to the electromagnetic calorimeter. This process is repeated in the subsequent layers until ideally all energy has been deposited and detected.

- **solenoid magnet**: A superconducting solenoid magnet generates a homogeneous magnetic field of 4 T strength inside the detector to bend particle paths for momentum measurement. A slightly weaker homogeneous magnetic field is also generated externally in the reverse direction via external feedback yokes.

- **myon chambers**[7]: Since muons are minimal-ionizing particles (MIPs), they pass through the detector layers without being stopped. Nevertheless, in order to measure their energy and momentum accurately, gas detectors (called drift tubes and resistive plate chambers) are installed between the iron layers of the return yoke for track measurement and triggering, since many (Higgs) analyses rely on the muon channel. In combination with the inner track detector, the muon properties can be accurately determined from the S-curved trajectory.

All subsystems of the CMS detector together generate 1.5 MB of data per collision of two proton packets, which occur every 50 ns. Recording the data is only possible if an appropriate trigger

[4] For more details, see: CMS Detector [II]
[5] trace detector
[6] calorimeter
[7] myon detector

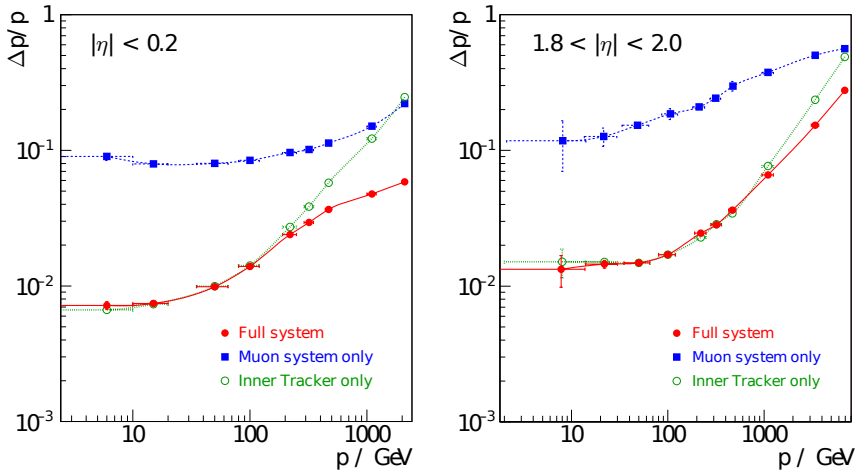

Figure 7.23: Pulse resolution of the muons reconstructed in the central region (left) and in the end caps (right).

system filters out events of interest in real time and forwards them to the data center for reconstruction. For this, a fast level 1 trigger and a software-based high level trigger are mainly responsible for reducing the data rate so that it can be stored and reconstructed.

For the reconstruction of the event, the CMS detector uses a so-called particle flow method. This method combines the information of as many subdetector systems as possible to allow a precise determination of the particles. From the energy depositions in the calorimeters and the tracks in the tracker and the muon chambers, charged and neutral particles are reconstructed. These include muons, electrons, photons, charged and neutral hadrons, which are particle-flow candidates. Based on the calculation of their origin location (vertex), they are assigned to different collisions.

Muons pass almost unhindered through the entire detector matter due to their minimal-ionizing property. Therefore, their track inputs from the inner track detector and the outer muon system are combined for the reconstruction. Thereby one gets a transverse momentum resolution depending on the detector geometry as shown in fig. 7.23.

For the electron reconstruction, on the other hand, the information from the track detector and the electromagnetic calorimeter is combined. This is complicated due to bremsstrahlung effects caused by the curved particle paths. The additional particles created may not be taken into account in the reconstruction, also the tracks changes due to the energy loss.

Quarks and gluons cannot exist freely due to the confinement effect. Since the attractive force between them increases with the distance, the divergence of the quarks creates such a high energy density that new quarks are created. These then form (color-neutral) hadronic bond states from 2 quarks (mesons) or 3 quarks (baryons). This can be seen from the peculiarity of the coupling constants of the strong interaction, see table 2. The newly formed hadrons are usually not stable and immediately disintegrate into a whole shower of secondary particles, which fly away from the point of interaction in a cone shape.

During the reconstruction, a distinction must now be made between which particle flow candidates must be assigned to a jet and which are free particles. For this purpose, a jet clustering algorithm (usually a so-called anti k_T algorithm) is applied on all particle flow candidates, which sequentially combines particles that meet certain criteria depending on the spatial separation and the transverse momentum. Isolated particles are left over and represent free particles.

For the spatial measurement of particle trajectories, the Cartesian coordinate system with the following configuration was chosen in the CMS experiment, which can also be seen in fig. 7.24.

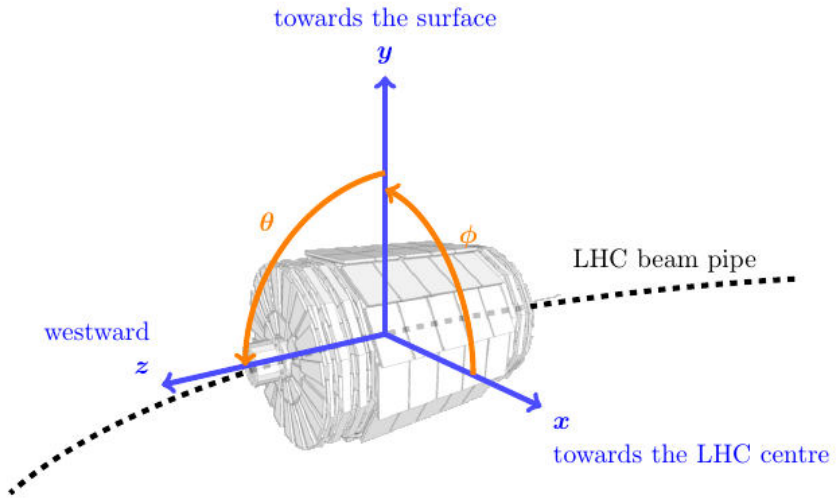

Figure 7.24: Coordinate system of the CMS detector.

- The x-axis is horizontal and points to the center of the LHC ring.
- The y-axis is vertical and points to the surface.
- The z-axis points west along the beam axis.

Since both the collisions and the structure of the CMS detector are symmetrical with respect to the beam axis, analyses like to use special cylindrical coordinates. Starting from the x-axis, the azimuthal angle ϕ can be calculated, which acts in the x-y plane. The polar angle Θ describes the y-z plane starting from the z-axis. Based on these definitions, the quantities rapidity y and pseudorapidity η are calculated. The rapidity y of a particle is defined as follows:

$$y = \frac{1}{2} \ln \left(\frac{E + p_z}{E - p_z} \right). \tag{7.104}$$

This variable can often be used to describe the kinematics of particles well. The main advantage of rapidity is its invariance under Lorentz transformations along the z-axis. In addition, the particle flux of a hadron collider is almost constant as a function of the rapidity. The pseudorapidity η is defined as:

$$\eta = \frac{1}{2} ln \left(\frac{|\vec{p}| + p_z}{|\vec{p}| - p_z} \right). \tag{7.105}$$

For high-energy particles ($p \to E$) this can be transformed to:

$$\eta = -\ln \left(\tan \frac{\Theta}{2} \right). \tag{7.106}$$

The advantage of this quantity is the independence from the particle mass. The spatial distance ΔR between two objects can therefore be calculated using:

$$\Delta R = \sqrt{(\Delta\eta)^2 + (\Delta\phi)^2} \tag{7.107}$$

For the initial proton-proton collisions, the transverse momentum perpendicular to the beam axis is negligible. Therefore the transverse impulse p_T of a collision event must be preserved. However, due to the fact that protons are composite objects, the longitudinal momentum of

the events cannot be determined. Therefore, particles produced from a collision are usually described with the observables p_T, η (or y) and ϕ. If one reconstructs the original particle from decay products, one can also calculate the invariant mass, which is unchangeable under Lorentz transformations. This can be expressed using the four-vector vectors of the decay products:

$$M = \sqrt{\sum_i P_i} = \sqrt{(E_1 + E_2)^2 - (p_{x,1} + p_{x,2})^2 - (p_{y,1} + p_{y,2})^2 - (p_{z,1} + p_{z,2})^2}, \tag{7.108}$$

in the case of 2 decay products. This variable can be used, for example, to make statements about the particle mass or decay width.

7.7.3 Experimental Setup and Preparation

These training exercises aim to introduce you to the common procedures encountered during the characterization of silicon strip sensors. At the ETP, electrical characterization is usually done at dedicated *probe stations*, while charge collection measurements are obtained using the `ALiBaVa` setup. State of the art and very special, as everything at the ETP, these *probe stations* feature metal jigs which contact the sensor ground plane while probing needles are used to measure and bias the sensor itself. However, we will lay the focus on the - also state of the art - `ALiBaVa` setup or - more precise - on the **E**ducational **A**libava **Sy**stem (EASY for short). The real `ALiBaVa` is housed inside of a table-sized aluminium box to shield it from light, electromagnetic radiation and to provide a defined temperature. A 3-way step motor stage is used to position a radiation source over the sensor to be investigated while a ground contact and strip bonds bias the sensor. The EASY we are going to use, however, doesn't need cooling (Why? If you don't know, pay close attention to the strip sensor section.) or a motor stage and is shielded from light with a smaller aluminium box that almost fits into your pocket. This enables us to conduct the measurements we need to familiarize ourselves with the topic. The measurements we are going to conduct are actually very common and prerequisites to operation of sensors in real detectors like CMS.

7.7.3.1 The EASY

Figure 7.25: Front and rear of the control unit [49].

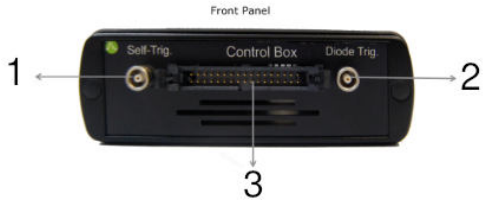

Figure 7.26: Rear of the sensor unit [49].

There are two components to the EASY: the **control unit** and **sensor unit** (shown in fig. 7.25 and fig. 7.26 respectively). Data is transferred between these two units via a flatband cable plugging into (2) of control unit and (3) of sensor unit (mind the locking mechanism!). An optical fiber (yellow cable) plugs into (1) of the control unit and top connector of the sensor

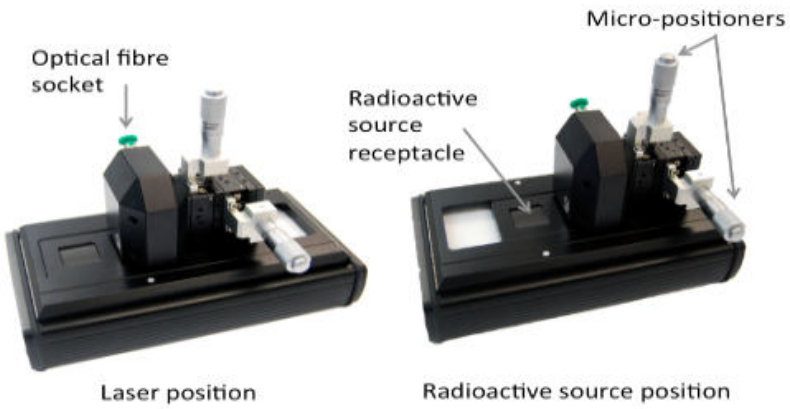

Figure 7.27: Sensor stage positions [49].

stage (again, mind the locking mechanism). In these exercises, we will use the diode trigger by connecting the brown LEMO cable to the jacks (7) of the control unit and (2) of the sensor unit.

The diode trigger uses a diode which is placed just below the sensor and, therefore, if a particle traverses the sensor on top, it automatically hits the diode below, causing data readout after a given latency. After connecting the USB cable to the control unit at (9) and to a PC and providing power at (12), we should be ready to go. Knob (4) on the control unit turns to set the bias voltage. fig. 7.27 illustrates two positions the sensor stage can slide into. Make sure to select the proper position for each measurement.

The sensor unit incorportes an electronic board, accommodating the BEETLE readout ASIC. The chip provides 128 analog input channels connecting to a clocked analog pipeline with a frequency of 40 MHz (like the LHC bunch crossing rate!).

Latency The pipeline structure of the readout channels allows us to correct for finite latency. Suppose a particle traverses the sensor and triggers readout by hitting the diode below. Diode triggering, electrical processing and other minor effects introduce latencies into the system which can be corrected for by specifying a readout latency in the system. The latency should be selected so as to sample the signal at its timing maximum.

7.7.3.2 Silicon Strip Sensors

p-in-n design The interaction of charged particles with matter is descibed by the Bethe formula [47] [48]

$$-\left\langle \frac{\mathrm{d}E}{\mathrm{d}x} \right\rangle = 4\pi N_{\mathrm{A}} r_e^2 m_e c^2 z^2 \frac{Z}{\beta A} \left(\frac{1}{2} \log \left[\frac{2 m_e c^2 \beta^2 \gamma^2 T_{\max}}{I^2} \right] - \beta^2 \right), \tag{7.109}$$

which you should be very familiar with. A p-in-n silicon strip sensor now consists of p-doped silicon strips embedded into an n-bulk, which is why we call p-in-n sensors **n-type** sensors. The standard technology nowadays uses n-in-p sensors, the basic functionality remains the same. Only the bias voltage has to be reversed. In the p-in-n case, we ground the bias ring, while applying a positive voltage to the backplane.

fig. 7.29 shows a schematic of an n-type strip sensor like the one we are going to use for this exercise. The sensor we are going to examine has a pitch of 160 µm and an active width of 300 µm.

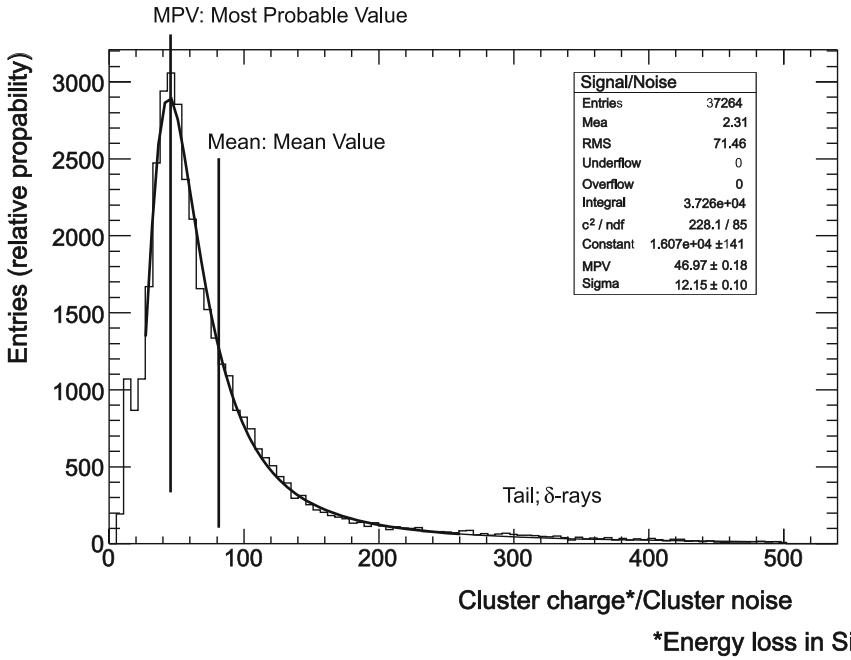

Figure 7.28: A Landau distribution. It is easy to see, that the MPV is at a lower signal than the mean. This is caused by the asymmetric tail [47].

The Bethe formula in eq. (7.109) only describes the *mean* energy loss of charged particles inside matter. Fluctuations of the energy loss around the mean caused by fluctuations of transferred kinetic energy are described by the so-called Landau distribution. This special distribution takes so-called δ-electrons into account. These electrons interact with atoms inside matter head-on, therefore, the transferred energy is higher than usual. This influence causes the asymmetric tail visible in fig. 7.28.

When charged particles pass through the bulk, they ionize the material and create electron-hole pairs. For silicon, the mean energy to create such a pair is 3.6 eV at a mean energy loss of around 390 eV µm^{-1}. This means, that per µm silicon, 108 electron-hole pairs are created. These electron-hole pairs drift towards the anode (backplane) and cathode (strips) respectively. By segmenting the sensor into strips, we are able to obtain a 1D information on where the charged particle passed through the sensor.

If a *minium ionizing particle* (particles with $\beta\gamma \approx 3$) traverses the detector of thickness 300 µm,

$$N = \frac{\mathrm{d}E}{\mathrm{d}x} \cdot \frac{d}{I} \cdot \sigma_{\mathrm{L}} = 22451 \tag{7.110}$$

electron-hole-pairs are created, where $\sigma_{\mathrm{L}} = 0.7$ is the corrective factor for the mean to MPV conversion by Landau. However, if one considers the number of thermally excited charge carriers in the bulk,

$$N_{\mathrm{th}} = d \cdot n_i \approx 421 \times 10^6\,\mathrm{cm}^{-2}, \tag{7.111}$$

one very easily realizes why we have to operate the sensor in reverse bias. It is only thanks to the full depletion (of thermally excited charge carriers) of the sensor material that we are able to measure such a faint amount of electron-hole pairs at all.

Leakage Current As explained earlier, in an ideal case, the sensor material should be devoid of any thermal charge carriers. However, a real reverse-biased semiconductor crystal has small damages in its lattice structure which creates allowed states within the band gap and thus enables

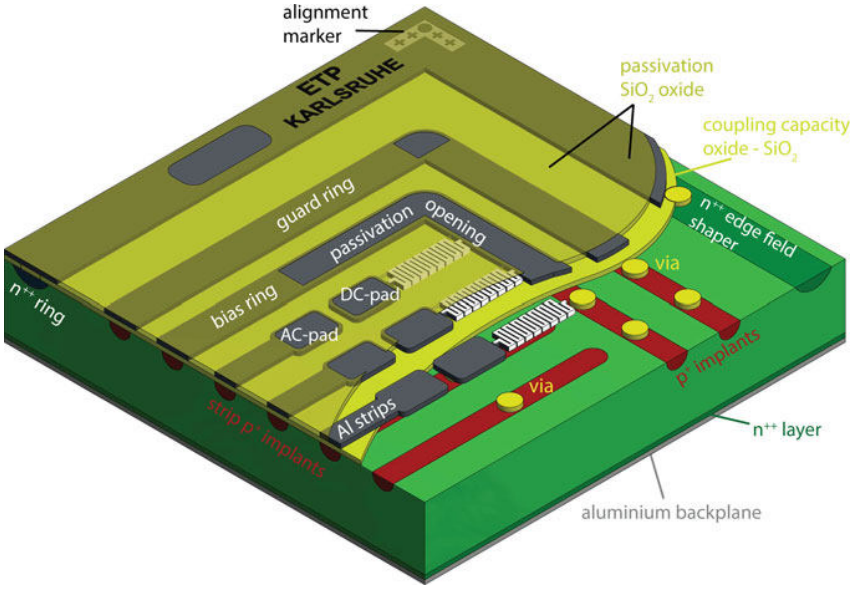

Figure 7.29: A p-in-n strip sensor [47].

carriers to be excited into the conduction band. These carriers are the cause of the so-called leakage current. Since the current inside of a semiconductor increases with temperature and temperature increases with current, we do care about the IV characteristics even in reverse bias. Full IV characterization provides feedback on thermal runaway which would have catastrophic consequences on detector operation/cost efficiency.

Temperature dependence of the leakage current can be described like

$$I(T) = I_0 \cdot \left(\frac{T}{T_0}\right)^2 \cdot \exp\left[-\frac{E_{\text{eff}}}{2k_{\text{B}}}\left(\frac{1}{T} - \frac{1}{T_0}\right)\right], \tag{7.112}$$

if we know the leakage current I_0 at a temperature T_0.

Irradiation Damage Charged particles do not only interact with hull electrons of the bulk atoms but also with the nuclei themselves. This process displaces bulk atoms within the lattice or even knocks them out of their places entirely, creating vacancies. As described earlier, consequently, the leakage current of the sensor rises like

$$\frac{\Delta I}{V} = \alpha \cdot \phi_{\text{rad}}, \tag{7.113}$$

where ΔI is the rise in leakage current, α the so called damage rate and ϕ_{rad} denotes the fluence of irradiation. The crystal deteriorates step-by-step and loses its ability to efficiently detect particles.

Charge Collection Efficiency As explained earlier, the maximum signal amplitude is detected if the sensor volume is fully depleted. Call that charge n_{dep}. If we now under-deplete the sensor by applying a voltage under the full-depletion voltage V_{dep}, charges recombine in the non-depleted region of the sensor. This part of the signal can not be recovered and is lost. Only the electron-hole-pairs within the depletion zone contribute to the signal. Call that charge n. Then, the CCE is defined as

$$\text{CCE} = \frac{n}{n_{\text{dep}}}.$$

7.7.4 Data Acquisition

To read out data from EASY we will use a program called `alibava-gui` which provides a (semi) user-friendly interface to work with. After taking data with the program, it is analyzed using `alibava-analysis`, a python script written in 2020.

7.7.4.1 `alibava-gui`

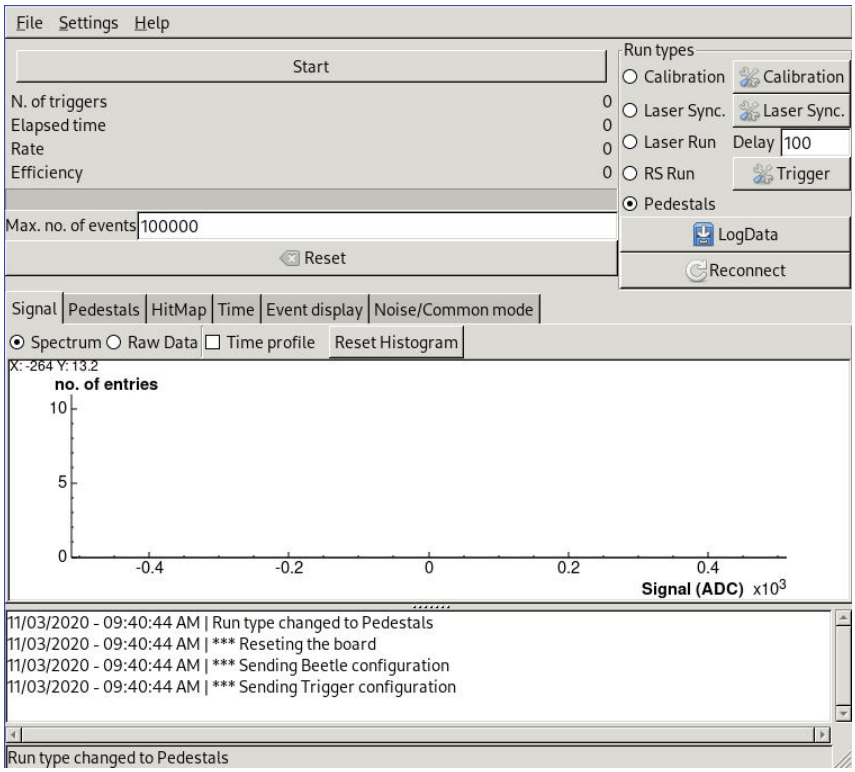

Figure 7.30: The `alibava-gui` interface.

`alibava-gui` features various tabs displaying different views i.e. raw event displays, noise graphs and so on. We start it by `cd`-ing into the appropriate directory (`~/alibava/src/`) and executing

```
./alibava-gui ~/ini/alibava_easy.ini,
```

which will load the program with the appropriate settings written into the `.ini`-file. We do not care about any special command-line flags for now, everything we need is visible in the GUI. You should be able to see a window like the one in fig. 7.30.

IMPORTANT: If you want to save a run, you have to specify a file name using "Log Data" **before** you start the run! Do not forget to append `.hdf5` to the file name.

7.7.4.2 Pedestal

Pedestals are recorded by reading out at random times while no signal is injected. The pedestal value of each individual readout channel is an effective noise offset.

The *common mode noise* is noise that affects each channel in the same way, caused by mainly external influences like stray EM fields. It can, therefore, by definition only be different from

event to event, not from channel to channel. When an actual charged particle passes through the detector, the corresponding signal can be divided into different parts

$$ADC(i,k) = P(i,k) + D(k) + S(i,k),$$

where $ADC(i,k)$, the total signal in ADC counts, is dependent on the strip number i and event number k. As explained, the CM $D(k)$ is only dependent on the event number k, whereas pedestal P and signal S can - of course - vary from channel to channel as well.

The total noise is defined as the RMS value of common mode noise corrected pedestal values

$$N(i) = \sqrt{\frac{1}{N-1}\sum_{k=1}^{N}\left(P_{\mathrm{c}}(i) - \overline{P_{\mathrm{c}}}(i)\right)^2},$$

where $P_{\mathrm{c}}(i) = \frac{1}{N}\sum_{k=1}^{N} ADC(i,k) - D(k)$.

The analysis script uses these simple concepts to extract the signal $S(i,k)$ and analyze noise distributions.

7.7.4.3 Latency

The latency for calibration runs has to be set to 128 in order for the calibration pulse to lie within the timing window.

7.7.4.4 Calibration

To make sense of signal amplitudes we are reading out, we have to convert arbitrary ADC counts into electrons by acquiring a calibration curve and using it to obtain a conversion factor between these two quantities.

For this, we do a calibration run. The system injects pulses of known charge into the readout ASIC. Then, the ADC reads out this signal in ADC counts. By fitting a polynomial funtion to this calibration curve and extracting its maximum the conversion factor is obtained.

7.7.4.5 Radsource Run

To simulate real LHC MIPs, we use a radiation test source. The source used in this training course is Sr-90. Sr-90 decays into Y-90 by β-decay with a half-life of 28.8 yr. The short-lived daughter nuclide decays with an endpoint energy of 2.2 MeV and can therefore be used as a MIP source.

In order to conduct a radiation source run, the latency should be adjusted first, as described earlier.

7.7.4.6 Clustering

When a charged particle traverses the sensor, obviously, not all of its generated charge is read out at exactly one strip but is distributed among several neighboring channels. This collection of channels with a signal is called a cluster. The main goal of an anaylsis is to recognize such clusters and their properties. The clustering algorithm of `alibava-analysis` is a seeding algorithm, which means that inside of a cluster, strips with signals above a certain threshold (*seed cut*) are defined to be a so-called seed. Neighbor strips are defined as strips whose signal lie above the *neighbor cut* that aren't seeds. Strips that are neither a seed nor a neighbor are discarded (Why?).

7.7.4.7 Laser synchronization

The EASY is able to send an internal pulse to trigger the laser system. Before conducting a laser run, the system readout and trigger pulse need to be synchronized. To do this, select *Laser sync* from the main window (right radio button list), default settings should be okay. Press OK and start the run. Observe the signal spectrum. You should be able to see a peak. The latency on the x-axis is the delay you should use for laser runs (see the input field next to *Laser Run*).

7.7.4.8 Laser run

After synchronizing the laser system, we can conduct a run. In a laser run, charge is injected into the sensor by a pulsed laser located in the control unit.

To inject a laser pulse at maximum energy deposition, the laser has to be focussed. To focus the laser, a laser run has to be started. The signal deposition should be observed in the event display. Move the beam position by adjusting the micrometer screws. Move up/down until you observe a larger signal. Then, move perpendicular to the strip direction until you observe a signal only on one strip. Next, move the laser right in between two strips and adjust up/down until you do not observe any signal anymore. Repeat these steps until you observe what is described.

7.7.4.9 File Format

The output file format is hdf5. The files basically contain a table with each row representing an event and the columns corresponding to the read out ADC values for each channel.

7.7.4.10 alibava-analysis

In order to analyze the digitally acquired data, we need an analysis program. Luckily, there already exists an analysis script (framework) called `alibava-analysis`. It is used for the real `ALiBaVa` system and can be used for the EASY as well since they are basically the same.

Once you have gathered calibration, pedestal and signal `.hdf5`-files, we can input them into the program by specifying the run number. The files have to have a specific naming in order for the script to recognize them: Let n be the run number you specify in the command-line (more later). Then, name the files like:

$$\begin{aligned} \texttt{source\_}n\texttt{.hdf5}, &\quad \text{for the signal file} \\ \texttt{pedestal\_}(n-1)\texttt{.hdf5}, &\quad \text{for the pedestal file} \\ \texttt{calibration\_}(n-2)\texttt{.hdf5}, &\quad \text{for the calibration file.} \end{aligned}$$

For further help concerning the usage of the script, execute

```
./alibava-analysis/main.py -h.
```

or contact your advisor.

7.7.5 Experimental procedure

7.7.5.1 Understanding the Setup

In the following exercises, we will use the EASY setup to characterize an n-type silicon strip sensor. This type of electrical and charge collection characterization is a common procedure to prepare for usage in a real detector like CMS. Let us first familiarize ourselves with the setup before conducting measurements.

- Describe the setup. What does it consist of?

- What is an n-type silicon strip sensor?
- How is the signal formed at the readout channels? How is readout triggered?
- What sources of noise is this method of triggering susceptible to?
- What are the properties of the sensor used in this setup?

But why should you take our word for granted? Measure the pitch using the built-in laser yourself!

Exercise Set the bias voltage to 110 V. Synchronize the laser and set up the laser delay. Start a laser run and focus the laser. Take multiple laser runs (don't forget to save to a file *before* you start each run), moving the laser 10 µm perpendicular to the strip direction each step. Cover at least a distance of 320 µm, which is twice the detector pitch. Read the signal either from an own analysis script or from the histogram itself and plot the charge as a function of the laser position.

7.7.5.2 Electrical Characterization

Next, we want to characterize the sensor electrically. Common procedures include recording an IV and CV curve.

- Why are we interested in the IV characteristics of a sensor? What is the purpose of a CV curve?
- Can you think of any characteristic that wasn't mentioned here but is important as well?

Exercise Ramp the voltage from 0 V to 110 V in 10 V steps and record the bias current for each step. Plot the result and discuss the shape. How would the curve change if the sensor was irradiated?

7.7.5.3 Noise

As for every measurement you will ever conduct, there are sources of noise. In this exercise, we will discuss the different sources of noise in the system and how we account for it.

- What is pedestal? How do we get rid of it? What happens in a pedestal run?
- What is common mode noise? How do we get rid of it?
- How is the RMS value of noise calculated?
- Does the sensor bias have an influence on noise?
- Have a look into `alibava-analysis/analysis/signal.py`. How is noise handled?

Exercise Ramp the bias voltage from 0 V to 110 V in 10 V steps and and save a pedestal run with $n_{\text{trig}} = 5000$ for each voltage step. Name each file like `noise_(voltage value).hdf5`. Calculate the mean noise for each voltage step using the pre-written helper script `noise_calc.py` (look into the code to understand how it works). The script will also produce an output plot. Discuss it.

7.7.5.4 Calibration

Next, we want to calibrate the setup for future charge collection signal measurements.

- What do we need a calibration for?
- How do we obtain a calibration run exactly? What are sources of error?
- Have a look into `alibava-analysis/analysis/gain.py`. How is the gain obtained from the calibration curves?

Exercise Set the bias voltage to 110 V and take a calibration run, saving it to a file. We will need it later.

7.7.5.5 Clustering

We will not discuss clustering in all depth for these exercises. However, for a thorough understanding of signal formation a general understanding of clustering is of utmost importance.

- What is a cluster? What is a seed? What defines a seed/neighbor?
- What is the more sensible measure of signal? Seed or cluster signal? When would you use what?
- Suppose we have a cluster with a big cluster size (> 3). What happened?
- How would you look for clusters in data? (Keep it simple)

7.7.5.6 Full Run

We will record a full blown run now and thus complete a default characterization process. As usual in this kind of setups, we will use Sr-90 as a particle source.

- Why Sr-90?
- What individual runs do we need to analyze the charge collection in electrons?
- What's latency and how do we select it properly?

Exercise Record a full radiation source run with $n_{\text{trig}} = 100000$. Analyze the output data with `alibava-analysis`. Discuss the output plots. What would the plots look like if our sensor suffered from irradiation damage?

7.7.5.7 Depletion Voltage and CCE

Lastly, we will determine the full depletion voltage V_{dep} of the sensor by recording the CCE as a function of the bias voltage.

- What is CCE? How can we use it to detemine the depletion voltage of the sensor?

Exercise Ramp the voltage from 0 V to 110 V in 10 V steps and record the MPV for each step. Plot the result and determine V_{dep}. How would the plot change if the sensor was irradiated?

7.7.5.8 Topics for Preperation:

Experiment: LHC + CMS, Detection of muons, interaction of particles with different detectors

Links

I https://cds.cern.ch/record/1260465?ln=de, visited: 13.04.2021

II https://cms.cern/detector/, visited: 13.04.2021

III https://opendata.cern.ch/visualise/events/cms: event display, visited: 05.05.2021

7.8 Experiment (M): Properties of Elementary Particles

7.8.1 Tasks

In this experiment, original data from the CMS experiment at the LHC will be analyzed for various physics questions. In the first step, you will learn about the signatures of different types of particles in the complex detector system. Then, using software that you will customize and run in the `Python` programming language in a `Jupyter` notebook environment, you will determine parameters of different particle species and derive further physical parameters from them.

1. Look at a selection of event displays and decide whether they are the decay of a Z boson candidate or a J/Ψ meson candidate.

2. Calculate invariant mass, transverse momentum, azimuthal angle, pseudorapidity, and spatial separation (ΔR) of the events in the present data set and examine their distributions.

3. Determine the mass, M_Z, and the decay width, Γ_Z, of the Z boson from its resonance in the mass spectrum of muon pairs. For this purpose, find a suitable background parameterization and estimate the detector resolution, σ_Z.

4. Determine the lifetime τ_Z of the Z boson and estimate the effective cross section $\sigma_{Z\to\mu\mu}$ for its decay into a muon pair.

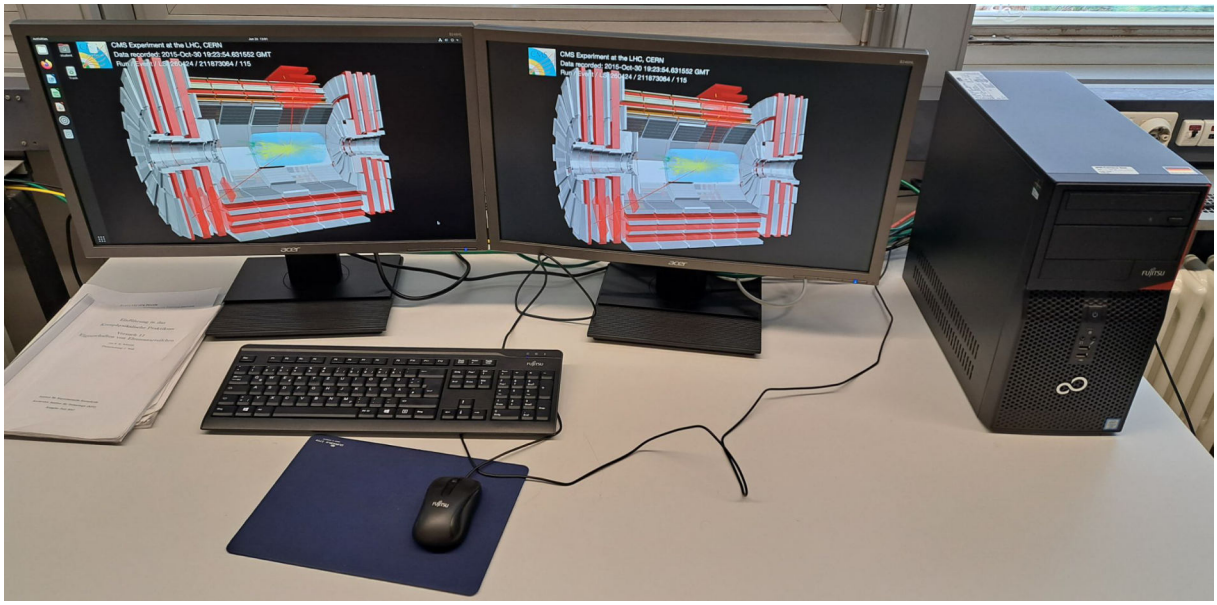

Figure 7.31: In the Elemetrary Particle experiment, data of the CMS experiment are analysed on a computer.

7.8.2 Introduction

→ Please read the general introduction for the particle physics experiments in section 7.7.2.

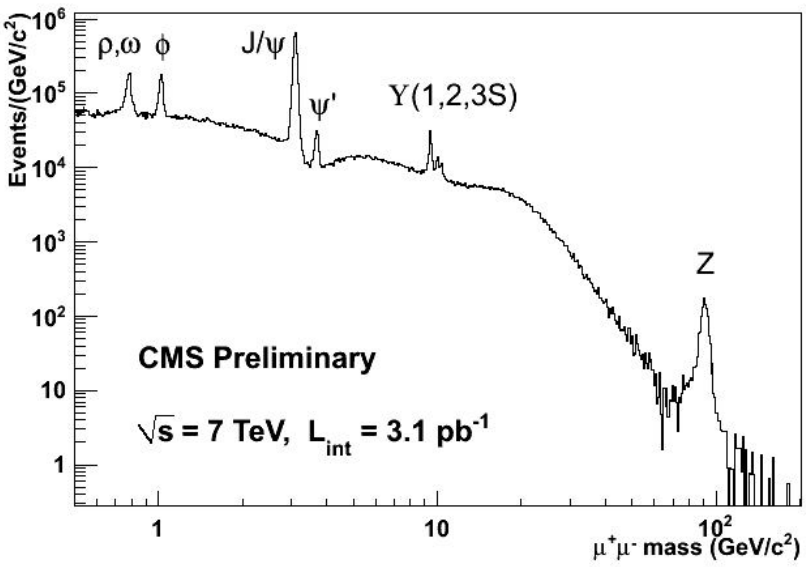

Figure 7.32: Mass spectrum of muon pairs recorded by the CMS detector at $\sqrt{s} = 7\,\text{TeV}$. The resonances are labeled in the figure and are associated with different mesons and the Z boson.

7.8.3 Basics

7.8.3.1 The Dimuon Spectrum

In this lab experiment, only processes whose final states consist of muons are to be considered. The observation of decays into muon final states is suitable, because in contrast to decays into hadronic final states, only single muons and no more complex objects, like jets, are produced. If an object decays into a muon and an antimuon, they will be referred to as a muon pair in the following. According to the invariant mass introduced above, the mass of the decayed object can be reconstructed from the energies and momenta of the muon final states.
The characteristic distribution of the invariant mass of dimuon pairs is called the dimuon spectrum and can be seen in Figure 7.32. The data used to create the plot are from 2010, when the experiments at the LHC accelerator started taking data. For a dimuon spectrum, apart from the shown plot of the number of events versus the invariant mass, also a plot of the effective cross section versus the invariant mass is conceivable.

Several resonances can be seen in the present plot. These can be assigned to various mesons and the Z boson and theoretically take the form of Breit-Wigner distributions with characteristic masses and decay widths. Since these resonances were already measured very precisely several decades before the start of the LHC experiment, they can be used to calibrate the detectors and are also referred to as "standard candles" in reference to astronomy.

7.8.3.2 The Drell-Yan Process

Physically, the resonances have their cause in the Drell-Yan process [**?**]. The Drell-Yan process describes the annihilation of a quark with its antiquark, producing a virtual photon or a Z boson, which subsequently decays into a lepton-antilepton pair. The existence of Z bosons in the dimyon spectrum thus follows directly from the Drell-Yan process. The appearance of meson resonances can also be explained by this process, since mesons are bound states of quark-antiquark pairs. Accordingly, these can also decay via a Drell-Yan process to form a muon-antimuon pair.

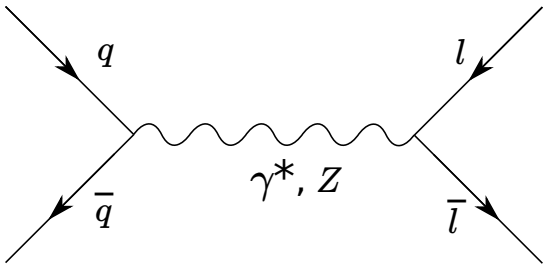

Figure 7.33: Feynman diagram of the Drell-Yan-process. This describes the annihilation of a quark with its antiquark, producing a virtual photon or a Z boson, which subsequently decays into a lepton-antilepton pair.

The fraction of decays into two muons in the meson decays is typically in the range of a few percent [?]. Concrete values for the resonances investigated in the later course of the experiment are given in the associated sections. Quark-antiquark pairs annihilating via Drell-Yan processes and decaying via a virtual photon form most of the background of the spectrum. This includes meson resonances and a continuous spectrum, as seen in fig. 7.32.

Other background processes are given by processes that produce a muon-antimuon pair without a Drell-Yan process directly taking place. An example of this are pair-producing photons originating from other processes. Additional contributions are provided by processes in which a muon and an antimuon are produced independently and reconstructed as a dimuon pair. This can be the case, among others, for a simultaneous decay of a τ and an anti-τ or differently charged W bosons. Based on the dimuon spectrum, various analyses can be performed. Central are the quantities that can be determined directly from the spectrum, such as the masses of the particles or their decay widths.

7.8.3.3 Decay Width and Lifetime

Peaks in the mass spectrum are resonances with a decay width, Γ, and certain lifetime, τ, which can be described by Breit-Wigner distributions. The decay width is given by the half-width of the resonance. The Lifetime of a particle is defined as the time that elapses until the particle number of a system consisting of the particles under study has dropped to $\frac{1}{e}$ of its original size. Γ and τ are according to the energy uncertainty relation:

$$\Delta E \Delta t \geq \frac{\hbar}{2}, \tag{7.114}$$

leading to

$$\Gamma = \frac{1}{\tau} \tag{7.115}$$

in neutral units. Since the lifetime of the particles studied here is so small that it can no longer be measured directly, this relation is used to determine the lifetime. For this purpose, the decay width is determined by fits to the resonances [?, ?].

7.8.3.4 Deviations of the Shape of the Resonances from the Expected Shape

Looking closely at the resonances in a real spectrum, as seen in figure 7.35, they do not perfectly follow a Breit-Wigner distribution. One reason for this is the influence of the finite detector resolution on the energies and momenta and thus the invariant masses of the particles. Another

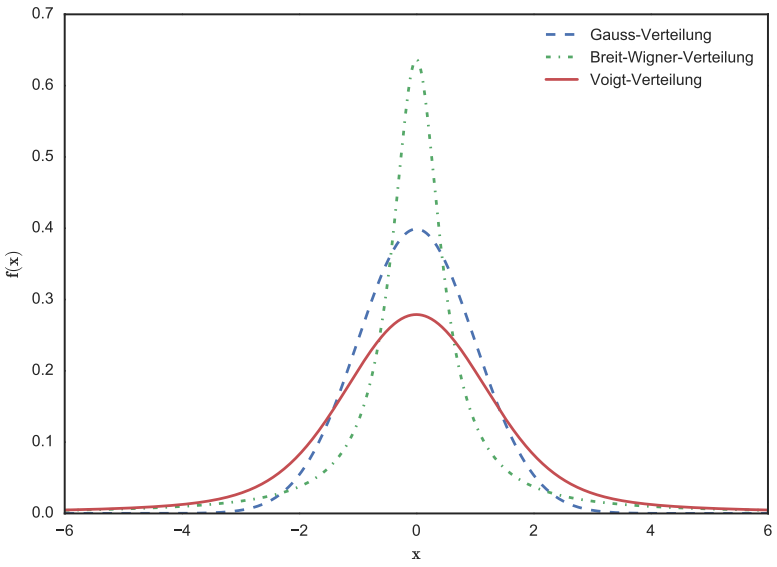

Figure 7.34: Normalized Breit-Wigner distribution with $\Gamma = 1$ and $M = 0$ and a normalized Gaussian distribution with $\sigma = 1$ and $M = 0$ and a normalized Voigt-distribution with the same parameters.

influence on the shape of the spectrum is the 'Final State Radiation', which leads to spurs and shifts of the resonances to lower energies.

The Voigt-Profile

The Breit-Wigner distribution, also called Lorentz- or Cauchy-distribution, describing by the resonances of the spectrum is given by:

$$B(m) = \frac{\frac{\Gamma}{2}}{\pi\left((m-M)^2 + \left(\frac{\Gamma}{2}\right)^2\right)}, \tag{7.116}$$

where Γ is the Half-width and M the mean value of the distribution.

In a real spectrum of this type recorded by a detector with finite mass resolution, the resonances no longer follow perfect Breit-Wigner distributions because of the influence of the limited resolution. The detector resolution follows a Gaussian distribution:

$$G(m) = \frac{1}{\sqrt{2\pi}\sigma} \exp -\frac{1}{2}\frac{(m-M)^2}{\sigma^2}, \tag{7.117}$$

with the standard deviation, σ, and the mean, M. It has to be considered for the form of the resonances, as they smear out due to the detector effects.
The resulting distribution is the so-called Voigt-distribution given as the convolution of a Breit-Wigner with a Normal distribution:

$$V(m) = (G * B)(m). \tag{7.118}$$

This is shown in fig. 7.34 No closed-form representation can be found for this distribution, but various approximation methods exist.

Final State Radiation
If a final state of a process emits a photon, this process is called Final State Radiation. It leads to discrepancies in the reconstruction of the invariant mass of the decayed particle towards lower energies. The reason is that the resulting photon can no longer be unambiguously assigned to the process and thus, during reconstruction, it cannot be directly recognized at which events Final State Radiation occurred. The outliers in the dimuon mass spectrum caused by final state radiation can be considered by simulation or various approximations. These approaches and methods are too complex for the following analysis within the lab course and will not be pursued further.

7.8.3.5 Particular Resonances in the Dimuon Sprectrum

Two resonances in the dimuon spectrum will be considered in more detail with respect to this experiment.

The Z Boson
The Z boson, discovered in 1983 at the Spp̄S storage ring at CERN, is a gauge boson - an exchange particle of the weak interaction - and an elementary particle in the SM. It carries no charge, has spin 1 and is its own antiparticle. The discovery confirmed the theory of a unification of the electromagnetic and weak interactions into the electroweak interaction and was honored with the Nobel Prize in Physics in 1984. Today, by being so well known, it serves as an important tool for the energy calibration of the detector.

The mass and the decay width of the Z boson are known with high precision and are given by [?]:

$$\begin{aligned} M_{\mathrm{Z}} &= 91,1876 \pm 0.0021\,\mathrm{GeV}, \\ \Gamma_{\mathrm{Z}} &= 2,4952 \pm 0.0023\,\mathrm{GeV}. \end{aligned} \tag{7.119}$$

Z bosons are generated in the reaction of quark-antiquark or lepton-antilepton pairs whose invariant mass is at least equal to the Z mass. The Z boson decays to about 70% hadronic, 20% neutrinos, and about 10% charged leptons, with equal decay probabilities among electrons, muons, and tauons. For muons, the branching fraction is (3.366 ±0.007)%. [?, ?, ?].

The lifetime of the Z boson is $\tau_{\mathrm{Z,Lit}} = 2.6379 \pm 0.0024 \times 10^{-25}\,\mathrm{s}$ [?] and the effective cross section for the decay into muons is given by [?]:

$$\sigma_{\mathrm{Z}\to\mu\mu,\mathrm{Lit}} = 0,968 \pm 0,008(\mathrm{stat.}) \pm 0,007(\mathrm{syst.}) \pm 0,018(\mathrm{th.}) \pm 0,039(\mathrm{lumi.})\ \mathrm{nb}.$$

The J/Ψ Meson
The J/Ψ meson is the bound state consisting of one charm and one anticharm quark, called "charmonium", with the lowest energy. This meson was discovered in 1974 by two research groups in parallel, which published their results on the same day, leading to the double denomination of the particle. The discovery was experimentally groundbreaking because it proved the existence of the charm quark. Therefore, the two discoverers were honored with the Nobel Prize in Physics in 1976. The mass of the J/Ψ meson is at:

$$M_{\mathrm{J/\Psi}} = 3096,900 \pm 0.006\,\mathrm{MeV}. \tag{7.120}$$

Characteristic for the J/Ψ meson is its extraordinarily small width compared to other mesons with comparable masses:

$$\Gamma_{J/\Psi} = 92,9 \pm 2.8\,\text{keV}. \tag{7.121}$$

This feature makes the resonance of the J/Ψ meson an important 'standard candle' that will be used within this exercise to investigate the detector resolution. The J/Ψ meson decays hadronically in 87.7% of the time and about 6% to dielectron or dimuon pairs [**?**, **?**].

Distinguishing Z boson and J/Ψ meson

To understand the differences between decays of Z bosons and J/Ψ mesons into dimyon pairs, the kinematics of the particles will be considered.

If energy is added to a proton by acceleration, it is not distributed evenly among all its constituents, called partons, but follows certain distributions, the parton density functions (PDFs). When two protons are colliding, individual partons with different momenta effectively collide. If two colliding partons with different momentum form a particle, it is, according to the conservation of momentum, accelerated in a certain direction. Since the protons were accelerated along the beam axis, the collision products are also accelerated along this direction.

Accordingly, particles with lower mass, such as the J/Ψ meson, can be formed by partons with very different momenta. Therefore, with larger potential momentum differences they are stronger accelerated along the beam axis and are more often scattered into the end caps of the CMS detector. The result is a smaller opening angle of their decay products on average than for decay products of particles that have been accelerated less.

The Z boson, on the other hand, has a much larger mass of about 90 GeV and can only be formed by two high energy partons. Since all parton density functions decrease towards high energies, two high energy partons have a much smaller momentum difference than partons forming lighter particles. This means, Z bosons are accelerated much less along the beam axis than J/Ψ mesons.and the opening angle between the decay products of the Z boson is larger than for the J/Ψ meson and the spatial distribution of the decay products is more homogeneous.

Furthermore, in the decay of a J/Ψ meson, less rest energy of the original particle is distributed to the decay products than in the decay of a Z boson. Consequently, the decay products of a J/Ψ-muon have significantly lower momentum or transverse momentum than the decay products of a Z boson. In some cases, the pulses of the decay products of a J/Ψ meson are so small that they are detected only in the tracker and not in the muon system. For these muons, the curvature of their track can be clearly detected within the magnetic field.

7.8.4 Experimental procedure

7.8.4.1 Dataset and Software

The present lab course uses data taken from the dataset containing all muon events detected in 2010. This dataset is published on the CERN Open Data Portal [8]. On this portal, the collaborations of the four large experiments at the LHC make available parts of the data they have taken, including the software needed to analyze them. In total, the dataset used includes 1281652 events with invariant masses between 2 and 110 GeV. The dataset corresponds to a luminosity of $33.02\,\text{pb}^{-1}$[**?**].

To obtain the events for the dimuon spectrum, the events were filtered out where exactly two muons with opposite signs are in the final state. For these events, energy, momentum in Cartesian coordinates, charge and type of the two muons are stored in `.csv` format. The read-in procedure of the date is already included in the program template used for the experiment.

[8] Mu primary dataset in AOD format from RunB of 2010: http://opendata.cern.ch/record/14, Accessed: May 28, 2017

For the analysis, jupyter notebookes with `Python3` are provided[9] with numpy[10], matplotlib [11], and the fittingtool kafe [12]. These should be familiar from previous semesters' lectures and labs. If not, introductions and tutorials can be found at the links provided.

7.8.5 Visualizing Events with the Event Display

As a first part of the exercise, a few events will be evaluated visually to learn how to interpret the signatures of particle collisions measured with CMS and how to distinguish between J/Ψ and Z candidates. From those events, one of each should be selected and described within the experimental documentation.

7.8.5.1 Classification of Muons

Within the data of an event, the muons are sorted by transverse momentum p_T. The muon with higher p_T is accordingly listed first and is called 'leading muon'. The second muon is consequently called 'second leading muon'. Furthermore, they are classified by 'type'. A 'global muon' is the term for a muon that could be reconstructed from traces in the tracker as well as from traces in the muon system of the detector. For such muons, the probability of a false reconstruction of a particle other than a muon is very low. On the other hand, if a muon is reconstructed only in the muon system, it is called a standalone muon. If only traces of a muon are found in the tracker, this is called a tracker muon. In the case of tracker muons, the probability of another particle being erroneously reconstructed as a muon is greatest. To avoid biases because of this, the used dataset only includes global muons.

7.8.5.2 Analysis of the Z Resonance

The general idea is that the Z resonance will be fitted – considering signal and background in the range of around 60 to 110 GeV (see fig. 7.35) – in the dimuon spectrum to obtain its mass and decay width . However, preparatory steps are necessary that will be described in the next sections. For the fitting to the signal the Voigt distribution explained before is used. The parameterization of the background is determined by a background study. After discriminating signal and background they should be summed up and fitted to the distribution to obtain the mass of the z boson ,M_Z, along with its decay width, Γ_Z.

7.8.5.3 Determination of a Background Parameterization

Since the convergence of fits with many parameters strongly depends on the chosen initial values, it makes sense to estimate as many of the parameters as possible in advance for a multi-parameter fit and to include them as constraints in the fit. This means that the fit program is passed a value as well as a containment for corresponding parameters. As a result, this parameter can only be adjusted to a value in the interval defined by it during fitting.

To determine the background underlying the signal, the areas of the distribution in which the signal has already dropped sharply should be used. These areas are called side bands, in which the distribution is mostly flat. It is reasonable to assume that the background in the Z resonance region runs in the same way as in the side bands. To test this assumption and justify the choice of a flat parameterization, a background study will be conducted at this point. For

[9] Python tutorial: https://www.python-kurs.eu/python3_kurs.php
[10] Numpy tutorial: https://docs.scipy.org/doc/numpy-dev/user/quickstart.html
[11] Matplotlib - Introduction to pyplot: https://matplotlib.org/tutorials/introductory/pyplot.html#sphx-glr-tutorials-introductory-pyplot-py
[12] Karlsruhe Fitting Environment: http://www-ekp.physik.uni-karlsruhe.de/~quast/kafe/htmldoc/

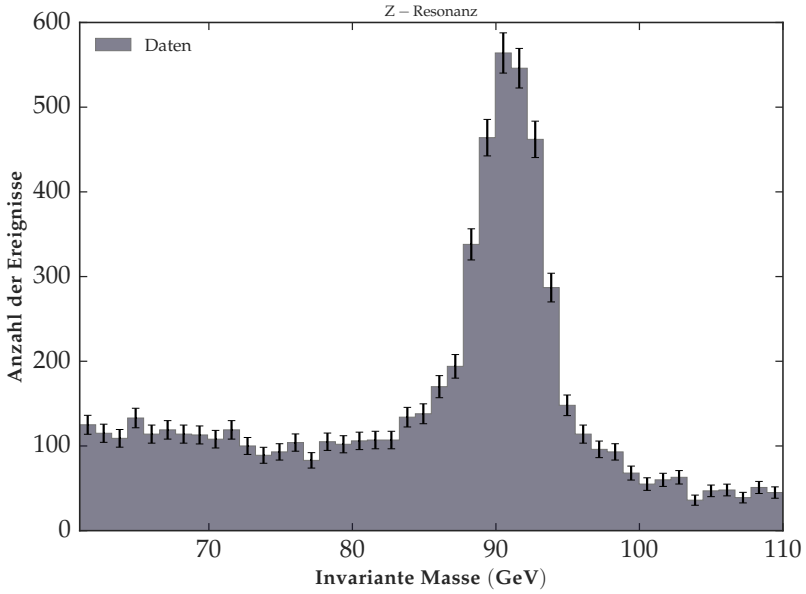

Figure 7.35: Z resonance in the dimuon spectrum between 61 and 110 GeV. The error bars plotted correspond to the Poisson errors of the entries.

this purpose, an evolution around the center of mass $\bar{m}$ of the histogram is to be performed and checked at which order the fitting is optimal. Specifically, a fit to polynomials of degree 0 to 4.

The goodness of fit can be quantified by the quotient of χ^2 of the fit over the number of its degrees of freedom ndf. If $\chi^2/ndf \approx 1$ holds, then the fit is optimal. The statistical fluctuations are in the range of uncertainty of the fit. A smaller χ^2/ndf could mean that statistical fluctuations were accounted for in the fit. If $\chi^2/ndf > 1$, the larger χ^2/ndf becomes, the worse the fit. Accordingly, for the subsurface, the parametrization should be chosen where $\mid \chi^2/ndf - 1 \mid$ becomes minimum.

For the documentation, the procedure should be described and a plot of the chosen background parametrization should be added.

7.8.5.4 Estimation of the Detector Resolution

The next step necessary to obtaine reliable results is the estimation of the detector resolution. When fitting a Voigt distribution to the signal, no information about the decay width of the Z boson can yet be obtained from the fit parameters of the two widths Γ_Z and σ_Z, since the parameters determining the widths are highly correlated. Therefore, in a fit, the fraction of the actual decay width within the whole width of the resonance would not be reflected only in Γ_Z and the fractions of the detector resolution would not be reflected only in σ_Z. Accordingly, one of these parameters must be estimated beforehand and introduced into the fit as a constraint, analogous to the procedure for the background. Since Γ_Z is to be determined, an estimation of σ_Z must be made. In the present case, this detector resolution corresponds to the mass resolution ΔM. For the latter, a correlation is to be found in the following on the basis of the J/Ψ resonance in the mass spectrum, from which the mass resolution can be determined, as it has physically a vanishing width. To find such a relation, the transverse mass M_T is considered:

$$M_\mathrm{T}^2 = 2p_{\mathrm{T},1}p_{\mathrm{T},2}(1-\cos\theta), \tag{7.122}$$

where p_T is the transverse momentum and θ is the angle between the momenta of the two muons. For the study of the mass resolution, the use of the invariant mass is approximately equivalent to the use of the transverse mass. In the following, for simplicity, it is assumed that for the transverse momentum of the two muons approximately applies: $p_{\mathrm{T},1} \approx p_{\mathrm{T},2} \approx \frac{p_{\mathrm{T},1}+p_{\mathrm{T},2}}{2} =: p_{\mathrm{T}}$, meaning they can be approximated by a mean transverse momentum. To obtain a relation between the uncertainty ΔM on the mass and the uncertainty Δp_{T} on the transverse momentum, these uncertainties are propagated in equation 7.122. Accordingly follow:

$$\Delta M^2 = 2M\Delta M = 4p_{\mathrm{T}}\Delta p_{\mathrm{T}}(1-\cos\theta) \tag{7.123}$$

and

$$\frac{\Delta M}{M} = \frac{\Delta p_{\mathrm{T}}}{p_{\mathrm{T}}} \tag{7.124}$$

for the relative uncertainties. With this, the mass resolution of the Z resonance can be estimated:

$$\Delta M_{\mathrm{Z}} = M_Z \frac{\Delta p_{\mathrm{T}}}{p_{\mathrm{T}}}|_{p_{\mathrm{T,Z}}}. \tag{7.125}$$

To determine the momentum resolution, p_{T}, the mass resolution, ΔM, of the selected resonance is determined for fixed ranges of p_{T} and converted to the momentum resolution using equation 7.124. The ranges of p_{T} will be referred to as bins in the following. It makes sense to use the J/Ψ resonance for this study because it has a lot of statistics and the widest p_{T} spectrum possible. In addition, it is isolated in the spectrum so that the background in the resonance region can be determined by fitting the side bands. And its vanishing width can be neglected in comparison to the mass resolution.

The results should be included into the documentation.

7.8.5.5 Fitting the Z Resonance

Once a background parameterization is found and the detector resolution is estimated, a fit to the Z resonance can be made. A possible result is shown in fig. 7.36.

Compare your results with the literature values in chapter **??**. Can your results be optimized for M_Z and Γ_Z? Why? Discuss.

7.8.5.6 Topics for Preparation

Experiment: LHC + CMS, detection of muons, dimuon spectrum + Drell-Yan process, Z boson, J/Ψ meson, shape of their resonances and underlying distributions, differences between their signatures within the detector (transverse momentum, pseudorapidity, and ΔR), course of the analysis for the determination of M_Z, Γ_Z, τ_Z, $\sigma_{\mathrm{Z}\to\mu\mu}$, error propagation, goodness of fit/ chi-square

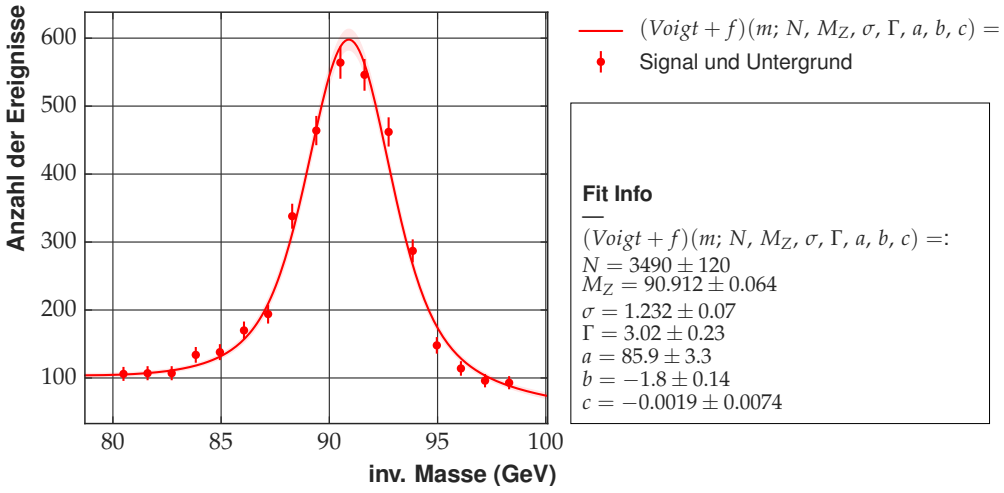

Figure 7.36: Fit of a Voigt distribution and the background parameterization to the Z resonance. Constraints on the detector resolution and background parameters were used for the fit.

7.9 Experiment (M): γ-coincidence spectroscopy

7.9.1 Tasks

1. Measurement of the γ-spectrum of ^{22}Na, ^{137}Cs and ^{57}Co with both detectors (NaI-detector and Ge-detector). Energy calibration with photo electron peaks.

2. Time calibration with a ^{22}Na source and an adjustable delay unit.

3. Measurement of the γ-spectrum of ^{60}Co with two detectors. Determination of the energy of the photo peaks and Compton edges and interpretation of the spectrum.

4. Coincidence analysis of ^{60}Co with different time cuts. Which decay scheme describes the decay? Are there other coincidences?

5. Analysis of the energy dependence of the energy resolution of the Ge-detector and the NaI detector. Explain the difference?

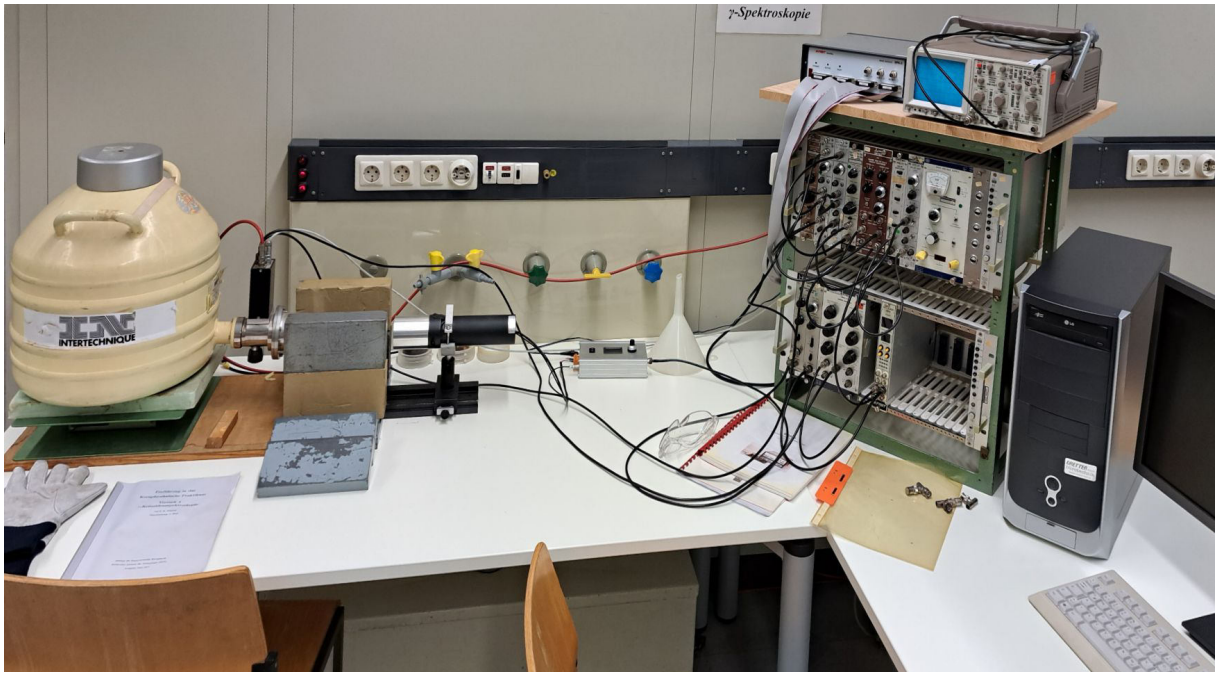

Figure 7.37: Setup of the γ-spectroscopy experiment. From left to right, you see the Ge-detector with the liquid nitrogen Dewer, the NaI scintillation detector, the data acquisition electronics and the analysis computer.

7.9.2 Introduction

A nucleus emits *gamma* quanta, if it is in an excited state after a preceding α or β-decay or after a nuclear reaction. The transition to the ground state can be done in one or several step. In the latter case one speaks of a γ-cascade. In general, there are several possible ways to the ground state for highly excited nuclei. The relative occurance of a particular path depends on the quantum numbers of the spins of the participating states and their parity and can be expressed by the so-called branching ratio. The aim of the γ-spectroscopy is to determine the energy and the quantum numbers of the states.

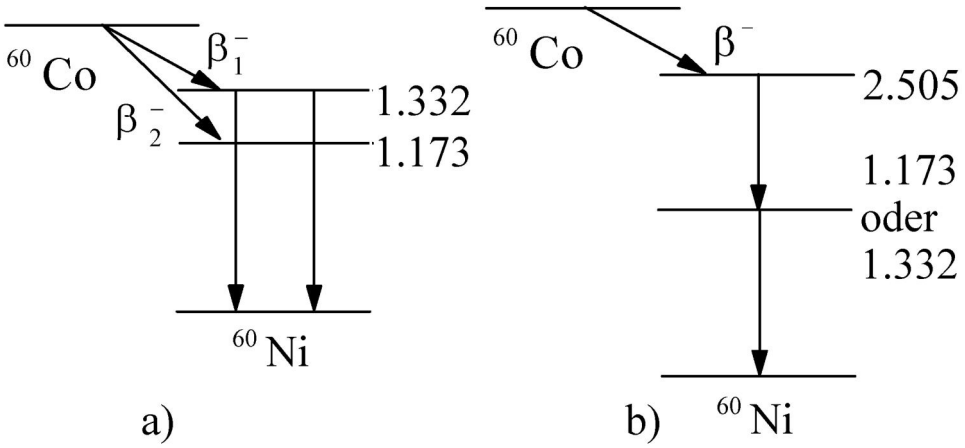

Figure 7.38: Possible energy level schemes for a two-γ decay.

In this experiment, a method is introduced, which is a first step towards establishing an energy level scheme of nuclei, the coincidence spectroscopy. It is also an essential part for further experiments to determine the quantum numbers, such as the measurement of the angular correlation.

7.9.3 Principle of measurement

The experimental setup consists of two γ-detectors (NaI scintillator and Ge semiconductor counters) whose energy signals are read by two ADCs. If both signals occur within a time window of about $\pm 2\,\mu$s, the time difference will be transformed into an analog signal by a TAC (Time-to-Analog Converter), which is converted by a third ADC. Thus, one γ-event consists either of one ADC value, if only one detector observed a signal, or three values, if both detectors triggered within the coincidence time of $\pm 2\,\mu$s. The ADC values are stored sequentially on a computer. Because of the longer conversion time of the TAC the two energy values are stored first, followed by the time value. After the end of the data taking, the data are converted into a format of the analysis program ROOT (http://root.cern.ch). The conversion program combines the data into so-called *events*. Each event has an entry for the measuring time, and three values that are assigned to the three ADCs. If an entry of the third ADCs (time difference) is found in the sequential data stream of the *raw data file*, the two preceding energy values are assigned to the same event (coincidence event). All other energy values are stored as individual events, where only one energy-ADC contains an entry, while the two other ADC values are set to 0.

With ROOT one can analyze not only single spectra, but also coincidence events, by searching for events with signals in both detectors within a certain time window. A short introduction into ROOT will be given during the experiment with some simple examples.

In the first step the respective energy and the time scales of the ADCs are calibrated with known calibration sources. Thereafter, the individual γ spectra and the distribution of the time differences of an unknown source are measured to determine the number and the energy of the energy transitions. Afterwards the events are examined in a coincidence analysis to find out which transitions belong to a cascade. The measurement principle will be explained using the example of a ^{60}Co source.

^{60}Co is a β^--emitter with two γ-transitions (1.173MeV and 1.332MeV), as one can see from the individual spectra. For the scheme of the energy levels there are basically two possibilities, as shown in Fig. 7.38. In case a) the excited states are occupied by two independent β-transitions. Therefore, the emitted γs are independent in time. In case b) there is only one β-decay to

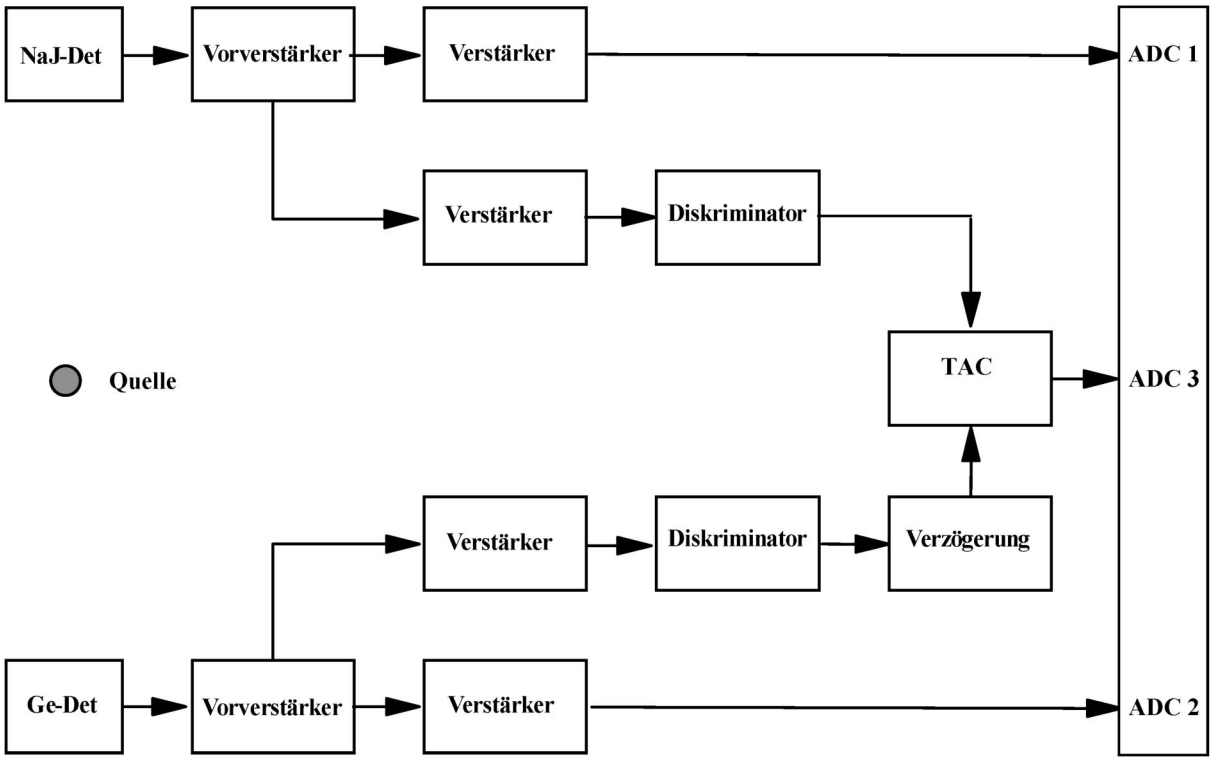

Figure 7.39: Block diagram of the γ-spectroskopy with three ADCs.

the highest excited state, and the subsequent γs form the simplest case of a cascade. If the intermediate state is sufficiently short-lived, as is the case for the daughter of ^{60}Co with a lifetime of 10^{-12} s, both photons appear virtually at the same time. With a coincidence experiment which tests the simultaneity of the decays, one can distinguish between the two possibilities. The γ-spectrum is measured in a detector under the additional condition that another photon with a specific energy is detected in a second detector *at the same time*. If the two photons belong to a cascade, the first detector sees only the spectrum of one transition. In case a), however, the spectrum in the first detector consists of those events which occur in a random coincidence with the event in the second detector. Both transitions occur, just like in the measurement without coincidence. Only the count rates are considerably smaller, since the actual measurement time is not the real time, but the number of events in the second detector times the time resolution of the coincidence.

The block diagram of the coincidence experiment is shown in Fig. 7.39. Both detector branches are nearly identical. The signals are amplified and split by pre-amplifiers integrated in the detector housing. The pulse of the first signal is shaped and further amplified by a spectroscopy amplifier, before being passed directly to the ADC as an energy signal. The ADC board has integrated discriminators, so that no external trigger signals need to be generated. The second signal is led through a fast timing amplifier and a *Constant fraction discriminator* to the TAC. The Ge-detector supplies the stop signal of the TAC and the NaI-detector supplies the start signal. To ensure that the start signal arrives ahead of the stop signal, an additional delay unit is included in the Ge-branch, which can delay the signal between 0 and 4.75 μs. The electronics accepts single events as well as correlated events. Only in the offline data analysis one decides whether an energy measurement, a time measurement or a coincidence measurement is made. Thus, one can realize all five measurement setups described in Chapter 5.7 after the measurement via software by appropriate data selection cuts.

If the photo peak of the high-energetic ^{60}Co transition in the NaI detector is discriminated (selected) with an appropriate energy cut, in case of a cascade the energy spectrum in the Ge-detector is expected to show only the spectrum of the low-energy γs. In a real spectrum one observers also some high-energetic γs, but with much lower intensity compared to the spectrum without the coincidence cut. These events are random coincidences. An estimate with Eq. 7.126 shows that with a time resolution of $\tau = 5\,\mu$s and an activity of the source of $A = 2 \cdot 10^5$ Bq the same number of random and real coincidences would be observed.

$$N_Z = \tau_A \cdot N_1 \cdot N_2 = \tau_A \cdot \epsilon_1 \cdot \epsilon_2 \cdot A^2 \tag{7.126}$$

The parameters ε_i are the detection efficiencies of the detectors, including the geometrical factors. In order to improve the real to random coincidence ratio, it does not make sense to reduce the activity, because then the individual rates become too small. It is better to reduce the coincidence time window, selecting only events close to the peak of the time spectrum.

7.9.4 Measurement procedure

For the energy calibration the energy spectra of the nuclides ^{22}Na, ^{57}Co, and ^{137}Cs, whose γ-energies are known, are measured. The line widths of the photo peaks are used for the determination of the energy-dependent energy resolution. In addition, the ^{22}Na source is used to calibrate the time spectrum by switching on and off different time delays in the delay unit. Afterwards the delay time is set so that the coincidence peak is approximately located at the center of the ADC spectrum. With this setting the spectrum of ^{60}Co is now measured and the photon peaks, Compton edges and backscatter edges are determined.

Afterwards, the real and random coincidences in the ^{60}Co data are analyzed with the methods introduced in the previous section. Have a closer look at the 2D energy spectrum of the events in the short coincidence time window. Are there possibly still other coincidences?

7.9.5 Literature

Introductory chapters 1 – 6 in this script
γ-spectroscopy: [1], [26]
Detectores: [19], [26]
Electronics: [21], [22]

7.10 Experiment (M): Cosmic Muon Background in the KATRIN Experiment

7.10.1 Tasks

1. Find coincidences inside and in-between of the scintillator modules.
2. Determine the mean lifetime of stopped muons.
3. Investigate the temporal variations of the muon rate.
4. Search for coincidences between through going muon tracks and events in the KATRIN detector.

7.10.2 Introduction

In this experiment you will investigate cosmic muons from air showers and their influence on the background rate in the KATRIN (KArlsruhe TRItium Neutrino) experiment, which aims to measure the effective neutrino mass with unprecedented accuracy.

7.10.3 Basics

7.10.3.1 The KATRIN Experiment

The KATRIN experiment is based on the β^- decay, in which a tritium atom decays into a helium atom, an electron and an electron anti-neutrino. The released energy is divided arbitrarily between electron and electron anti-neutrino, the recoil energy of the daughter nucleus is negligible.

In order to determine the mass of the anti-neutrino, the integral energy spectrum of the electron is measured around the endpoint of the β-decay, i.e. in the high-energy region. In this region, the neutrino is assumed to possess almost only its rest energy, since most of the available energy was transferred to the electron during decay. However, since the number of electrons in this region is very small, the background must be known precisely. A contribution to the background of the experiment is created by muons from air showers. More details about their composition and creation can be found in chapter 7.11.3. If muons from air showers hit the tank wall of the main spectrometer, electrons can be released, which can create secondary electrons that might reach the detector and leading to additional background.

The tritium for the decay is provided in the **windowless gaseous tritium source** (WGTS). It consists of a 10 m long tube with a diameter of 9 cm. Tritium is continuously fed into its center and pumped out at both ends. It is followed by a two-stage **pumping section**, which on the one hand is intended to prevent neutral tritium molecules from entering the main spectrometer, creating additional background. On the other hand, strong magnetic fields are used to guide

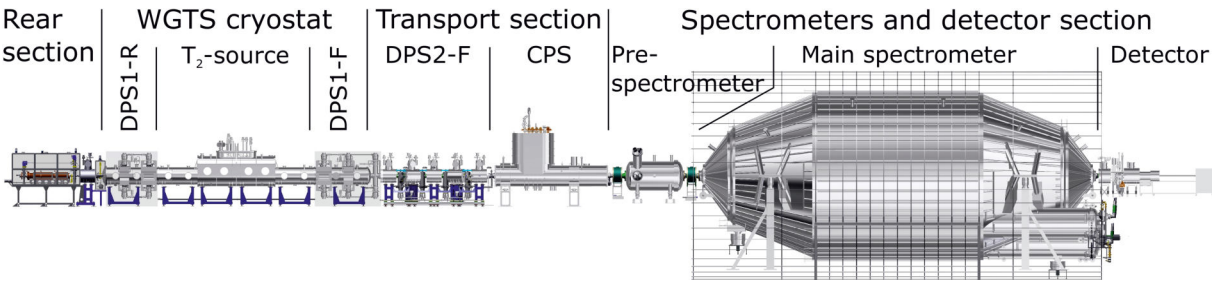

Figure 7.40: KATRIN experiment

the decay electrons through the vacuum beam line toward the spectrometer. First, the electrons pass through a **pre-spectrometer**. Here they are pre-selected by a high-pass filter to let only high energy electrons into the **main spectrometer**. Both spectrometers work according to the MAC-E filter principle. A strong magnetic field is induced by two superconducting solenoid magnets along the trajectory of the electrons, the field lines of which are strongly expanded in the center. This converts the transverse momentum of the electrons into longitudinal momentum. In the center, at the point of lowest flux density, is the analysis plane with the maximum of a negative electrostatic retarding field. The potential of the field is directed against the electron flow. Accordingly, only electrons above a certain energy can pass through the filter. Towards the end of the spectrometer with a conical electrode on ground potential, they are accelerated again and reach the **Focal Plane Detector** (FPD, 148-pixel PIN-diode detector). There the event rate is counted for different retarding potentials and the individual trajectories of the electrons are determined through the pixel location.

7.10.3.2 Muon telescope

Four scintillator modules, each equipped with eight photomultipliers, serve as the muon telescope (see Fig. 7.41). More detailed information about the operation of scintillation detectors can be found in chapter 4.2. The modules are mounted around the main spectrometer of the KATRIN experiment in such a way that they detect mainly muons whose trajectory passes through the spectrometer vessel. Two scintillators each are combined to form a measurement plane. The two scintillator planes are arranged in west (top) – east (bottom) direction at an angle of approximately 45° with the spectrometer in its center according to Fig. 7.42.

The modules are wrapped with aluminum foil to improve reflectivity. In addition, the background from the room light is greatly reduced by wrapping the modules with black foil.

7.10.3.3 Data acquisition

The data are recorded by a **Data acquisition Crate** (DAQ), which is controlled and read out by the ORCA software of the KATRIN experiment. The modules are read out each end individualle, whereas the signals of the four PMTs at each end are combined passivly. For each event, the location (represented by the data channel) of the PMT-group, time and deposited energy are stored. These data are bundled into so-called runs, where a run corresponds to the time interval over which a measurement, and thus the data recording, runs. The time resolution of the experimental setup is 100 ns in order to allow accurate analysis of coincidences.

7.10.3.4 Coincidences

A *coincidence* refers to events that occur within a certain time window, such that it can be assumed that these events were produced by a single muon. Two types of coincidence are distinguished. One is the coincidence between the two ends of a module, the other is the coincidence between the two measurement planes. In the case of coincidences between a module's ends, it should be noted that the observed signals of the two PMT-groups can be different, due the different light paths and attenuation of the scintillation light. In order to compensate the positin dependent signals, the energie signals from both ends are added. If the spectrum of the sum energies of the events of these coincidences is now displayed, it can be clearly seen that it is a Landau distribution. In order to reduce low-energetic random background noise signals, a threshold value must be found below which the events are discarded. A myon passing through both scintillator groups, producing almost simultaniously signals in the four PMT groups, reduces random background events even further.

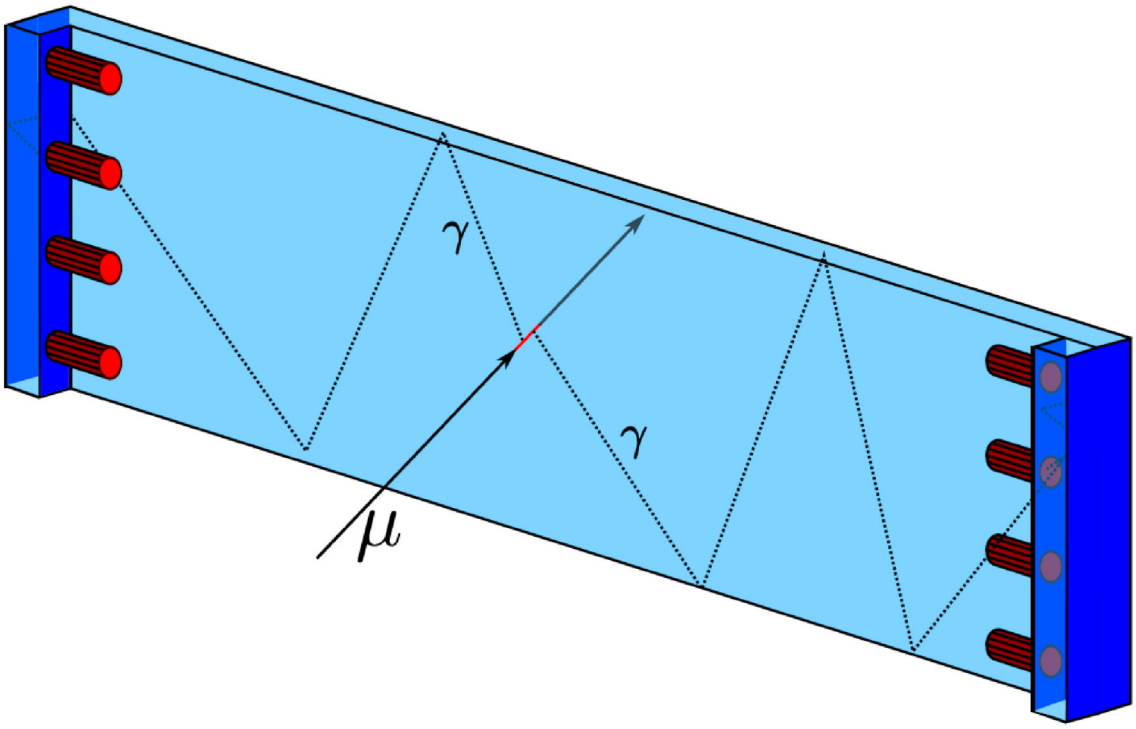

Figure 7.41: Schematic picture of a scintillation module. The red cylinders at both ends represent the photo-multipliers. Each module has a length of 3.15 m, a width of 0.65 m and a thickness of 0.05 m.

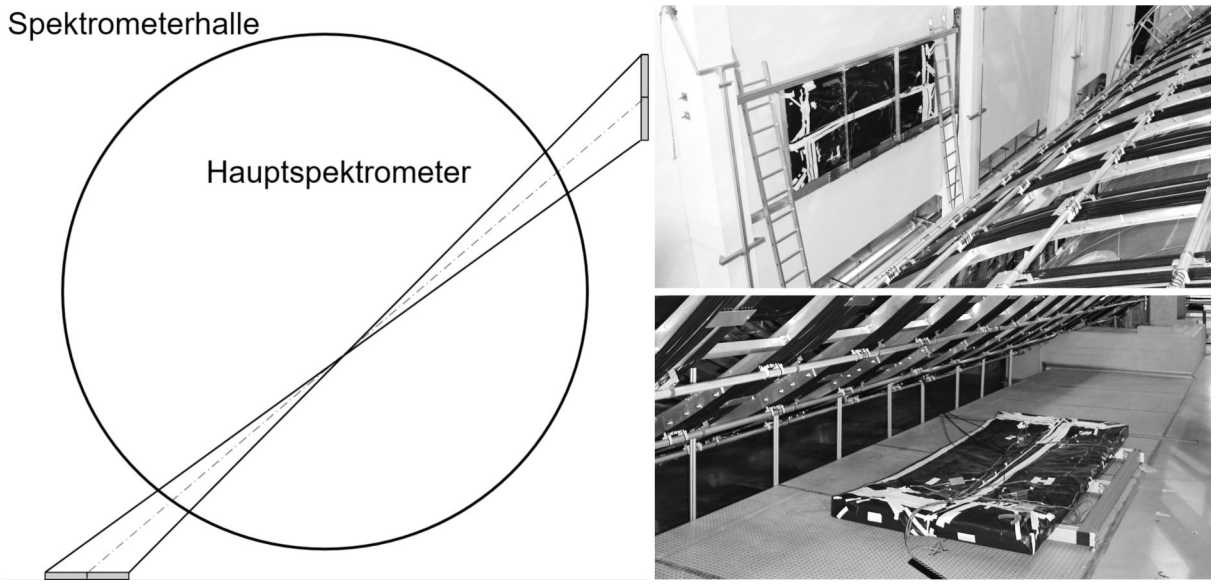

Figure 7.42: Arrangement of the scintillation modules around the KATRIN Main Spectrometer vessel.

Another type of coincidence is produced by muons which, after passing through one or even better through both module planes, are stopped in the concrete behind it and decay. In this decay an electron or positron is produces, which can also generate a signal in the scintillator directly above the decay location. Since these events are very close together, it is useful to evaluate the time differential spectrum for short time differences.

7.10.4 Performing the measurement

7.10.4.1 Measurements

This experiment is less about setting up an experiment and more about preparing and analyzing the data appropriately. In order to determine a reasonable maximum time difference between signals of a coincidences, the time interval between two events must be evaluated from the data. If this time interval is plotted into a histogram, it can be used to determine a time limit below which the events can be taken as coincidences. To do this, first, the events between the two ends of a module must be compared. This results in the upper time limit for events to be add up the energies to the sum energy. assigned to a muon. The same must then be carried out between the two module levels.

To be able to determine the lifetime of the muons, the time differential spectrum is evaluated for short time intervals (e.g. 1 - 10 μs) between an event with coincident signals in both scintillator planes and an event in one of the bottom scintillators. It is expected that the differential time spectrum decrease exponentially

$$N(t) = N_0 e^{-t/\tau} \tag{7.127}$$

with the mean lifetime τ of the muon.

Furthermore, the event rate shall be investigated in more detail. Here fluctuations occur, which are caused by changes in the air pressure, the temperature and the atmospheric density. In order to examine these fluctuations, measured values of several days are examined. Here, the number of events per second is given as a rate and averaged over one hour to make a long-term fluctuation recognizable. In addition, a finer binning in the seconds range should be used, in order to be able to recognize short-term fluctuations.

In order to find coincidences between muon events and the KATRIN detector, coincidences between the module levels must first be found. Here, the event occurs first in the upper module of the muon telescope and then in the lower module. Accordingly, these muons have passed the spectrometer tank and could trigger secondary electrons in the tank wall. These secondary electrons can then be detected in the KATRIN detector, depending on the magnetic field setting, leading to a brief increase of the event rate. To analyze the data, the timing of the muon events is compared to the event rate of the KATRIN detector.

7.10.4.2 Software for data analysis

The software for data processing and analysis is based on the *Python* programming language. Basics of it should be known. The analysis scripts are stored and run in *JuniperLab*, but must be completed by the students. The files with the raw data to be analyzed are also stored in JuniperLab.

7.10.5 Data evaluation

All data must first be preselected and processed. Various events and values are stored in the raw data that are not relevant for the data analysis. In the first step of data reduction, the data relevant for the subsequent analysis are combined (and calibrated if necessary) into events and

saved in a text file. This can be, for instance, the event time, the total energy for each module, or just the module numbers that are above the energy threshold. First, coincidences are determined in different stages: coincidences between the PMT groups of a scintillator module, between module planes and finally between through going muon tracks in both planes and subsequent events. Depending on the objective of the analysis, these are particles from the decay of stopped muons in the floor of the experimental hall, or temporally correlated events in the KATRIN detector.

- For the coincidence search within a module, the data must first be filtered according to the corresponding module number. The assignments of the PMT groups to the readout cards and channels of the DAQ electronics are required for this. There are four scintillator modules, each with two PMT groups. Each PMT group is read out via a separate ADC channel. Four PMT groups, i.e. two modules, are read out by one ADC card. Here, the modules with the numbers 4 and 8, the two lower modules, are together on one card, and the two upper modules with the numbers 6 and 7 are connected to the second card. After the data has been filtered, a timestamp with 100 ns resolution must be created, which always refers to the first event of a measurement. The data generated in this way must then be examined for coincidences between the two module ends. A maximum time difference is required for this, which specifies up to when two events are considered as coincidence. Then the energies of the measured events of a coincidence must be added. This total energy can then be displayed as a histogram. An energy cut value can be determined from this spectrum to remove noise events.

- For the coincidence search between the module levels, basically the same procedure can be followed. The difference is that here the data of the lower modules are summarized, as well as the data of the upper modules. Since here no additional energy spectrum is required, it is only checked whether coincidences between both modules occur in a measuring plane, in order to discard duplications. Here, we are only interested in whether almost simultanious events are found in both measurement planes that meet the coincidence criterion. Such events correspond to the track of a through going muon.

- For the determination of the lifetime of muons again only single modules have to be considered. Here, again the coincidences within individual modules are sought. The energy is again irrelevant, but it should be above the threshold for random background events. Only the coincidences within a time interval of $10\,\mu$s after a preceeding muon track are interesting here. These time differences are plotted in a histogram and an exponential fit with equation 7.127 is performed to obtain the lifetime of the muons.

- For the determination of the longterm fluctuations of the average muon rate, multiple runs are read in, combined, and a common start time is defined. Then the average rates are determined in one hour steps and plotted as a histogram. The mean value then corresponds to the average rate of the coincidence events.

- Corresponding data are read in for the coincidence search between the muon telescope and the KATRIN data. The first problem that needs to be avoided is that the KATRIN data use different timestamps than the muon data. Here, too, a common start time must be defined. After that, a loop is required, which on the one hand runs through the muon events, on the other hand searches the KATRIN data for events in a time window from $20\,\mu$s before to $100\,\mu$s after the muon event and saves the KATRIN events. The KATRIN data is then displayed as a histogram from which the average transit time of the electrons generated in the spectrometer's wall to the detector can be determined. There are two options for the KATRIN data. In the normal setting used for measuring the neutrino

mass, the magnetic flux tube is used that focuses the tritium β-electrons onto the detector. It does not touch the detector wall, so that electrons knocked out of the wall material by the muons only have a low probability of being detected in the detector. The second setting is the so-called asymmetric magnetic field setting, in which the air coils of the main spectrometer are inverted so that the flux tube expands extremely and touches the spectrometer wall. In this case, electrons starting from the wall are magnetically guided to the detector. With this setting, clear coincidences between muons and events in the KATRIN detector should be found.

7.10.6 Topics for preparation

Experiment: KATRIN experiment, detection of muons, muon decay, ... Python basics (simple loops, conditions) and the packages Pandas, Numpy, Scipy (exponential fit) should be known.

7.11 Experiment (M): Properties of cosmic muons

7.11.1 Tasks

1. Determination of the noise threshold of the detectors
2. Recording a pulse height spectrum
   (a) Determination of suitable thresholds for muons and electrons/positrons
   (b) Calibrating the pulse heights of the individual modules
3. Determination of the efficiency of the individual detector modules
4. Determination of the lifetime of the muon
5. Proof of the precession of the muon spin in the magnetic field and determination of the statistical significance

Figure 7.43: Setup of the cosmic muon experiment. The stack of three scintillation panels is seen on the right side. On the left side, the data acquision electronics and the analysis computer can be seen.

7.11.2 Introduction

7.11.3 Composition of the cosmic rays

The primary cosmic rays, which originate partly in space and partly in the Sun, consist predominantly of protons (about 85%). It also contains a small fraction of α particles (about 12%), and with even lower abundance heavier nuclei (about 2% in total), electrons, and γ quanta.

It is a very high energy radiation. The energies of the particles range from 10^6 eV to 10^{21} eV. The primary spectrum has approximately the form

$$N(>E) = K \cdot \left(\frac{E}{E_0}\right)^{-\gamma} \qquad \begin{aligned} E_0 &= 10^{16}\,\text{eV} \\ K &= 3 \cdot 10^{-4} m^{-2} h^{-1} \\ \gamma &= 1.7...2.1 \end{aligned} \tag{7.128}$$

$N(>E)$ is the rate of particles with energies greater than E. The spectral index γ changes around $4 \cdot 10^{15}$ eV, at the so-called "knee".

When the primary cosmic radiation hits the Earth's atmosphere, secondary particles are generated by the interaction of the nucleons, which in turn initiate further reactions. Therefore, the composition of the cosmic radiation within the atmosphere is substantially different from the original one. It also changes with altitude. At sea level, there are almost no primary particles left.

The following processes take place: The primary nucleons first collide with air nuclei via the strong interaction and lose kinetic energy in the process. Large numbers of secondary, high-energy nucleons and pions are created, which themselves initiate further spallations through collisions. These processes stop only when the kinetic energy of the hadrons is no longer sufficient to produce pions. This happens at 300 MeV. A single primary nucleon thus produces a shower of very many strongly interacting particles, the so-called nuclear cascade. It does not reach the Earth's surface because the mean free path of pions and nucleons in matter is too small due to the strength of the interactions. Only a few protons and neutrons make it all the way.

The neutral pions of the nuclear cascade are unstable. They quickly decay electromagnetically into two γ quanta.

$$\pi^0 \rightarrow 2\gamma \qquad \tau = 8.4 \cdot 10^{-17}\,\text{s}. \tag{7.129}$$

The decay is very fast, so it takes place in the immediate vicinity of the nuclear cascade.

Those very energetic γ quanta are the starting point of the so-called **electromagnetic cascade**. At these high energies, the most probable process is pair production, whereas the Compton and photoelectric effects are negligible. In the Coulomb field of nuclei, particle-antiparticle pairs (see 3.2.2.3) are formed, most frequently the lightest of them, the electron-positron pair. Except for the small recoil energy of the nucleus, the leptons acquire the entire γ energy and are therefore themselves relativistic. Their direction of flight deviates only slightly from that of the incident quantum because of conservation of momentum.

Leptons lose their energy in matter either by ionization (chapter 3.1.1) or by bremsstrahlung (chapter 3.1.2). At high energies, bremsstrahlung predominates because it is proportional to $Z^2 \cdot E$, while ionization goes with $Z \cdot \ln(E)$. The two processes are equally likely at $800/Z$ MeV. Thus, the fast leptons generate Bremsquanta, which take over a large fraction of the energy and are preferentially emitted in the direction of flight. The Bremsquanta produce further lepton pairs, which in turn create γ quanta. In this way, the number of leptons doubles in each generation. A shower of leptons and γ-quanta is formed which propagates within a cone around the direction of flight of the primary particle. This electromagnetic cascade also terminates when the energy has become so small that the ionization processes (or Compton scattering) predominate. Only at primary energies $> 10^{12}$ eV appreciable parts of these electromagnetic air showers reach sea level.

The charged pions decay by the weak interaction into muons and muon neutrinos.

$$\begin{aligned} \pi^+ &\to \mu^+ + \nu_\mu \\ \pi^- &\to \mu^- + \bar{\nu}_\mu \end{aligned} \qquad \tau = 2,60 \cdot 10^{-8}\,\mathrm{s} \tag{7.130}$$

Their average lifetime is much longer than that of the neutral pion. Therefore, the decay can take place at a considerable distance from the nuclear cascade. But also here, the mean free path length is not sufficient; again they hardly reach the Earth.

This is achieved by the muons created in pion decays. They are subject to the weak interaction and can induce nuclear transformations in matter. However, the effective cross sections for this are extremely small, so that their behavior is determined only by the electromagnetic interaction. Like electrons, they generate electromagnetic cascades, but with the essential restriction that due to their approximately 200 times larger mass, the probability of this is $4 \cdot 10^4$ times smaller (see chapter 3.1.2, Eq. 3.9). Their range is therefore greater than that of electrons. They reach the earth's surface and even penetrate deep into the earth.

The charged muons can also further decay via the weak interaction into an electron (or positron) with electron and a muon neutrinos:

$$\begin{aligned} \mu^+ &\to e^+ + \nu_e + \bar{\nu}_\mu \\ \mu^- &\to e^- + \bar{\nu}_e + \nu_\mu \end{aligned} \qquad \tau = 2.19 \cdot 10^{-6}\,\mathrm{s}. \tag{7.131}$$

Their average lifetime is much longer than that of neutral pions.

Accordingly, the cosmic radiation on the earth's surface consists of two components. The penetrating one, which has a large mean free path, is called the hard component and consists of muons. The short-range, so-called soft component consists of electrons, positrons and bremsstrahlung quanta of the electromagnetic cascades. Only a small part comes from the decay of muons.

During the mean lifetime given in Eq. 7.131, an extremely relativistic muon travels approximately 600 m. This corresponds to the mean distance travelled by muons between their creation and their decay. It is too short to explain the abundance of muons at the earth's surface. This is solved by the theory of special relativity. Those lifetimes are valid in the rest system of the particles. However, in a system with a velocity v relative to the particle, time dilation becomes noticeable. The mean lifetime τ_E of the relativistic particle measured on earth is longer.

$$\tau_E = \frac{1}{\sqrt{1 - \frac{v^2}{c^2}}} \cdot \tau = \gamma \cdot \tau \tag{7.132}$$

γ is the ratio of the total energy to the rest energy of the muon, c the speed of light. If E is the total energy, E_{kin} is kinetic energy and m_0 the rest mass, so is

$$\gamma = \frac{E}{m_0\,c^2} = \frac{E_{\mathrm{kin}} + m_0\,c^2}{m_0\,c^2} = \frac{1}{\sqrt{1 - \frac{v}{c}^2}}. \tag{7.133}$$

For extremely relativistic particles the rest energy is negligible compared to the kinetic energy, and one obtains

$$\gamma \approx \frac{E_{\mathrm{kin}}}{m_0\,c^2} \tag{7.134}$$

In numbers: for a muon of 10 GeV the mean lifetime on Earth is about 100 times longer than in the rest frame, so that this muon decays only after a mean distance of 60 km and thus has a good chance of reaching the ground.

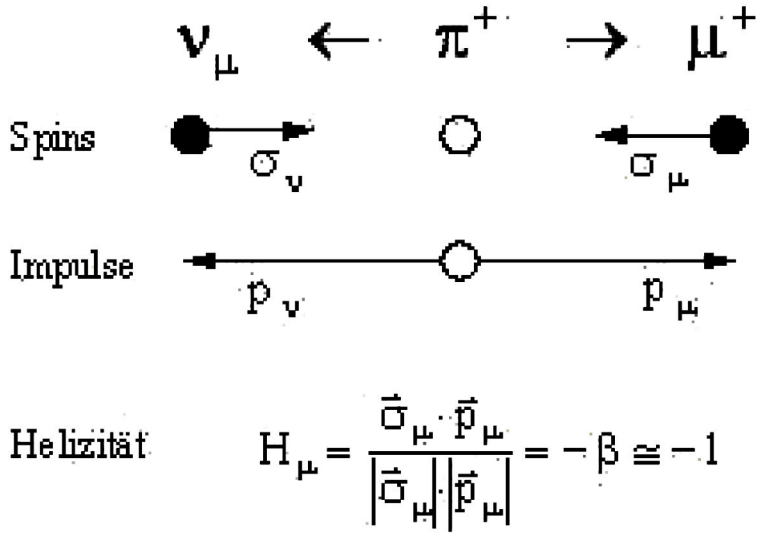

Figure 7.44: Decay of the π^+ and helicity of the μ^+.

7.11.4 The deceleration of muons in matter

The high-energy muons lose their energy in matter through Bremsstrahlung at the nuclei. Only at energies in the GeV range and below also ionization processes become noticeable through the Coulomb interaction. These processes are independent of the sign of the charge. However, at the end of their range, just before they come to rest, the positive and negative muons behave differently.

The negative muons, which differ from electrons only by their mass, are captured by the atoms mostly in excited states and land very quickly in the K-shell under emission of X-rays. The Pauli principle allows this, even if the shell is already occupied by electrons, because the particles are not identical. From there they are captured by the nucleus, where analogous to the K-capture of the electrons, the nucleons are transformed by the weak interaction. Thus, a second decay channel opens for the μ^-, which means that their average lifetime is lowered. In Cu, for example, one measures $\tau = 0.163\,\mu$s. As a result of this strong reduction of the lifetime, in measurements of cosmic muons, where the positive and negative particles arrive with equal frequency, one records almost only μ^+, since the μ^- are captured very quickly. In Cu, they are practically absent after a microsecond.

At low energies, the positive muons capture electrons from the atomic shells, with which they build a hydrogen-like structure in which the μ^+ replaces the hydrogen nucleus, it is called muonium. Subsequently, it can be ionized, rebuilt, alternating between capture and loss of an electron. The electrically neutral muonium is also further decelerated by collisions with electrons and atoms until it is finally thermalized.

The time scale on which these processes occur is short compared to the average lifetime of the muon. Deceleration due to scattering losses to a few keV takes about 10^{-10} s. The capture and ionization processes of the muonium last about $5 \cdot 10^{-13}$ s, after which it still has an energy of about 200 eV. At this energy, it becomes stable and thermalizes within another 10^{-12} s.

7.11.5 Muon polarization

The totality of muons in a given energy range is polarized in their momentum direction, i.e. the number of particles with a spin in parallel to their direction of flight is not equal to the number with an antiparallel spin. This is a consequence of the parity violation in the weak interaction and is explained in detail for the μ^+ as follows.

According to the V-A theory of the weak interaction there are only left-handed particles (negative helicity, i.e. spin antiparallel to the momentum direction) and right-handed antiparticles. The probability for the expectation values of these helicities is proportional to $\beta = v/c$. π^+ has spin 0 and ν_μ as a (nearly) massless particle must have a negative helicity. Because of the conservation of angular moment, the antiparticle μ^+ has no other choice but to be emitted with the wrong helicity, i.e. a negative one. This the reason why the pion decays rarely ($\approx 10^{-4}$) into the lighter lepton, which would be preferred by the phase space. The probability for wrong helicity is lower for the highly relativistic electron.

The total energy of the muon in the pion's rest frame is

$$W_\mu = \frac{(m_\pi c^2)^2 + (m_\mu c^2)^2}{2 m_\pi c^2} \tag{7.135}$$

The rest mass of the pion is 140 eV, that of the muon 106 MeV. This leads to a total energy of the muon of 110 MeV, leaving only 4 MeV as the kinetic energy.

On Earth, the muons have different energies depending on whether they are emitted in the direction of the pion's flight or in the opposite direction. For example, if the pions fly toward the detector with a total energy of 1 GeV, then the forward-moving muons have a total energy of 998 MeV, while those emitted backward have 662 MeV. The spin of the high-energy group is opposite to the direction of flight, while the spin of the low-energy particles is parallel to it. Since the decay of the pions is isotropic in their rest frame, there should be equal numbers of muons in each group. Now, if both groups are detected in the same way in a detector, the totality of muons is not polarized. If, on the other hand, one of the energies is discriminated and registered separately, one has complete polarization.

In reality, the pion spectrum is continuous, and the direction of incidence is also not perpendicular from above, but a distribution around this direction. The effect of the shape of the spectrum on the polarization can be easily understood. The muons whose lifetime is measured have been stopped in a Cu plate. They have lost only a few MeV of energy in the Cu, but much more before that on their way through the atmosphere. Since this path is of different length for the individual particles, depending on their place of origin, the muons ending in the Cu had energies in the GeV range with a broad but finite distribution when they were created. They have been emitted either forward or backward in the pion's rest frame. From relativistic kinematics we know that in the first case the kinetic energy of the pion must have been only a little bit, in the second case much larger than that of the muon. A numerical example: A muon with the (total) energy 1 GeV is created from a pion with 1.002 GeV for a forward decay, for a backward decay the pion must have 1.67 GeV.

The totality of stopped muons is polarized if the pion spectrum depends on the energy, because only then the number of muons produced at a fixed energy by forward and backward decays is not the same. It is known that the spectrum of pions in cosmic rays decreases with increasing energy, as expressed in Eq. 7.128. Therefore, for the μ^+ a negative polarization is to be expected, i.e. opposite to the direction of flight. In fact, for perpendicular incidence one measures the value $P = -1/3$ and this is only slightly dependent on the energy.

These considerations remain valid even if the condition of perpendicular incidence is no longer maintained. Then the polarization is averaged over the direction of incidence. In this case, the polarization is somewhat smaller, but always clearly different from zero.

There remains the question of the depolarization of the muons, which interact with matter after thermalization. The deceleration itself happens so fast that the muon, whether free or bound in the muonium, does not noticeably precess in external or internal magnetic fields and thus maintains the alignment. This is different after thermalization. Most of the time the muon remains (on average) in this state and is exposed to depolarizing interactions. The relaxation of the polarization depends strongly on the magnetic and crystal structure of the solids. In

paramagnetic metals, such as Cu, it is caused by the inhomogeneous magnetic fields of the nuclear moments or magnetic impurities. The relaxation time (this is the time in which the polarization has decreased on average to 1/e of its original value) in these materials is long. For Cu at room temperature, for instance, values greater than 50 μs have been measured. They are large compared to the average lifetime of muons. Therefore the depolarization is not noticeable.

7.11.6 A proof of muon decay

The end of the lifetime of a μ^+ is characterized by the appearance of a positron. The double differential spectrum of the positrons from the decaying μ^+ has the form

$$\frac{\mathrm{d}N}{\mathrm{d}\varepsilon\,\mathrm{d}\Omega} = \frac{\varepsilon^2}{2\pi} \cdot [(3-2\varepsilon) - P \cdot (1-2\varepsilon) \cdot \cos\theta] \tag{7.136}$$

where $\varepsilon = E/E_{\max}$ is the positron energy in units of $E_{\max} = m_\mu c^2/2$, the maximum energy a positron can carry away in a decay, and θ is the angle between the spin of the muon and the momentum of the positron. P is the polarization of the muon.

This expression has the form

$$\frac{\mathrm{d}N}{\mathrm{d}\varepsilon\,\mathrm{d}\Omega} = a \cdot (1 + b \cdot \cos\theta) \tag{7.137}$$

b depends on the positron energy and runs from $b = -1/3$ at $\varepsilon = 0$ through $b = 0$ at $\varepsilon = 1/2$ to the maximum value $b = 1$ at $\varepsilon = 1$. It states that the emission of the β^+ is not isotropic with respect to the spin of the μ^+: the positron is preferentially emitted in the direction of the spin.

The spatial asymmetry is the greater, the more energetic the positrons are. Usually positrons with different energies are not detected with the same sensitivity. The low-energy ones do not reach the detector at all, because of their energy losses. For this reason, there is a lower threshold for the detection, on which, of course, the magnitude of the measured asymmetry depends. When integrating Eq. 7.137 over the energy one obtains

$$\frac{\mathrm{d}N}{\mathrm{d}\Omega} = k \cdot (1 + A \cdot \cos\theta) \tag{7.138}$$

k is a constant determined by the threshold. The size of the asymmetry depends on the chosen integration interval. When integrating over the whole spectrum, it is $A = P/3$. Useing only the upper half results in $A = 0.44\,P$. For still higher thresholds A increases further until the upper limit $A = P$. Thus, it is advantageous to measure at high thresholds, where the effect is at its maximum. However, the counting rate becomes smaller and smaller, requiring a compromise.

The above expression has to be integrated over a finite solid angle if the angular distribution of the positrons is to be taken into account. Because of the averaging over the angle θ, the asymmetry decreases, e.g. to half when integrating over the half-space.

7.11.6.1 The precession of muons in the magnetic field

A magnetic moment associated with the angular momentum $\vec{J}$.

$$\vec{\mu} = \gamma \cdot \vec{J} \tag{7.139}$$

in a magnetic field $\vec{B}$ has the equation of motion

$$\frac{\mathrm{d}\vec{J}}{\mathrm{d}t} = \vec{\mu} \times \vec{B} \tag{7.140}$$

from which it follows that the magnetic moment precedes around the field direction with the angular frequency

$$\omega = \gamma \cdot B \tag{7.141}$$

The precession is counterclockwise when looking in the direction of the magnetic field. The gyromagnetic ratio γ of a particle is

$$\gamma = \frac{g \cdot \mu_B}{\hbar} \tag{7.142}$$

Where μ_B is the Bohr magneton. For an electron this is

$$\mu_B(\text{Electron}) = \frac{e \cdot \hbar}{2 \cdot m_e} = 9,273 \cdot 10^{-24} \frac{\text{J}}{\text{T}} \tag{7.143}$$

for a muon

$$\mu_B(\text{Muon}) = \frac{e \cdot \hbar}{2 \cdot m_\mu} = \frac{m_e}{m_\mu} \cdot \mu_B(\text{Elektron}) = 4,485 \cdot 10^{-26} \frac{\text{J}}{\text{T}} \tag{7.144}$$

The dimensionless quantity g is called the Landé factor. It is different for the orbital angular momentum of a charged particle and its spin. In the first case it is exactly equal to one, in the second case it is 2 plus higher order corrections. It can be determined by measuring the precession frequency of a free particle in a magnetic field

$$g = \frac{\gamma \cdot \hbar}{\mu_B} = \frac{\hbar \cdot \omega}{\mu_B \cdot B} \tag{7.145}$$

7.11.7 Principle of measurement

The measurement of the precession frequency of μ^+ is similar to the measurement of the mean lifetime, only extended accordingly. The deceleration of the muon in the detector marks the start time of the measurement, and the stop time is defined by the appearance of the positron from the decay. If the measurement is repeated for many muons, the number $N(t)$ of particles decaying at time t is obtained. It obeys the exponential law for radioactive decay

$$N(t) = N_0 \cdot \mathrm{e}^{-t/\tau} \tag{7.146}$$

τ is the mean lifetime and N_0 is the number of muons stopped in the detector during the measurement time. As long as we just want to determine τ, it is sufficient to simply detect the positrons regardless of their energy and direction. For this purpose the detector can be used as stop target.

To measure the precession, it is necessary to extend the measurement with two aspects. First, a constant magnetic field is placed over the stop target transverse to the direction of muon incidence, in which the spins precess. Second, only positrons emitted in a particular direction are measured. The count rate is then modulated with the precession frequency; it is largest when the muon spin points in that direction, smallest when pointing in the opposite direction. The angle θ in Eq. 7.138 is then no longer constant in time, it has to be replaced by the precession angle ωt.

The number of positrons detected at a time t is obtained by cobining Eq. 7.138 and Eq. 7.146.

$$N(t) = K \cdot \mathrm{e}^{-t/\tau} \cdot \left[1 + \bar{A} \cdot \cos(\omega t + \delta)\right] \tag{7.147}$$

The exponential function describes the decrease due to the decay. The expression in the parenthesis describes the modulation due to the precession. The bar in the asymmetry $\bar{A}$ indicates that this quantity is obtained by averaging over the geometry of the detector. It is time dependent because of the depolarization of the stopped μ^+ and is sometimes written as

$$\bar{A} = \bar{A}_0 \cdot \mathrm{e}^{-t/T_\mathrm{R}} \tag{7.148}$$

with T_R the relaxation time of the polarization. For Cu, the asymmetry can be assumed to be constant within the measurement time.

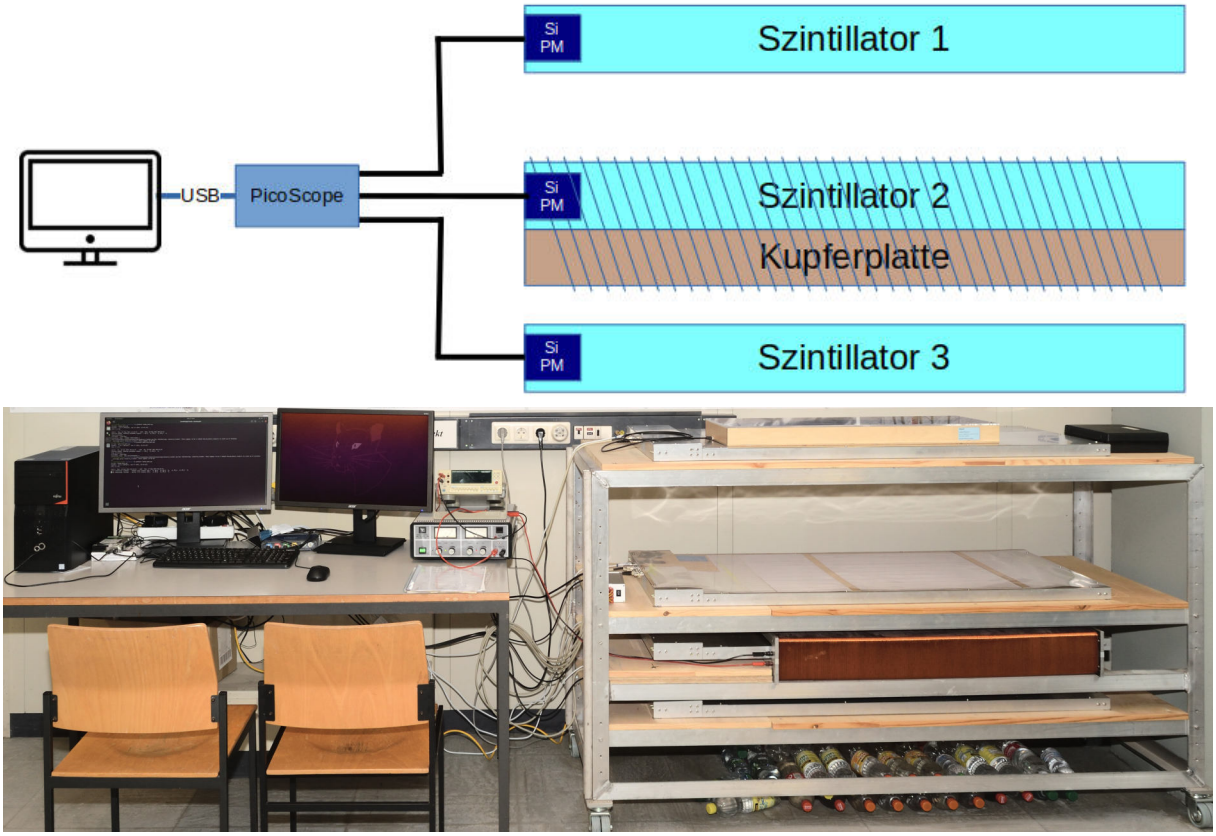

Figure 7.45: Top: sketch of the setup. Bottom: experimental setup in the lab.

7.11.8 Setup and execution

The experiment was revised in 2021 and the new setup is sketched in Fig. 7.45. It consists of three modules lying one above the other, each with 10 horizontally adjacent scintillator blocks made of plastic, each 1 cm thick, 5 cm wide and 93.5 cm long, which are connected via internal light guides (wavelength shifter) to a Si-photomultiplier (see Fig. 7.46). Between the second and the third scintillator module there is a 2.5 cm thick copper plate, in which the μ^+ should preferably be stopped due to the higher density. The second module and the copper plate are located within a 1 m long coil with 960 windings. The signals from the three Si-photomultipliers are digitized with a 4-channel USB oscilloscope (PicoScope 3404D) and transferred to a PC (Linux). As described in chapter 5.5, in this experiment the analog signal is digitized directly using a USB oscilloscope and the analysis of pulse height and coincidence then takes place in the software and is therefore highly configurable. The transfer of data from the USB oscilloscope to the PC requires a certain amount of time during which no new data can be digitized (cf. dead time of analog circuits). It is therefore not advisable to permanently transfer all data to the PC. Otherwise you would lose potentially relevant data that fall into the dead time. This loss can be minimized by setting a trigger threshold above which the signal must be, in order to be considered relevant. Only a certain time range before and after the signal was above this

threshold (trigger time) is then transferred to the PC where it is further evaluated. A good way of finding a suitable threshold is provided by the manufacturer's PicoScope software, which allows you to clearly test and graphically evaluate different thresholds. An optimal operating point for this threshold is just above the inherent noise of the detector modules and below all signal peaks assumed to be relevant. The processing, filtering and saving of the data in the following parts of the experiment is done with the help of a modular software specially written in the language *Python*, the structure of which is explained in more detail below. All relevant parameters, such as the signal thresholds and coincidence conditions, can be set for the individual measurements using configuration files in *yaml* format (text files with a predefined syntax that can be edited with a standard text editor).

Figure 7.46: Scintillator module with ten scintillating bars, Si-PM, and electronics.

For the following measurements it is necessary to determine thresholds for typical muon and positron signals. Therefore, a pulse height spectrum is first recorded for all detected signals from all modules. A signal is saved as soon as it is above the trigger threshold of the USB oscilloscope in the top detector module. Furthermore, signals from other detector modules are registered and stored if they occur in coincidence with the top module. If a signal occurs in each of the detectors at the same time, it can be assumed with high probability that it was triggered by a muon. These "throughgoing muons" are suitable for calibrating the signal height of the individual detector modules, since their pulse height distribution must be the same in all modules. In order to obtain a robust estimated value for the individual modules, the top and bottom 10

Furthermore, the efficiency of the individual detector modules can be estimated from the collected measured values. Due to strict constraints on the coincidence of two signals from two different modules, it is very unlikely that they were accidentally triggered by two independent particle events. Since the detector modules are precisely aligned on top of each other, it can generally be assumed that a signal in the top and bottom detectors is a significant indication of a throughgoing muon, and consequently a signal should also be seen in the middle detector. The efficiency of the middle detector can be calculated from the ratio of events with a signal in all three detectors to events in which only the top and bottom detectors responded. This method called "tag and probe" can also be used with unequal detector modules, as long as it is ensured that an event with a coincidence signal in the top and bottom detector must always trigger a signal in the detector to be tested.

The signature of a muon stopped in the Cu plate is $1{+}2{+}\bar{3}$, i.e. a coincidence of the two upper ones in anticoincidence with the lower scintillator. Such an event triggers the start of the lifetime measurement. The end of life is marked by the appearance of a positron in either scintillator 2 or 3. The random coincidences with passing muons are suppressed when an anticoincidence with the counter opposite is required. The signals $2 + \bar{3}$ and $3 + \bar{2}$ are equivalent, the best signature

for the stop is $1 + 2 + \bar{3}$. It improves the ratio of true to random coincidences, albeit with a loss of counting rate, because it shifts the threshold for e^+ detection to higher energies in the region of greater asymmetry.

In order to keep the measurement time for the lifetime measurement as short as possible, the decay function is fitted to the measurement data using the maximum likelihood method instead of being fitted to a histogram.

You are required to work on this evaluation with the help of your supervisor while the measurement is running. For this purpose, a prepared Jupyter notebook is provided that uses the packages *kafe2* and *PhyPraKit*. An excellent source of information are the examples of the two Python packages on the Internet, as well as the lectures on computer application for bachelor students.

In order to measure the precession frequency, the magnetic field is turned on and data is recorded for at least a week. The signature is the same as in the lifetime measurement, but a strict distinction must now be made between positrons emitted upwards and downwards, since the modulation of the two decay functions is phase-shifted by 180° (i.e. they would just cancel out). Since the modulation signal due to the precession of the muon spin is extremely weak and the fitting of the decay function proves to be difficult due to the large number of free parameters, the Landé factor cannot be reliably determined with the data from one week. Therefore, the task is a simple hypothesis test of whether an expected precession modulation is present and how significantly it differs from a decay function without modulation. Again, it is recommended to use packages such as *kafe2* or *PhyPraKit* for the fitting to function, since most of the other simple tools do not provide the required functionality for analyzing likelihoods. Follow the analysis strategy outlined below, which is also provided as a template in a Jupyter notebook:

1. Discard events with decay times smaller than 0.6 µs because they are dominated by nuclear captures of negative muons with shorter decay times.

2. Calculate the expected oscillation frequency ω from the magnetic field of the coil and the literature values and plot the decay function with expected values and a modulation amplitude of $\bar{A} \approx 15\%$.

3. Plot the decay times in a histogram using as few bins as possible, but still enough to safely resolve the modulation (see plotted decay function).

4. Fit a decay function *without* modulation to the histogram and determine the decay time of the muon τ and the background portion f_{bkg}.

5. Now fit the decay function *with* the modulation to the histogram, fixing all free parameters except the modulation amplitude $\bar{A}$ to the literature values or the parameters found in the previous fitting.

6. Use the additional variables to include only those decay times in the histogram that show a pronounced modulation signal (e.g. only events with a stop signature $1 + 2 + \bar{3}$, or only events with a certain minimum/maximum signal height for muon and/or positron).

7. If you have found good cuts in the previous step with $\bar{A}$ as large as possible and $\sigma_{\bar{A}}$ as small as possible, calculate the log-likelihood ratio $nl\mathcal{L}$ between the decay function with modulation and the decay function without modulation. As a simple statistical test, $2 \cdot nl\mathcal{L}$ follows a χ^2 distribution with as many degrees of freedom as the two models differ in the number of fitted parameters (in this case one parameter). For the special case with one parameter, $z = \sqrt{2 \cdot nl\mathcal{L}}$ can also be considered; the $z$value indicates by "how many standard deviations" σ of the discriminating parameter the two models differ.

The software for data acquisition uses a general basic package (mimoCoRB = "multiple-in, multiple-out Configurable RingBuffer"), which can also be used in other problems, to which experiment-specific code must be added.

The `mimoCoRB` package provides a central component of any data acquisition system, which is used to record and process data from random processes before it is written to a permanent storage. Typical examples are digitized waveform data as they arise from detectors in nuclear, particle and astroparticle physics or in quantum mechanical measurements of single particles, for instance from photo-multiplier tubes, Geiger counters, avalanche photodiodes or modern SiPMs.

The random nature of such processes and the need to minimize read-out dead-times requires the use of an input buffer into which data is copied rapidly. While a data source feeds the data into the buffer, the subsequent processes are supplied with an almost constant stream of data in order to filter, reduce, analyze or visualize them. Such so-called consumer processes can be mandatory, i.e. they have to process all data. In this case, data acquisition pauses when the input buffer is full and a mandatory consumer is still busy processing. A second type of consumer, an "observer" process, receives a copy of the data only upon request without interrupting the data collection. A typical example of this is the graphical display of a subset of the recorded data.

Although it is possible to use the buffer manager in the mimoCoRB package directly, it makes more sense and is easier to use specially defined access classes with a well-defined user interface. The class structure is shown in Fig. 7.47. The main configuration shown at top left is in the working directory; the experiment-specific code indicated in the boxes with blue background and the necessary configuration files as well as the output data reside in subdirectories.

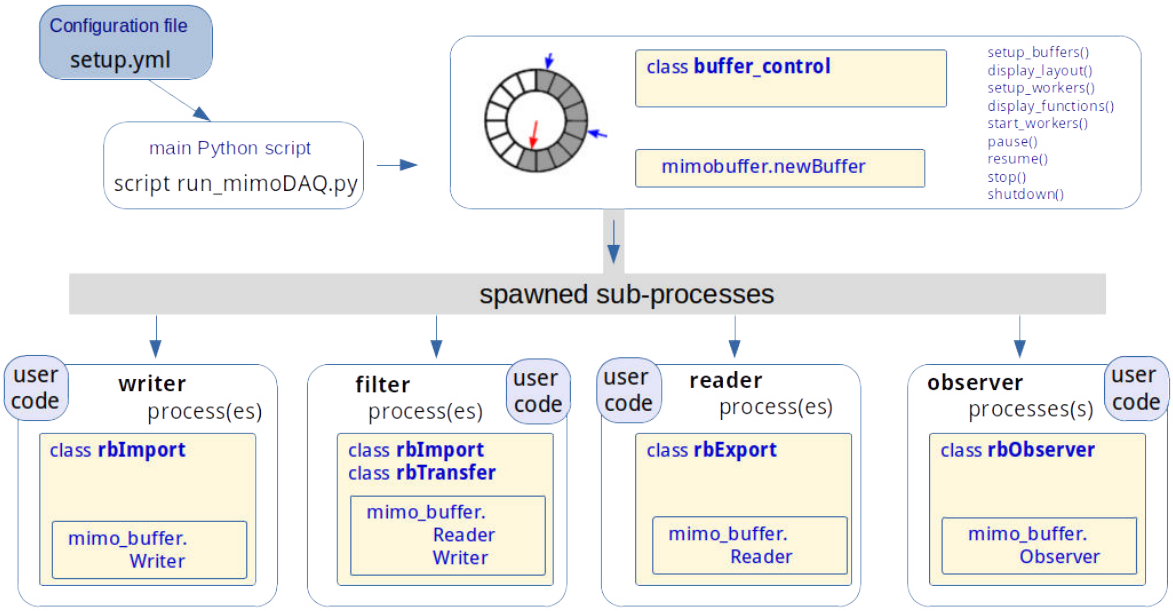

Figure 7.47: Structure of the software package mimoCoRB

The structure of the buffers and functions for measuring the muon lifetime is shown in Fig. 7.48.

The first buffer contains all data from events that met the oscilloscope's trigger condition. The filter reads this raw data, searches for double pulses of stopped and subsequently decayed muons and writes this raw data into the second buffer. The parameters of the pulses found are stored in the third buffer. Two further reader processes then write this data from the ring buffer to the permanent storage device (file on disk). Additional configuration options can be used to

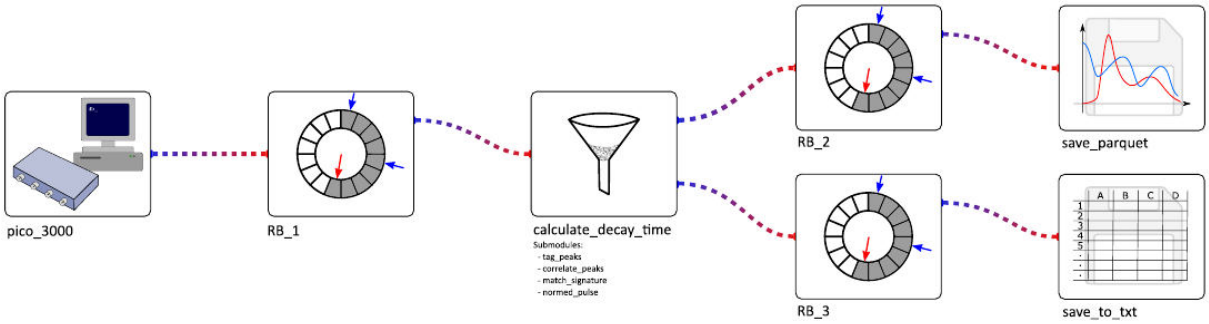

Figure 7.48: Software setup for the measurement of the muon lifetime.

launch processes that plot the raw data from the first or second buffer, or create histograms of variables in the third buffer and display updated versions of them in real-time.

The code with the configuration shown is started by typing

```
./run_daq.py lifetime_setup.yaml
```

on the command line. In the configuration script more configuration files are specified, which you can find in the subdirectories of your working directory. There, you can also find the experiment-specific code and Juypter notebooks for the data evaluation:

```
|--> <working directory> # Location of main configuration files
                |
                | --> analysis/ # Jupyter notebooks for evaluation
                | --> config/   # Configuration files in yaml format
                | --> modules/  # experiment-specific Python code
                | --> target/   # output files
```

The complete package `mimoCoRB` including an executable example based on simulated data, as well as the documentation can be found on the `gitlab` server of KIT under the URL https://git.scc.kit.edu/etp-teaching/mimoCoRB.

To support the evaluation, there are Jupyter notebooks for evaluating the pulse height spectra (*spectrum.ipynb*), for measuring the lifetime (*lifetime.ipynb*) and one spin measurement template (*spin_for_students.ipynb*) in subdirectory *analysis/*. The first two notebooks are almost completely operational and should be used on the day of the experiment to set the thresholds and coincidence conditions and to measure the lifetime. The included code sections also serve as examples and templates for the evaluation of the long-term measurement to provide prove of the muon spin and can be transferred to the notebook provided for this purpose.

Remark: This experiment has been rebuilt with new data acquisition and analysis methods. Therefore, details may still be adjusted over time, with which the supervisor will familiarize you.

7.11.9 Literature

Introductory chapters 1 - 6 in this script
Muons, cosmic rays [30], [31], [32], [43], [44]
Detectors [18], [19]

7.12 Experiment (M): The Mössbauer effect

7.12.1 Tasks

1. Measurement of the γ spectrum of a ^{57}Co source and selection of the 14.4 keV line of the ^{57}Fe with the discriminator.

2. Measurement of the Mössbauer spectrum of iron, Vacromium (stainless steel) and iron compounds ($FePO_4$, $FeSO_4$). Determination of the position of the absorption peaks and the isomer shifts.

3. Determination of the lifetime of the 14.4 keV state of Vacromium.

4. Determination of the internal magnetic field and the magnetic moment μ_a of the excited state of iron.

5. Determination of the electric field gradient of the crystal field of iron compounds.

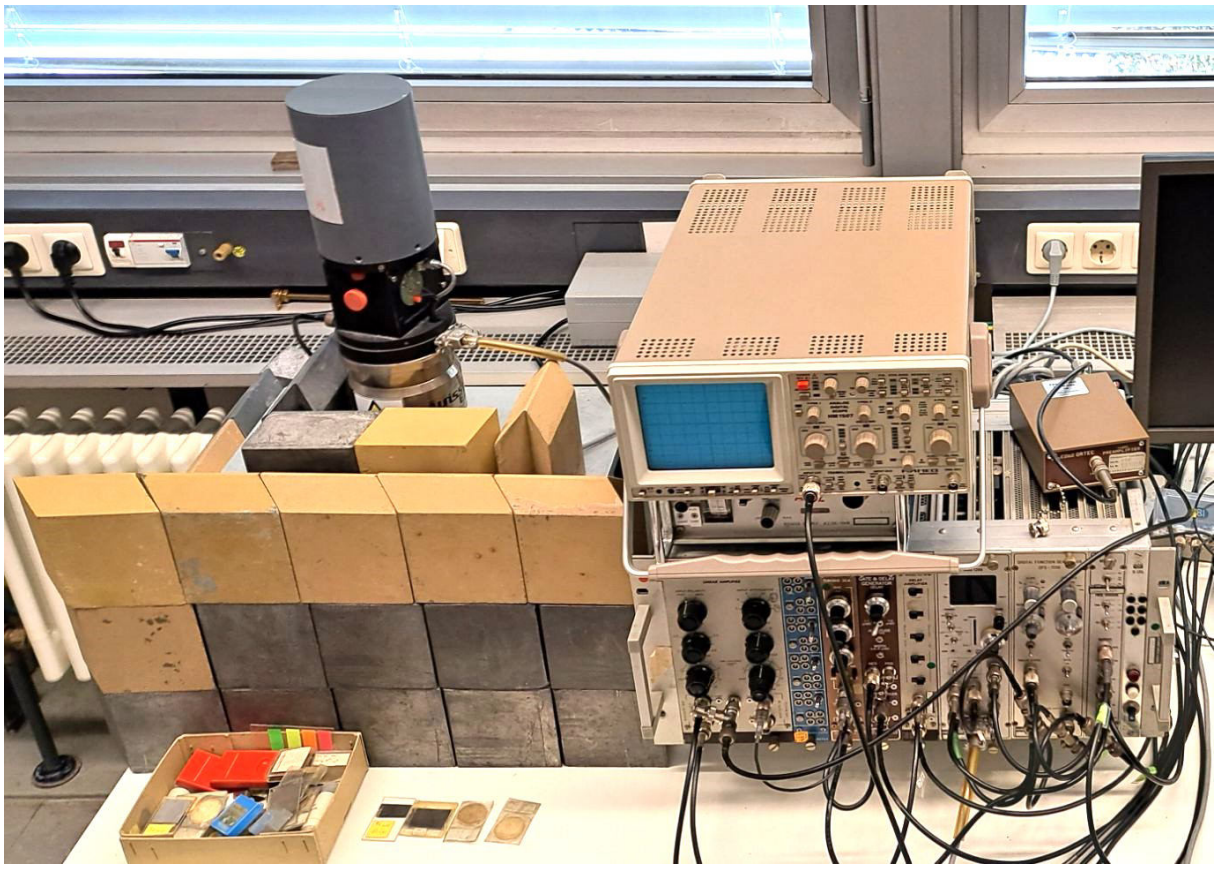

Figure 7.49: Setup of the Mössbauer experiment.

7.12.2 Introduction

7.12.2.1 Resonance absorption

If a resting atom (nucleus) with the excitation energy E_a emits a photon during the transition to the ground state E_g, its energy E_γ is not equal to the transition energy because the atom

(nucleus) experiences a recoil. The momentum $\vec{P}_R$ of the atom (nucleus) after the emission is opposite to the momentum $\vec{p}_\gamma$ of the photon

$$\vec{P}_R = -\vec{p}_\gamma = \frac{\hbar\,\vec{\omega}_\gamma}{c} \tag{7.149}$$

and thus the recoil energy E_R

$$E_R = \frac{\left|\vec{P}_R\right|^2}{2 \cdot M} = \frac{p_\gamma^2}{2 \cdot M} \tag{7.150}$$

with M the atomic mass (nuclear mass). The energy E_γ of the photon is then

$$E_\gamma = E_a - E_g - \frac{p_\gamma^2}{2 \cdot M} = E_0 - \frac{p_\gamma^2}{2 \cdot M} \tag{7.151}$$

It is smaller than the transition energy by the amount of the recoil energy. This energy and therefore also the energy of the photon are not arbitrarily sharp. If no broadening effects are effective, the energy uncertainty Γ_0, the so-called natural line width, is given by the mean lifetime τ of the emitting state.

$$\Gamma_0 \cdot \tau = \hbar \tag{7.152}$$

An analogous consideration for the process of absorption, in which the absorbing atom (core) receives the excitation energy E_0, shows that the photons in this case must be more energetic by the recoil energy ,

$$E_\gamma = E_0 + \frac{p_\gamma^2}{2 \cdot M} \tag{7.153}$$

so that the absorption spectrum is also shifted, but this time to higher energies.

If a photon, which has been emitted by an atom (nucleus) with the destruction of a certain excited state, is absorbed by a similar atom (nucleus) and the same state is excited, this is referred to as resonance absorption. It can only occur if the natural line width of a transition is larger than the energy shift caused by the recoil, provided that both the emitting and the absorbing system are at rest.

Looking at this quantitatively, one finds that with optical transitions in the atomic shell the relative line width $\Delta\nu/\nu$ is greater than the relative line shift E_R/E_0.

$$\begin{aligned} \Delta\nu/\nu &= 10^{-6} \text{ relative line width for light} \\ E_\mathrm{R}/E_0 &= 10^{-8} \text{ relative shift for light} \end{aligned}$$

The opposite is true for γ transitions. For the example of ^{57}Fe, it is

$$\begin{aligned} \Delta\nu/\nu &= 10^{-13} \text{ relative line width for } \gamma \text{ - transitions} \\ E_\mathrm{R}/E_0 &= 10^{-5} \text{ relative shift for } \gamma \text{ - transitions} \end{aligned}$$

Here the natural line width is much smaller than the displacement caused by the recoil.

The emission and absorption lines for the optical transitions in the envelope therefore completely overlap. This is why there is resonance absorption in the range of visible light, of which the best-known example is the Na-D line. For the γ transitions, however, it is excluded.

In reality this is not as strict, since the thermal movement of the nuclei broaden the lines. If P is the momentum of the nucleus before the emission and θ is the angle it encloses with the momentum of the photon, then the energy of the quantum is

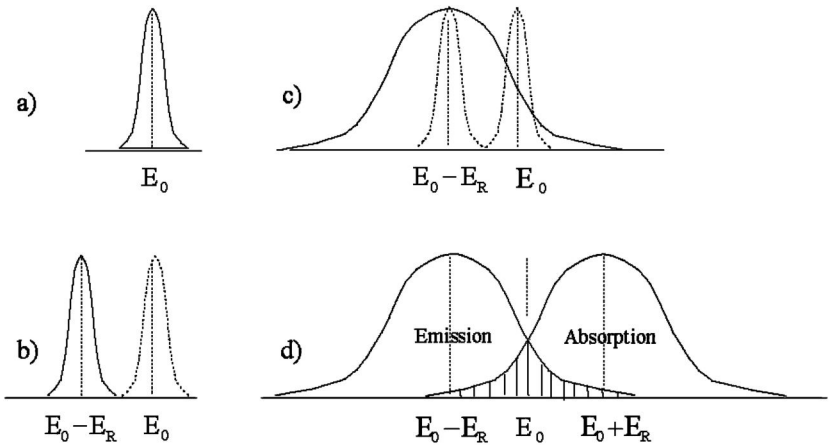

Figure 7.50: γ-Spectrum of an atom.

$$E_\gamma = E_0 - \frac{p_\gamma^2}{2 \cdot M} + \frac{p_\gamma \cdot P}{M} \cdot \cos\theta \tag{7.154}$$

Since the emission is isotropic, θ takes on all values between 0 and 2π and the maximum broadening becomes

$$E_\gamma = E_0 - \frac{p_\gamma^2}{2 \cdot M} \pm \frac{p_\gamma \cdot P}{M} \tag{7.155}$$

In addition to the shift of the line due to the Doppler effect there is also a broadening which is in the same order of magnitude at room temperature. In the spectrum one now has a very strongly broadened line (up to 10^6), which is shifted by the recoil energy from the transition energy to smaller energies in the case of emission and to higher energies in the case of absorption. The broadening is so large that the emission and absorption lines partially overlap. Therefore, resonance absorption is also to be expected with γ transitions, albeit not with the high probability as in the visible range, where the overlap is complete.

This is shown qualitatively in Fig. 7.50. The drawing in a) represents the line with its natural width. In b) the shifts by the recoil energy during emission. When absorbed, it shifts in the other direction of increasing energy. When the lines do not overlap, there is no resonance absorption. In c), the broadening of the emission line due to the Doppler effect (not indicated to scale; in reality it is much larger). Finally, the case of resonance absorption is drawn in d). The probability of this is proportional to the overlap integral of the broadened lines, i.e. the hatched area. Because of the line broadening associated with this, it increases as the temperature of the absorber and emitter rises.

The previous considerations apply to a free atom, which has no internal degrees of freedom except for the excitation. Already with molecules the conditions change. First, because of the larger mass, the displacement and broadening of the line are smaller. Compared with Fig. 7.50d, the lines are closer together and narrower. In addition, they are split because oscillatory and rotational states exist in addition to electronic excited states. Their energies are quantized, so only discrete amounts of energy can ever be exchanged. These are larger than the Doppler broadening, therefore the lines split. In the expression for the photon energy there is an additional term ΔE_M,

$$E_\gamma = E_0 - \frac{p_\gamma^2}{2 \cdot M} \pm \frac{p_\gamma \cdot P}{M} - \Delta E_\mathrm{M} \tag{7.156}$$

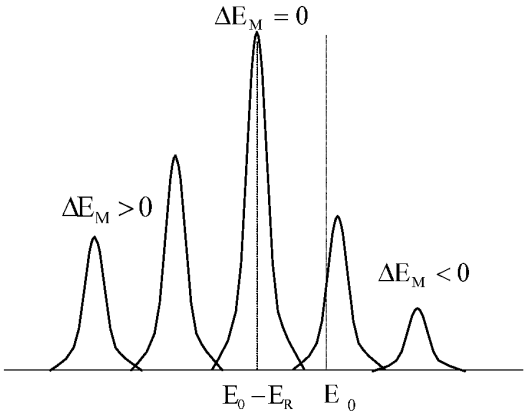

Figure 7.51: γ emission spectrum of a molecule.

is the difference of the internal energies of the molecule at vibrational or rotational transitions. If the internal state of a molecule does not change during emission ($\delta E_{\mathrm{M}} = 0$), one observes a shifted and broadened line as in the atom. If an oscillation is excited during emission, then $E_M > 0$ and another line appears at even smaller energies. Conversely, vibrational or rotational energy can also be transferred to the photon, producing more emission lines, but this time above $\Delta E_{\mathrm{M}} = 0$. Schematically, this is shown in Fig. 7.50.

7.12.2.2 The Mössbauer effect

However, what changes if the emitting atom is incorporated into a crystal lattice? If we first assume that the crystal atoms are infinitely tightly bound to their lattice sites, then they are at rest relative to each other and the crystal cannot change its internal energy. The momentum in the emission or absorption of a photon cannot be absorbed by a single atom, but only by the crystal as a whole. The atomic mass M is replaced by the total mass of the macroscopic crystal, with the consequence that the lines have the natural width and overlap completely: The ideal case of resonance absorption exists.

In reality, the binding energy of the atoms in the lattice is finite, although much larger than the recoil energy. Therefore, the atoms can perform oscillations around their rest position. In doing so, they are not independent of each other. There is a finite number of oscillations with different frequencies Ω_i, whose number is given by the number of degrees of freedom. These, in turn, are determined by the number of lattice bricks. The total internal energy of the crystal is

$$E_K = \sum_{S=0}^{3N} \hbar \cdot \Omega_S \cdot (n_S + 1/2) \quad n_S = 0, 1, 2... \tag{7.157}$$

N is the number of lattice elements. The states denoted by Ω_S are the phonons. The number of phonons of a certain type is given by the quantum number n_{S}. The crystal is in the ground state when no phonons are excited. If a crystal exchanges energy with its environment, the phonon number changes. The energy change is

$$\Delta E_{\mathrm{K}} = E_{\mathrm{K}'} - E_{\mathrm{K}} = \sum_{S=0}^{3N} \hbar \cdot \Omega_S \cdot (n'_{\mathrm{S}} - n_{\mathrm{S}}) \tag{7.158}$$

If one of the nuclei emits a γ quantum, its energy is

$$E_\gamma = E_0 - \Delta E_{\mathrm{K}}. \tag{7.159}$$

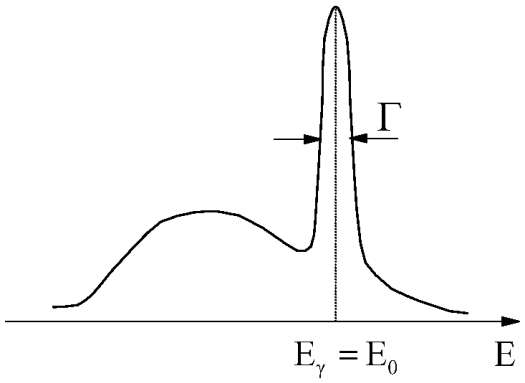

Figure 7.52: γ emission spectrum of a crystal with Mössbauer lines.

Since the possible values of ΔE_{K} are less than the natural linewidth apart, the emission spectrum is continuous. As with the molecule, it can extend into regions higher than the transition energy if phonons are annihilated in the process. The same applies to the absorption processes.

Rudolf Mößbauer discovered in his investigations of the resonance absorption of γ-rays that in some crystals there is a certain probability of recoil-less emission and absorption. In this case, the crystal does not change its internal energy and behaves as described above, i.e. as if it were a particle with macroscopic mass. As indicated in Fig. 7.52, a line of natural width, the Mössbauer line, is superimposed on the continuous emission spectrum at the location of the transition energy. It is not drawn to scale. In reality it is higher and much narrower compared to the continuous spectrum.

The continuous spectrum is asymmetrical to the Mössbauer line. There are more emissions where photons are produced than vice versa. This is a consequence of the Boltzmann distribution of phonon numbers. The states with few phonons are more occupied than those with a lot of them. Therefore, even if the probability of generation and annihilation are equal, more phonons are generated than annihilated in total. At absolute zero, where no phonons exist ($n_S = 0$), annihilation is not possible at all. The continuous spectrum then lies completely below the Mößbauer line.

The fraction of recoil-less processes can be calculated with quantum mechanics. At absolute zero it is

$$f(T=0) = \exp\left(-\frac{p_\gamma^2}{2\cdot M}\cdot\frac{1}{\langle\hbar\cdot\Omega_S\rangle}\right) \tag{7.160}$$

$f(T)$ is called Debye-Waller factor. The first term in the parenthesis is the recoil energy that the atom (lattice element) would receive if it were free, $\langle\hbar\Omega_S\rangle$ is the mean value of the phonon spectrum, a measure of the strength of the lattice bond. One can see: the recoil-less processes increase very strongly with decreasing recoil energy (or equivalently with decreasing transition energy). An increase can also be observed with stronger crystal bonding. The Mössbauer effect occurs when the recoil energy is small compared to the binding energy of the atoms in the lattice.

There are different models for the energy spectrum of phonons. One of them is from Debye. With it, one obtains the temperature dependence $f(T)$

$$f(T) = \exp\left\{-\frac{p_\gamma^2}{2\cdot M}\cdot\frac{3}{2\cdot k_{\mathrm{B}}\cdot\Theta}\cdot\left[1+\frac{2\pi^2}{3}\cdot\left(\frac{T}{\Theta}\right)^2\right]\right\} \tag{7.161}$$

Here the material constant Θ is introduced, the so-called Debye temperature. The energy $E_G = k_{\mathrm{B}}\cdot\Theta$, where k_{B} is the Boltzmann constant, is the upper limit of the energy of the phonon

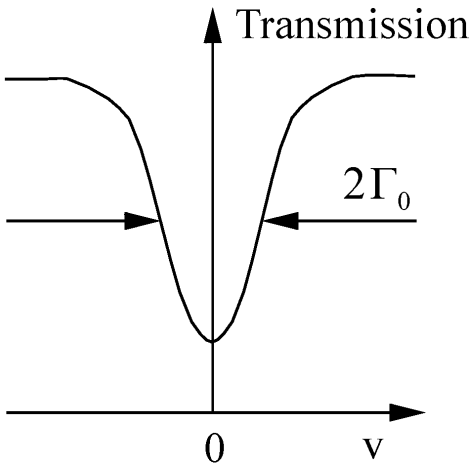

Figure 7.53: Transmissions spectrum.

spectrum. A high Debye temperature means a high binding energy of atoms. The nucleus ^{57}Fe, for example, has such a high Debye temperature of $\Theta = 480\,\mathrm{K}$. The Debye-Waller factor is $f = 0.92$ at absolute zero and $f = 0.7$ at room temperature. This is one reason for the great importance of ^{57}Fe in Mössbauer spectroscopy, one does not need a cryostat.

7.12.2.3 The experimental detection of the Mössbauer effects

The 14.4 keV line of ^{57}Fe has the natural width of $5 \cdot 10^{-9}$ eV absolute and $3 \cdot 10^{-13}$ relative. Even in optics, with its high-resolution interferometers, we are still several orders of magnitude short of resolving such lines by direct measurement of the spectrum. In nuclear physics, where resolutions of a few parts per thousand are achieved with semiconductor detectors, this is not at all conceivable. Nevertheless, there is a possibility to determine the line widths, which is based on the small width: one measures the resonance absorption. To do this, one allows the γ quanta of a given nucleus through an absorber and measures the transmission (or absorption), which is the rate of quanta that are transmitted (absorbed). For this purpose, the detector does not need to be energy sensitive; detection of the quanta is sufficient. The magnitude of transmission is given by the overlap of the probabilities for emission and absorption, as indicated in Fig. 7.51d, but this time not for the broadened lines, but for the natural lines. If one succeeds in superimposing the two lines and measuring the changing transmission, one can scan the line profile.

For this one uses the Doppler effect. Resonance absorption (let it be assumed that it is maximal when emitter and absorber are at rest, which, as will be shown below, is not self-evident) can be disturbed by a small relative motion because of the extreme line sharpness. According to relativity, a γ quantum has energy E and momentum $\vec{p}$ in its rest frame, but energy E^* in a system moving with constant relative velocity $\vec{v}$.

$$E^* = \frac{1}{\sqrt{1-\beta^2}} \cdot (E + \vec{v} \cdot \vec{p}) \qquad \beta = \frac{v}{c}. \tag{7.162}$$

For $\beta \ll 1$ and collinear motion, the energy shift of the γ quanta is

$$\Delta E_\gamma = E^* - E = \pm \frac{v}{c} \cdot E. \tag{7.163}$$

The γ-energy is higher by this value when emitter and absorber move towards each other (+sign), or lower in the opposite case (-sign). For ^{57}Fe, a shift of $10^{-8}\,\mathrm{eV}$ is sufficient to terminate the resonance. This corresponds to a relative motion of $0.02\,\mathrm{cm/s}$.

The measurement of the transmission as a function of the relative velocity v results in the curve drawn in Fig. 7.53. The absorption is greatest at v=0. Here, resonance absorption prevails. As the relative velocity increases, it decreases to both sides as the overlap of the emission and absorption lines decreases until it ceases altogether. The half-width (FWHM = full width at half maximum) of the transmission curve is equal to twice the natural width of the transition.

7.12.2.4 Splitting and shifing of the resonance line

So far, it has been tacitly assumed that both the excited state and the ground state of the Mössbauer transition are simple states, which moreover have the same energy in source and absorber. In general, this is not the case.

A splitting of the nuclear states in an internal magnetic field is caused by the Zeeman effect. It can be larger than the natural linewidth and manifests itself in a splitting of the Mössbauer line, the so-called. *hyperfine structure splitting.*

Also, the interaction of the potentially existing nuclear quadrupole moment with gradients of the crystal field suspends the degeneracy. One has then the so-called *quadrupole splitting.*

A shift of the line is observed when, caused by different chemical bonds, the electron density at the nuclear site in emitter and absorber is not the same. This is called *isomeric shift* or *chemical shift.* In the following, these effects will be discussed in more detail.

The hyperfine structure splitting: Some nuclei have internal magnetic fields at the location of the nucleus due to the motion of the shell electrons. If a nuclear state has total spin (or nuclear spin) I, there are adjustments of the spin in the field because of the directional quantization $2I+1$. Since there is a magnetic dipole moment associated with the spin, the degenerate state without a magnetic field splits due to the Zeeman effect. The energy gap of these hyperfine structure states is

$$\Delta E_{\mathrm{m}} = -\left(\vec{\mu}\cdot\vec{B}\right) = -\frac{m}{I}\cdot\mu\cdot B \tag{7.164}$$

where m is the magnetic quantum number, which takes the 2I+1 different values from $-I$ to $+I$. According to the agreed rule, the negative sign is valid when a positive nuclear moment is in the direction of the magnetic field. For a recoilless transition between the excited state (index a) and the ground state (index g) the γ-energy is

$$E_\gamma = \left(E_a - \frac{m_a}{I_a}\cdot\mu_a\cdot B\right) - \left(E_g - \frac{m_g}{I_g}\cdot\mu_g\cdot B\right) = E_0 - \frac{m_a}{I_a}\cdot\mu_a\cdot B + \frac{m_g}{I_g}\cdot\mu_g\cdot B \tag{7.165}$$

Magnetic quantum numbers do not take all values, they are subject to selection rules. The equation

$$\Delta m = m_a - m_g = 0, \pm 1 \qquad \text{Dipolstrahlung} \tag{7.166}$$

applies to dipole radiation. Experimental observation of the hyperfine structure is simpler, if source and absorber are not split *both at the same time.* Therefore, the emitting nucleus, in our case ^{57}Fe, is placed in a crystal which has no internal magnetic fields, such as rhodium or platinum. This is called a single line source. As absorber one uses natural or ^{57}Fe-enriched iron with its high internal fields. Resonance absorption occurs when the emission line of the source moving with velocity v, shifted by the Doppler effect, coincides with the absorption spectrum Eq. 7.165 of the absorber at rest. One has

$$E_0\cdot\left(1+\frac{v}{c}\right) = E_0' - \frac{m_a\cdot\mu_a\cdot B}{I_a} + \frac{m_g\cdot\mu_g\cdot B}{I_g} \tag{7.167}$$

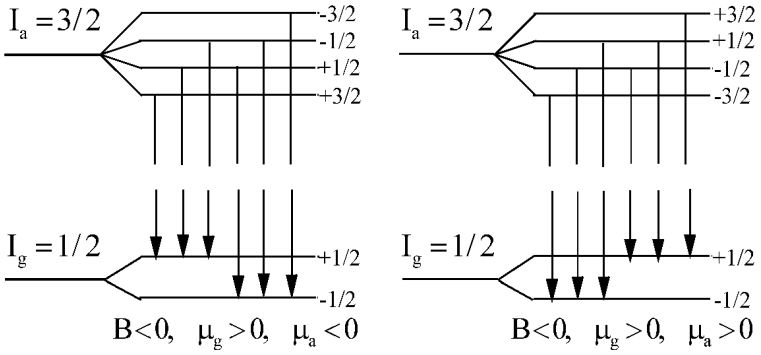

Figure 7.54: Possible term diagrams of ^{57}Fe.

and for the speed

$$v = \frac{(E_0' - E_0)\cdot c}{E_0} - \frac{m_a \cdot \mu_a \cdot Bc}{I_a \cdot E_0} + \frac{m_g \cdot \mu_g \cdot B \cdot c}{I_g \cdot E_0}. \tag{7.168}$$

Here, the energy E_0' was introduced for the unshifted line of the absorber to account for the isomeric shift that may exist. For ^{57}Fe, the velocity spectrum consists of six resonance lines. The ground state has spin $I_g = 1/2$ and is doubly split, the excited state has $I_a = 3/2$ and splits four times. The magnetic moment of the ground state is known from nuclear resonance studies. It is positive and has the value

$$\mu_g = (0,0903 \pm 0,0007)\,\mu_K \tag{7.169}$$

μ_K is the nuclear magneton. Furthermore, it is known that the moment of the ground state is directed against the internal magnetic field, so this is taken to be negative. Therefore, according to Eq. 7.166, the state with $m_g = 1/2$ is higher than the one with $m_g = -1/2$. As long as the magnetic moment of the excited state is not known, the two term schemes shown in Fig. 7.54 are possible. The indicated transitions correspond to the selection rules for dipole radiation.

The measurement of the velocity spectrum decides between the two possibilities and leads to the determination of the internal magnetic field, the magnetic moment and the isomeric shift. From Eq. 7.168 follows with the abbreviations

$$A = \frac{\mu_a \cdot B \cdot c}{I_a \cdot E_0}; \qquad G = \frac{\mu_g \cdot B \cdot c}{I_g \cdot E_0}; \qquad I = \frac{(E_0' - E_0)\cdot c}{E_0} \tag{7.170}$$

and $v = v^*(m_a, m_g)$ for the six transitions

$$\begin{aligned}
v^*\left(\frac{3}{2},\frac{1}{2}\right) &= -\frac{3}{2}A + \frac{1}{2}G + I \\
v^*\left(\frac{1}{2},\frac{1}{2}\right) &= -\frac{1}{2}A + \frac{1}{2}G + I \\
v^*\left(\frac{1}{2},-\frac{1}{2}\right) &= -\frac{1}{2}A - \frac{1}{2}G + I \\
v^*\left(-\frac{1}{2},\frac{1}{2}\right) &= +\frac{1}{2}A + \frac{1}{2}G + I \\
v^*\left(-\frac{1}{2},-\frac{1}{2}\right) &= +\frac{1}{2}A - \frac{1}{2}G + I \\
v^*\left(-\frac{3}{2},-\frac{1}{2}\right) &= +\frac{3}{2}A - \frac{1}{2}G + I
\end{aligned} \tag{7.171}$$

The unknowns A, G and I and the term scheme are obtained by inserting the measured velocities into this system of equations and comparing the different possibilities. The isomeric shift is obtained immediately because of

$$\sum_{m_g,m_a} v^*\left(m_a,m_g\right) = 6\cdot I \tag{7.172}$$

This allows the six isomeric corrected velocities to be

$$v\left(m_a,m_g\right) = v^*\left(m_a,m_g\right) - I, \tag{7.173}$$

which are symmetric about I:

$$\begin{aligned} v\left(m_a,m_g\right) &= -v\left(-m_a,-m_g\right) \\ v_i &= \frac{1}{2}\cdot\left(v\left(m_a,m_g\right) - v\left(-m_a,-m_g\right)\right) \end{aligned} \tag{7.174}$$

Now you have three different positive velocities ordered by magnitude: $v_1 > v_2 > v_3 > 0$ and three associated negative quantities of the same magnitude. There are four cases to distinguish:

1st case: $A > 0$, $G < 0$, $|A| > |G|$

$$\begin{aligned} v_1 &= v\left(-\frac{3}{2},-\frac{1}{2}\right) = +\frac{3}{2}A - \frac{1}{2}G \\ v_2 &= v\left(-\frac{1}{2},-\frac{1}{2}\right) = +\frac{1}{2}A - \frac{1}{2}G \\ v_3 &= v\left(-\frac{1}{2},+\frac{1}{2}\right) = +\frac{1}{2}A + \frac{1}{2}G \end{aligned} \tag{7.175}$$

From this we get the unknowns and a condition for the velocities

$$\begin{aligned} A &= +v_1 - v_2 \\ G &= -v_2 + v_3 \\ 0 &= +v_1 - 2v_2 - v_3 \end{aligned} \tag{7.176}$$

2nd case: $A > 0$, $G < 0$, $|A| < |G|$

$$\begin{aligned} v_1 &= v\left(-\frac{3}{2},-\frac{1}{2}\right) = +\frac{3}{2}A - \frac{1}{2}G \\ v_2 &= v\left(-\frac{1}{2},-\frac{1}{2}\right) = +\frac{1}{2}A - \frac{1}{2}G \\ v_3 &= v\left(+\frac{1}{2},-\frac{1}{2}\right) = -\frac{1}{2}A - \frac{1}{2}G \end{aligned} \tag{7.177}$$

with the solutions

$$\begin{aligned} A &= +v_1 - v_2 \\ G &= -v_2 - v_3 \\ 0 &= +v_1 - 2v_2 + v_3 \end{aligned} \tag{7.178}$$

3rd case: $A < 0$, $G < 0$, $|A| > |G|$

$$\begin{aligned} v_1 &= v\left(+\frac{3}{2}, +\frac{1}{2}\right) = -\frac{3}{2}A + \frac{1}{2}G \\ v_2 &= v\left(+\frac{1}{2}, -\frac{1}{2}\right) = -\frac{1}{2}A - \frac{1}{2}G \\ v_3 &= v\left(+\frac{1}{2}, +\frac{1}{2}\right) = -\frac{1}{2}A + \frac{1}{2}G \end{aligned} \tag{7.179}$$

with the solutions

$$\begin{aligned} 2A &= -v_1 - v_2 \\ G &= -v_2 + v_3 \\ 0 &= +v_1 - v_2 - 2v_3 \end{aligned} \tag{7.180}$$

4th case: $A < 0$, $G < 0$, $|G/3| < |A| < |G|$

$$\begin{aligned} v_1 &= v\left(+\frac{1}{2}, -\frac{1}{2}\right) = -\frac{1}{2}A - \frac{1}{2}G \\ v_2 &= v\left(+\frac{3}{2}, +\frac{1}{2}\right) = -\frac{3}{2}A + \frac{1}{2}G \\ v_3 &= v\left(-\frac{1}{2}, -\frac{1}{2}\right) = +\frac{1}{2}A - \frac{1}{2}G \end{aligned} \tag{7.181}$$

with the solutions

$$\begin{aligned} 2A &= -v_1 - v_2 \\ G &= -v_1 - v_3 \\ 0 &= -v_1 + v_2 + 2v_3 \end{aligned} \tag{7.182}$$

First, it is checked which of the conditions is fulfilled by the measured velocities. In this way it is decided which term scheme is present. For this the constants A and G are calculated and from this the magnetic moment of the excited state and the magnetic field.

The quadrupole splitting: Nuclei with a spin I can have an asymmetric charge distribution. It is described by the quadrupole moment Q. It is

$$e \cdot Q = \int \left(2z^2 - x^2 - y^2\right) \cdot \rho\,(x, y, z) \cdot \mathrm{d}V \tag{7.183}$$

e is the elementary charge and ρ is the charge density. The coordinate system is chosen so that its z axis coincides with the symmetry axis of the charge distribution, which is the direction of spin I. Q measures the anisotropy of the charge distribution with respect to the spin direction. For spherical nuclei $Q = 0$, for cucumber-shaped $Q < 0$, for disk-shaped $Q < 0$.

In an electric gradient field, the electrostatic interaction between the field and the charge distribution gives rise to a splitting of the energy states of the nucleus, depending on the direction of the quadrupole to the field. The electric field gradient at the lattice site of the nucleus is caused by the electron distributions in the shells. If a lattice has a preferred direction, let it be the z-axis, the field gradient is in this direction, and for the interaction energy we get

$$\Delta E_{\mathrm{Q}}(m) = \frac{e \cdot Q}{4} \cdot \left(\frac{\partial^2 V}{\partial z^2}\right) \cdot \frac{3 \cdot m^2 - I \cdot (I+1)}{3 \cdot I^2 - I \cdot (I+1)} \tag{7.184}$$

The second term is the field gradient, m is the magnetic quantum number of the spin I, which describes the orientation of the spin in the field. Quadrupole splitting occurs only for nuclei whose spin $I > 1$. Therefore, for ^{57}Fe, only the excited state with $I = 3/2$ is split. It depends on the *square* of the magnetic quantum number, which is why the excited state splits only twofold and not fourfold, as in the hyperfine structure. One has

$$\Delta E_{\mathrm{Q}}\left(\pm\frac{3}{2}\right) = +\frac{e \cdot Q}{4} \cdot \left(\frac{\partial^2 V}{\partial z^2}\right) \qquad \Delta E_{\mathrm{Q}}\left(\pm\frac{1}{2}\right) = -\frac{e \cdot Q}{4} \cdot \left(\frac{\partial^2 V}{\partial z^2}\right) \tag{7.185}$$

In the velocity spectrum, two lines occur which are symmetric with respect to the unshifted line, i.e., symmetric with respect to $v = 0$ when there is no isomeric shift. Their *distance* is independent of isomeric effects.

$$v_{\mathrm{Q}} = v_{\mathrm{Q}}\left(\pm\frac{3}{2}\right) - v_{\mathrm{Q}}\left(\pm\frac{1}{2}\right) = \frac{e \cdot Q}{2} \cdot \frac{\partial^2 V}{\partial z^2} \cdot \frac{c}{E_0} \tag{7.186}$$

It can be used to calculate the field gradient for a given quadrupole moment.

The isomeric shift: The electromagnetic interaction between the shell and the nucleus contains a term for the Coulomb repulsion between the electron cloud and the charge of the nucleus. If the latter is not point-like, but has a charge distribution with the mean radius $\bar{R}$, the energy of a nuclear state changes by the magnitude

$$\Delta E(R) = \frac{2\pi}{3} \cdot e \cdot |\Psi(0)|^2 \cdot Z \cdot e \cdot \bar{R}^2 \tag{7.187}$$

Where $e \cdot |\Psi(0)|^2$ is the charge density of the shell electrons at the location of the nucleus, and Ze is the total charge of the nucleus. Since the average charge radius of a nucleus in the excited state (index a) is usually different from that in the ground state (index g), the transition energy changes as follows

$$\begin{aligned} E_\gamma &= (E_{\mathrm{a}} + \Delta E(R_{\mathrm{a}})) - (E_{\mathrm{g}} + \Delta E_{\mathrm{g}}(R_{\mathrm{g}})) \\ &= E_0 + \Delta E(R_{\mathrm{a}}) - \Delta E(R_{\mathrm{g}}) \end{aligned} \tag{7.188}$$

As long as the source and absorber have the same chemical composition, i.e., the same $|\Psi(0)|$, the Mössbauer line is *not* shifted because the transition energies in the source and absorber have both changed *in the same way*. Only for different electron configurations a shift appears, which results without hyperfine structure and quadrupole splitting from the condition that the Doppler-shifted emission line coincides with the absorption line of the resting absorber.

$$E_0 \cdot \left(1 + \frac{v}{c}\right) + \Delta E_{\mathrm{Q}}(R_{\mathrm{a}}) - E_{\mathrm{Q}}(R_{\mathrm{g}}) = E_0 + \Delta E_{\mathrm{A}}(R_{\mathrm{a}}) - \Delta E_{\mathrm{A}}(R_{\mathrm{g}}) \tag{7.189}$$

The indices A and Q denote the absorber and the source. Inserting Eq. 7.187 yields

$$v = \frac{2\pi \cdot c}{3 \cdot E_0} \cdot Z \cdot e^2 \cdot \left(|\Psi_{\mathrm{A}}(0)|^2 - |\Psi_{\mathrm{Q}}(0)|^2\right) \cdot \left(\bar{R}_{\mathrm{a}}^2 - \bar{R}_{\mathrm{g}}^2\right) \tag{7.190}$$

Thus, the isomeric shift occurs only if the *core* has different charge radii for the states involved in the transition *and* if the electron distributions of the *shell* in the source and absorber are different.

The isomeric shift is superimposed on the hyperfine structure and quadrupole splitting. Therefore, the velocity spectra are no longer symmetric with respect to $v = 0$. They are obtained by determining the center of gravity of pairs of lines belonging together.

7.12.3 Principle of the measurement

The transmission of gamma radiation is measured for different absorbers at rest as a function of the velocity of the source. A single-line source is used, where the ^{57}Co is diffused into a material without internal magnetic fields (Rh). A velocity range (from 0 to about 12 mm/s) is periodically traversed by the source. The velocity is digitally controlled during the whole process and is recorded for each measured gamma quantum. The velocity is recorded as integer by the measuring device and must be converted into a velocity in the analysis. For the analysis, the speed range covered in one period is divided into 1024 ranges. In each of these sections, the speed can be assumed to be almost constant. The sections are numbered consecutively with an integer between 0 and 1023. This number can be used as a channel address in a multi-channel scaler that counts the number of detected gammas in a separate channel for each speed range. In this experiment, the address value of the velocity is recorded together with the gamma energy for each measured gamma quanta. In the analysis, the number still has to be converted into a speed. An energy spectrum is generated for each velocity and a suitable energy cut is chosen for the two-dimensional representation in order to optimally filter out the resonance absorption of the 14.4 keV gammas from the data.

7.12.4 Setup of the experiment

The source is moved by an electromagnetic drive, the Mössbauer Velocity Transducer (MVT), which works similar to a loudspeaker. The drive is the silver cylinder at the base of the cylindrical device. The speed is actively controlled by the Mössbauer Driving Unit (MDU). The MDU receives an analog voltage from a digital function generator (DFG). The analog voltage of this function generator defines the speed of the source. The DFG can generate two waveforms, a sinusoidal voltage and a triangular voltage. In this experiment only the triangular voltage is used.

The gamma quanta that pass through the absorber are detected with a proportional counter that has a thin beryllium entrance window so as not to absorb the low-energy gammas. In the original version of the setup, the energy signals of the 14.4 keV line of the excited ^{57}Fe nucleus (see decay scheme of the ^{57}Co source in the appendix) were selected in the photopeak region, using a window discriminator. The photopeaks and Compton spectra of the higher energy gammas (122 keV and 136 keV) were suppressed as far as possible by the upper threshold of the discriminator. The lower threshold of the selected energy range suppressed the low-energy noise. This energy range, which was fixed for the duration of the measurement, could only be set imprecisely. The discriminator pulses for different speeds were counted with a multi-channel scaler (MCS). Each of the 1024 counters corresponded to a narrow speed range that the source was passing through at the time of the counter tube signal. The address of the active counter at this intant was controlled via signals from the DFG (Start: reset the counter address to 0; Chn: increment the counter address by one.) and was thus automatically synchronized with the MVT.

In the updated version of the experiment, the detector signal is digitized in a fast analog to digital converter (ADC) and analyzed directly by an FPGA (field-programmable gate array), which also reads out the control signals from the DFG. This system, implemented on a "Red Pitaya", thus records the energy of the gamma together with the address counter of the current speed of the source. In this way, the energy range for the optimal representation of the resonance

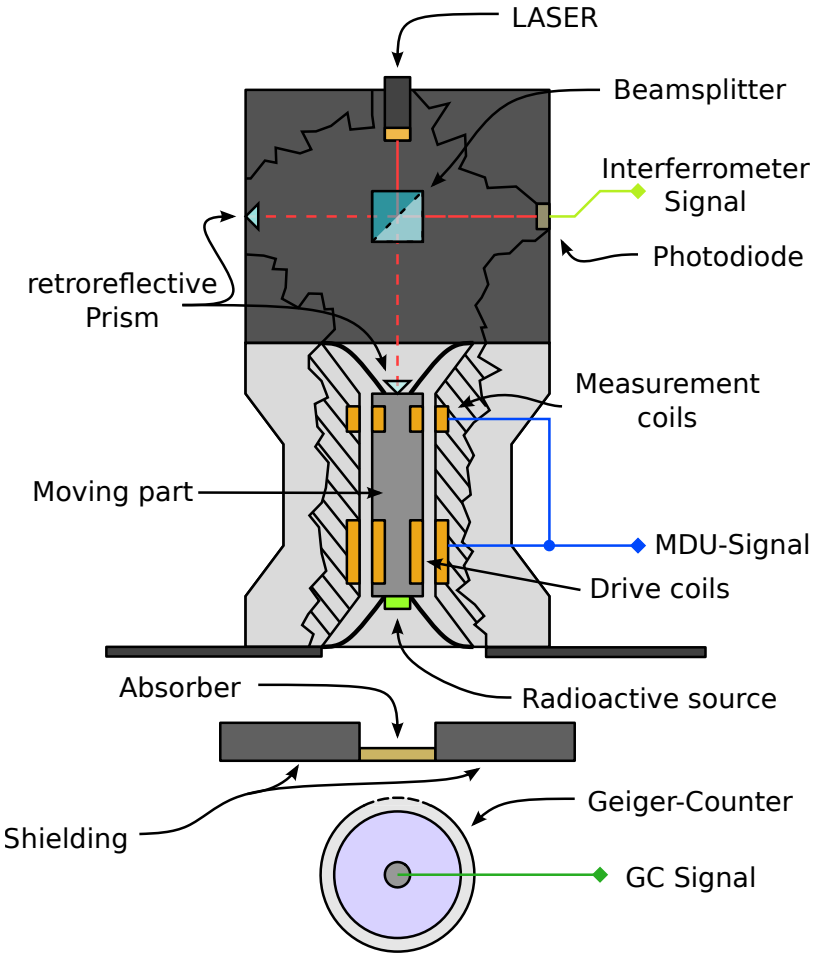

Figure 7.55: Schematic setup of the Mössbauer drive system (MVT) with the laser interferometer for speed calibration, the absorber and the counter tube for detecting the 14.4 keV gammas from the ^{57}Co source.

absorption can be determined even after the measurement. The actual data analysis takes place on a Linux PC. Examples are available in Python, which are executed in a Jupyter Notebook.

In the following, the functions of the various components of the experimental setup are described and the analysis steps are explained.

7.12.4.1 The Mössbauer drive system

As already mentioned, the MVT is based on the loudspeaker principle. On the axis of a hollow cylinder, an aluminum rod with membranes is guided in such a way that it can only move axially (see Fig. 7.55). At one end is the source, at the other end the prism of the interferometer, which is used to measure the velocity. Firmly connected to the rod are two permanent magnets. Each is surrounded by magnetic coils with homogeneous field, which in turn are firmly connected to the cylinder.

The MDU receives the analog signal of the selected motion form from the function generator. It generates a voltage proportional to this signal, which is used to control the drive coil of the MVT. The permanent magnet moves together with the rod at a speed proportional to the coil current and thus to the specified function. The second coil is not driven by the MDU. However, since it is subjected to the now moving field of the permanent magnet mounted on the

cylinder, a voltage is induced in the second coil which is proportional to the speed of the rod with the source. This voltage is used to compare the actual velocity with the target velocity. The difference between the actual and target value is used in the readjustment to adjust the actual speed more precisely to the target speed. In addition, the relative deviation between the actual and target voltage is displayed by an LED bar on the front panel of the MDU. The deviation can be minimized by matching the frequency of the function generator to the mechanical resonance frequency of the drive unit. The maximum speed of the movement can be changed via the amplitude of the signal. In connection with a laser interferometer, which is explained in chapter 7.12.4.3, the MDU can also be used to measure the speed.

7.12.4.2 The Function generator (DFG: Digital Function Generator)

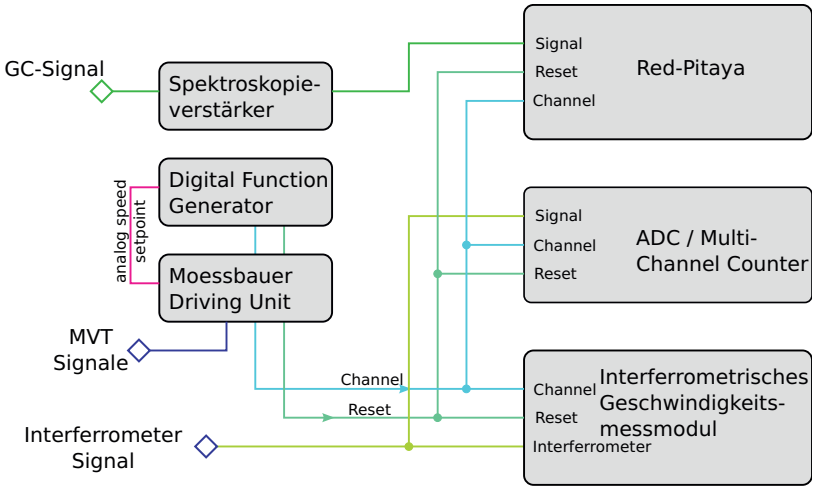

Figure 7.56: Design of the measuring system.

The DFG generates three signals, a rectangular pulse (channel) with an adjustable frequency that increments the channel address of the MCS, a reset pulse that regularly resets the address counter to zero, and the analog signal that controls the speed of the Mössbauer source via the MDU. The analog output voltage is generated by means of a digital to analogue converter (DAC). As input of a DAC a binary encoded number is required that the DAC can convert to a voltage. In the case of the sine wave, this number is implemented via a lookup table in the internal memory of the DFG, to which the address counter points. The triangle signal, used here, is derived directly from the internal address pointer.

The address pointer is incremented in 1024 steps (10 bits) (the DFG can generate the signal in different resolutions between 512 and 4096 steps). Together with the last step, the reset pulse is triggered, which resets the address pointer to zero. The frequency of the generated pulse can be adjusted via a potentiometer on the DFG and should be adjusted to the resonance frequency of the MVT (approx. 17 – 18 Hz). With an optimal setting, the error display (deviation of the target and actual value of the speed) is minimized.

The analog triangular pulse has its largest positive value directly after the reset signal (address = 0) and decreases with a constant gradient (→ constant acceleration of the source). After the zero crossing at address 256, the direction of movement of the source is reversed. When running through a complete oscillation, each speed is run through twice. With a positive voltage, the source moves towards the absorber, so the γ energy is slightly larger than the value at rest, with a negative voltage it is smaller. In order to determine the actual speed, a calibration measurement can be carried out using the laser interferometer of the Mössbauer Velocity Calibrator (MVC).

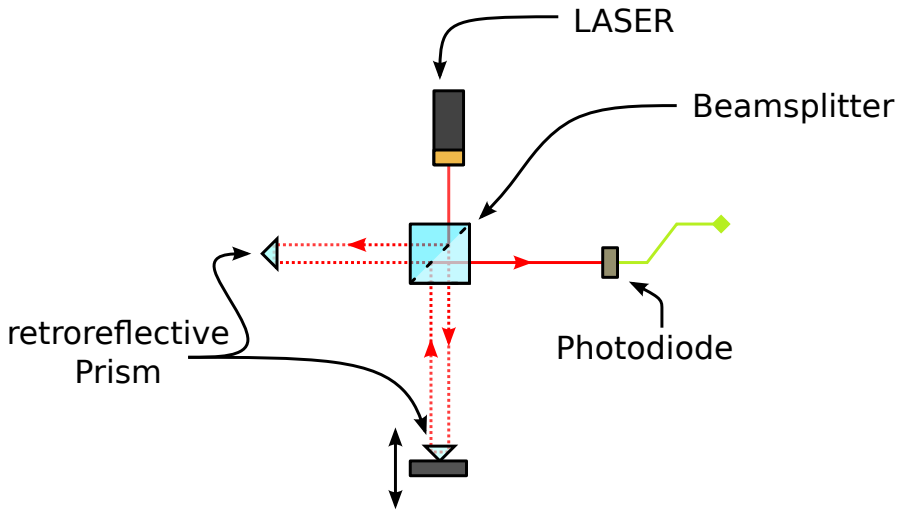

Figure 7.57: The Michelson Interferometer.

7.12.4.3 The Mössbauer Velocity Calibrator

The MVC is used to measure the velocity of the sample. The measurement process is explained below. It consists of a laser, a Michelson interferometer and a photodiode, with which the light-dark transitions of the superimposed laser beams of the two interferometer arms are detected. A complete light-dark cycle corresponds to a movement of the rod on which the source is mounted by half a wavelength of the laser light. It is assumed that the speed is almost constant over the time that an address is active. By counting the transitions in the MCS, synchronized with the address pointer, the average speed can be determined for each individual channel. The calibration function for the speed is determined by a linear fit of the speed via the channel address.

The Michelson interferometer is sketched in Fig. 7.57. On the free end of the movable rod is a Cat's eye prism attached as a reflector, which is part of the interferometer. The beam of a semiconductor laser is split at a beam splitter cube. The through-going ray drawn in dashed lines is reflected in the movable prism by 180°, partially deflected in the beam splitter, before reaching the photodiode. The second beam is deflected in the beam splitter onto a fixed cat's eye prism, which reflects the beam by 180°. Part of the light goes straight through the beam splitter and is superimposed on the first beam. Both beams reach the photodiode, where the intensity of the interference signal resulting from the phase shift is measured.

The prisms have the property to reflect a light beam by 180° that impinges in a certain angular range around the axis of symmetry, *independent of the angle of impingement*, whereby the reflected ray however is in general shifted parallel to the incident beam. Such a prism therefore does not have to be precisely adjusted, in contrast to an ordinary mirror, which reflects only *perpendicular* incident light exactly back into itself. It consists of a regular pyramid, formed when the corner of a glass cube is symmetrically cut off. A ray entering the base of the pyramid more or less perpendicularly is then totally reflected at each face of the cube.

As long as both prisms are at rest, a constant interference pattern arises due to the phase difference of the interfering rays. If a prism moves, the phase difference is no longer constant over time, and the interference pattern moves. At a fixed location, e.g. at the photodiode, the maxima and minima alternate with one another with a certain frequency, which is proportional to the speed of the prism. This is the principle of interferometric velocity measurement.

Quantitatively, it looks like this. The two beams are plane waves

$$\begin{aligned} y_1 &= y_0 \cdot \sin(kx - \omega t) \\ y_2 &= y_0 \cdot \sin(kx - \omega t - \delta) \end{aligned} \tag{7.191}$$

with the phase difference δ. The total amplitude at the fixed location $x = L$ is

$$y = y_1 + y_2 = 2 \cdot y_0 \cdot \cos(\delta/2) \cdot \sin(kL - \omega t - \sigma/2) \tag{7.192}$$

The signal S at the photodiode is proportional to y^2 averaged over measurement times, which are very large compared to $1/\omega$. So

$$S \approx \langle y^2 \rangle = y_0^2 \cdot \cos^2(\delta/2) \tag{7.193}$$

So the magnitude of the signal depends on the phase difference. It is the difference of the light paths of the two beams

$$\delta = k \cdot (L_1 - L_2) = k \cdot \Delta L = \frac{2\pi}{\lambda} \cdot \Delta L \tag{7.194}$$

If a prism moves for a time t with constant velocity v, the following holds true

$$\Delta L = 2 \cdot v \cdot t \tag{7.195}$$

The factor 2 occurs because the light passes twice through the distance L by which the prism has shifted. One has

$$S \approx \cos^2(\frac{2\pi}{\lambda} \cdot v \cdot t) \tag{7.196}$$

a time periodic change of intensity. Since the square of the cosine has two maxima (or minima) in one period, their frequency is

$$f = 2 \cdot \frac{v}{\lambda} \tag{7.197}$$

This frequency is measured directly as the number N of maxima during the measurement time T.

$$f = \frac{N}{T} = \frac{N}{B \cdot Z} \tag{7.198}$$

B is the temporal width of the measurement interval and Z the number of measurement cycles passed. Thus, the velocity is

$$v = \frac{\lambda}{2} \cdot \frac{N}{B \cdot Z} \tag{7.199}$$

and with the wavelength $\lambda = 650\,\mathrm{nm}$ for the red line of the solid state laser

$$v = 325 \cdot \frac{N}{B \cdot Z} \frac{\mathrm{mm}}{\mathrm{s}} \qquad \text{mit } B \text{ in } \mu\mathrm{s} \tag{7.200}$$

The product $B \cdot Z$ is therefore the total time in μs during which a counter channel of the MCS is active and counts N pulses (light-dark transitions) of the interferometer. In the measurement mode VEL (velocity calibration), counting pulses with constant frequency (1 MHz) are generated by the Mössbauer electronics for the first two channels of the MCS instead of the interferometer pulses. Reduced by a factor of 10, the pulses in the second channel are counted and thus measure the measurement time per channel: $B \cdot Z = N(2) \cdot 10\,\mu\mathrm{s}$

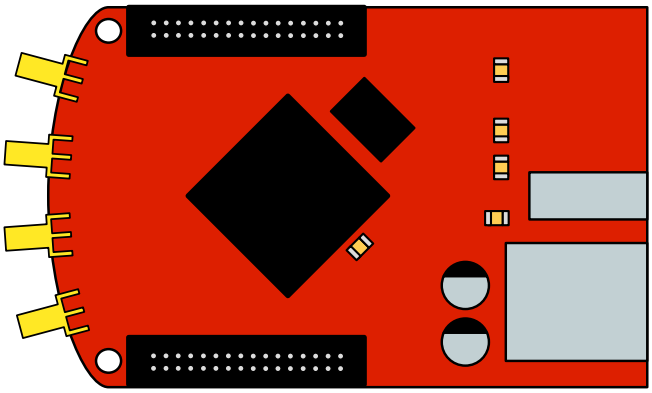

Figure 7.58: A schematic representation of the Red-Pitaya.

7.12.4.4 The Red-Pitaya

The Red-Pitaya, together with the program on a Linux-computer, form the core of the measurement system for measuring the actual Mössbauer effect. The Red-Pitaya itself consists of three components, a "traditional" CPU, an FPGA and two fast ADC. The data to be measured in this experiment is the height of the pulse from the detector and the corresponding velocity. To obtain this information, the signal generated by the proportional counter tube is sampled by the ADC on the Red-Pitaya at a high rate of $125 \cdot 10^6$ samples/s. The sampled voltage is then represented as a number (14-bit resolution) and transferred to the FPGA.

A digital signal filter is implemented in the FPGA, which detects the pulses of the proportional counter tube and then reads out their height together with the velocity. The data extracted by the filter is then passed to the CPU, which then forwards it to the Linux-computer. The FPGA has an important role in the processing chain, since only a FPGA can provide the computing resources required to handle the amount of data produced by the ADC. An FPGA can be configured for any data processing method with relatively little effort, which explains the very frequent and successful use of these chips in high energy physics experiments at CERN and other accelerator facilities.

In this case a trapezoidal filter with the necessary periphery is implemented so that a pulse is detected and its height is read out together with the velocity of the sample. However, the velocity is not stored as the actual velocity, but as the MCS-address of the function generator. Through the calibration measurement with the laser interferometer the address can be translated into a velocity in the offline analysis.

The trapezoidal filter has five parameters that must be determined for this experiment and transfered to the Red Pitaya. The parameters are described in Tab. 7.2.

Table 7.2: Red Pitaya parameters for die definition of the trapezoidal filter.

Name	Description
K	Duration of rising and declining slope of the resulting trapezoid.
L	Duration of the upper "plateau" of the trapezoid.
M	Mean lifetime of the exponentially declining slope of the peaks to which the trapezoidal filter should be sensitive.
peakthresh	Minimum height of a trapezoid to be recorded.
accumtime	This time specifies an interval in which all measured peaks are combined to one peak.

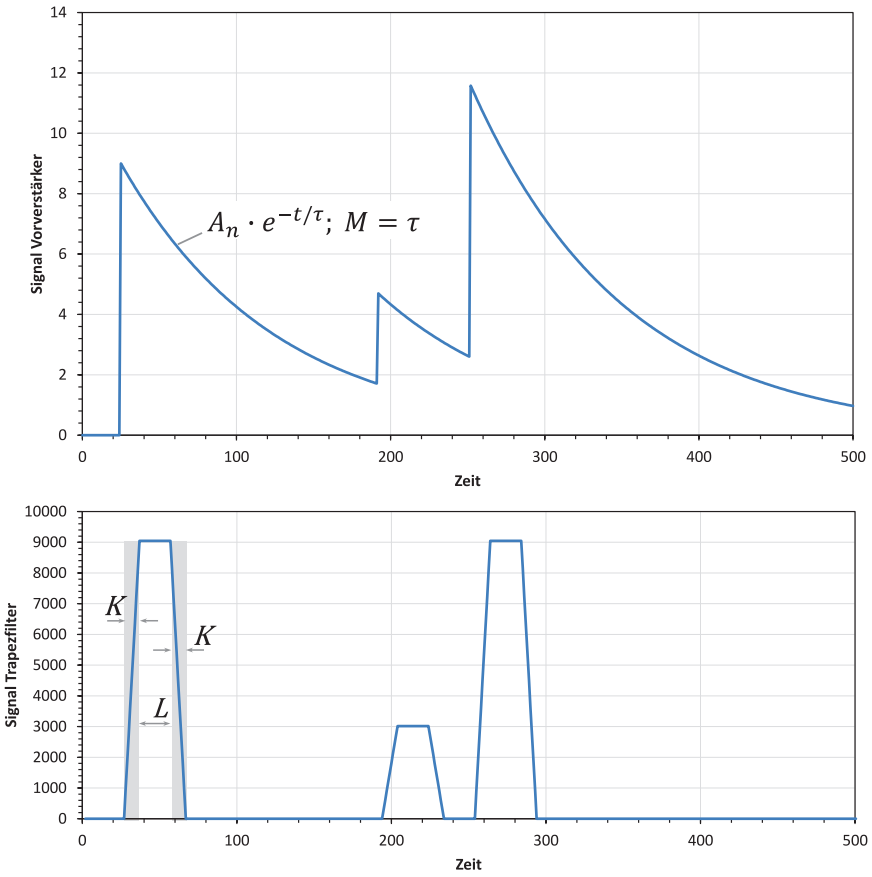

Figure 7.59: Schematic picture of the funtion of a trapezoidal filter. Top: signal from the pre-amplifier. Bottom: signal after the trapezoidal filter.

The parameters K and L of the filter affect the duration of the output trapezoid. At the same time, they indicate over how many ADC samples the filter should average for the generation of the trapezoid from the input signal. Accordingly, the period of the noise superimposed on the actual pulse should be significantly shorter than $T_{\text{Filter}} \cdot (2K + L)$. T_{Filter} is the sampling time of the ADC/filter system. However, the total time of the trapezoid should not be too long, otherwise a so-called "pileup" can occur when two trapezoids overlap and can no longer be separated from one another.

The M parameter is part of the algorithm in the FPGA program that compensates for the exponential decay of the input signal. M indicates which Time constant for the decay of the signal is assumed. If M does not match the real time constant of the signal to be measured, then artefacts arise in the output signals that come from the erroneous correction of the time decay. The following applies: $\tau = M \cdot T_{\text{Filter}}$.

The program of an FPGA corresponds to a clocked digital circuit, which in principle executes each program line per clock simultaneously. The incoming data is shifted to the next program step with each clock cycle. The previous program step is free for the next data. An FPGA thus allows maximum parallelized processing of digital data.

Since the output signal of the filter still shows noise at low energies, a threshold must be set, below which the noise pulses can be suppressed already in the circuit of the FPGA. If the threshold is set too low, the circuit of the FPGA can still keep up, but the Linux system following the FPGA is overloaded and the measurement is then automatically aborted. The data already measured are not lost, but this complicates and slows down the execution of the experiment and

the evaluation becomes more complex. If the threshold is set too high, the pulses of the signal to be measured will be discarded. The rule of thumb for this parameter is as low as possible, but as high as necessary.

The "accumtime" parameter is a consequence of the specific implementation of the filter. A peak detector algorithm is used to indicate that there is a pulse. However, this is just a very simple filter that triggers, for instance, with the number sequence 123, 124, 123, since the central number is larger than its neighbors. Below the "peakthresh", all peaks found in this way are discarded. A problem occurs however, when a sequence of numbers, like the one shown above, occurs several times on the plateau of a trapezoid. A single trapezoid would then appear in the measured data set as multiple events and falsify the results. The steps of the solution chosen here to avoid this problem are listed in Table 7.3.

Table 7.3: Steps to suppress multiple peaks caused by signal fluctuations.

Step	description
1	If a peak is detected in the output signal of the trapezoidal filter, which is above "peakthresh", a countdown is started.
2	While the countdown is running, all measured peaks are stored in a temporary memory. It is assumed that all these peaks have occurred on the plateau of a trapezoid, i.e. belong to the same signal peak.
3	After the countdown, the measured peak with the highest value is forwarded to the Linux system as the final peak.

Due to the way it works, this parameter should be chosen so that it is of the duration of the plateau. However , the exact values affect the appearance of the pulse height spectrum, as dead-time artifacts arise. The value should therefore be set in the experiment in such a way that "accumtime" is chosen neither too large nor too small, but at the same time minimize the artefacts. The artifacts are in the pulse height spectrum seen as a fine, comb-like structure superimposed on the actual spectrum. Since "accumtime" is only a result of the specific implementation, this does not have to be specified for the experiment and is calculated automatically by the software.

Caveat: Since the measurement with the Red Pitaya is still under development, it is possible that the data acquisition is not working reliably. In this case the previous hardware setup is used for this experiment without prior notice. Here, the energy window is set to a fixed value with a window discriminator. The Multi-Channel-Scaler is a PCI board in a Windows computer. Apart from the fixed energy window, the analysis steps are the same as with the R:P. measurement.

7.12.5 Literature

Introduction Chapters 1 – 6 in this script
Mössbauer effect [1], [26], [36], [39]
Detectors [18], [19]
Electronics [18], [19], [21]
Nuclear physics [1], [26], [27]

7.12.6 Details

The nuclear magneton is

$$\mu_K = 5.050783699(31) \cdot 10^{-27}\,\mathrm{J/T} = 3.1524512550(15) \cdot 10^{-8}\,\mathrm{eV/T} \tag{7.201}$$

The quadrupole moment of the excited state of ^{57}Fe is

$$Q = (0,21 \pm 0,01) \cdot 10^{-28}\mathrm{m}^2 \tag{7.202}$$

The following applies to the cycle time of the Red Pitaya filter system

$$T_{Filter} = 256\mathrm{ns} \tag{7.203}$$

Appendix A

Tables

A.1 Energy level schemes of applied nuclides

In the following, the term schemes of the nuclides used in the laboratory course are given. They are all excerpts, only the relevant states and transitions are shown. The states are characterised by angular momentum and parity. As far as available, the average lifetimes are also given. The numbers on the right side indicate the energy of the states in MeV. They refer to the *atomic*, not *nuclear* masses converted into energies. This is based on historical grounds: in mass spectrometers, the *atomic* masses are determined.

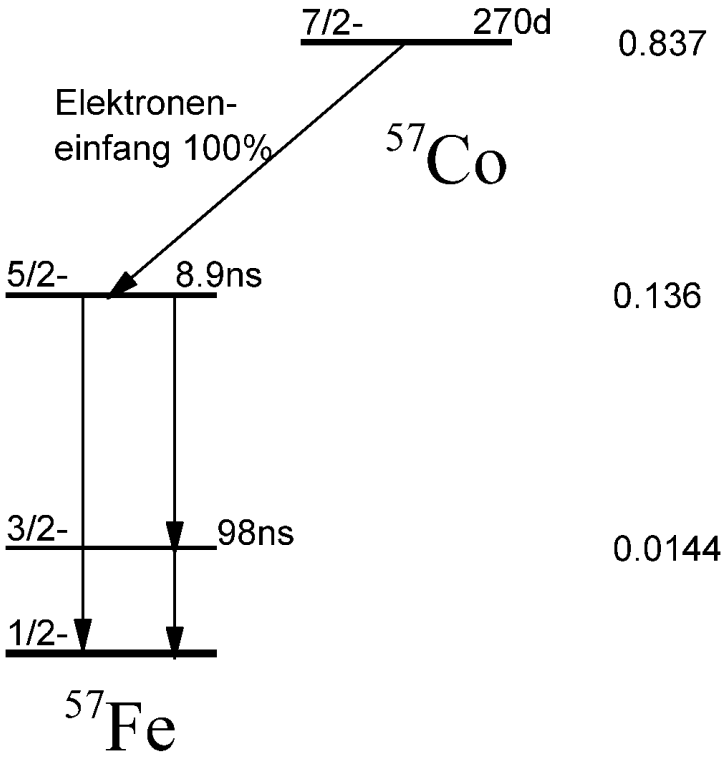

Energy levels of ^{57}Co $\rightarrow^{57}$Fe.

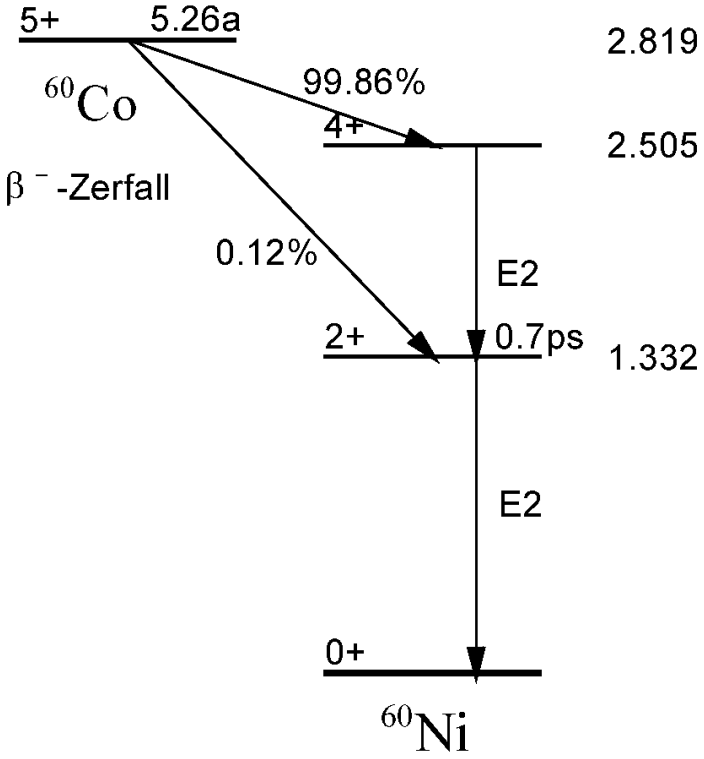

Energy levels of ^{60}Co $\rightarrow^{Ni}$Fe.

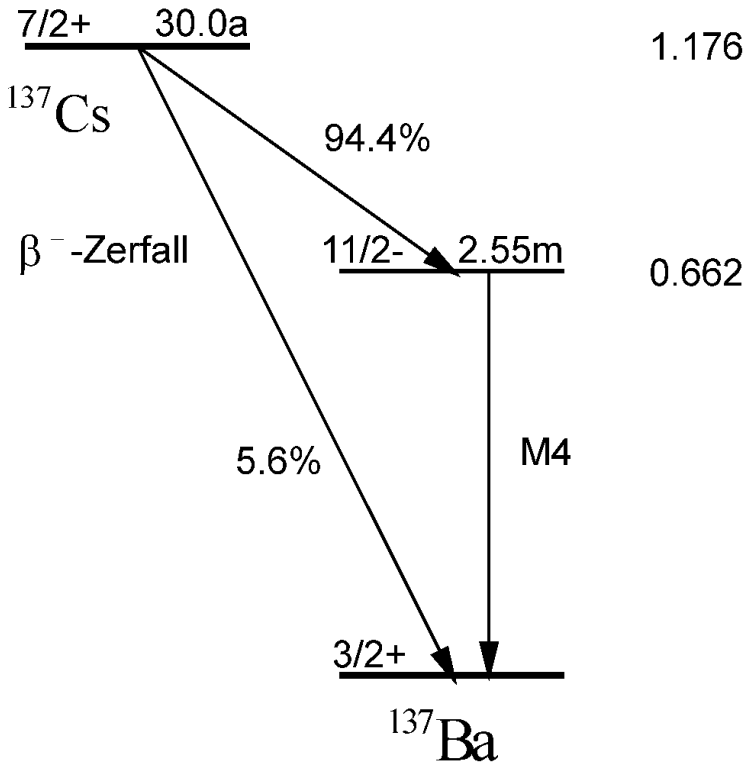

Energy levels of ^{137}Cs $\rightarrow^{137}$Ba.

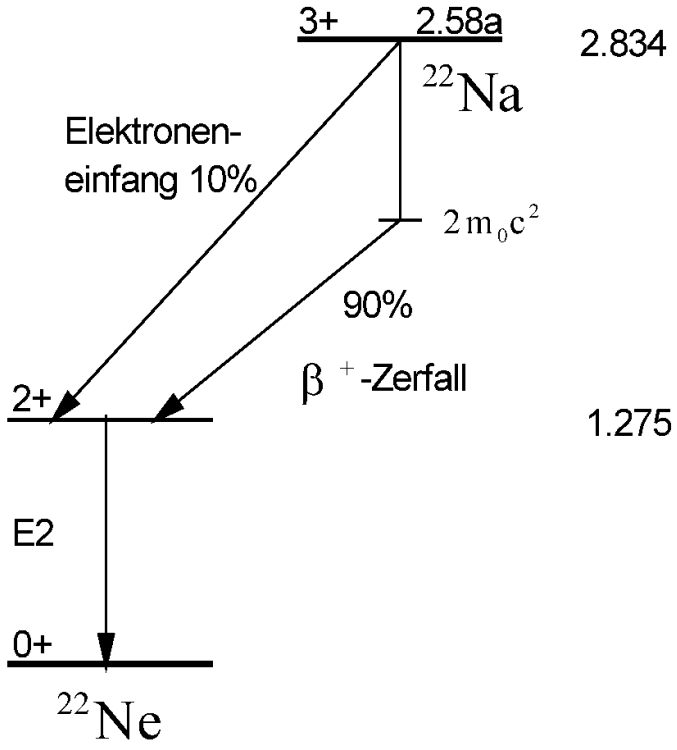

Energy levels of ^{22}Na $\rightarrow^{22}$Ne.

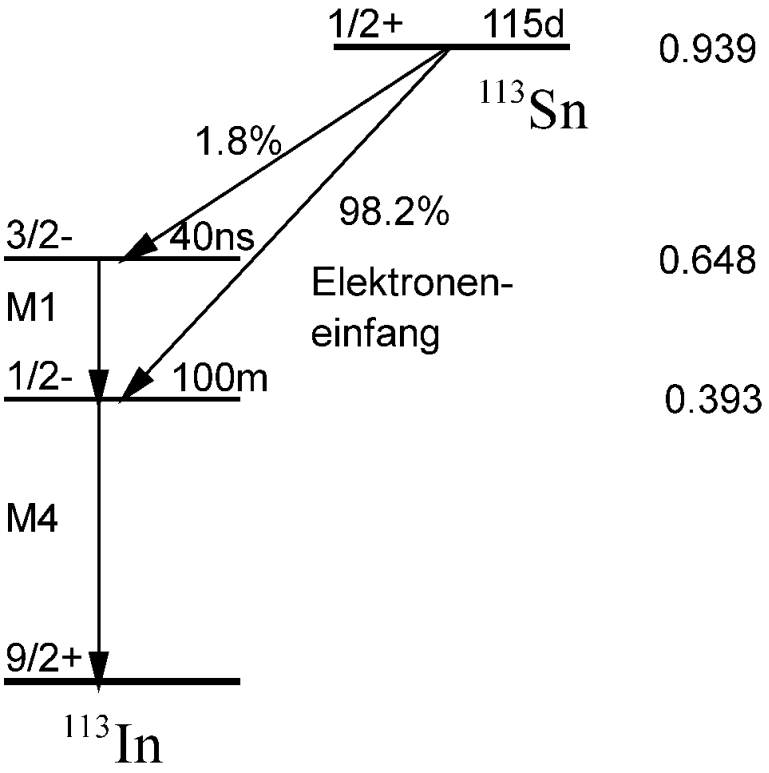

Energy levels of ^{113}Sn $\rightarrow^{113}$In.

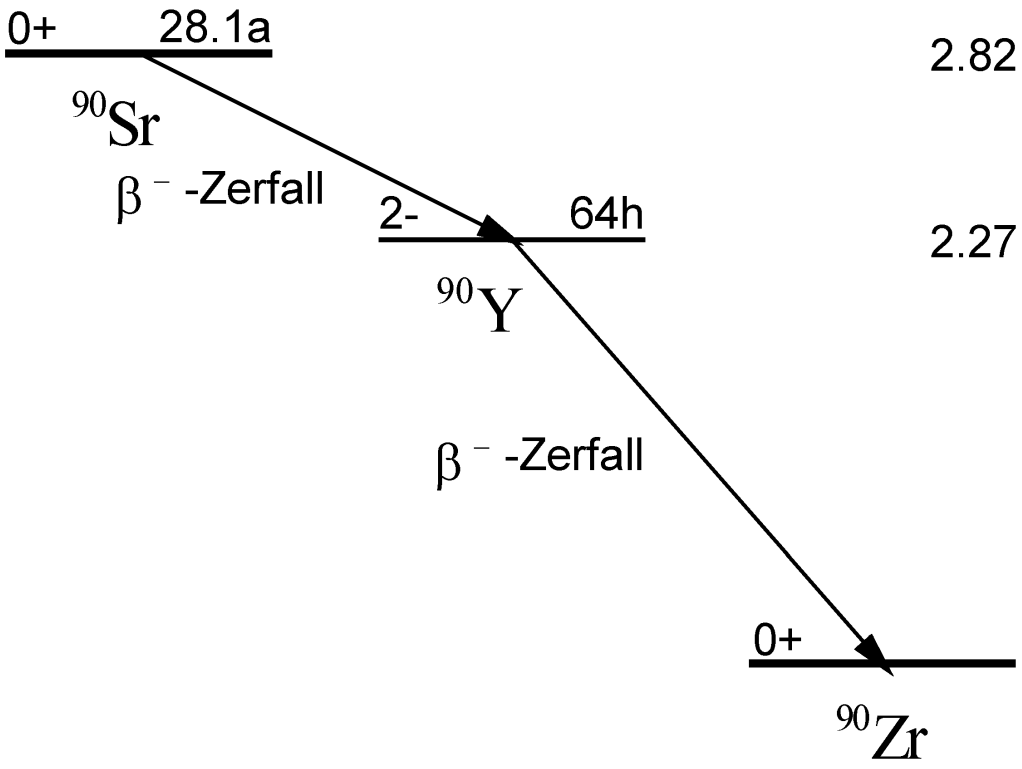

Energy levels of ^{90}Sr $\rightarrow^{90}$Y $\rightarrow^{90}$Zr.

A.2 Fermi funktionen

The electron or positron emitted during the β-decay is decelerated or accelerated by the Coulomb field of the daughter nucleus. The Fermi function $F(Z, E_\beta)$ is a correction factor which takes into account this effect on the shape of the energy spectrum E_β of the β particles. The introduction of dimensionless expressions for the reduced energies and momenta

$$\epsilon = \frac{E + m_0c^2}{m_0c^2}, \quad \epsilon_0 = \frac{E_0 + m_0c^2}{m_0c^2}, \quad \eta = \frac{p}{m_0c}, \quad \epsilon = \sqrt{\eta^2 + 1} \tag{A.1}$$

and the reduced Fermi function

$$G(Z, \eta) = \frac{\eta}{\epsilon} \cdot F(Z, \epsilon) \tag{A.2}$$

simplify the complex calculation. It was tabulated by Rose (1955) [10] for all nuclear charge numbers Z over a wide momentum range for β^- and β^+ decays. A further simplification is provided by the parameterization in [46]. Here the Fermi function is described as

$$F(Z, \epsilon) = \sqrt{A(Z) + \frac{B(Z)}{\epsilon - 1}} \tag{A.3}$$

which is parameterized using A and B listed in table A.1 for different allowed β^- decays. Since this parameterization only depends on the atomic number Z, but not on the number of neutrons, it can also be used for other β^- isotopes of the same element if it is an allowed transition. For forbidden transitions, the nuclear radius plays a greater role, so this simplification no longer applies. The accuracy of the parameterization is given as 3%. The function applies to $\eta > 0.3$ ($\epsilon = \sqrt{\eta^2 + 1} > 1.044$). The reduced Fermi function can be obtained with

$$G(Z, \epsilon) = \sqrt{A + \frac{B}{\epsilon - 1}} \cdot \frac{\eta}{\epsilon}. \tag{A.4}$$

For $\eta < 0.3$, $G(Z, \epsilon)$ can be approximated by linear extrapolation.

Table A.1: Values for different β^- isotopes (Z: nuclear charge number of the daughter nucleus) of A and B in the approximate formula for the Fermi function [46].

isotope	E_0 (keV)	$Z(daughter)$	A	B
$^{6}_{2}$He	3500	3	1.1578	0.0208
$^{10}_{4}$Be	560	5	1.2985	0.0391
$^{14}_{6}$C	156	7	1.4864	0.0616
$^{19}_{8}$O	3200	9	1.5606	0.1015
$^{24}_{11}$Na	1390	12	1.8275	0.1711
$^{32}_{15}$P	1730	16	2.2243	0.3206
$^{35}_{16}$S	167	17	2.4496	0.3527
$^{36}_{17}$Cl	713	18	2.4981	0.4128
$^{45}_{20}$Ca	257	21	2.9595	0.5895
$^{49}_{21}$Sc	2001	22	3.0634	0.6814
$^{51}_{22}$Ti	2140	23	3.2342	0.7655
$^{69}_{30}$Zn	925	31	5.0709	1.8500
$^{75}_{32}$Ge	1190	33	5.7344	2.2849
$^{81}_{34}$Se	1510	35	6.4481	2.8135
$^{90}_{38}$Sr	546	39	8.2372	4.2458
$^{90}_{39}$Y	2274	40	8.6994	4.7116
$^{93}_{40}$Zr	600	41	9.3330	5.2025
$^{99}_{43}$Tc	292	44	11.1489	7.0753
$^{105}_{45}$Rh	565	46	12.9051	8.6289
$^{121}_{50}$Sn	393	51	17.8821	14.2645
$^{137}_{55}$Cs	1173	56	25.2007	23.6665
$^{170}_{69}$Tm	967	70	69.6398	103.7297
$^{185}_{74}$W	430	75	106.2196	179.7139
$^{204}_{81}$Tl	770	82	161.9399	403.5753
$^{210}_{83}$Bi	1170	84	180.5666	512.7254

Appendix B

Radiation protection instruction

Radiation protection instruction for the performance of laboratory courses in nuclear physics at the Faculty of Physics in the context of the physics studies at the Karlsruhe Institute of Technology (KIT).

(Version 1.3 from Oct. 2016)

Introduction

These radiation protection instructions contain the radiation protection regulations to be observed when carrying out laboratory training. They refer to the following legal principles:

- Regulation on the protection against damage caused by ionising radiation (Radiation Protection Ordinance - StrlSchV) of 20.7.2001; (last amended Jan 2008)
- Approval Notice LU/321/84 of 21.01.1985 from the Gewerbeaufsichtsamt Karlsruhe.

The radiation protection instructions are to be handed out to all lab supervisors who may be exposed to radiation. As part of the briefing they have to acknowledge the receipt of the instructions by signature before they begin their work.

The material scope of application covers laboratory courses in which radioactive substances are handled.

The lab supervisors are obliged to comply with the radiation protection instructions and require the students to do so.

B.1 Organization of radiation protection

- **The duties of the radiation protection officer are performed by:**
  Dr. Frank, Gerhard, Radiation Protection Officer, Tel.: (KIT)24660
- **The responsible radiation safety officer is:**
  . Dr. Simonis, Hans Jürgen, Tel.: 43577 (North Campus: 24300 [0721 608 24300])
- **The representative of the radiation safety officer is:**
  . Dr. Wolf, Joachim, Tel.: 47510 (North Campus: 25532 [0721 608 25532])
- **At the experimental setups the respective supervisor is responsible for the observation of the radiation protection regulations.**

The radiation protection officer is in charge of implementing the necessary protective measures in his area of responsibility and is authorized to give instructions to the employees. They must follow his instructions. During the absence of the radiation protection officer, all rights and duties are transferred accordingly to his representatives. The laboratory supervisors are responsible for compliance with the radiation protection regulations at the experimental setups assigned to them.

B.2 Operating procedure essential for radiation protection

B.2.1 Objective of the laboratory courses

The physics laboratory courses P-II and the advanced laboratory course are an integral part of the physics studies. In the nuclear physics experiments, the students should become familiar with the properties of ionising radiation and the different instruments used in experiments with radioactive materials.

The radioactive materials used are enclosed in a solid, inactive casing or permanently embedded in solid inactive materials in such a way that under normal operational stress, the escape of radioactive materials is safely prevented.

B.2.2 Prerequisites for work

Students must have participated in the radiation protection training before the start of the practical work. This takes place at the beginning of each semester as part of the introductory lecture to the laboratory course. In addition, the students must have prepared themselves for the specific experimental activity prior to each experiment based on the information provided in advance. The supervisor of the respective experiment has the duty to prohibit unprepared students from carrying out the experiment.

B.2.3 Rules of conduct

- Only those students are allowed to enter the rooms F2-(19-22) who work there on experiments.
- In rooms F2-(19-22), rod dosimeters are carried to control the personal dose.
- The supervisors take the sources from the bunker and bring them back after use.
- Eating, drinking and smoking are strictly prohibited in rooms F2-(19-22).
- When leaving the rooms, the hand-and-foot radiation monitor must be used.

B.2.4 Rules of Operation

General regulations:

- The radioactive materials may only be handled by persons who have been designated for this purpose by the radiation protection officer and who have received appropriate training.
- The radioactive materials are to be stored in the lead bunker in the room adjacent to F2-19. (Excluded are the permanently installed sources in the experiments neutron activation, alpha absorption, Compton scattering, Mößbauer effect, neutron diffusion)
- Dangerous goods (e.g. flammable liquids) and corrosive substances must not be stored in the source storage room.

- The bunker is locked separately during the periods when there is no laboratory course.
- **Students are not allowed to enter the bunker.**
- The radioactive sources must be visually inspected for damage before use. Among other things, it is to be pay attention to deformation, cracks, scratches, porous areas, corrosion.
- If damage or leakage is suspected, the radioactive source must not be used and the radiation protection officers has to be notified immediately.
- Defective radioactive sources must be stored separately until disposal. They must not be used, opened, be repaired or eliminated.
- Detailed records must be kept of the receipt and removal of radioactive materials. In case of loss or discovery of radioactive substances, the radiation protection officer shall be informed immediately.
- Labels, which have been affixed by the radiation protection officer or on his instructions, must not be removed or changed without his knowledge and consent.
- The radioactive sources are only to be used for their intended purpose.
- No changes are made to the sources which may affect radiation protection.

When handling radioactive materials, the following measures must be taken to prevent theft or other loss and unauthorized interference with them:

- At the beginning of the experiment, the supervisor fetches the sources intended for his experiment from the bunker.
- During the laboratory course at least one supervisor must be present in the rooms at all times.
- At the end of the experiment, the supervisor brings the sources back into the bunker.
- The supervisor of the experiment completed last ensures that the bunker is locked again.

B.2.5 Conveyance of Radioactive Materials

The transport of radioactive materials (packaging, transfer for transport, receipt, unpacking) is subject to the conditions of the StrlSchV and the GGVSE. Such a procedure does not occur in the normal course of laboratory work. For the transport of radioactive materials, the instructions of the radiation protection officer must be strictly observed.

B.2.6 Radiation Protection Areas and Access Regulations

The use of radioactive materials establishes a supervised operational area. This includes the entire suite of rooms F2-19, F2-20, F2-21, F2-22.

Access is only possible via room F2-19. Before leaving the area, the available hand-and-foot radiation monitor must be used. The direct access doors of the three other rooms are escape doors and as such may only be used in the event of fire.

B.2.7 instruction

Before the first laboratory day a radiation protection instruction takes place at the beginning of the semester. Participation is mandatory for students and supervisors and is documented by signing an attendance list. If a student could not be present for important reasons, he or she must arrange a new date with the radiation protection officer. Students who have not taken part in a radiation protection instruction are excluded from carrying out nuclear physics experiments.

Participants of the advanced laboratory course must attend radiation protection training again after one year at the latest if they still have to carry out further nuclear physics experiments.

B.2.8 Determination of body dose

Supervisors and students do not become occupationally exposed persons within the meaning of the Radiation Protection Ordinance through their work. The expected value of the effective dose is below 1 mSv per year. It is therefore not necessary to measure the personal dose with official dosimeters. Instead, the radiation dose is monitored with rod dosimeters. For this purpose, each student carries a rod dosimeter during the entire experiment. The scale value read off must be entered with name and signature in the available logbook at the beginning and after completion of the experiment. In addition, the hand-and-foot monitor must be used before leaving the laboratory.

B.3 Functional test and maintenance

All facilities, installations and equipment necessary for radiation protection must be inspected regularly at least once a year. The functional test of the monitoring equipment must be carried out before each use. It includes checking the battery and measuring the ambient radiation.

B.4 Alarm drills, accidents and incidents

The storage rooms are in accordance with the provisions of the Radiation Protection Ordinance and in agreement with the fire brigade, marked clearly visible at the entrance with the radiation sign, the word “RADIOACTIVE” and the required hazard group classification of the fire department.

The behaviour in the event of incidents and accidents must be discussed in the context of the instructions.

In case of safety-relevant events (e.g. damage to radiators, suspected contamination, theft, fire), the radiation protection officer shall be informed immediately.

B.4.1 Alarm drills

Special alarm drills are not necessary and therefore not planned.

B.4.2 Accidents and incidents

e.g. damage to a sealed radioactive material:

- Notification according to alarm plan
- All unaffected students leave the laboratory
- The radiation protection officer shall supervise the contamination or incorporation control and, if necessary decontamination, primarily of persons

- The radiation protection officer decides on the release of the rooms
- In the event of fire, each of rooms F2-19, 20, 21, 22 may be directly exited through an escape door.

B.5 Interference of third parties, loss of a radioactive sources

The following measures shall be taken to prevent the loss of radioactive materials and prevent unauthorized use:

- All radioactive materials not permanently installed in your apparatus shall be stored in the lead bunker in the adjacent room of F2-19 as long as they are not used for their intended purpose. The apparatus with permanently installed sources are the measuring set-ups for neutron activation, alpha absorption, Compton scattering, Mößbauer effect and neutron diffusion.
- Unauthorized persons have no access to the storage room.
- Outside the laboratory hours, the entire area F2-(19-22) must be kept locked. In addition, access to the bunker must be kept separately locked.
- The storage rooms are to be marked with the radiation sign, the word “RADIOACTIVE” and the required hazard group classification of the fire brigade. mark.
- Detailed records must be kept of all incoming and outgoing radioactive substances.
- In the event of loss or discovery of radioactive materials, the radiation protection officer must be informed immediately.
- When handling the radiation sources, the following measures must be taken to prevent theft, loss of radioactive materials and unauthorised interference with them:
  - During the handling of the sources, at least one supervisor must be present in the room.
  - During the breaks the laboratory room must be locked.
  - After the experimental work, the radiation sources must be kept under lock and key.

This amended radiation protection instruction comes into force with immediate effect.

Karlsruhe, 31.10.2016

Bibliography

[1] Marmier, Sheldon, *Physics of Nuclei and Particles*, Vol. I, Academic Press, New York, London, 1969

[2] Aker, M. et al., *Improved Upper Limit on the Neutrino Mass from a Direct Kinematic Method by KATRIN*, Phys. Rev. Lett. **123** (2019)

[3] M. Aker et al., *Analysis methods for the first KATRIN neutrino-mass measurement*, Phys. Rev. D 104, 012005 (2021)

[4] M. Aker et al., *First direct neutrino-mass measurement with sub-eV sensitivity*, arXiv:2105.08533 (2021) JINST 16 T08015 (2021)

[5] M. Aker et al., *The design, construction, and commissioning of the KATRIN experiment*, JINST 16 T08015 (2021)

[6] Thomas Berghöfer, *Messung der Driftgeschwindigkeit von Elektronen in Gasen*, Diplomarbeit, Universität Karlsruhe, 2001 (Auszug als PDF-File auf der Praktikumsseite verfügbar)

[7] Th. Berghöfer, J. Blümer, J.R. Hörandel, *A measurement of drift velocities of electrons in xenon-methane mixtures*, Nucl. Inst and Meth. A 525 (2004) 544-552

[8] L.G.H. Huxley und R.W. Crompton, *The Diffusion and Drift of Electrons in Gases*, John Wiley + Sons, Inc. New York (Wiley Series in Plasma Physics), 1974

[9] William R. Leo, *Techniques for Nuclear and Particle Physics Experiments*, Springer-Verlag Berlin/Heidelberg, 1987

[10] K. Siegbahn *Beta- and Gamma-Ray Spectroscopy*, North Holland Publishing Company, Amsterdam, 1955

[11] K. Siegbahn *Alpha-, Beta- and Gamma-Ray Spectroscopy*, Vol. 1+2, North Holland Publishing Company, Amsterdam, 1966

[12] R.G. Helmer and V.P. Chechev, `http://www.nucleide.org/DDEP_WG/Nuclides/Cs-137_tables.pdf`, (2007)

[13] Benedetti, Corben, Am. Nucl. Sci., 4, (1950)

[14] Benedetti; *Nuclear Interaction*, J. Wiley & Sons, New York, 1964

[15] Feynman; *Theory of Fundamental Processes*, Benjamin Inc., New York, 1962

[16] Weizel; *Lehrbuch der theoretischen Physik*, Band 2, Springer Verlag, Berlin, Heidelberg, New York, 1958

[17] Loeb; *Basic Processes of Gaseous Electronics*, University of California Press, 1961

[18] Neuert; *Kernphysikalische Meßverfahren*, G. Braun, Karlsruhe

[19] Smith; *A Textbook of Nuclear Physics*, Pergamon Press, New York, 1965

[20] Hamamatsu Photonics K. K.; *Photomultiplier Tubes – Basics and Applications*, 2007, http://www.hamamatsu.com/resources/pdf/etd/PMT_handbook_v3aE.pdf

[21] Birks; *The Theory and Praxis of Scintillation Counting*, Pergamon Press, New York, 1964

[22] Kowalsky; *Nuclear Electronics*, Springer Verlag, Berlin, Heidelberg, New York, 1970

[23] Weinzierl, Drosg; *Nuklearelektronik*, Springer Verlag, Berlin, Heidelberg, New York, 1971

[24] Simons; *Handbuch der Physik*, Band 34, Springer Verlag, Berlin, Heidelberg, New York

[25] Deutsch, Berka, Siegbahn (Editor), *Alpha-, Beta- and Gamma-Ray Spectroscopy*, Vol 2, 1965

[26] Stewart, Roellig; *Positron Annihilation*, Academic Press, New York, 1964

[27] Melissinos; *Experiments in Modern Physics*, Academic Press, New York, 1964

[28] Segré; *Nuclei and Particles*, Academic Press, New York, 1965

[29] Wu, Moszkowski; *Beta Decay*, J. Wiley & Sons, New York, 1966

[30] Schopper; Fortschritte der Physik 5 (1957) u. 8 (1960)

[31] Schpolski; *Atomphysik*, Band 2, 1965

[32] Heisenberg; *Kosmische Strahlung*, Springer Verlag, Berlin, 1956

[33] Hayakawa; *Cosmic Ray Physics*, J. Wiley & Sons, New York, 1969

[34] Beckurts, Wirtz; *Neutron Physics*, Springer Verlag, Berlin

[35] Wirtz; *Elementare Neutronenphysik*, Springer Verlag, Berlin

[36] Riezler u. Kopitzki; *Kernphysikalisches Praktikum*, G. B. Teubner, Stuttgart

[37] Wegener; *Der Mößbauereffekt und seine Anwendungen*, BI-Taschenbuch, Mannheim

[38] Valvo; *Halbleiterhandbuch*

[39] Büker; *Theory und Praxis der Halbleiterdetektoren für Kernstrahlung*, Springer Verlag, Berlin, Heidelberg, New York, 1971

[40] Frauenfelder; *The Moessbauereffect*, W. A. Benjamin Inc., New York, 1962

[41] Schopper; *Weak Interactions and Nuclear Beta Decay*, North Holland Publishing Company, Amsterdam, 1966

[42] Schopper; *Measurement of Circular Polarization of γ-Rays*, Nucl. Instr., 3 (1958)

[43] McMaster; *Matrix Representation of Polarization*, Rev. Mod. Phys. 33 (1961)

[44] Wolfendale; *Cosmic Rays*, G. Newnes Ltd., London, 1963

[45] Hughes a. Wu; *Muon Physics*, Academic Press, New York, San Francico, London, 1975

[46] P. Venkataramaiah et al., *A simple relation for the Fermi function*, J. Phys. G: Nucl. Phys. **11** (1985) 359–364

[47] F. Hartmann, *Evolution of Silicon Sensor Technology in Particle Physics*, Springer Tracts Mod. Phys. (2017)

[48] U. Elicabuk, *Charakterisierung von n-in-p Streifensensoren für das Phase-2-Upgrade des CMS-Detektors*, BA (ETP/KIT) (2019)

[49] Alibava Systems, *Activity Book for Students*, www.alibavasystems.com

[50] G. Quast, *Vorlesung "'Computergestützte Datenauswertung (CgDA)"'*, http://www.etp.kit.edu/~quast/CgDA

[51] G. Quast, *Skript zur Anapssung von Modellen an Messdaten*, http://ekpwww.etp.kit.edu/~quast/Skripte/Chi2Method.pdf

[52] G. Quast, *Jupyter Tutorials zu Statistik, Fehlerrechung und Datenanalyse*, http://ekpwww.etp.kit.edu/~quast/jupyter/jupyterTutorial.html

[53] G. Quast, *Tutorial zur Modellanpassung im Fortgeschrittenenpraktikum Physik*, http://ekpwww.etp.kit.edu/~quast/jupyter/advancedFitting.ipynb

[54] G. Quast, *Tutorial zur Modellanpassung mit der Maximum-Likelihood Methode*, http://ekpwww.etp.kit.edu/~quast/jupyter/negLogLFits.ipynb

[55] J. Gaeßler, C. Verstege, G. Quast, D. Savoiu, *kafe2 - an open-source package for parameter estimation from measured data*, https://github.com/dsavoiu/kafe2

[56] G. Quast, *PhyPraKit.phyFit - a package for data acquisition, data visualisation and parameter estimation*, https://github.com/GuenterQuast/PhyPraKit

[57] A Jupyter-friendly Python interface for the Minuit2 C++ library maintained by CERN's ROOT team, https://iminuit.readthedocs.io/en/stable/

[58] M. Aker, et al., *Improved upper limit on 3038 the neutrino mass from a direct kinematic method by KATRIN*, Phys. Rev. Lett. 123 (2019) 221802

[59] KATRIN collaboration, *KATRIN design report*, FZKA scientific report 7090 (2005), https://publikationen.bibliothek.kit.edu/270060419

[60] KATRIN collaboration, *The Design, Construction, and Commissioning of the KATRIN Experiment*, submitted to JINST (2021), arXiv 2103.04755

[61] A. Picard, et al., *A solenoid retarding spectrometer 3056 with high resolution and transmission for keV electrons*, NIM B **63** (1992) 345

Index